Energy Systems, Sustainable Manufacturing, and Intelligent Engineering Technologies

---

Hasan Köten

BİDGE Yayınları

Energy Systems, Sustainable Manufacturing, and Intelligent Engineering Technologies

Editor: HASAN KÖTEN

ISBN: 978-625-8567-92-2

1st Edition
Page Layout By: Gözde YÜCEL
Publication Date: 2025-12-25
BİDGE Yayınları

Certificate No: 71374

www.bidgeyayinlari.com.tr - bidgeyayinlari@gmail.com
Krc Bilişim Ticaret ve Organizasyon Ltd. Şti.
Güzeltepe Mahallesi Abidin Daver Sokak Sefer Apartmanı No: 7/9 Çankaya / Ankara

Energy Systems, Sustainable Manufacturing, and Intelligent Engineering Technologies

Preface

The growing global demand for sustainable, energy-efficient, and environmentally responsible engineering solutions has placed advanced manufacturing processes, energy systems, and thermal sciences at the forefront of contemporary research. Rapid developments in computational methods, experimental techniques, and data-driven modeling approaches are reshaping traditional engineering practices and enabling more efficient, resilient, and sustainable technological systems. This book brings together a collection of original and high-quality research studies that address critical challenges in sustainable manufacturing, advanced energy conversion, thermal management, and intelligent engineering systems. The chapters presented in this volume reflect a multidisciplinary perspective, integrating mechanical engineering, energy systems, materials science, and artificial intelligence to offer both fundamental insights and practical engineering solutions. The contributions cover a wide range of topics, including the relationship between power consumption, vibration, and surface integrity in machining processes, advanced energy and exergy analyses of photovoltaic-thermal systems enhanced with nanofluid cooling and phase change materials, and the performance optimization of PEM electrolyzers through mechanical and structural design considerations. In addition, the book presents state-of-the-art studies on natural convection modeling using finite element methods, data-driven prediction of combustion characteristics using machine learning and Gaussian process regression, and comprehensive assessments of electric versus internal combustion engine UAVs in terms of performance, cost, and sustainability. Further chapters address emerging themes such as thermal aging and performance degradation in building envelopes, bibliometric analyses of global research trends, machine learning applications in thermal comfort, and strategic perspectives on the role of nuclear energy in achieving carbon-neutral maritime transportation. The volume is complemented by critical reviews on innovative wind turbine blade designs and recent technological advancements in cold chain transportation systems, highlighting both opportunities and sustainability challenges. This book is intended to serve as a valuable reference for academicians, researchers, graduate students, and industry professionals working in the fields of sustainable manufacturing, renewable and alternative energy systems, thermal engineering, and intelligent system design. By combining experimental investigations, numerical modeling, and data-driven methodologies, the chapters aim to contribute to the advancement of knowledge and to inspire future research and technological innovation. The editor would like to express sincere gratitude to all contributing authors for their scientific rigor and dedication, as well as to the reviewers and editorial team for their valuable support throughout the publication process. It is our hope that this volume will make a lasting contribution to the scientific literature and support the global transition toward a more sustainable and energy-efficient future.

Prof. Dr. Hasan KÖTEN
Head of Mechanicale Engineering Department
Istanbul Medeniyet University

İÇİNDEKİLER

INVESTIGATION OF THE RELATIONSHIP BETWEEN POWER CONSUMPTION AND VIBRATION UNDER DIFFERENT CUTTING CONDITIONS FOR SUSTAINABLE MANUFACTURING 1
ABİDİN ŞAHİNOĞLU

EXPERIMENTAL ENERGY AND EXERGY ANALYSIS OF A PHOTOVOLTAIC THERMAL SYSTEM INCORPORATING NANOFLUID COOLING AND PHASE CHANGE MATERIAL 27
KÜBRA KURTOĞLU SONTAY, ELİF ÖĞÜT, ABİD USTAOĞLU

INVESTIGATION OF ENERGY, VIBRATION AND SURFACE ROUGHNESS FOR SUSTAINABLE MANUFACTURING IN THE MACHINING OF 17 4 PH STAINLESS STEEL 57
ABİDİN ŞAHİNOĞLU

EFFECTS OF MECHANICAL ASSEMBLY AND STRUCTURAL PARAMETERS ON THE PERFORMANCE OF PEM ELECTROLYZERS 86
MUHAMMED ASIM KESERCİOĞLU, KUBİLAY HAN

FINITE ELEMENT-BASED STUDIES OF NATURAL CONVECTION IN ENCLOSURES FOR ENGINEERING SYSTEMS 117
GÜLNUR HAÇAT

PREDICTION OF ADIABATIC FLAME TEMPERATURE IN HYDROCARBON-HYDROGEN BLENDS: A GAUSSIAN PROCESS REGRESSION APPROACH CONSIDERING C/H ATOMIC RATIO, HYDROGEN FRACTION, AND EQUIVALENCE RATIO 130
MELİH YILDIZ, AHMET AKTÜRK

A PERFORMANCE, COST, AND SUSTAINABILITY OF ELECTRIC AND INTERNAL COMBUSTION ENGINE UAVS 153
OZTURK OZDEMIR KANAT, YASİN ÖZCAN

THERMAL AGING IN BUILDING ENVELOPES: A GLOBAL BIBLIOMETRIC MAPPING OF RESEARCH TRENDS 168
KAAN YAMAN, FATİH ÜNAL

THE IMPACT OF DYNAMIC AGING ON THERMAL PERFORMANCE DEGRADATION AND ENERGY CONSUMPTION OF BUILDING INSULATION MATERIALS 199
KAAN YAMAN, FATİH ÜNAL

ADVANCES IN THERMAL COMFORT WITH MACHINE LEARNING APPLICATIONS 223
M. ÖZGÜN KORUKÇU

THE NUCLEAR ENERGY RENAISSANCE IN MARITIME: A STRATEGIC OUTLOOK FOR A CARBON-NEUTRAL FUTURE 244
MEHMET ALİ KALLİOĞLU

DESIGN PRINCIPLES AND MATERIAL STRATEGIES FOR ARCHIMEDES SPIRAL WIND TURBINE BLADES: A CRITICAL REVIEW 274
BUKET ÖZTÜRK, UMUT SUCU, MUSTAFA ÖNCÜL

COLD CHAIN TRANSPORTATION: RECENT TRENDS, TECHNOLOGICAL INNOVATIONS, AND SUSTAINABILITY CHALLENGES 309
SERVET GİRAY HACIPAŞAOĞLU

CHAPTER 1

INVESTIGATION OF THE RELATIONSHIP BETWEEN POWER CONSUMPTION AND VIBRATION UNDER DIFFERENT CUTTING CONDITIONS FOR SUSTAINABLE MANUFACTURING

ABİDİN ŞAHİNOĞLU[1]

Introduction

Reducing energy consumption and consequently the carbon footprint in machining processes is of critical importance. This study investigates specific energy consumption and its associated carbon footprint. In this study, machining experiments were conducted at 3 different feed rates, 3 different cutting speeds, and 3 different depths of cut. Instantaneous power consumption was measured, and CO_2 emissions were calculated. The data obtained show that cutting parameters significantly affect energy consumption. It was calculated that CO_2 emissions related to energy consumption can be reduced. In this experimental study, power consumption, vibration,

---

[1] Assoc.Prof.Dr, Manisa Celal Bayar University, Technical Sciences Vocational School,Department of Machinery and Metal Technologies,0000-0003-0040-442X

and surface quality were examined together. Feed rate is the parameter that most significantly affects surface roughness with 78.26%, vibration with 70.39%, and power consumption with 62.86%. Depth of cut was found to have an effect of 4.35% on surface roughness, 21.92% on vibration, and 27.94% on power consumption. The cutting tool radius affects surface roughness by 15.73%, vibration by 2.16%, and power consumption by 2.25%. High-accuracy mathematical models have been created. Mathematical equations have been formulated to relate vibration and power consumption, power consumption and surface roughness, and surface roughness and vibration. Finally, optimum cutting conditions have been determined using multiple optimization techniques.

Global carbon emissions have a significant impact on industry. In machining, cutting forces are generated when removing chips from the workpiece. Friction and heat are generated. Machine tools require high motor power. Therefore, energy consumption is high. Efficient use of energy is important. With the increasing population and quality of life, more machines are used. The production of more machines leads to increased energy consumption. As energy consumption increases, CO_2 emissions increase. Increased CO_2 triggers global warming. Global warming causes many disasters. Energy efficiency is important to reduce the environmental damage caused by CO_2 emissions. It is important not only in the production phase but also in the use phase of machine parts. Surface quality in machine parts affects energy efficiency. Hardened steels provide a grinding-quality surface finish. Therefore, high surface quality is achieved with less energy consumption. Hard turning is a significant alternative to grinding. Hard turning is important for environmentally friendly manufacturing[1–12].

AISI 4340 steel has high toughness, strength, corrosion resistance, and wear resistance. Therefore, its use is becoming widespread in industry. Hardened AISI 4340 steels have a long service life due to their high wear resistance. They are used in the defense industry, aerospace, and other applications requiring high strength. However, machining AISI 4340 steel is difficult. Tool wear is very rapid. Machining has become possible with developed CBN and ceramic tools. However, these tools are expensive. Production has also become possible with developed high-quality coated carbide tools. However, determining appropriate cutting parameters is of great importance[13, 14].The aim of this study is to experimentally investigate the power consumption, vibration and surface roughness values in machining AISI 4340 steel.

Material Method

In this experimental study, AISI 4340 steel was used. The workpiece material was cut to a length of 270 mm. The surface and face of the material were machined. A center hole was drilled. Then, heat treatment was applied. It was cooled in oil. After tempering, a hardness value of 48 HRC was achieved.

The experiments were carried out on the CNC lathe. Measurements were taken in real-time with an energy analyzer integrated into the power unit of the machine. The PCE brand device was used as the power analyzer.

Hard turning is a finishing turning process. Good surface quality is desired. Therefore, cutting speeds of 120, 160, and 200 m/min were preferred. In addition, since the feed rates affect the surface roughness, 0.15, 0.20, and 0.25 mm/rev were selected. Due to the hardness and high yield strength of the material, the depth of cut was 0.2, 0.3, and 0.4 mm.

Experimental Results and Discussion

Experimental data showed that power consumption increased with increasing cutting speed, depth of cut, and feed rate. Since cutting force decreases with increasing cutting speed, instantaneous power consumption decreases somewhat. Cutting forces increase with increasing depth of cut and feed rate. Friction increases. Therefore, power consumption increases[15–20].

Energy Consumption; instantaneous current and machining time affect energy consumption. The energy required to remove chips is different for each material. As the hardness of the workpiece increases, its yield and fracture strength increase. As hardness increases, cutting force increases. Therefore, instantaneous current increases. Cutting force increases with increasing feed rate and depth of cut. Instantaneous power consumption increases. However, since machining time decreases, energy consumption decreases. However, when the hardness of the workpiece changes, although the instantaneous current increases, the machining time does not change. Therefore, energy consumption increases.

In machining hard materials, low cutting parameters are preferred because of their high fracture strength.

The test results with tools having tip radii of 0.4 mm and 0.8 mm, at cutting speeds of 130, 160, and 190 m/min, and depths of cut of 0.06, 0.1, and 0.14 mm are given in the table.

Table 1. Test results

	Re	a (mm)	v (m/min)	f (mm/rev)	Ra(μm)	Vib (mm/sn2)	Power C (W/h)
1	0,4	0,06	130	0,06	0,65	3,2	3140,7
2	0,4	0,06	130	0,1	1,05	3,8	3465,6
3	0,4	0,06	130	0,14	1,45	4,4	3790,5
4	0,4	0,06	160	0,06	0,6	3	3032,4

5	0,4	0,06	160	0,1	1,01	3,6	3357,3
6	0,4	0,06	160	0,14	1,4	4,2	3682,2
7	0,4	0,06	190	0,06	0,55	2,8	2924,1
8	0,4	0,06	190	0,1	0,95	3,4	3249
9	0,4	0,06	190	0,14	1,36	4,1	3573,9
10	0,4	0,12	130	0,06	0,75	3,5	3357,3
11	0,4	0,12	130	0,1	1,15	4,1	3682,2
12	0,4	0,12	130	0,14	1,56	4,7	4007,1
13	0,4	0,12	160	0,06	0,71	3,3	3249
14	0,4	0,12	160	0,1	1,12	3,9	3573,9
15	0,4	0,12	160	0,14	1,53	4,5	3898,8
16	0,4	0,12	190	0,06	0,63	3,2	3140,7
17	0,4	0,12	190	0,1	1,03	3,8	3465,6
18	0,4	0,12	190	0,14	1,47	4,5	3790,5
19	0,4	0,18	130	0,06	0,83	3,8	3573,9
20	0,4	0,18	130	0,1	1,23	4,5	3898,8
21	0,4	0,18	130	0,14	1,64	5,1	4223,7
22	0,4	0,18	160	0,06	0,83	3,7	3465,6
23	0,4	0,18	160	0,1	1,21	4,2	3790,5
24	0,4	0,18	160	0,14	1,62	4,9	4115,4
25	0,4	0,18	190	0,06	0,72	3,5	3357,3
26	0,4	0,18	190	0,1	1,09	4,2	3682,2
27	0,4	0,18	190	0,14	1,52	4,9	4007,1
28	0,8	0,06	130	0,06	0,35	3	3249
29	0,8	0,06	130	0,1	0,72	3,6	3573,9
30	0,8	0,06	130	0,14	1,15	4,2	3898,8
31	0,8	0,06	160	0,06	0,28	3,2	3032,4
32	0,8	0,06	160	0,1	0,69	3,4	3465,6
33	0,8	0,06	160	0,14	1,12	4	3790,5
34	0,8	0,06	190	0,06	0,32	2,6	3032,4
35	0,8	0,06	190	0,1	0,62	3,2	3357,3
36	0,8	0,06	190	0,14	1,07	3,9	3682,2
37	0,8	0,12	130	0,06	0,46	3,3	3465,6

38	0,8	0,12	130	0,1	0,85	3,9	3790,5
39	0,8	0,12	130	0,14	1,18	4,5	4115,4
40	0,8	0,12	160	0,06	0,42	3	3357,3
41	0,8	0,12	160	0,1	0,83	3,7	3682,2
42	0,8	0,12	160	0,14	1,26	4,3	4007,1
43	0,8	0,12	190	0,06	0,33	3	3249
44	0,8	0,12	190	0,1	0,75	3,6	3573,9
45	0,8	0,12	190	0,14	1,19	4,3	3898,8
46	0,8	0,18	130	0,06	0,56	3,6	3682,2
47	0,8	0,18	130	0,1	0,88	4,3	4007,1
48	0,8	0,18	130	0,14	1,36	4,9	4223,7
49	0,8	0,18	160	0,06	0,54	3,5	3573,9
50	0,8	0,18	160	0,1	0,89	4,1	3898,8
51	0,8	0,18	160	0,14	1,36	4,8	4223,7
52	0,8	0,18	190	0,06	0,42	3,3	3465,6
53	0,8	0,18	190	0,1	0,81	4,1	3790,5
54	0,8	0,18	190	0,14	1,26	4,7	4115,4

The ANOVA results for Ra are given in Table 2. The effect of the cutting radius on surface roughness is 15.73%. The effect of the feed rate is 78.26%. The effect of the depth of cut is 4.35%. The effect of the feed rate on the cutting radius is 5 times greater. The feed rate increased from 0.06 to 0.14 mm/rev. The increase in feed rate is 2.3 times greater. The 2.3-fold increase in feed rate also contributes to the higher effect rate. The increase in cutting radius is 2 times greater. Re, a, V, and f have an effect on surface roughness. Similar results have been found in other studies[6, 19–22].

Table 2. Analysis of Variance for Ra

Source	DF	Adj SS	Adj MS	F-Value	P-Value	% Cont.
Re	1	1,18222	1,18222	1991,97	0,000	15,73
a	1	0,32680	0,32680	550,64	0,000	4,35

v	1	0,08314	0,08314	140,08	0,000	1,11
f	1	5,88062	5,88062	9908,46	0,000	78,26
a x a	1	0,00101	0,00101	1,70	0,200	0,01
v x v	1	0,00801	0,00801	13,49	0,001	0,11
f x f	1	0,00441	0,00441	7,43	0,009	0,06
Re x a	1	0,00023	0,00023	0,38	0,542	0,00
Re x v	1	0,00174	0,00174	2,93	0,095	0,02
Re x f	1	0,00000	0,00000	0,00	0,946	0,00
a *v	1	0,00135	0,00135	2,27	0,139	0,02
a x f	1	0,00015	0,00015	0,25	0,618	0,00
v x f	1	0,00107	0,00107	1,80	0,188	0,01
Error	40	0,02374	0,00059			0,32
Total	53	7,51448				100,00

Figure 1 shows the Pareto chart. Parameters with a value below 2.0 are ineffective. This value is given in Table 2. While the R^2 value was 99.40%, removing these values resulted in 99.49%. When the ineffective parameters are removed, a simpler model with a higher R^2 value is obtained.

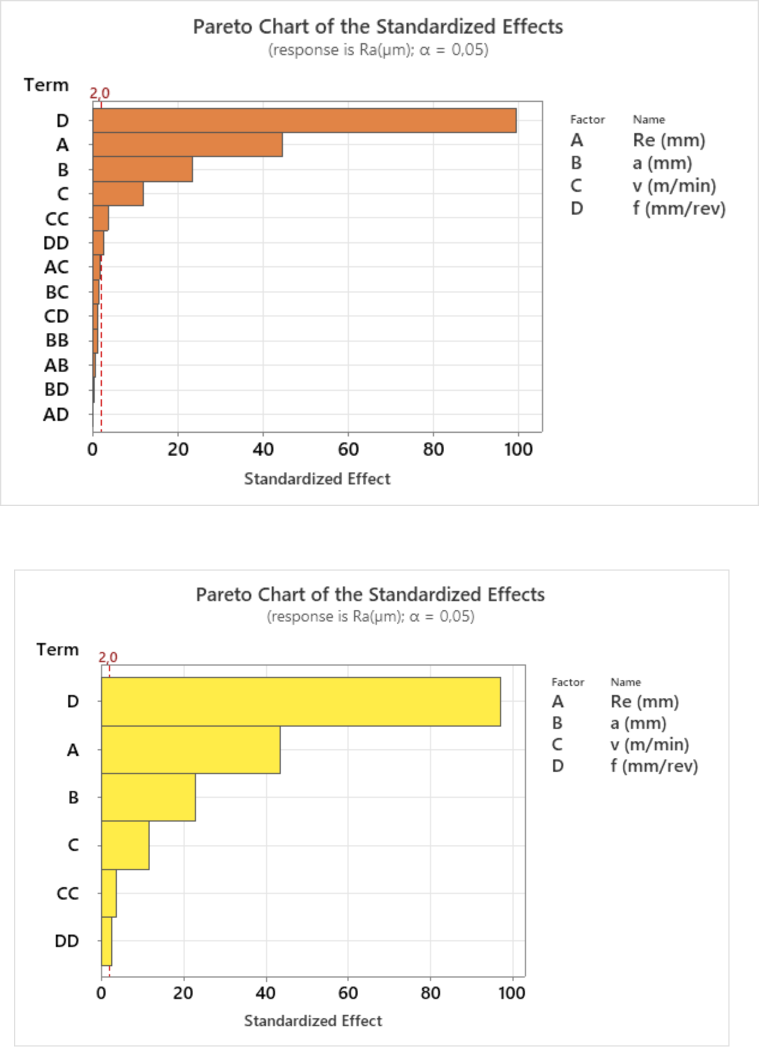

Figure 1. Influence ratios of parameters on surface roughness value

$$Ra=-0{,}046-0{,}947\,Re \quad +2{,}637\,a \quad +0{,}00683\,v \quad +6{,}72\,f$$
$$-2{,}55\,a*a \quad -0{,}000029\,v*v \quad +11{,}98\,f*f+ \quad 0{,}208\,Re*a$$

$$+ 0{,}001157\, Re *v - 0{,}035\, Re *f - 0{,}00417\, a *v + 1{,}04\, a *f$$
$$+ 0{,}00556\, v *f$$

$$R\text{-}sq(pred) = 99{,}40\%$$

$$Ra = -0{,}161 \quad - 0{,}7398\, Re \quad + 1{,}5880\, a \quad + 0{,}00758\, v$$
$$+ 7{,}708\, f - 0{,}000029\, v *v + 11{,}98\, f *f$$

$$R\text{-}sq(pred) = 99{,}49\%$$

As shown in Table 3, the effect feed rate is 78.26%, and the effect of tool radius is 15.73%.

Table 3. Analysis of Variance for Ra

Source	DF	Adj SS	Adj MS	F-Value	P-Value	
Model	6	7,48520	1,24753	2002,62	0,000	99,61
Linear	4	7,47279	1,86820	2998,95	0,000	99,45
Re (mm)	1	1,18222	1,18222	1897,78	0,000	15,73
a (mm)	1	0,32680	0,32680	524,60	0,000	4,35
v (m/min)	1	0,08314	0,08314	133,46	0,000	1,11
f (mm/rev)	1	5,88063	5,88063	9439,95	0,000	78,26
Square	2	0,01242	0,00621	9,97	0,000	0,17
v (m/min)*v (m/min)	1	0,00801	0,00801	12,86	0,001	0,11
f (mm/rev)*f (mm/rev)	1	0,00441	0,00441	7,08	0,011	0,06
Error	47	0,02928	0,00062			0,39
Total	53	7,51448				100,00

Vibration values are important in manufacturing. Vibration affects surface quality and machine tool life. Cutting conditions have a linear effect on vibration with 98.41%. Feed rate has a 70.39% effect; depth of cut 21.92%; cutting speed 3.94%; and tool radius

2.16%. The error rate is determined as 1.07%. Feed rate directly determines the instantaneous chip cross-section (Ac = f x ap). Feed rate and depth of cut increase the cutting force. The increase in cutting force causes dynamic force fluctuations. Depth of cut increases cutting forces but is more stable. It does not cause dynamic force fluctuations as much as feed rate. Therefore, it is the second parameter affecting vibration. Vibration in the Z-axis increases due to the direction of the feed rate. In turning, Z-axis vibration is more pronounced than X-axis vibration. With an increase in cutting speed, the chip flows more easily. The chip cross-section decreases. A more stable flow occurs. This reduces the vibration value. Increasing cutting speed reduces tool vibration. The effect ratio of cutting speed was found to be 3.94%. Tool tip radius slightly alters the cutting force. Similar results have been found in other studies[23–30].

Table 4. Analysis of Variance for Vib

Source	DF	Adj SS	Adj MS	F-Value	P-Value	% Cont.
Model	13	19,5875	1,5067	283,62	0,000	98,93
Linear	4	19,4850	4,8713	916,94	0,000	98,41
Re (mm)	1	0,4267	0,4267	80,31	0,000	2,16
a (mm)	1	4,3403	4,3403	816,99	0,000	21,92
v (m/min)	1	0,7803	0,7803	146,88	0,000	3,94
f (mm/rev)	1	13,9378	13,9378	2623,58	0,000	70,39
Square	3	0,0317	0,0106	1,99	0,131	0,16
a (mm)*a (mm)	1	0,0208	0,0208	3,92	0,055	0,11
v (m/min)*v (m/min)	1	0,0075	0,0075	1,41	0,242	0,04
f (mm/rev)*f (mm/rev)	1	0,0033	0,0033	0,63	0,433	0,02
2-Way Interaction	6	0,0708	0,0118	2,22	0,061	0,36
Re (mm)*a (mm)	1	0,0003	0,0003	0,05	0,820	0,00

Re (mm)*v (m/min)	1	0,0003	0,0003	0,05	0,820	0,00
Re (mm)*f (mm/rev)	1	0,0011	0,0011	0,21	0,650	0,01
a (mm)*v (m/min)	1	0,0204	0,0204	3,84	0,057	0,10
a (mm)*f (mm/rev)	1	0,0337	0,0337	6,35	0,016	0,17
v (m/min)*f (mm/rev)	1	0,0150	0,0150	2,82	0,101	0,08
Error	40	0,2125	0,0053			1,07
Total	53	19,8000				100,00

The significant and insignificant parameters, expressed as percentages in Table 4, are shown in Figure 2. A linear model was created for a simpler regression equation. With this model, the R^2 value increased from 98.08% to 98.18%. Thus, a simpler and more effective model was created. Moreover, applicability increased with a simpler equation. This improved the controllability of the equation. The effect of feed rate of 48.77 and depth of cut of 27.21 is observed in the creation of the regression equation.

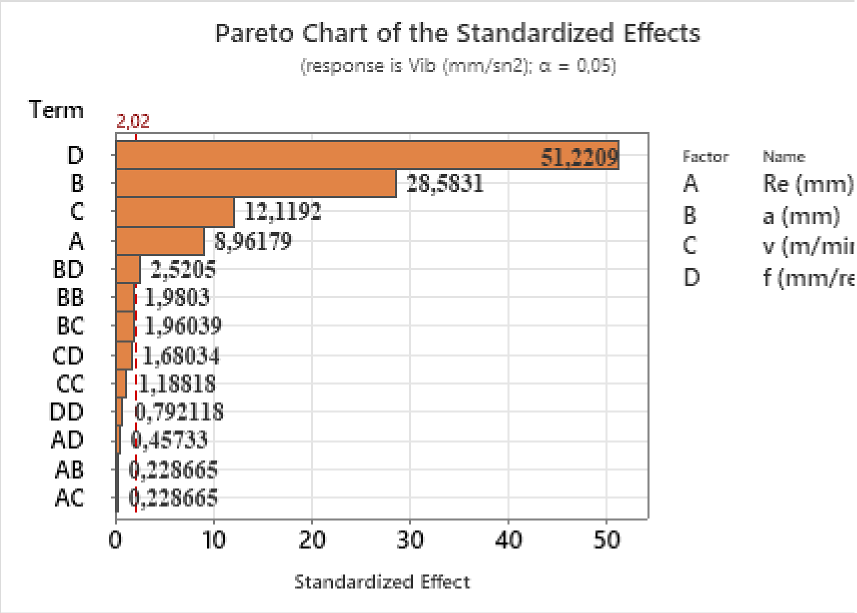

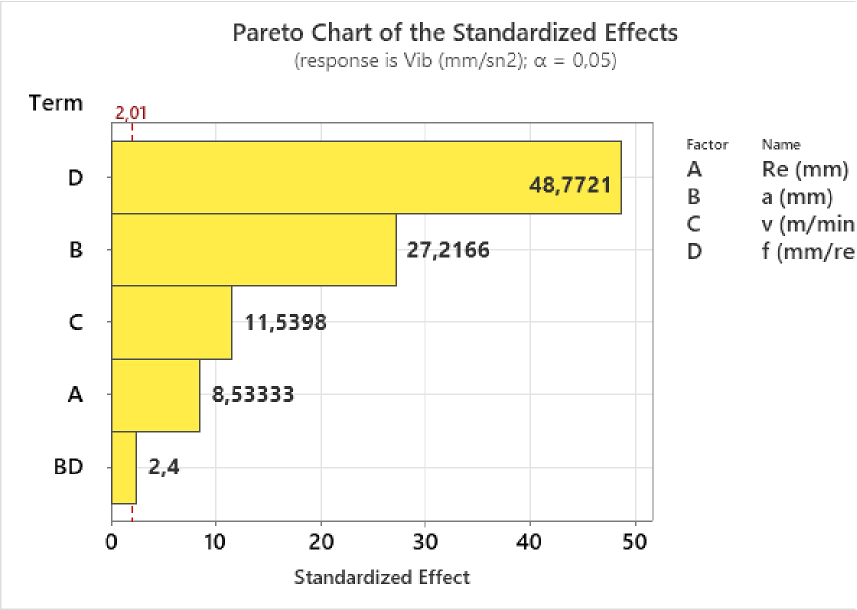

Figure 2. Effect of parameters on vibration

$$Vib(mm/sn2)=4{,}413-0{,}421\,Re-1{,}01\,a-0{,}01810\,v+8{,}68\,f+11{,}57\,a*a+0{,}000028\,v*v+10{,}4\,f*f-0{,}23\,Re*a+0{,}00046\,Re*v-0{,}69\,Re*f+0{,}01620\,a*v+15{,}62\,a*f+0{,}0208\,v*f\qquad R^2=98{,}08\%$$

$$Vib\ (mm/sn2)=2{,}856-0{,}4444\,Re+4{,}225\,a-0{,}004907\,v+13{,}681\,f+15{,}62\,a*f$$

$$98{,}18\%$$

Table 4 shows the ineffective parameters, and Table 5 shows the ANOVA table. Table 5 shows that feed rate has an effect of 70.39% and depth of cut has an effect of 21.92%. The error rate increased from 1.07% to 1.42%. a x a was also removed from the equation. Although very small, a x a also has an effect on vibration.

Table 5. Analysis of Variance for Vib

Source	DF	Adj SS	Adj MS	F-Value	P-Value	% Cont.
Model	5	19,5188	3,9038	666,24	0,000	98,58
Linear	4	19,4850	4,8713	831,36	0,000	98,41
Re (mm)	1	0,4267	0,4267	72,82	0,000	2,16
a (mm)	1	4,3403	4,3403	740,74	0,000	21,92
v (m/min)	1	0,7803	0,7803	133,17	0,000	3,94
f (mm/rev)	1	13,9378	13,9378	2378,71	0,000	70,39
2-Way Interaction	1	0,0337	0,0337	5,76	0,020	0,17
a (mm)*f (mm/rev)	1	0,0337	0,0337	5,76	0,020	0,17
Error	48	0,2812	0,0059			1,42
Total	53	19,8000				100,00

Power consumption is one of the most important problems in the developing world. Increased power consumption means shorter processing times. Increased power consumption increases cutting forces, accelerates friction and wear, reduces tool life, and damages the machine's lifespan. However, very low power consumption means the machine is not being used efficiently. Consequently, energy consumption increases, energy efficiency decreases, the CO_2 footprint grows, investment costs increase, and labor costs rise. Therefore, if the machine tool allows, cutting parameters can be increased. If the feed rate increases, surface quality may deteriorate. Cutting parameters must be carefully selected. Similar results have been found in other studies[31–35].

Table 6. Analysis of Variance for power

Source	DF	Adj SS	Adj MS	F-Value	P-Value	% Cont.

Model	13	6028215	463709	1080,97	0,000	99,72
Linear	4	6023980	1505995	3510,70	0,000	99,65
Re	1	135751	135751	316,46	0,000	2,25
a	1	1688960	1688960	3937,22	0,000	27,94
v	1	399108	399108	930,38	0,000	6,60
f	1	3800160	3800160	8858,73	0,000	62,86
a *a	1	434	434	1,01	0,320	0,01
v *v	1	109	109	0,25	0,618	0,00
f *f	1	434	434	1,01	0,320	0,01
Re *a	1	0	0	0,00	1,000	0,00
Re *v	1	326	326	0,76	0,389	0,01
Re *f	1	0	0	0,00	1,000	0,00
a *v	1	489	489	1,14	0,292	0,01
a *f	1	1955	1955	4,56	0,039	0,03
v *f	1	489	489	1,14	0,292	0,01
Error	40	17159	429			0,28
Total	53	6045374				100,00

In Figure 3, insignificant parameters below 2.02 have been removed. The equation has been simplified. Only the mathematical equation relating Re, a, V, and f has been formed. The effect of f is 93.21, a is 62.19, V is 30.23, and Re is 17.63. These ratios show the effect of each parameter individually on the regression. They are found by dividing the effect ratios by the error rate. Values below 2.01 have been removed.

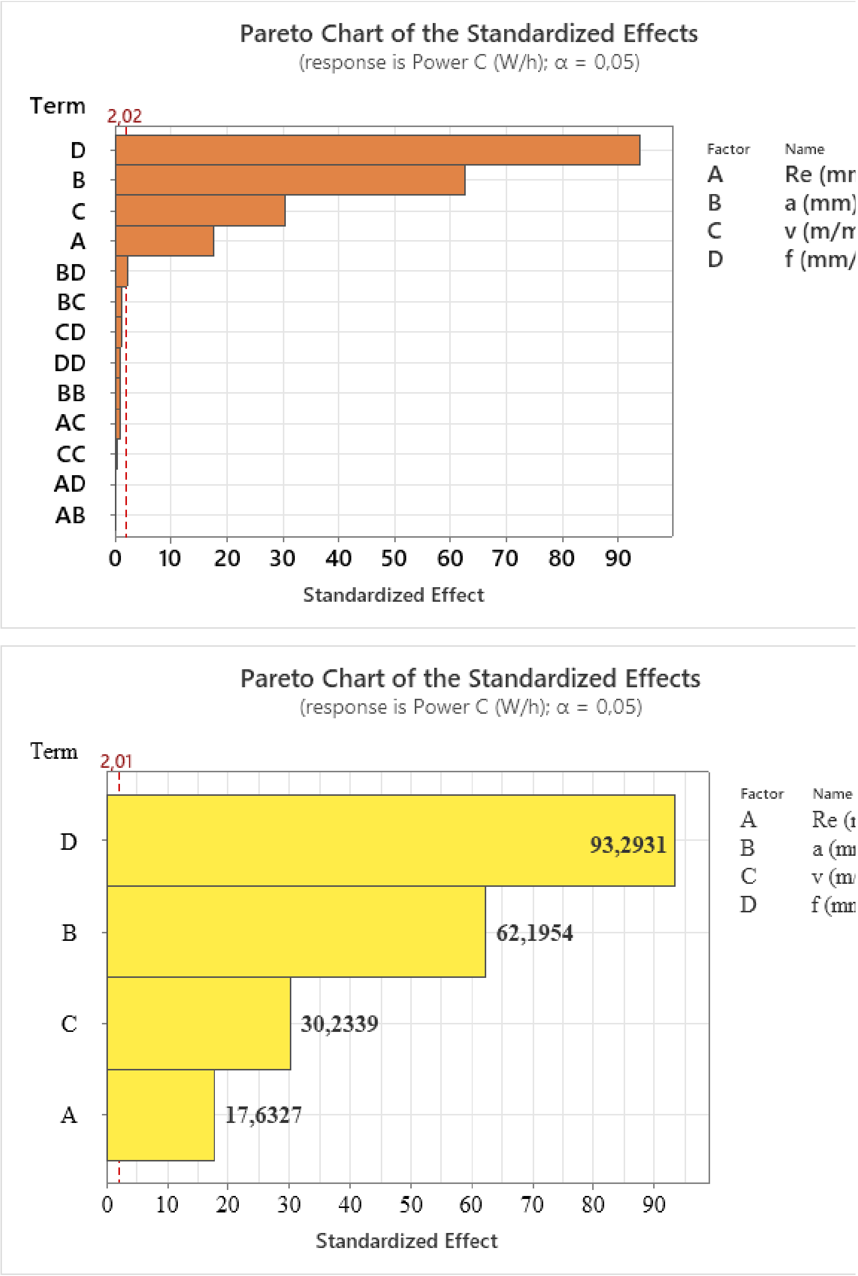

Figure 3. Standard effects of factors on power

$$PowerC(W/h)=2931+170\ Re+3986\ a-5{,}56\ v+8724\ f-1671\ a\ a+0{,}00334\ v\ v-3760\ f\ f-0\ Re\ a+0{,}501\ Re\ v-0\ Re\ f+2{,}51\ a\ v-3760\ a\ f+3{,}76\ v\ f \quad R2=99{,}56\%$$

$$PowerC(W/h)=2789{,}7+250{,}7\ Re+3610{,}0\ a-3{,}510\ v+8122{,}5\ f$$

The re-ANOVA results, after removing the ineffective parameters, are given in Table 7.

Table 7. ANOVA for Power.

Source	DF	Adj SS	Adj MS	F-Value	P-Value	% Cont.
Model	4	6023980	1505995	3449,21	0,000	99,65
Linear	4	6023980	1505995	3449,21	0,000	99,65
Re (mm)	1	135751	135751	310,91	0,000	2,25
a (mm)	1	1688960	1688960	3868,26	0,000	27,94
v (m/min)	1	399108	399108	914,09	0,000	6,60
f (mm/rev)	1	3800160	3800160	8703,59	0,000	62,86
Error	49	21394	437			0,35
Total	53	6045374				100,00

A mathematical equation for Ra (Ra value) has been formulated, depending on the tip radius, power, and vibration value.

$$Ra=-0{,}2882-0{,}6239\ x\ Re+6{,}048\ x\ f+0{,}2608\ x\ Vib \quad R^2\ 98.91\ \%$$

$$Ra=-0{,}032-0{,}000741\ x\ Power+0{,}9487\ x\ Vib \quad R^2=89{,}35\ \%$$

$$Power=1332+670{,}1\ x\ Vib-19{,}55\ Vib^2 \quad R^2=87{,}99\ \%$$

Furthermore, a simpler power and vibration equation has been formulated.

$$Power=1620+518{,}2\ x\ Vib\ R^2=87{,}94\ \%$$

There is a positive correlation of 0.94 between vibration and power.

$Ra = -1,233 + 0,5647 \times Vib \quad R^2 = 84,02\ \%$ *correlation + 0,92.*

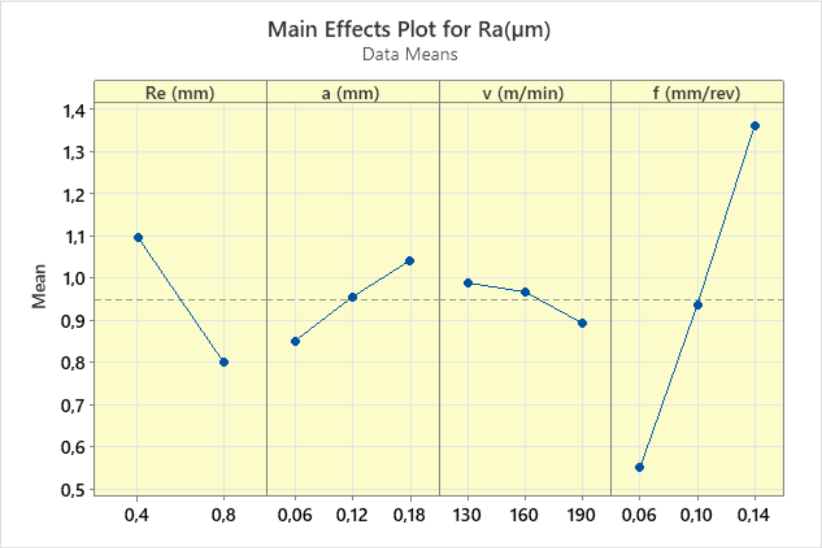

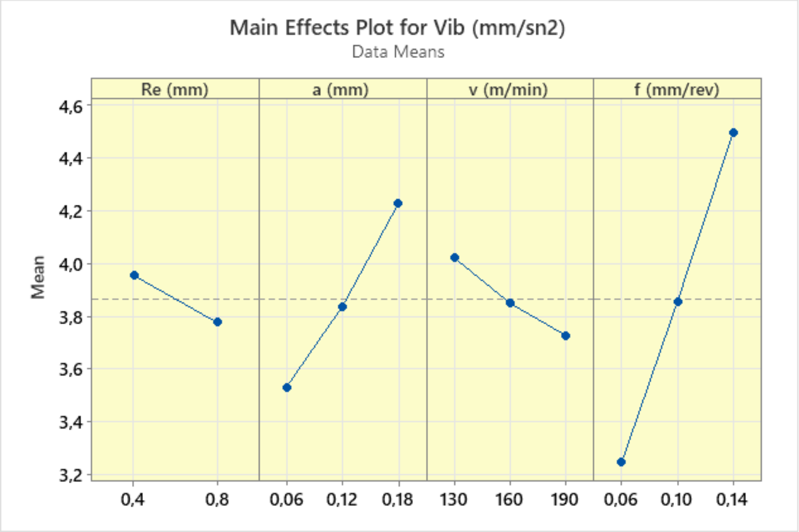

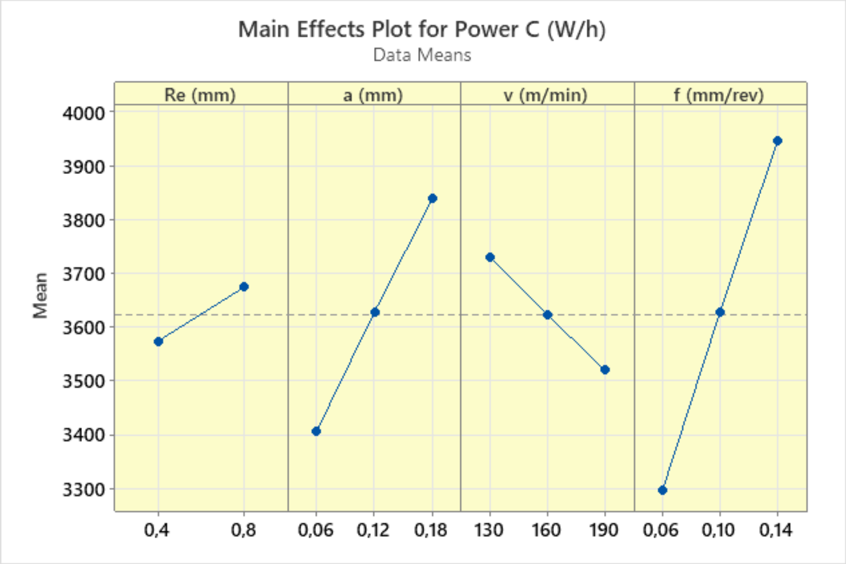

Figure 4. Effect of cutting parameters on Ra, Vib and Power

Multiple Optimization

Determining the optimum parameters is of great importance in manufacturing. In this experimental study, vibration and energy consumption were examined together. Since there are many input parameters, the multiple optimization technique was used to determine the optimum cutting conditions.

Table 8. Weighted multiple optimization

	Re	a	v	f	Ra	Nor	40%	Vib	Nor.	30%	PowerC	Nor	30%	total
1	0,4	0,06	130	0,06	0,65	0,40	0,16	3,20	0,63	0,19	3140,70	0,74	0,22	0,57
2	0,4	0,06	130	0,1	1,05	0,64	0,26	3,80	0,75	0,22	3465,60	0,82	0,25	0,73
3	0,4	0,06	130	0,14	1,45	0,88	0,35	4,40	0,86	0,26	3790,50	0,90	0,27	0,88
4	0,4	0,06	160	0,06	0,6	0,37	0,15	3,00	0,59	0,18	3032,40	0,72	0,22	0,54

5	0,4	0,06	160	0,1	1,01	0,62	0,25	3,60	0,71	0,21	3357,30	0,79	0,24	0,70
6	0,4	0,06	160	0,14	1,4	0,85	0,34	4,20	0,82	0,25	3682,20	0,87	0,26	0,85
7	0,4	0,06	190	0,06	0,55	0,34	0,13	2,80	0,55	0,16	2924,10	0,69	0,21	0,51
8	0,4	0,06	190	0,1	0,95	0,58	0,23	3,40	0,67	0,20	3249,00	0,77	0,23	0,66
9	0,4	0,06	190	0,14	1,36	0,83	0,33	4,10	0,80	0,24	3573,90	0,85	0,25	0,83
10	0,4	0,12	130	0,06	0,75	0,46	0,18	3,50	0,69	0,21	3357,30	0,79	0,24	0,63
11	0,4	0,12	130	0,1	1,15	0,70	0,28	4,10	0,80	0,24	3682,20	0,87	0,26	0,78
12	0,4	0,12	130	0,14	1,56	0,95	0,38	4,70	0,92	0,28	4007,10	0,95	0,28	0,94
13	0,4	0,12	160	0,06	0,71	0,43	0,17	3,30	0,65	0,19	3249,00	0,77	0,23	0,60
14	0,4	0,12	160	0,1	1,12	0,68	0,27	3,90	0,76	0,23	3573,90	0,85	0,25	0,76
15	0,4	0,12	160	0,14	1,53	0,93	0,37	4,50	0,88	0,26	3898,80	0,92	0,28	0,91
16	0,4	0,12	190	0,06	0,63	0,38	0,15	3,20	0,63	0,19	3140,70	0,74	0,22	0,56
17	0,4	0,12	190	0,1	1,03	0,63	0,25	3,80	0,75	0,22	3465,60	0,82	0,25	0,72
18	0,4	0,12	190	0,14	1,47	0,90	0,36	4,50	0,88	0,26	3790,50	0,90	0,27	0,89
19	0,4	0,18	130	0,06	0,83	0,51	0,20	3,80	0,75	0,22	3573,90	0,85	0,25	0,68
20	0,4	0,18	130	0,1	1,23	0,75	0,30	4,50	0,88	0,26	3898,80	0,92	0,28	0,84
21	0,4	0,18	130	0,14	1,64	1,00	0,40	5,10	1,00	0,30	4223,70	1,00	0,30	1,00
22	0,4	0,18	160	0,06	0,83	0,51	0,20	3,70	0,73	0,22	3465,60	0,82	0,25	0,67
23	0,4	0,18	160	0,1	1,21	0,74	0,30	4,20	0,82	0,25	3790,50	0,90	0,27	0,81
24	0,4	0,18	160	0,14	1,62	0,99	0,40	4,90	0,96	0,29	4115,40	0,97	0,29	0,98
25	0,4	0,18	190	0,06	0,72	0,44	0,18	3,50	0,69	0,21	3357,30	0,79	0,24	0,62
26	0,4	0,18	190	0,1	1,09	0,66	0,27	4,20	0,82	0,25	3682,20	0,87	0,26	0,77
27	0,4	0,18	190	0,14	1,52	0,93	0,37	4,90	0,96	0,29	4007,10	0,95	0,28	0,94
28	0,8	0,06	130	0,06	0,35	0,21	0,09	3,00	0,59	0,18	3249,00	0,77	0,23	0,49
29	0,8	0,06	130	0,1	0,72	0,44	0,18	3,60	0,71	0,21	3573,90	0,85	0,25	0,64
30	0,8	0,06	130	0,14	1,15	0,70	0,28	4,20	0,82	0,25	3898,80	0,92	0,28	0,80
31	0,8	0,06	160	0,06	0,28	0,17	0,07	3,20	0,63	0,19	3032,40	0,72	0,22	0,47
32	0,8	0,06	160	0,1	0,69	0,42	0,17	3,40	0,67	0,20	3465,60	0,82	0,25	0,61
33	0,8	0,06	160	0,14	1,12	0,68	0,27	4,00	0,78	0,24	3790,50	0,90	0,27	0,78
34	0,8	0,06	190	0,06	0,32	0,20	0,08	2,60	0,51	0,15	3032,40	0,72	0,22	0,45
35	0,8	0,06	190	0,1	0,62	0,38	0,15	3,20	0,63	0,19	3357,30	0,79	0,24	0,58
36	0,8	0,06	190	0,14	1,07	0,65	0,26	3,90	0,76	0,23	3682,20	0,87	0,26	0,75
37	0,8	0,12	130	0,06	0,46	0,28	0,11	3,30	0,65	0,19	3465,60	0,82	0,25	0,55

38	0,8	0,12	130	0,1	0,85	0,52	0,21	3,90	0,76	0,23	3790,50	0,90	0,27	0,71
39	0,8	0,12	130	0,14	1,18	0,72	0,29	4,50	0,88	0,26	4115,40	0,97	0,29	0,84
40	0,8	0,12	160	0,06	0,42	0,26	0,10	3,00	0,59	0,18	3357,30	0,79	0,24	0,52
41	0,8	0,12	160	0,1	0,83	0,51	0,20	3,70	0,73	0,22	3682,20	0,87	0,26	0,68
42	0,8	0,12	160	0,14	1,26	0,77	0,31	4,30	0,84	0,25	4007,10	0,95	0,28	0,84
43	0,8	0,12	190	0,06	0,33	0,20	0,08	3,00	0,59	0,18	3249,00	0,77	0,23	0,49
44	0,8	0,12	190	0,1	0,75	0,46	0,18	3,60	0,71	0,21	3573,90	0,85	0,25	0,65
45	0,8	0,12	190	0,14	1,19	0,73	0,29	4,30	0,84	0,25	3898,80	0,92	0,28	0,82
46	0,8	0,18	130	0,06	0,56	0,34	0,14	3,60	0,71	0,21	3682,20	0,87	0,26	0,61
47	0,8	0,18	130	0,1	0,88	0,54	0,21	4,30	0,84	0,25	4007,10	0,95	0,28	0,75
48	0,8	0,18	130	0,14	1,36	0,83	0,33	4,90	0,96	0,29	4223,70	1,00	0,30	0,92
49	0,8	0,18	160	0,06	0,54	0,33	0,13	3,50	0,69	0,21	3573,90	0,85	0,25	0,59
50	0,8	0,18	160	0,1	0,89	0,54	0,22	4,10	0,80	0,24	3898,80	0,92	0,28	0,74
51	0,8	0,18	160	0,14	1,36	0,83	0,33	4,80	0,94	0,28	4223,70	1,00	0,30	0,91
52	0,8	0,18	190	0,06	0,42	0,26	0,10	3,30	0,65	0,19	3465,60	0,82	0,25	0,54
53	0,8	0,18	190	0,1	0,81	0,49	0,20	4,10	0,80	0,24	3790,50	0,90	0,27	0,71
54	0,8	0,18	190	0,14	1,26	0,77	0,31	4,70	0,92	0,28	4115,40	0,97	0,29	0,88
				max	1,64			5,10			4223,70			1,00
				min	0,28			2,60			2924,10			0,45

Normalization was performed for Ra, Vib, and Power for weighted optimization. Weights were set at 0.4 for Ra, and 0.3 for Vib and Power. Weighted ratios were summed. The lowest value yields the best results. The highest value yields the most unfavorable results.

Results

In this experimental study, which investigated the effect of different cutter radii, surface roughness, power, and vibration values were measured. ANOVA and regression analysis were performed. In summary, the results are as follows:

Feed rate is the parameter that most significantly affects surface roughness (78.26%), vibration (70.39%), and power consumption (62.86%). Depth of cut is found to have a 4.35% effect on surface roughness, a 21.92% effect on vibration, and a 27.94% effect on power consumption. The cutter radius has a 15.73% effect on surface roughness, a 2.16% effect on vibration, and a 2.25% effect on power consumption.

High-accuracy mathematical models have been created. Mathematical equations have been formulated for the relationships between vibration and power consumption, power consumption and surface roughness, and surface roughness and vibration.

Vibration, surface roughness, and power consumption increased with increasing feed rate. Vibration and power consumption also increased with increasing depth of cut.

Finally, optimum cutting conditions were determined using a multiple optimization technique. In the optimization, a ratio of 40% was given for surface roughness, 30% for power consumption, and 30% for vibration. This ratio takes into account the significant impact of surface quality on manufacturing.

References

1. Nguyen TT (2021) An energy-efficient optimization of the hard turning using rotary tool. Neural Comput Appl 33:2621–2644. https://doi.org/10.1007/s00521-020-05149-2

2. Ghule GS, Sanap S, Chinchanikar S, et al (2024) Investigation of conventional and ultrasonic vibration-assisted turning of hardened steel using a coated carbide tool. Front Mech Eng 10:1–11. https://doi.org/10.3389/fmech.2024.1391315

3. Sivaiah P, Guru Prasad M, Singh M M, Uma B (2020) Machinability evaluation during machining of AISI 52100 steel with textured tools under Minimum Quantity Lubrication–A comparative study. Mater Manuf Process 35:1761–1768. https://doi.org/10.1080/10426914.2020.1802034

4. Afazov SM, Ratchev SM, Segal J (2012) Prediction and experimental validation of micro-milling cutting forces of AISI H13 steel at hardness between 35 and 60 HRC. Int J Adv Manuf Technol 62:887–899. https://doi.org/10.1007/s00170-011-3864-7

5. Ahmad A, Akram S, Jaffery SHI, Khan MA (2023) Evaluation of specific cutting energy, tool wear, and surface roughness in dry turning of titanium grade 3 alloy. Int J Adv Manuf Technol 127:1263–1274. https://doi.org/10.1007/s00170-023-11580-1

6. Şahinoğlu A, Rafighi M, Kumar R (2022) An investigation on cutting sound effect on power consumption and surface roughness in CBN tool-assisted hard turning. Proc Inst Mech Eng Part E J Process Mech Eng 236:1096–1108. https://doi.org/10.1177/09544089211058021

7. Bhadoria NS, Bartarya G (2022) On the improvement in process performance of ceramic inserts during hard turning in MQL environment. Mater Manuf Process 37:283–293. https://doi.org/10.1080/10426914.2021.1967978

8. Mane S, Kumar S (2020) Analysis of surface roughness during turning of AISI 52100 hardened alloy steel using minimal cutting fluid application. Adv Mater Process Technol 00:1–12. https://doi.org/10.1080/2374068X.2020.1855965

9. Kam M (2021) Effects of deep cryogenic treatment on machinability, hardness and microstructure in dry turning process of tempered steels. Proc Inst Mech Eng Part E J Process Mech Eng 235:927–936. https://doi.org/10.1177/0954408920979446

10. Benlahmidi S, Aouici H, Boutaghane F, et al (2017) Design optimization of cutting parameters when turning hardened AISI H11 steel (50 HRC) with CBN7020 tools. Int J Adv Manuf Technol 89:803–820. https://doi.org/10.1007/s00170-016-9121-3

11. FNIDES B, YALLESE MA, MABROUKI T, RIGAL JF (2011) Application of response surface methodology for determining cutting force model in turning hardened AISI H11 hot work tool steel. Sadhana - Acad Proc Eng Sci 36:109–123. https://doi.org/10.1007/s12046-011-0007-7

12. Sivaiah P, Bodicherla U (2020) Effect of Surface Texture Tools and Minimum Quantity Lubrication (MQL) on tool Wear and Surface Roughness in CNC Turning of AISI 52100 Steel. J Inst Eng Ser C 101:85–95. https://doi.org/10.1007/s40032-019-00512-2

13. Şahinoğlu A, Rafighi M (2020) Investigation of Vibration, Sound Intensity, Machine Current and Surface Roughness Values of AISI 4140 During Machining on the Lathe. Arab J Sci Eng 45:. https://doi.org/10.1007/s13369-019-04124-x

14. Sahinoğlu A, Ulas E (2020) An investigation of cutting parameters effect on sound level, surface roughness, and power consumption during machining of hardened AISI 4140. Mech Ind 21:. https://doi.org/10.1051/meca/2020068

15. Şahinoglu A, Rafighi M (2021) Machinability of hardened

AISI S1 cold work tool steel using cubic boron nitride. Sci Iran 28:2655–2670. https://doi.org/10.24200/sci.2021.55772.4398

16. İYNEN O, ŞAHİNOĞLU A, ÖZDEMİR M, YILMAZ V (2020) Investigation of the Effect of Cutting Parameters on the Surface Roughness Value in the Machining of AISI 4140 Steel with Taquchi Method. J Inst Sci Technol 10:2840–2849. https://doi.org/10.21597/jist.736802

17. Şahinoğlu A, Rafighi M (2020) Optimization of cutting parameters with respect to roughness for machining of hardened AISI 1040 steel. Mater Test 62:85–95. https://doi.org/10.3139/120.111458

18. Karaaslan F, Şahinoğlu A (2020) Determination of Ideal Cutting Conditions for Maximum Surface Quality and Minimum Power Consumption During Hard Turning of AISI 4140 Steel Using TOPSIS Method Based on Fuzzy Distance. Arab J Sci Eng 45:9145–9157. https://doi.org/10.1007/s13369-020-04635-y

19. Şahinoğlu A (2022) Investigation of machinability properties of AISI H11 tool steel for sustainable manufacturing. Proc Inst Mech Eng Part E J Process Mech Eng 236:2717–2728. https://doi.org/10.1177/09544089221122004

20. Şahinoğlu A (2020) Investigation of energy consumption and surface roughness in hot work tool steel (DIN 1.2367) and cold work tool steel (DIN 1.2550). China Glob 32:173–192. https://doi.org/10.4324/9780203121450-9

21. Karabulut Ş, Şahinoğlu A (2017) R260 Çeliklerinin İşlenmesinde Kesme Parametrelerinin Yüzey Pürüzlülüğü, Güç Tüketimi ve Makine Gürültüsü Üzerine Etkileri. J Polytech 0900:237–244. https://doi.org/10.2339/politeknik.371299

22. Şahinoğlu A, Rafighi M (2021) Investigation of tool wear, surface roughness, sound intensity, and power consumption

during hard turning of AISI 4140 steel using multilayer-coated carbide inserts. J Eng Res 9:377–395. https://doi.org/10.36909/jer.8783

23. Al-Shayea A, Abdullah FM, Noman MA, et al (2020) Studying and Optimizing the Effect of Process Parameters on Machining Vibration in Turning Process of AISI 1040 Steel. Adv Mater Sci Eng 2020:. https://doi.org/10.1155/2020/5480614

24. Prasad BS, Babu MP (2017) Correlation between vibration amplitude and tool wear in turning: Numerical and experimental analysis. Eng Sci Technol an Int J 20:197–211. https://doi.org/10.1016/j.jestch.2016.06.011

25. Deshpande Y, Andhare A, Sahu NK (2017) Estimation of surface roughness using cutting parameters, force, sound, and vibration in turning of Inconel 718. J Brazilian Soc Mech Sci Eng 39:5087–5096. https://doi.org/10.1007/s40430-017-0819-4

26. Deshpande Y V., Andhare AB, Padole PM (2019) Application of ANN to estimate surface roughness using cutting parameters, force, sound and vibration in turning of Inconel 718. SN Appl Sci 1:1–9. https://doi.org/10.1007/s42452-018-0098-4

27. Kam M, Şeremet M (2021) Experimental investigation of the effect of machinability on surface quality and vibration in hard turning of hardened AISI 4140 steels using ceramic cutting tools. Proc Inst Mech Eng Part E J Process Mech Eng 09544089211007366. https://doi.org/10.1177/09544089211007366

28. Shah D, Bhavsar S (2019) Effect of Tool Nose Radius and Machining Parameters on Cutting Force, Cutting Temperature and Surface Roughness-An Experimental Study of Ti-6Al-4V (ELI). Mater Today Proc 22:1977–1986. https://doi.org/10.1016/j.matpr.2020.03.163

29. Ambhore N, Kamble D, Chinchanikar S (2020) Evaluation of Cutting Tool Vibration and Surface Roughness in Hard Turning of AISI 52100 Steel: An Experimental and ANN Approach. J Vib Eng Technol 8:455–462. https://doi.org/10.1007/s42417-019-00136-x

30. Kam M, Demirtaş M (2021) Analysis of tool vibration and surface roughness during turning process of tempered steel samples using Taguchi method. Proc Inst Mech Eng Part E J Process Mech Eng 235:1429–1438. https://doi.org/10.1177/09544089211001976

31. Zhao G, Zhao Y, Meng F, et al (2020) Prediction model of machine tool energy consumption in hard-to-process materials turning. Int J Adv Manuf Technol 106:4499–4508. https://doi.org/10.1007/s00170-020-04939-1

32. Airao J, Nirala CK, Bertolini R, et al (2022) Sustainable cooling strategies to reduce tool wear, power consumption and surface roughness during ultrasonic assisted turning of Ti-6Al-4V. Tribol Int 169:107494. https://doi.org/10.1016/j.triboint.2022.107494

33. Wang Q, Liu F, Wang X (2014) Multi-objective optimization of machining parameters considering energy consumption. Int J Adv Manuf Technol 71:1133–1142. https://doi.org/10.1007/s00170-013-5547-z

34. Nguyen TT (2021) An energy-efficient optimization of the hard turning using rotary tool. Neural Comput Appl 33:2621–2644. https://doi.org/10.1007/s00521-020-05149-2

35. Khanna N, Shah P, Sarikaya M, Pusavec F (2022) Energy consumption and ecological analysis of sustainable and conventional cutting fluid strategies in machining 15–5 PHSS. Sustain Mater Technol 32:e00416. https://doi.org/10.1016/j.susmat.2022.e00416

CHAPTER 2

Experimental Energy and Exergy Analysis of a Photovoltaic Thermal System Incorporating Nanofluid Cooling and Phase Change Material

Kübra KURTOĞLU SONTAY[1]
Elif ÖĞÜT [2]
Abid USTAOĞLU [3]

1. Introduction

Rapidly growing global energy needs and the dwindling supply of traditional fossil fuels have driven a worldwide transition toward sustainable energy technologies. Energy consumption is often used a key parameter in the development of a country. On the other hand, the growth in the manufacturing or industry accelerates the energy demand. Recent studies indicates that renewable energy sources including wind, geothermal, biomass and solar energy have a great potential of replacing fossil fuels in the future [1] [2]. Although the use of renewable energy is considered a suitable alternative energy strategy, biodiesel blends are generally avoided because they can cause an increase in NOx emissions [3]. Among various energy sources, solar energy appears as a promising option for the energy market due to its minimal environmental impact and wide

---

[1] Dr., National Defence University, Turkish Naval Academy, Mechanical Engineering Department, Orcid: 0000-0002-9656-063X

[2] Prof., Kocaeli University, Mechanical Engineering Department, Orcid: 0000-0002-5647-4040

[3] Assoc. Prof., Bartin University, Mechanical Engineering Department, Orcid: 0000-0003-3391-5015

applicability. Moreover, it is particularly effective in hot climates [4] [5].

The thermal and photovoltaic-PV system have become promising technology to utilize solar radiation efficiently. Conventional PV modules convert only a limited part of incoming solar radiation (about 5-25%) into electrical energy. The remaining energy is lost as heat or absorbed by the PV panel. The increase in the temperature of PV panel negatively affects its electrical efficiency. To address this issue, recent studies have increasingly focused on converting conventional PV panels into photovoltaic–thermal (PV/T) systems by integrating phase change materials (PCMs) and nanofluids, thereby enhancing electrical power generation [6]. Researchers are continuously conducting research studies on the economic feasibility and distribution of PV/T results.

Photovoltaic (PV) panels are used to convert solar energy into electricity. Although PV panels can absorb about 90% of the incident radiation, the electrical conversion efficiency usually is around 4%-17%. A significant share of the absorbed energy is converted into heat. It raises the cell temperature. This temperature increase reduces the open-circuit voltage and decreases the overall electrical performance. Moreover, high cell temperatures cause thermal stress within the photovoltaic structure. It may negatively affect long-term material durability. Therefore, effective cooling of PV is very important. The waste heat in the PV system can be utilized by integrating a heat recovery unit into a PV module. This kind of hybrid system is known as a photovoltaic-thermal (PVT) system [7]. PV/T systems can utilize thermal energy and generate electricity from solar radiation. In recent decades, PVT systems have attracted considerable attention as clean renewable energy technologies. Most of the research related to these technologies has focused on improving the energy efficiency of PVT systems.

Sun (2025) showed that integrating phase change materials (PCMs) into PV/T systems effectively regulates panel temperature. It results in improvements in thermal and electrical performance. Moreover, the PCM was found to stabilize temperature and enhance the overall efficiency of the PV module [8]. Mazzeo et al. experimentally investigated the effects of integrating three different inorganic phase change materials into photovoltaic modules. The results indicated that PCM effectively cooled the PV surface temperature. Thus, electrical power output increased by 6.84% due to reduced temperatures. PCM selection plays a significant role in determining the overall efficiency of PV systems [9].

Alsaqoor et al. (2023) numerically investigated the effects of phase change materials (PCMs) on the thermal and electrical performance of PVT systems. The results showed that the use of PCM significantly reduced the PV cell temperature, thereby improving electrical efficiency. In the PCM-integrated configuration, the cell temperature decreased by 24%. It causes a significant enhancement in efficiency and maximum power output [10]. Rejeb et al. (2023) investigated a PVT system integrated with a thermoelectric generator and phase change material (PCM). The results showed that PCMs with high latent heat capacity effectively cooled the thermoelectric modules and increased the system's electrical performance. Higher solar irradiance enhanced electricity generation, while PCM was more effective under warmer conditions [11]. Liu et al. (2023) carried out an optimization study of a geothermal-photovoltaic hybrid system with nanofluids [12]. Al-Waeli et al. (2019) experimentally investigated the use of nano-PCM/nanofluid in a PVT system [13]. The results indicated that the proposed system is economically feasible and shows significant potential.

In this study, the effects of a water-based nanofluid and a hydrocarbon-based phase change material (PCM) were experimentally investigated on the electrical performance of a PVT systems. The main objective of this study to achieve improvements in thermal and electrical conversion efficiencies by utilizing PCM.

1. Renewable Energy Resources

Energy sources are divided into two main groups: exhaustible and sustainable. Examples of renewable energy sources include solar, wind, and geothermal energy sources [14]. Renewable energy is a type of energy that can continuously renew itself [15]. The fundamental characteristic that distinguishes green energy from traditional fossil fuels is its capacity to be naturally reproduced through environmental cycles. The reasons why renewable energy systems are gaining more and more importance stem from their critical roles in protecting the environment, reducing greenhouse gas emissions, and decreasing external dependence. A significant upward trend in the use of renewable energy is observed globally. Furthermore, the increasing energy crisis, the gradual depletion of oil and natural resource reserves, and the high economic and environmental costs associated with the extraction of fossil fuels have further increased the need for sustainable energy alternatives. For these reasons, a significant increase in interest in renewable energy technologies has been observed in recent years, strengthening the strategic importance of these technologies for future energy systems [16].

Renewable energy sources play an important role in reducing energy dependence and effectively protecting the environment. Furthermore, the use of renewable energy sources is becoming increasingly widespread globally, and the number of countries using this type of energy is steadily increasing. With this upward trend, it is predicted that a significant portion of future energy needs will be met by renewable energy technologies. Fig. 1 [17] shows the projected increase in global electricity production demand to be met by renewable energy technologies for the period 2023–2030.

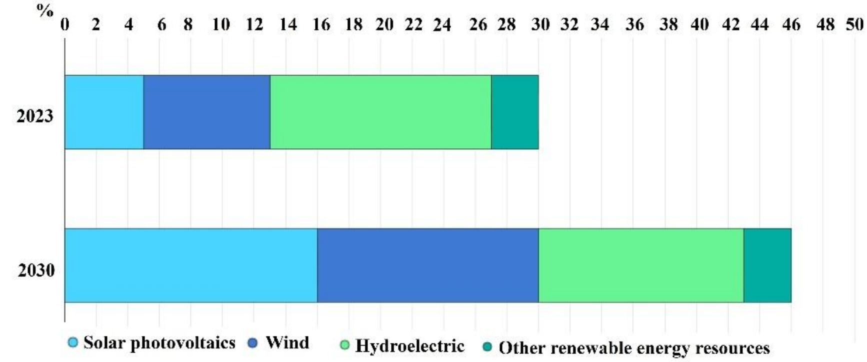

Figure 1. Global baseline outlook for electricity generation from renewable energy technologies between 2023 and 2030 [17]

Fig. 1 shows a significant upward trend in global green electricity production, with expectations that it will exceed 17000 TWh by 2030. This represents approximately a twofold increase compared to the initial level recorded in 2023. Furthermore, solar photovoltaic (PV) electricity production is expected to surpass hydroelectric power to become the number one renewable electricity source by 2029. By 2030, renewable energy technologies are projected to account for approximately 46% of global electricity production, with wind and solar PV technologies contributing approximately 30% to total production. During the same period, solar energy is expected to emerge as the primary renewable electricity source, with wind energy ranking second and both technologies eventually surpassing hydroelectric power. Additionally, these two sources together are expected to constitute approximately two-thirds of global renewable electricity production. It is expected that the contribution of solar energy to meeting global electricity needs will approximately triple, and the contribution of wind energy will approximately double. This will lead to a decrease in the share of hydroelectric energy. The shares of other renewable energy technologies such as bioenergy, concentrated solar energy and geothermal energy are expected to remain below 3% and show limited change during the period. In addition, although these technologies have important roles in supporting the integration of wind and solar photovoltaic energy into the global electricity system, it is stated that their level of adoption will remain limited [17].

2. Photovoltaic Thermal Systems (PV/T)

Photovoltaic thermal (PV/T) systems are among the new technologies designed to transform solar energy into electricity and heat production concurrently. PV/T systems are highly advantageous from an environmental and economic perspective because they enable the simultaneous production of electricity and heat. Considering these advantages, research conducted for PV/T technologies has become increasingly important. Therefore, researchers have focused on maximizing the overall efficiency obtained from these systems [18].

Photovoltaic-thermal (PV/T) systems consist of solar cells, mechanical and electrical interconnects, mounting components, and various power conditioning units that regulate or convert the electrical output. These systems are typically classified according to their peak kilowatt (kWp) value, which represents the maximum electrical power they can provide under clear sky conditions with the highest solar radiation [19]. An increase in photovoltaic cell temperature causes a significant decrease in the electrical efficiency of the modules. This is due to the conversion of some of the solar energy that cannot be converted into electricity into heat energy. This also leads to the formation of a thermal load. Furthermore, rising temperatures lead to an increase in the internal resistance of the photovoltaic material, further reducing electrical efficiency. Therefore, research into developing innovative designs to maximize the overall performance of PV/T systems is attracting interest. In PV/T collectors, the photovoltaic panel is cooled with the help of a refrigerant. This contributes to better electrical efficiency levels within the module. In addition to the improvement in electrical performance, the waste heat carried by the working fluid can be utilized to meet various thermal demands in various industrial and domestic processes [20]. Moreover, PV/T units often produce unstable thermal outputs due to constantly changing environmental conditions throughout the day. This highlights the importance of thermal energy storage strategies. One of the most effective approaches to overcome this challenge is the utilize of PCMs or other thermal storage media that can store heat at nearly constant temperatures [21].

3. Phase Change Materials

Phase change materials (PCMs) function by capturing and discharging vast quantities of thermal energy throughout their phase shift processes. By absorbing heat during the solid-to-liquid transition and releasing it during solidification, PCMs enhance the performance of thermal management systems [21]. Because PCMs have the properties of absorbing, storing and releasing thermal energy, they increase the efficiency of thermal energy storage systems. In addition, these properties make it possible to consider PCMs as sustainable and renewable thermal energy storage media by ensuring that energy is absorbed from the environment when it is most available and released when energy demand is highest [22].

A wide variety of solid-liquid phase change materials (PCMs) with varying melting point ranges are available. Solid-liquid PCMs are classified into organic, inorganic, and eutectic groups according to their chemical composition [24]. PCMs are generally divided into two groups, organic and inorganic, as shown in Fig. 2. The latent heat of melting – and therefore the energy storage capacity – of organic materials is approximately half that of inorganic salts.

Inorganic salts, on the other hand, generally exhibit higher latent heat values. They also have some disadvantages, such as requiring a larger storage volume due to the lower energy densities of organic compounds.

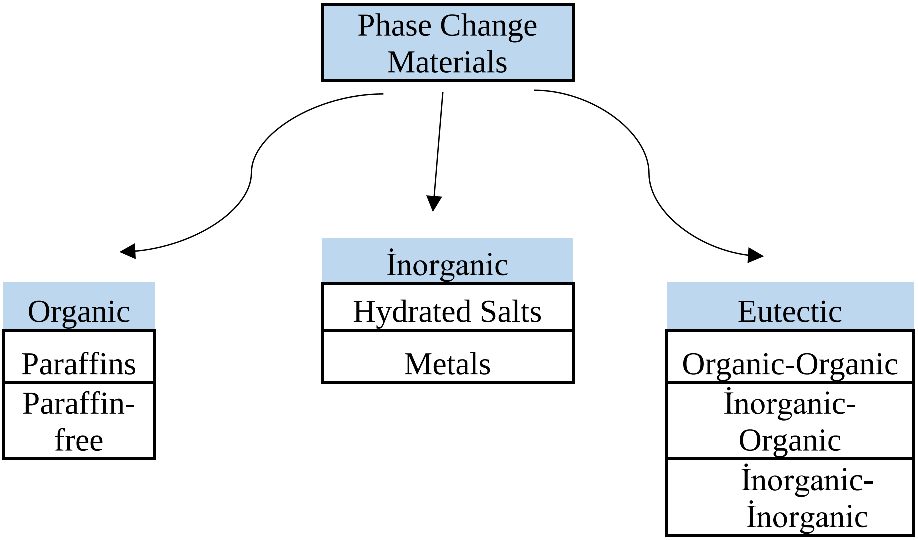

Figure 2. Categorization and types of PCMs [23] [21]

In addition, they offer several advantages, including suitable melting points, self-nucleation ability, and the ability to solidify under supercooled conditions. Among inorganic PCMs, salt hydrates have been extensively investigated due to their high heat storage capacity. On the other hand, organic PCMs exhibit superior chemical stability and longer service life compared to inorganic options [21]. Eutectic mixtures are formed by combining at least two different atoms or molecules. These materials undergo a phase transition at a constant temperature, during which the liquid transforms into two different solid phases. Eutectic PCMs consist of mixtures of organic-organic, organic-inorganic, or inorganic-inorganic components [25]. The service life of PCMs is directly related to the long-term stability of their chemical stability, phase change temperatures, and latent heat storage capacity. For these reasons, parameters such as latent heat of melting, phase decomposition, supercooling behavior, and phase change temperature are critical in selecting a suitable PCM [21]. PCMs are widely utilized in various industries, including textiles, food, medical applications, and the automotive sector [26].

Phase change materials must maintain their chemical stability due to repeated melting-solidification cycles. Therefore, chemical stability is very important for their performance. They should not exhibit corrosive effects. They should not be flammable, toxic, or explosive. Finally, they should have high thermal conductivity. Generally, the thermal conductivity of PCMs is not at the desired value. Therefore, there is a need to increase thermal conductivity. For this reason, applications such as adding metal plates, incorporating the PCM into a metal structure, mixing high thermal conductivity powders into the PCM, and microencapsulating the phase change material are carried out to increase thermal conductivity. During freezing, heat transfer occurs only through conduction and is generally low. During melting, heat is transferred through natural convection. This causes the heat transfer rate in melting to be faster than in freezing. Low thermal conductivity increases the heat storage and recovery time during heat storage and causes a decrease in heat storage efficiency. To overcome this problem, materials that will increase thermal conductivity are added to the environment [27].

4. Nanofluids

By dispersing 1–100 nm sized particles into conventional liquids like water or oil, nanofluids are synthesized to enhance the thermal properties of the working medium. Nanofluids were first proposed by Choi in 1995 [28]. Applications of nanofluids include microelectronics, pharmaceutical processes, fuel cells, optical applications, and lubrication systems.

Nanofluids exhibit higher thermal conductivity [29], improved convective heat transfer properties [30] [31], and much superior optical properties compared to conventional heat transfer fluids used in PTC systems [32]. In addition, nanofluids can also be described as fluids formed by adding solid particles to liquids in order to rise the heat transfer coefficient. Among the commonly utilized nanofluid production are aluminum oxide, copper, copper oxide, gold, silver and silicon dioxide nanoparticles. The production of nanoparticles involves various techniques, including chemical precipitation, mechanical abrasion, and gas condensation. Research suggests that the gas condensation method often yields more favorable results for nanofluid stability and performance compared to other synthesis pathways [33].

Solid metals, which have importantly higher thermal conductivities than liquids, are predicted to enhance the effective thermal conductivity and heat transfer of a fluid by adding suspended solid metal particles in a fluid, thus increasing the heat transfer rate [35]. In addition, nanoparticle size and geometry are among the main parameters determining thermal conductivity. Therefore, it has been noted that nanoparticle size is inversely proportional to thermal conductivity, meaning that thermal conductivity increases as particle size decreases. In terms of nanoparticle geometry, it has been determined that cylindrical nanoparticles exhibit superior thermal conduction performance compared to spherical nanoparticles. Furthermore, it has been observed that nanofluids with high thermal conductivity values positively affect the overall thermal performance of the system. The parameters affecting the thermal conductivity of nanofluids are shown in Fig. 3.

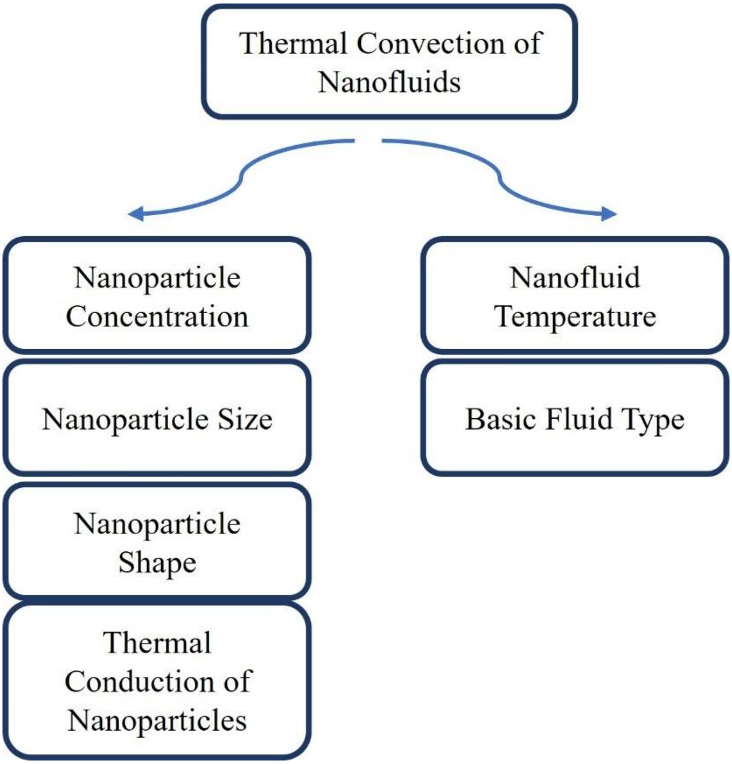

Figure 3. Factors that influence the heat conduction capabilities of nanofluids [34] [21]

5. Application of Nanofluid and PCM in PV/T Systems

As living standards rise globally, energy demand is also increasing day by day. Renewable energy sources are coming to the forefront to meet the growing energy demand. The main reason for this is that solar energy has the ability to be converted into various forms of energy, including electrical energy. Thanks to solar cell technologies such as photovoltaic cells, solar energy can be directly converted into electrical energy [36]. In the search for solutions to the increasing energy demand, the transition to alternative and environmentally friendly energy sources has become inevitable. In this context, solar energy has emerged as a sustainable and renewable energy source [28]. Hybrid photovoltaic/thermal (PV/T) collectors provide integrated structures that can produce electrical and thermal energy from solar radiation simultaneously by combining photovoltaic power generation with thermal energy systems [29]. Effectively removing thermal energy from the system allows for a reduction in the operating temperature of photovoltaic panels, thus improving overall system efficiency. A notable decline in photovoltaic efficiency, typically ranging between 0.4% and 0.65% for every degree Celsius rise in cell temperature, underscores the necessity of thermal control. Consequently, implementing robust cooling mechanisms is vital to mitigate heat-induced losses and preserve the module's performance standards. Hybrid PV/T systems have been developed by integrating cooling systems into photovoltaic panels. Photovoltaic modules with different sizes and geometries form the main components of hybrid collector systems [30]. In general, in photovoltaic thermal systems, heat is removed through tubes mounted on the back surface of solar cells according to a specific design configuration. It is important that these tubes are made of materials with high thermal conductivity to effectively draw heat from the photovoltaic panel. The heat absorbed from the panel is transferred to the cooling working fluid inside the tubes via convection and carried by the fluid. The working fluid, which accumulates thermal energy, is then directed to a storage unit; here, the heat carried by the fluid is dissipated to the environment through a heat exchanger or natural cooling processes. Then, the working fluid is recirculated within the system [31]. Literature reports that nanofluids exhibit superior thermophysical properties compared to conventional working fluids such as water, air, and oil commonly used in photovoltaic thermal systems. In summary, the application of nanofluids in PV/T systems has become an important research topic in recent years. Nanofluids are defined as solid-liquid composite materials in which solid nanoparticles with sizes ranging from 1 to 100 nm are suspended in a liquid phase. Numerous studies in the literature have investigated the use of nanofluids in photovoltaic thermal systems and have shown that PV/T systems cooled with nanofluids perform better than systems using conventional coolants [32].

Phase change materials (PCMs) are very important due to their ability to improve photovoltaic module performance and convert solar energy into stable thermal output. The main purpose of integrating PCMs into photovoltaic-thermal (PV/T) systems is to ensure that the absorbed portion of solar radiation is converted into electrical or thermal energy as efficiently as possible. It has been shown that reducing the excessive thermal load that occurs during electricity generation in PV modules through PCM integration provides significant improvements in instantaneous electrical efficiency. Therefore, the integration of PCMs into PV/T configurations has been beneficial in improving overall energy production efficiency as well as achieving a more stable thermal output throughout the day. In addition, since the PV panel temperature is reduced with PV/T systems, a more sustainable and efficient energy conversion process is possible. Therefore, PV/T systems have been accepted as an important alternative technological solution [37].

Although photovoltaic-thermal (PV/T) systems are effective in converting solar energy into electrical and thermal energy, further research is needed to investigate how the integration of phase-change materials (PCMs) can improve their performance [10]. PCMs have been applied in many different systems, including PV/T collectors where they are utilized to maximize electrical efficiency, regulate and store thermal energy [38]. PV/T systems incorporating PCMs have advantages over conventional PV/T configurations such as improved heat storage capacity and reduced photovoltaic cell temperatures. PCMs have high latent heat. Therefore, they begin to store thermal energy as soon as the material reaches its melting temperature and release this energy upon solidification under cooler conditions. Thus, PCMs can maintain sensitive heat properties similar to solid or liquid phase under all operating conditions [39] [40].

6. Photovoltaic Thermal System Characteristics

In this study, it was aimed to enhance the energy and exergy efficiencies by reducing the temperature of the photovoltaic panel through an effective cooling method. To meet the research objectives, three parallel and identical PV/T configurations were experimentally evaluated. The experimental matrix included a standard water-cooled reference system, a secondary unit utilizing a specialized nanofluid for cooling, and a final hybrid setup that integrated both nanofluidic heat transfer and a phase change material layer. The schematic diagram of the experimental setup is presented in Fig.4.

The rear surface of the photovoltaic panels was covered with a 1 mm thick copper plate. Serpentine-shaped copper tubes were welded onto the copper plate. Water and a water-based nanofluid (zirconium oxide) were utilized as the cooling working fluids. The photovoltaic panel has an open-circuit voltage of 21.6 V and a short-circuit current of 5.15 A. Additionally, the panel dimensions were approximately 1200 × 530 × 3.5 mm. Solid paraffin wax was employed as the phase change material. In addition, the rear side of the panel was insulated with polystyrene foam to reduce heat transfer losses.

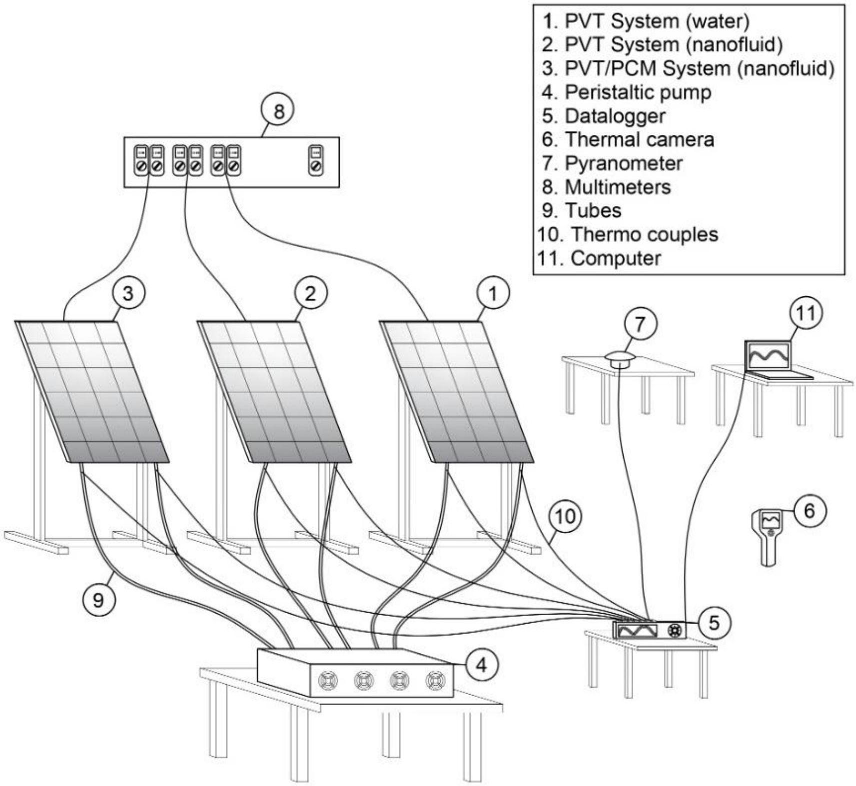

Figure 4. Experimental setup diagram [21] [41]

The general equations utilized in the study are Eqs.[1-4] [21] [41].

Electrical power produced by the photovoltaic panel:

$$\dot{Q}_e = V \times I \tag{1}$$

$\dot{Q}_e$ is the acquired electrical power, while the variable V denotes the voltage output and I represents the current generated by the system.

Electrical efficiency produced by the photovoltaic panel:

$$\eta_e = \frac{V_{oc} \times I_{sc} \times FF}{P_{in}} \tag{2}$$

In this expression, η_e represents the electrical efficiency, while V_{oc} and I_{sc} denote the open-circuit voltage and short-circuit current, respectively. Additionally, P_{in} signifies the incident solar power on the panel, and FF indicates the fill factor.

Thermal efficiency produced by the photovoltaic panel:

$$\eta_{th} = \frac{\dot{Q}_{th}}{\dot{Q}_{solar,in}} \tag{3}$$

$$\eta_{ex,overall} = \frac{\dot{E}_{x,out}}{\dot{E}_{x,in}} = 1 - \frac{\dot{E}_{x,destruction}}{\dot{E}_{x,in}} \tag{4}$$

The parameter $\dot{Q}_{th}$ denotes the effective thermal energy captured by the unit, while $\dot{Q}_{solar,in}$ accounts for the overall solar radiation reaching the PV layer. The variables $\dot{E}_{x,in}$, $\dot{E}_{x,out}$ and $\dot{E}_{x,destruction}$ identify the input, output, and exergy destruction rates, respectively.

7. Results and Discussions

This experimental work is fundamentally driven by the need to mitigate excessive heat accumulation in PV/T panels. By maintaining lower operating temperatures, the research aims to boost not only the electrical output but also the comprehensive energy performance of the entire installation. Within this scope, three different panel configurations were evaluated. In order to more clearly elucidate the effects of the PCM and the nanofluid, a conventional PV/T system was examined in the first stage, a PV/T system employing a nanofluid in the second stage, and finally a PV/T system incorporating both a nanofluid and a hydrocarbon-based phase change material was comparatively investigated. The experimental study was conducted in the province of Bartın on September 14, 2022. During the measurements obtained from the panels, current and direct current (DC) voltage values were recorded separately. The experimental findings revealed that the highest electrical power output and electrical efficiency values were achieved in the PV/T panel configuration integrating both the nanofluid and the phase change material.

Fig. 5 presents the time-dependent current, voltage, electrical power, and electrical efficiency values measured in photovoltaic thermal systems under unloaded conditions (i.e., without electrical load). As observed in Fig. 5(a), the cooling system applied to Panel 3 reduced the panel temperature; consequently, the short-circuit current (I_{sc}) values of Panel 3 were higher than those of the other panels throughout the experimental period. Fig. 5(b) shows that the open-circuit voltage (V_{oc}) decreased with increasing temperature, and the highest voltage values among the panels were obtained for Panel 3. In terms of electrical power comparison, Fig. 5(c) clearly indicates that Panel 3 exhibited the highest power values throughout the experiment.

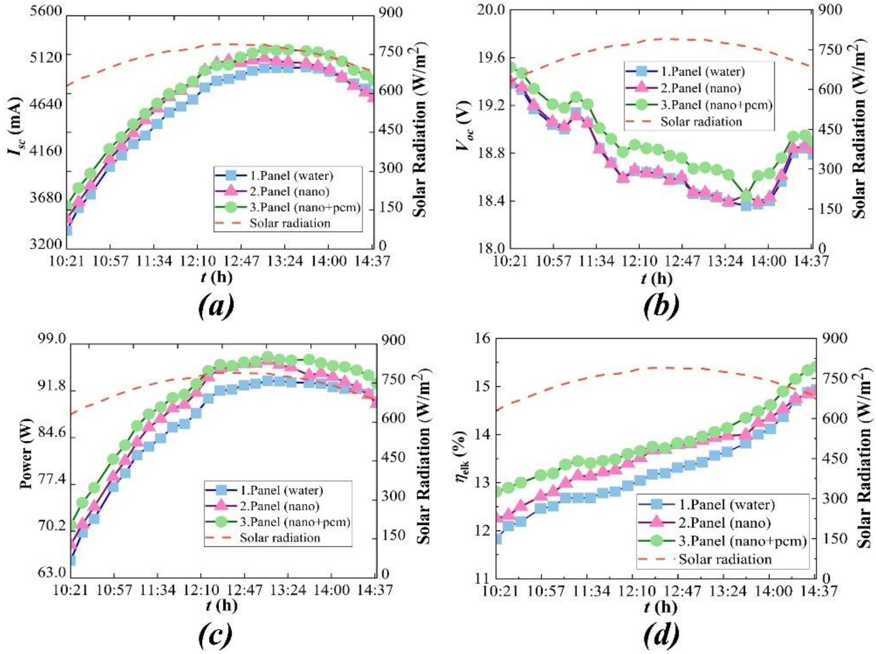

Figure 5. For PV/T systems I_{sc} (a), V_{oc} (b), power (c) and electrical efficiency (d) [21]

For Panel 3, the maximum electrical power was measured as 97.1 W at 13:07, while at the same time, the power values of Panel 1 and Panel 2 were calculated as 93.3 W and 96.4 W, respectively. Accordingly, the electrical power of Panel 3 was found to be approximately 4% and 1% higher than that of Panel 1 and Panel 2, respectively. In addition, the electrical power of Panel 2 was determined to be 3.3% higher than that of Panel 1. At 12:37, when the highest solar irradiance was recorded (789.5 W/m²), the electrical power values of the panels were measured as 92 W, 95.4 W, and 95.6 W, respectively. From the analysis of Fig. 5(d), it is evident that the highest electrical efficiency throughout the experimental period was achieved by Panel 3, which incorporated both a hydrocarbon-based phase change material and a nanofluid. When the average electrical efficiencies were compared, Panel 3 was found to be 4.6% and 2.1%

more efficient than Panel 1 and Panel 2, respectively, while Panel 2 exhibited an electrical efficiency 2.4% higher than that of Panel 1.

The thermodynamic analysis results of the experimental study are presented in Figures 6-8.

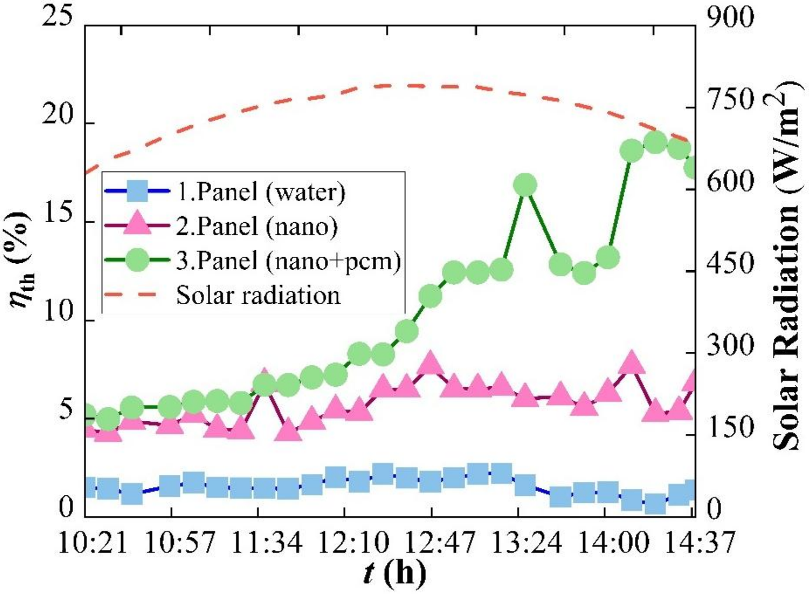

Figure 6. Thermal efficiency of PV/T systems *[21]*

Fig. 6 presents a comparison of the thermal efficiency results of the photovoltaic thermal systems. It was observed that the highest thermal efficiency throughout the experimental period was achieved by Panel 3. The maximum thermal efficiency was determined to be 19% for Panel 3 at 14:22. At the time when the thermal efficiencies reached their peak values, the thermal efficiency of Panel 3 was found to be 8.6 times and 2.5 times higher than those of Panel 1 and Panel 2, respectively. In addition, the thermal efficiency of Panel 2 was determined to be 3.5 times higher than that of Panel 1.

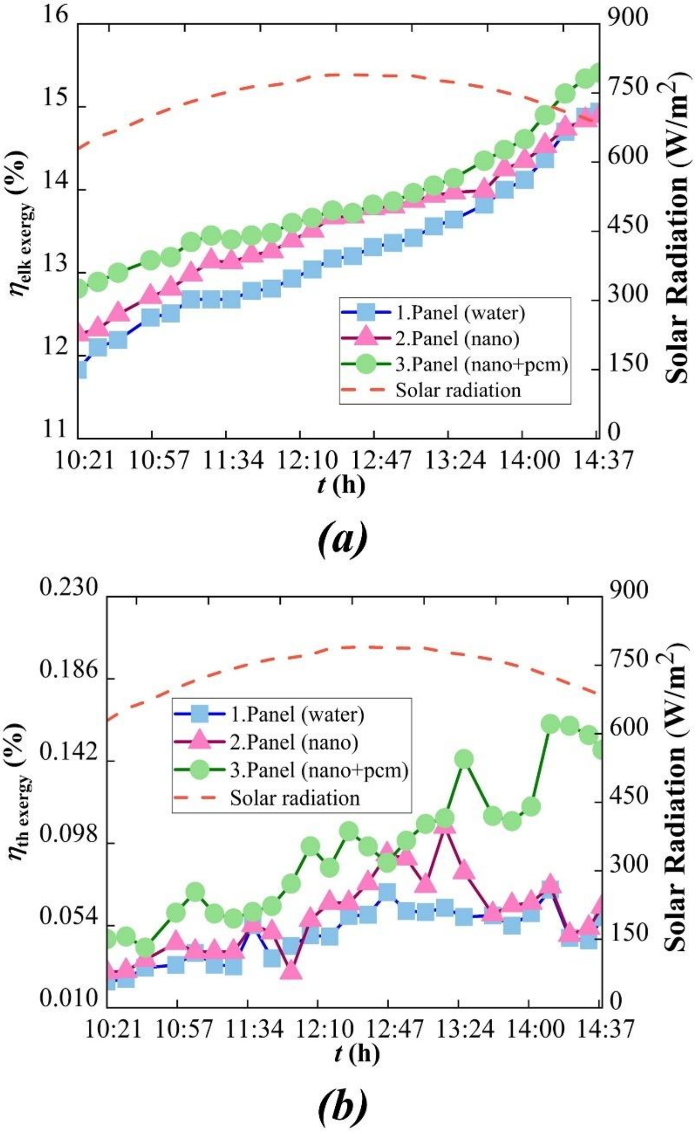

Figure 7. Electrical exergy efficiency (a) and thermal exergy efficiency (b) of PV/T systems [21]

Fig. 7 presents comparisons of the electrical and thermal exergy efficiencies of the photovoltaic thermal systems. Throughout the experimental period, the highest electrical exergy efficiency was obtained for Panel 3, with a maximum average value of 13.9% (Figs. 7(a) and (b)). The lowest average electrical exergy efficiency was recorded for Panel 1 at 0.05%. In the comparative assessment, the electrical exergy efficiency of Panel 3 was found to be 4.6% higher than that of Panel 1 and 2.1% higher than that of Panel 2. In addition, the electrical exergy efficiency of Panel 2 increased by 2.4% compared to Panel 1. With respect to thermal exergy efficiency, Panel 3 was observed to achieve values that were 93.9% higher than those of Panel 1 and 61.9% higher than those of Panel 2. Furthermore, the thermal exergy efficiency of Panel 2 was determined to be 19.7% higher than that of Panel 1.

Fig. 8 compares the overall efficiency and overall exergy efficiency of the photovoltaic thermal systems. For both performance criteria, the highest values were obtained for Panel 3 (Figs. 8(a) and (b)). The maximum overall efficiency for Panel 3 was determined to be 33.8%, which is 2.1 times higher than that of Panel 1 and 1.5 times higher than that of Panel 2. The overall efficiency of Panel 2 was found to be 1.4 times higher than that of Panel 1. Similarly, with respect to overall exergy efficiency, the highest performance was also observed for Panel 3. The overall exergy efficiency of Panel 3 was found to be 4.2% and 2.6% higher than those of Panel 1 and Panel 2, respectively. In addition, the overall exergy efficiency of Panel 2 increased by 1.6% compared to Panel 1.

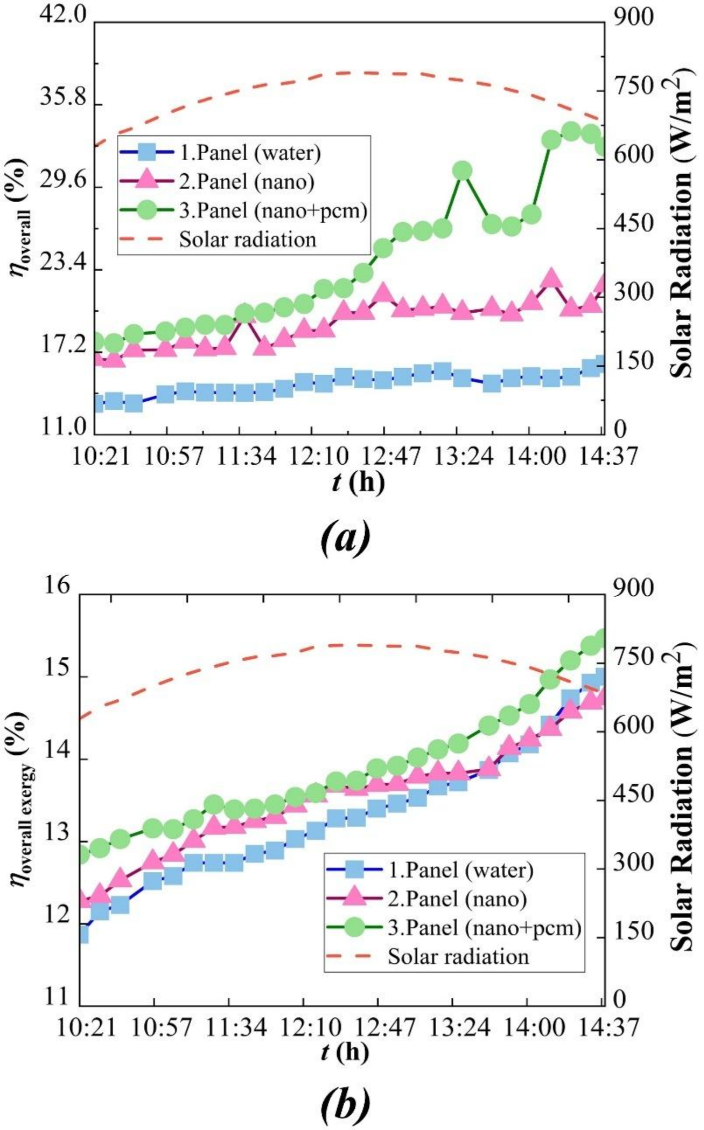

Figure 8. Overall efficiency (a) overall exergy efficiency (b) of PV/T systems [21]

8. Conclusions

In this study, the energy and exergy performance of a photovoltaic thermal (PV/T) system using a phase change material (PCM) and a water-based nanofluid (zirconium oxide) was experimentally investigated. The comparative analysis focused on three distinct configurations: (i) a baseline PV/T unit with water cooling, (ii) a nanofluid-enhanced thermal management system, and (iii) an advanced setup incorporating a combination of nanofluids and hydrocarbon-derived PCMs. Empirical data from the experiments demonstrated that the synergistic effect of integrating PCMs with nanofluid cooling led to a substantial reduction in PV module temperatures. This thermal mitigation directly resulted in a marked enhancement of the system's electrical output and overall stability. In particular, the system containing nanofluid and PCM exhibited superior performance compared to other systems in terms of both electrical power output and electrical efficiency. With the reduction in panel temperature, the open-circuit voltage was better maintained, thus contributing to a reduction in electrical efficiency losses.

In terms of thermal performance, it was determined that the latent heat storage capacity of the phase change material significantly improved the thermal efficiency of the system. By incorporating phase-change substances, the system achieved a more consistent thermal profile across daily cycles, allowing for the effective recovery and utilize of captured heat. Furthermore, the exergy assessment indicated that the hybrid PV/T system—employing both nanofluids and PCMs—offers significant benefits from the perspective of the second law of thermodynamics, surpassing simple energy efficiency metrics in terms of quality-based performance. To conclude, the evidence presented confirms that implementing sophisticated thermal management and heat storage strategies offers a practical pathway to optimize the total efficiency of PV/T units.

References

[1] S. Manigandan, R. Sarweswaran, P. Booma Devi, Y. Sohret, A. Kondratiev, S. Venkatesh, M. Rakesh Vimal ve J. Jensin Joshua, «Comparative study of nanoadditives TiO2, CNT, Al2O3, CuO and CeO2 on reduction of diesel engine emission operating on hydrogen fuel blends,» *Fuel,* cilt 262, no. 116336, 2020.

[2] A. Savvides, C. Vassiliades, A. Michael ve S. Kalogirou, «Siting and building-massing considerations for the urban integration of active solar energy systems,» *Renewable Energy,* cilt 135, pp. 963-974, 2019.

[3] S. Manigandan, P. Gunasekar, S. Nithya, J. Devipriya, S. Raja ve S. Venkatesh, «Influence of injection parameters on NOx emission from biodiesel powered diesel engine by Taguchi technique,» *International Journal of Ambient Energy,* cilt 41, no. 8, pp. 906-910, 2020.

[4] J. Haschke, . J. P. Seif, . Y. Riesen, . A. Tomasi, J. Cattin, . L. Tous, . P. Choulat, . M. Aleman, . E. Cornagliotti, A. Uruena, . R. Russell, F. Duerinckx, . J. Champliaud, J. Levrat, . A. A. Abdallah, . B. Aïssa, N. Tabet, . N. Wyrsch, . M. Despeisse, . J. Szlufcik, . S. D. Wolf ve C. Ballif, «The impact of silicon solar cell architecture and cell interconnection on energy yield in hot & sunny climates,» *Energy & Environmental Science,* no. 5, 2017.

[5] G. Zhang, J. Wei , H. Xie, . Z. Wang, . Y. Xi ve M. Khalid, «Performance investigation on a novel spectral splitting

concentrating photovoltaic/thermal system based on direct absorption collection,» *Solar Energy,* cilt 163, pp. 552-563, 2018.

[6] N. Abdollahi, I. Jeffrey ve J. LoVetri, «Non-Iterative Eigenfunction-Based Inversion (NIEI) Algorithm for 2D Helmholtz Equation,» *Progress In Electromagnetics Research,* cilt 85, pp. 1-25, 2019.

[7] M. Hosseinzadeh, A. Salari, M. Sardarabadi ve M. Passandideh-Fard, «Optimization and parametric analysis of a nanofluid based photovoltaic thermal system: 3D numerical model with experimental validation,» *Energy Conversion and Management,* cilt 160, pp. 93-108, 2018.

[8] C. Sun, «Experimental investigation on the thermal performance of a photovoltaic thermal (PV/T) system incorporating phase change materials,» *Solar Energy,* 2025.

[9] D. Mazzeo, E. Ogliari, A. Lucchini, A. Dolara, I. Carraretto, G. Manzolini, L. Colombo ve S. Leva, «Integration of photovoltaic modules with phase change materials: Experimental testing, model validation and optimization,» *Energy,* pp. 319, 134959, 2025.

[10] S. Alsaqoor, . A. Alqatamin, . A. Alahmer, . Z. Nan, Y. Al-Husban ve . H. Jouhara, «The impact of phase change material on photovoltaic thermal (PVT) systems: A numerical study,» *International Journal of Thermofluids,* cilt 18, p. 100365, 2023.

[11] O. Rejeb, B. Lamrani, R. Lamba, T. Kousksou, T. Salameh, A. Jemni, A. K. Hamid, M. Bettayeb ve C. Ghenai, «Numerical

investigations of concentrated photovoltaic thermal system integrated with thermoelectric power generator and phase change material,» *Journal of Energy Storage ,* cilt 62, p. 106820, 2023.

[12] Z. Liu, X. Yang, H. M. Ali, R. Liu ve J. Yan, «Multi-objective optimizations and multi-criteria assessments for a nanofluid-aided geothermal PV hybrid system,» *Energy Reports,* cilt 9, pp. 96-113, 2023.

[13] A. H. Al-Waeli, H. A. Kazem, M. T. Chaichan ve K. Sopian, «Experimental investigation of using nano-PCM/nanofluid on a photovoltaic thermal system (PVT): Technical and economic study,» *Thermal Science and Engineering Progress,* cilt 11, pp. 213-230, 2019.

[14] İ. Şen, Fotovoltaik Panellerde Faz Değiştiren Madde Kullanımının Verim Üzerine Etkisinin Deneysel Olarak Araştırılması, Batman: Yüksek Lisans Tezi, Batman Üniversitesi Fen Bilimleri Enstitüsü, 2019.

[15] Z. Şen, Solar Energy Fundamentals and Modeling Techniques. Atmosphere, Environment, Climate Change and Renewable Energy, Spain: Springer, 2007.

[16] A. Selam, S. Özel ve Ö. Arıoğlu Akan, «YENİLENEBİLİR ENERJİ KULLANIMI AÇISINDAN TÜRKİYE'NİN OECD ÜLKELERİ ARASINDAKİ YERİ,» *Dumlupınar Üniversitesi Sosyal Bilimler Dergisi,* pp. 317-334, 2014.

[17] Y. E. 2. ,. I. P. IEA (2024), «Renewables 2024 Analysis and forecast to 2030,» International Energy Agency, Paris, 2024.

[18] M. Vaka, R. Walvekar, A. Rasheed, M. Khalid ve H. Panchal, «A Review: Emphasizing the Nanofluids Use in PV/T Systems,» *IEEE Access,* cilt 8, p. 58227–58249, 2020.

[19] B. Paridaa, S. Iniyanb ve R. Goic, «A review of solar photovoltaic technologies,» *Renewable and Sustainable Energy Reviews,* cilt 15, pp. 1625-1636, 2011.

[20] N. Aste, C. Del Pero ve F. Leonforte, «Water PVT Collectors Performance Comparison,» *Energy Procedia,* cilt 105, p. 961–966, 2017.

[21] K. Sontay, Investigation of the effect of phase change material and water-based nanofluid use on the performance of photovoltaic thermal systems, Kocaeli: Kocaeli University / Institute of Science / Department of Mechanical Engineering, 2025.

[22] X. Cao, K. Wang, L. Xia, W. Yu, B. Li, j. Yao ve R. Yao, «A three-stage decision-making process for cost-effective passive solutions in office buildings in the hot summer and cold winter zone in China,» *Energy and Buildings,* cilt 268, p. 112173, 2022.

[23] İ. Kuloğlu, Faz Değiştiren Madde İle Prefabrik Yapıların Soğutulması, Elazığ: Fırat Üniversitesi Fen Bilimleri Enstitüsü, Yüksek Lisans Tezi, 2018.

[24] A. Sharma, V. Tyagi, C. Chen ve D. Buddhi, «Review on thermal energy storage with phase change materials and applications,» Feb. 2009.

[25] M. Mert , M. Sert ve H. Mert, «A Review of the Current Status of Organic Phase Change Materials for Thermal Energy Storage Systems,» *Journal of Engineering Sciences and Design,* cilt 6(1), pp. 161-174, 2018.

[26] Y. Seong ve J. Lim, «Energy Saving Potentials of Phase Change Materials Applied to Lightweight Building Envelopes,» *Energies,* cilt 6(10), p. 5219–5230, 2013.

[27] F. A. Çakmak, Faz Değiştiren Malzemelerin Bina Dış Duvarlarında Kullanımının Isı Kazanç ve Kaybına Etkisinin Araştırılması, Elazığ: Yüksek Lisans Tezi, Fırat Üniversitesi Fen Bilimleri Enstitüsü, 2019.

[28] . V. Sridhara ve L. N. Satapathy , «Al2O3-based nanofluids: a review,» *Nanoscale Research Letters,* cilt 6, p. 456, 2011.

[29] H. Fayaz , N. R., . N. A. Rahim ve . M. Hasanuzzaman, «Energy and exergy analysis of the PV/T system: Effect of nanofluid flow rate,» *Solar Energy,* cilt 169, pp. 217-230, 2018.

[30] M. S. Ebaid , A. M. Ghrair ve M. Al-Busoul , «Experimental investigation of cooling photovoltaic (PV) panels using (TiO2) nanofluid in water-polyethylene glycol mixture and (Al2O3) nanofluid in water-cetyltrimethylammonium bromide mixture,» *Energy Conversion and Management,* cilt 155, pp. 324-343, 2018.

[31] J. Sengers ve . J. T. R. Watson, «Improved international formulations for the viscosity and thermal conductivity of

water substance,» *Journal of physical and chemical reference data,* cilt 15, pp. 1291-1314, 1986.

[32] M. KAYFECI, S. ALOUS ve A. UYSAL, «PV/T SİSTEMLERDE SOĞUTUCU OLARAK ÇDKNT-SU NANO AKIŞKAN KULLANIMININ DENEYSEL İNCELENMESİ,» *mmo.org.tr.*

[33] S. Lee, S. Choi, S. Li ve J. Eastman, «Measuring Thermal Conductivity Of Fluids Containing Oxide Nanoparticles Transaction Of ASME,» *Journal Of Heat Transfer,* cilt 121, pp. 280-289, 1999.

[34] M. Tawfik, «Experimental Studies Of Nanofluid Thermal Conductivity Enhancement And Applications: A Review,» *Renewable and Sustainable Energy Reviews,* cilt 75, pp. 1239-1253, 2017.

[35] H. Zhu, Y. Lin ve Y. Yin, «A novel one-step chemical method for preparation of copper nanofluids,» *Journal of Colloid and Interface Science,* p. 277, 2004.

[36] J. Estman ve S. Chol , «Enhancing thermal conductivity of fluids with nanoparticles,» *SME-Publications-Fed,* cilt 231, pp. 99-106, 1995.

[37] M. Ergene, Fotovoltaik Termal (FV/T) Sistemlerde Nanoakışkanlı Isı Borusu Ve Faz Değiştiren Madde (FDM) Kullanımının Deneysel Olarak Araştırılması, Elazığ: Yüksek Lisans Tezi, Fırat Üniversitesi Fen Bilimleri Enstitüsü, 2021.

[38] S. Mengjie, N. Fuxin, M. Ning, H. Yanxin ve . D. Shiming, «Review on building energy performance improvement using

phase change materials,» *Energy and Buildings,* cilt 158, pp. 776-793, 2018.

[39] A. Alahmer, S. Ajib ve X. Wang, «Comprehensive strategies for performance improvement of adsorption air conditioning systems: A review,» *Renewable and Sustainable Energy Reviews,* cilt 99, pp. 138-158, 2019.

[40] M. I. Al-Amayreh ve A. Alahmer, «On improving the efficiency of hybrid solar lighting and thermal system using dual-axis solar tracking system,» *Energy Reports,* cilt 8, pp. 841-847, 2022.

[41] K. Sontay, E. Öğüt, A. Ustaoğlu, D. Özkan ve B. Kurşuncu, «Experimental and optimization study of nanofluid utilized PVT systems with hydrocarbon based PCM: An Energetic-exergetic approach,» *Applied Thermal Engineering,* cilt 273, p. 126468, 2025.

CHAPTER 3

INVESTIGATION OF ENERGY, VIBRATION AND SURFACE ROUGHNESS FOR SUSTAINABLE MANUFACTURING IN THE MACHINING OF 17 4 PH STAINLESS STEEL

ABİDİN ŞAHİNOĞLU[1]

Introduction

Machinability, chuck vibration, tool vibration, surface roughness, energy consumption, and power consumption are essential investigation subjects. It is necessary to examine and compare these values together. Therefore, in this experimental study, 17-4 PH stainless steel with two different hardness values (30-35 HRC) was machined at three different cutting speeds, feed rates, and cutting depths, with two different insert radii cutting tools. Machinability tests were carried out according to the L36 experimental design. According to ANOVA results, the feed rate (***f***) is the most influential parameter on chuck vibration (49.14%), tool vibration (59.42%) and energy consumption (47.88%). The depth of cut (***ap***) is the most influential parameter on the amount of power (60.74%) and sound intensity (43.54%). Tool nose radius (***Re***) is the

---

[1] Assos. Prof. Dr., Manisa Celal Bayar University,
Machine and Metal Technology, 0000-0003-0040-442X

most significant parameter on the surface roughness (***Ra***), with an impact rate of 49.83%. As the material hardness value and the tool nose radius increase, the vibration values, power/energy consumption and sound intensity increase, while the surface roughness value decreases. In this study, mathematical models were created depending on the cutting conditions. In addition, the regression and correlation relationship between sound and vibration, between sound and power consumption (***PC***), and between power consumption and vibration value is explained. Finally, the weighted multiple optimisation methods determined the optimum cutting condition. It has been defined as the ideal cutting condition, hardness of 30 HRC, cutting speed (***v***) of 160 m/min, feed rate of 0.1 mm/rev, depth of cut of 0.9 mm and nose radius of 0.8 mm. According to these processing conditions, the machine performance increased by 20.76%; chuck vibration decreased by 14.28%, tool vibration by 33.50%, energy consumption **(*EC)*** by 2.48%, surface roughness by 56.25%, and sound intensity by 1.61% decreased.

Martensitic stainless steel (17 4 PH) has high strength, corrosion resistance and easy machinability. In their study, Palanisamy et al. [3] made processing experiments on 17-4 stainless steel. The effects of ***v***, ***ap*** and ***f*** on cutting force (Fz) and ***Ra*** were investigated. Lai et al. compared the effect of coolants in finishing turning 17-4 PH stainless steel. [1].

Leyland et al. stated that it significantly increased wear resistance without affecting the desired corrosion properties of 17-4 PH stainless steel [2]**.** Aydemir, different heat treatments were applied on 17-4PH stainless steel. He stated that heat treatment improves the performance and hardness of the material [3]. Lai et al. studied the effects of cooling systems in turning 17-4PH stainless steel [1] [4]**.** As the workpiece hardness increases, it becomes difficult to machine the workpiece [5].

The tool nose radius (***Re***), especially the ***Ra*** [6], is an effective parameter in machining. As the ***Re*** increases, the ***Ra*** decreases [6] [7] and the tool life increases. However, the cutting forces increase with increasing nose radius [6][8][7]. In addition, as the ***Re*** increases, the thickness of the white layer formed in hard materials decreases [8]. The cutting energy increases as the ***Re*** increases [9]. The friction area increases as the ***Re*** increases [10], but the resulting heat is easier to carry. Therefore, the tool and the workpiece are less affected by the temperature with more heat transfer. Although it significantly affects the processing of 17-4 PH stainless steel materials, there has not been enough work on this subject. Therefore, this experimental study investigated the effects of ***Re*** in 17-4 PH stainless steel.

More electrical energy is produced [11]**.** Most of the energy production comes from fossil fuels. The industry sector has 30% of the energy used globally [12]**.** The manufacturing industry has 60% of the energy used in the industrial sector. Therefore, energy efficiency is essential in machine tools [13][14]**.** Because most of the electrical energy used in machine tools is obtained from fossil fuels [12]**.** Due to the energy used in machine tools, the carbon dioxide emission rate is 90%. [14]**.** For sustainable manufacturing, suitable processing conditions must be determined[15] [16][17]. Chou et al. reported that the cutting energy increased when the ***Re*** [8] and tool wear increased [18]. Instant cutting energy increases with increasing ***f*** and ***ap***. However, the total ***EC*** is decreasing [9]. In addition, the rotation of the spindle in the machine tool increases the ***Re***. When the chip is not removed, the lathe chuck does not rotate, which reduces ***EC*** [13]. Estimating ***EC*** is of great importance for green manufacturing [19]. Therefore, processing conditions were examined in this experimental study to reduce ***EC***, and models were created to predict ***EC***.

One of the critical research topics studied in machining is vibration[20]. The vibration occurs due to heavy mechanical loads [5]. As vibration increases, surface quality deteriorates [21][22], cutting efficiency decreases, and tool wear increases [5][10].

Vibration must be controlled for stable production [10][21]. Ambhore et al. [5]studied the vibration values in turning AISI 52100 Steel, Al-Shayea et al. [10]AISI 1040 Steel. However, although high vibration values occur in the processing of 17-4PH stainless steel, the vibration issue related to this material has not been investigated.

Surface quality is critical in machinability. The ***Ra*** is the most important indicator of surface quality [10]. The lower the ***Ra*** of the machine parts, the lower the friction value [23]. The research shows that the ***Ra*** increases the ***f*** [7][10]. Therefore, many researchers conduct experimental studies to reduce the ***Ra*** [22]. This experimental study investigated the effects of many cutting conditions on the ***Ra*** in 17 4PH stainless steel machining.

One of the current research topics has been sound intensity in machinability [24][22]. The sound generated during turning is easily measured. In addition, the sound produced in machining indicates many machinability parameters. Sound intensity indicates vibration, ***PC***, cutting forces and tool wear [25]. This study explains the relationship between sound intensity and cutting parameters, ***Re***, and material hardness value. Since sound intensity is relatively easy to measure, explaining the equations between sound intensity and ***PC*** and between sound intensity and machine vibration values will significantly contribute to machinability. It is aimed to predict vibration and machine tool ***PC*** values by measuring sound intensity with the predictive models obtained in this study.

In the studies, RSM [16]**,** ANN [5] [7], different regression models were created in different materials [10][19]. Effect ratios of cutting parameters were determined. However, vibration, sound intensity and ***PC*** analyses were not performed on 17-4 PH stainless steel with ANN, RSM, and ANOVA. In addition, machinability properties such as ***PC*** and chuck vibration value, tool vibration and sound intensity, and ***PC*** were not examined in 17 4PH materials.

Therefore, this experimental study investigated 17 4 PH stainless steel machinability.

The optimisation has significant in machining[22]. Optimum cutting conditions may be different for different materials. Panday et al. [26] in AISI 1060 Steel, Karaaslan and Şahinoğlu [23] in AISI 4140 Steel, and Sing et al. [27] in EN 31 Steel determined optimum cutting conditions. This experimental study determined optimum cutting parameters for the lowest ***Ra***, the lowest ***EC***, the highest machine performance, the lowest sound intensity, and the lowest vibration values in 17 4PH stainless steel.

In machinability conditions with many input and output parameters, the weigh optimisation technique is an effective solution [23][27] because the importance of each output parameter can differ. The weighted optimisation technique was used in this experimental study since there are five input and six output parameters. The experimental results were ordered from the most ideal to the non-ideal results.

When the studies are examined, critical studies have been made about ***PC***, ***Ra*** and vibration value separately. However, in the literature studies, lathe chuck vibration value, tool vibration in the lathe, machine tool ***PC***, ***EC***, sound intensity and ***Ra*** have not been examined. In addition, lathe chuck vibration and tool vibration were not compared in any study. The relationship between vibration and ***PC***, the relationship between vibration and sound intensity, and the relationship between ***PC*** and sound were not examined. Therefore, in this study, two different hardness17-4 PH Stainless steel, with two different insert radii cutting tools, three different cutting speeds, three different feed rates and three different depths of cut have been machined. Thus, these parameters, which are very important in machinability, were examined and compared, ANOVA Results were obtained, and mathematical models were created.

Material Method

This section explains the material properties used in the experimental study, cutting conditions, machine tool, cutting tool, and measuring devices. In addition, information is given about the methods used in measurement and data analysis.

50 mm diameter, 250 mm length 17 4 PH Stainless steel, tailstock hole is drilled before heat treatment. 1 mm of material was removed from the surface to make the processing experiments more homogeneous. Cutting parameters were determined using the used cutting tool catalogue and literature studies. Primarily since it is aimed to obtain a good surface quality, the ***f*** was chosen a little low.

The experimental study, shown in Figure 1, was carried out on a Taksan TTC630 model CNC lathe. In vibration measurements, the machine tool must be rigid. This machine tool has been used in previous scientific studies[28][15]. Carbide tools of Simutomo Company are used for turning 17 4 PH material. Coated inserts with geometry WNMG080404- WNMG080408 are used. The tool holder has a 95-degree approach angle and a -6 degree rake angle. The vibration value is reduced by connecting the tool holder at a distance of 10 mm.

Immediately after the machining test, the ***Ra*** was measured. The ***Ra*** was measured with a PCE RT-1200 roughness device. The arithmetic mean of the measurements taken from 3 different points was calculated.

The vibration amount was measured with PCE VM 5000 brand Vibration measuring device. The vibration measurement probe is attached to the mirror and tool holder.

PCE brand clamp meter was used to measure the current value during processing. The current value passing through a single-phase was measured. Voltage values were measured using the regulator. ***PC*** is calculated according to current and voltage values.

The test results were transferred to the computer. Minitab 20 was used. Figure 1. Experiments setup and flow chart

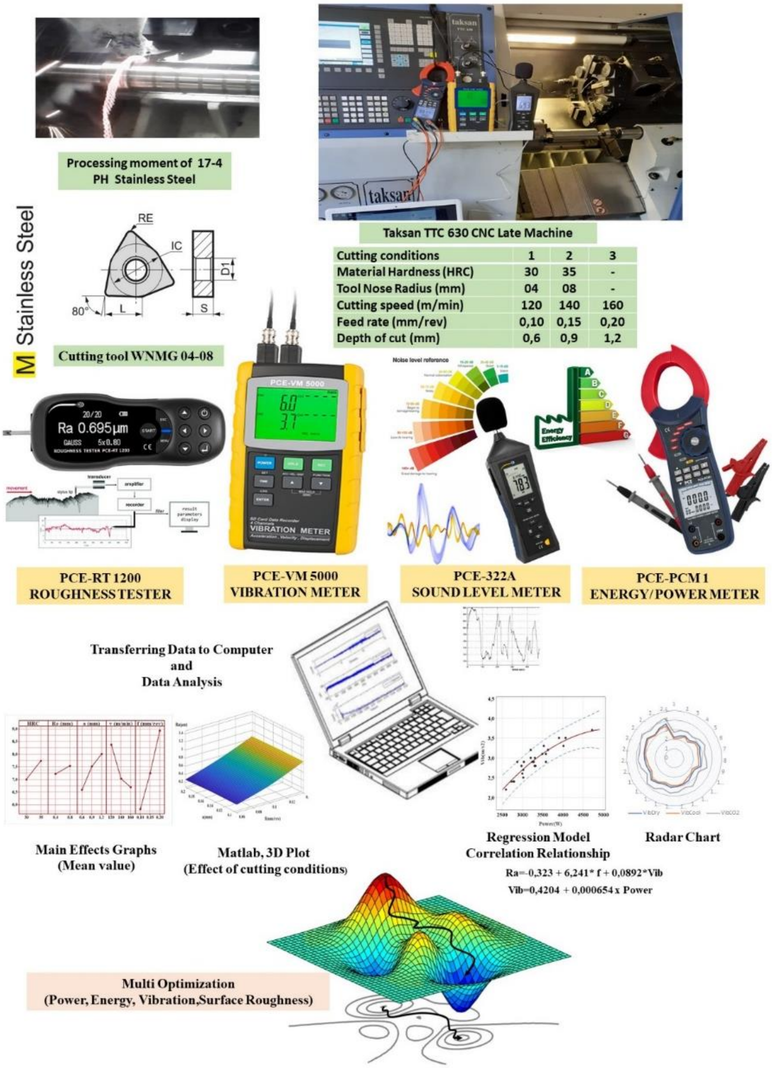

Cutting conditions	1	2	3
Material Hardness (HRC)	30	35	-
Tool Nose Radius (mm)	04	08	-
Cutting speed (m/min)	120	140	160
Feed rate (mm/rev)	0,10	0,15	0,20
Depth of cut (mm)	0,6	0,9	1,2

$Ra = -0{,}323 + 6{,}241 * f + 0{,}0892 * Vib$

$Vib = 0{,}4204 + 0{,}000654 \times Power$

Figure 1. Experiments setup and flow chart

Experimental results and discussion

This section shows experimental results, ANOVA results, main effect graphs and regression equations. ***PC*** and ***EC***, chuck vibration and tool vibration were compared. The relationship between power and vibration, power and sound, vibration and sound has been explained. In addition, the sound intensity, ***EC***, vibration, and ***Ra,*** depending on the machining time are shown. Finally, the optimum cutting conditions were determined using the weighted multiple optimisation methods. The test results are shown in Table 1.

Table 1. Experimental results

	HRC	**Re (mm)**	**ap (mm)**	**V (m/min)**	**f (mm/rev)**	**VibM (m/s2)**	**VibC (m/s2)**	**Power (W)**	**EC (j/mm3)**	**Sound (dB)**	**Ra (µm)**
1	30	0.4	0.6	120	0.1	0.6	5.2	1516.2	41.06	73,2	1.33
2	30	0.4	0.9	140	0.15	1	6.8	2707.5	27.93	77,9	2.48
3	30	0.4	1.2	160	0.2	1.5	8.3	4007.1	20.35	82,5	3.79
4	30	0.4	0.6	120	0.1	0.6	5.2	1516.2	41.06	73,3	1.33
5	30	0.4	0.9	140	0.15	1	6.8	2707.5	27.93	77,9	2.48
6	30	0.4	1.2	160	0.2	1.5	8.3	4007.1	20.35	82,6	3.79
7	30	0.4	0.6	120	0.15	0.8	7.5	1949.4	35.20	74,8	2.42
8	30	0.4	0.9	140	0.2	1.3	7.9	3032.4	23.47	79,9	3.76
9	30	0.4	1.2	160	0.1	1	5.5	3140.7	31.90	78,3	1.35
10	30	0.8	0.6	120	0.2	1.1	9.3	2382.6	32.26	77,2	1.35
11	30	0.8	0.9	140	0.1	0.9	5.2	2490.9	38.55	77,0	0.81
12	30	0.8	1.2	160	0.15	1.4	6.8	3790.5	25.66	81,3	0.96
13	30	0.8	0.6	140	0.2	1.1	7.4	2382.6	27.66	77,8	1.31
14	30	0.8	0.9	160	0.1	1	4.9	2490.9	33.73	77,6	0.77
15	30	0.8	1.2	120	0.15	1.2	8.7	3357.3	30.31	78,8	1.05
16	30	0.8	0.6	140	0.2	1.1	7.4	2382.6	27.66	77,8	1.31
17	30	0.4	0.9	160	0.15	1	6.1	2815.8	25.42	78,1	2.43
18	30	0.8	1.2	120	0.15	1.2	8.7	3357.3	30.31	79,1	1.05

19	35	0.4	0.6	140	0.1	0.9	5.1	1949.4	50.42	75,3	1.12
20	35	0.4	0.9	160	0.15	1.2	6.8	3465.6	31.29	79,7	2.23
21	35	0.4	1.2	120	0.2	1.7	11.2	4548.6	30.80	82,2	3.62
22	35	0.4	0.6	140	0.15	1	6.8	2490.9	38.55	76,9	2.25
23	35	0.4	0.9	160	0.2	1.5	8.4	4007.1	27.13	82,3	3.52
24	35	0.4	1.2	120	0.1	1.1	7.6	3682.2	49.86	78,3	1.24
25	35	0.4	0.6	160	0.15	1	6.2	2599.2	35.20	77,1	2.24
26	35	0.4	0.9	120	0.2	1.5	10.6	3573.9	32.26	80,4	3.65
27	35	0.4	1.2	140	0.1	1.1	6.8	3790.5	44.00	79,3	1.25
28	35	0.8	0.6	160	0.15	1.2	6.2	2924.1	39.60	79,0	0.81
29	35	0.8	0.9	120	0.2	1.5	10.9	4115.4	37.15	81,9	1.25
30	35	0.8	1.2	140	0.1	1.2	6.8	4115.4	47.77	80,2	0.71
31	35	0.8	0.6	160	0.2	1.4	7.9	3465.6	32.15	80,6	1.21
32	35	0.8	0.9	120	0.1	1	6.9	3140.7	52.69	77,8	0.62
33	35	0.8	1.2	140	0.15	1.5	7.9	4440.3	34.36	82,7	1.02
34	35	0.8	0.6	160	0.1	1	4.9	2490.9	50.60	77,0	0.61
35	35	0.8	0.9	120	0.15	1.2	8.8	3573.9	43.02	78,7	0.91
36	35	0.8	1.2	140	0.2	1.7	9.5	4765.2	27.66	83,5	1.33

ANOVA Results

The ANOVA results show the effect ratios of the input parameters on the output parameters. The parameters effective in the 95% ($p<0.05$) confidence interval are shown. The most influential parameter is shown in bold.

As seen in Table 2, the ***f*** (49.14%) is the most critical parameter of the lathe chuck vibration value. The ***ap*** follows the ***f*** of 31.04%. The ***f*** is the most influential parameter on tool vibration values with 59.42%. In tool vibration, the ***v*** has an effect of 19.99%.

Similarly, Kam et al. [20] explained in their study that the most effective parameter on vibration is the feed rate.

The most influential parameters on ***PC*** are ***ap*** (60.74%), material hardness value (20.26%) and ***f*** (15.69%). The effects of ***f***, hardness value and ***v*** on ***EC*** are 47.88%, 24.76% and 8.23%, respectively.

The most critical parameters are the ***Re*** and the ***f*** on the ***Ra***, with 49.83% and 34.36% effect rates. The most critical parameter of the sound intensity is the ***ap*** with 43.54%. After the ***ap***, the most crucial parameter is the ***f***, with an impact rate of 33.83%.

Table 2. ANOVA results

VibM (m/s2)					**VibC (m/s2)**				
Source	**DF**	**Adj SS**	**Adj MS**	**% Cont**	**Source**	**DF**	**Adj SS**	**Adj MS**	**% Cont**
HRC	1	0,33284	0,33284	13,00	HRC	1	5,9154	5,9154	6,10
Re	1	0,06676	0,06676	2,61	ap	1	12,0417	12,0417	12,42
ap	1	0,7947	0,7947	31,04	v	1	19,3751	19,3751	19,99
v	1	0,05188	0,05188	2,03	**f**	**1**	**57,5979**	**57,5979**	**59,42**
f	**1**	**1,25791**	**1,25791**	**49,14**	v *v	1	1,6123	1,6123	1,66
Re *v	1	0,02845	0,02845	1,11	v *f	1	1,1012	1,1012	1,14
ap *f	1	0,02046	0,02046	0,80	Error	29	0,9026	0,0311	0,93
Error	28	0,03844	0,00137	1,50	Total	35	96,9364		100,00
Total	35	2,56		100,00					
Power (W)					**EC (j/mm3)**				
Source	**DF**	**Adj SS**	**Adj MS**	**% Cont**	**Source**	**DF**	**Adj SS**	**Adj MS**	**% Cont**
HRC	1	4991743	4991743	20,26	HRC	1	647,92	647,92	24,76

Re	1	325566	325566	1,32	Re	1	37,83	37,83	1,45
ap	**1**	**14966552**	**14966552**	**60,74**	ap	1	140,61	140,61	5,37
v	1	188089	188089	0,76	v	1	215,3	215,3	8,23
f	1	3867434	3867434	15,69	**f**	**1**	**1252,84**	**1252,84**	**47,88**
HRC* Re	1	158333	158333	0,64	f *f	1	45,07	45,07	1,72
Error	29	247483	8534	1,00	HRC *f	1	58,29	58,29	2,23
Total	35	24642072		100,00	Error	28	45,69	1,63	1,75
					Total	35	2616,82		100,00
Ra (µm)					**Sound (dB)**				
Source	**DF**	**Adj SS**	**Adj MS**	**% Cont**	**Source**	**DF**	**Adj SS**	**Adj MS**	**% Cont**
HRC	1	0,1753	0,1753	0,47	HRC	1	23,390	23,3904	10,24
Re	**1**	**18,5416**	**18,5416**	**49,83**	Re	1	5,088	5,0885	2,23
ap	1	0,054	0,054	0,15	**ap**	1	99,438	99,4382	43,54
f	1	12,7848	12,7848	34,36	v	1	15,369	15,3692	6,73
f *f	1	0,0608	0,0608	0,16	f	1	77,249	77,2485	33,83
Re *f	1	4,2951	4,2951	11,54	Error	30	5,755	0,1918	2,52
Error	29	0,0521	0,0018	0,14	Total	35	228,375		100,00
Total	35	37,2104		100,00	HRC	1	23,390	23,3904	10,24

Chuck Vibration and Tool Vibration

Vibration has a significant effect on machining[29][22][30]. As seen in Figure 2, lathe chuck vibration and tool vibration increase with increasing ***ap*** and ***f***. Similar results were found in research on other materials[20]. In AISI 1040 steels [10] and AISI 4140 [22][31] steel the vibration value increased with ***f*** and cut depth. The chip thickness increases with increasing ***f*** [26]. The amount of loading increases with increasing chip thickness. Therefore, the vibration value rises. Greater cutting forces increase the ***ap*** and ***f*** [6]. *Fc=Ac x Ks (Ac: chip area mm^2, ks: specific cutting force N/mm^2).* Vibration values also increase with increasing cutting forces. The increase in the hardness value of the workpiece causes more vibration due to the cutting forces[31][20]. With the increased ***v***, the vibration on the lathe chuck increases while the vibration on the tool decreases. The temperature increases with increasing ***v*** [26][6]. The rise in temperature causes thermal softening[32]. This makes cutting easier. Thus, the vibration on the tool is reduced. In addition, easier cutting occurs as the ***v*** increases. Therefore, the lathe chuck vibration value has increased. As the ***Re*** increases, the tool and workpiece contact area increases. Therefore, more friction area is created. Thus, the temperature and shear force increased [6]. Thus, as the ***Re*** increases, the lathe chuck vibration and the vibration on the tool increase. Similar result find other study [29][30].

Power Consumption -Energy Consumption

In recent years, the importance of researching energy efficiency and environmentally friendly production methods has increased [17][33]. High ***EC*** in machine tools is a significant problem [32]. Reducing ***EC*** with cutting parameters and different cutting conditions is an essential subject of investigation [34].

The instantaneous current value increases with increasing cutting parameters. Therefore, the ***PC*** increases [32]. But the processing time is shortened [35]. Therefore, the total ***EC*** decreases [17][23] [18]. The equation shows that instantaneous ***PC*** increases with increasing cutting forces. *P=fc x V/ 60000 (P=power consumption, fc=cutting force, V=cutting speed)*. Since the cutting force is directly related to ***PC***, sustainability is important [16]. The higher the ***f***, the shorter the machining time. Therefore, the cutting energy (j/mm^3) decreases [8][9]. Similarly, the ***PC*** increases as the ***v*** (turning chuck revolution number) increase [13]. However, as the ***v*** increases, the total ***EC*** decreases as the machining time is shortened.

Ahmat at all. [36], explain as the v increases, the EC decreases as the thermal softening and decreases cutting force.

The effect of ***Re*** on energy and ***PC*** is shown in figure 2. The larger the ***Re***, the greater the friction between the chip and the tool [37]. Therefore, the ***PC*** increases. Since the change of the ***Re*** does not affect the machining time, ***EC*** and ***PC*** increase. In other studies, it has been stated that the cutting energy increases as the ***Re*** increases [8].

When the ***Ra*** is low, the friction in the machine parts is low. The lower the friction, the lower the energy loss. In addition, as the workpiece's hardness increases, the workpiece's service life also extends. Due to these properties, it is advantageous to increase the hardness value.

Surface Roughness

As seen in Figure 2, the ***Ra*** increased with increasing ***f***. In the researches, In AISI 1060 Steel [26] and AISI D2 Steel [7][32], the ***Ra*** increased as the ***f*** increased. As the ***f*** increases, the depth of the helical grooves increases[35]. Therefore, the roughness value increases. In addition, with increasing ***ap*** and ***v***, temperature and BUE formation increase. With the formation of BUE, the tool geometry changes. Changing the tool geometry causes the surface quality to deteriorate [16]. The ***Ra*** increased with increasing ***v*** and ***ap***. The temperature increases with increasing ***v*** [26][16] and the ***ap***. With increasing temperature, material removal becomes easier [38]. However, the chip is larger because the material is easier to move away from the workpiece. Large material removal causes the increasing ***Ra***.

The ***Ra*** decreased with increasing ***Re***. In similar studies, the ***Ra*** decreased with increasing ***Re*** [6][7]. Theoretically, the ***Ra*** is expressed in the equation $Ra=f^2/32Re$ *(Ra= Surface roughness, f= feed rate, Re= nose radius)*. The studies show that the ***f*** [10] and the ***Re*** [9] are the most effective cutting parameter on the ***Ra***.

As the hardness value in steel increases, the grain boundary of the material decreases; therefore, the removed material is more minor. Therefore, the ***Ra*** is lower.

Sound intensity

Sound is easily measured in the turning process. The increase in noise indicates increased tool wear, vibration and ***EC***. As seen in Figure 2, the noise intensity increases with ***f***, so the ***Ra***, ***PC***, chuck and tool vibration have increased. This is because with increasing feed, the chip cross-section increases, and the vibration increases. Therefore, the sound intensity increases. Similar results have been found in other studies[33]. Mallick et al.[32] AISI D2 Steel, Asiltürk et al.[22] AISI 4140 steel in machining found similar results.

Increasing ***ap***, chuck vibration, tool vibration, ***PC*** and noise intensity[35] increased. This is because a larger cross-section chip is broken with increasing ***ap***. Greater strength and power are generated[38]. Therefore, the sound intensity increases. Similarly, as the material hardness value and ***Re*** increase, sound intensity, chuck vibration value, tool vibration and ***PC*** increase. Similar results have been found in other studies[35][39], the sound intensity increases as the number of chuck revolutions increases [40]**.**

Figure 2. Main effect graphs

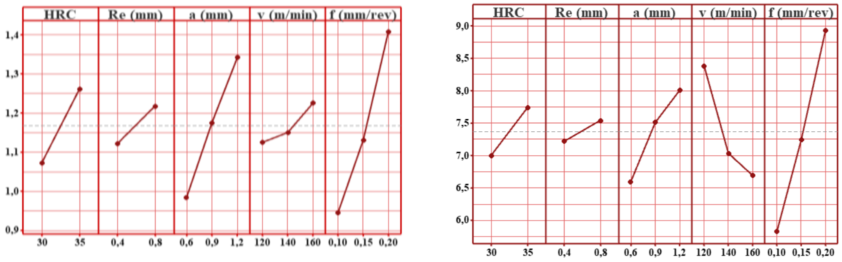

a) VibM (m/s2) *b) VibC (m/s2)*

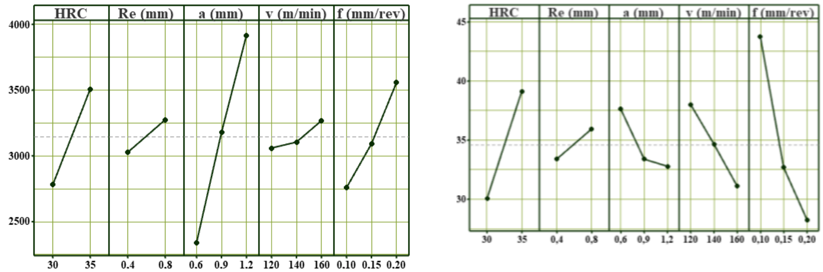

c)Power (W) d) EC (j/mm3)

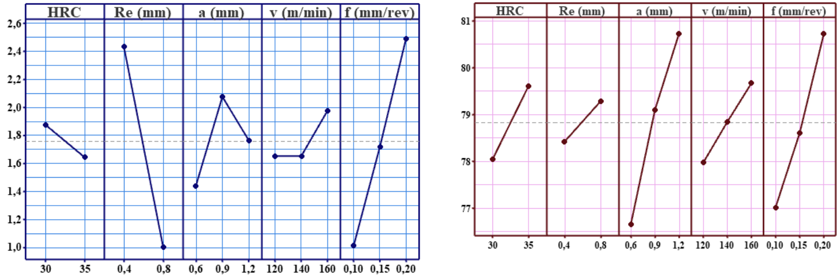

e)Ra (µm) f) Sound (dB)

Regression equations

Mathematical models are fundamental in both scientific studies and practical applications[15][22]. Knowing the vibration, energy/power consumption, ***Ra***, and sound intensity that will occur in various cutting situations is significant. It is helpful to estimate the more difficultly measured ***Ra*** and vibration values with the more easily measured sound intensity and ***PC***.

Many mathematical models have been created for the ***Ra***. A mathematical model based only on feed and ***Re*** was created. In the first-order model, $R^2= 0.8455$. According to the quadratic equation, it was calculated as $R^2=0.9924$.

$$Ra = 1.756 + -0.7473\ Re + 0.6281\ f\ (R^2= 0.8455\ \ R^2(adj)= 0.8361)$$

$$Ra = -1.84 + 3.246\ Re + 33.18\ f + -45.8\ Re\ f + 31.09\ f^2\ \ (R^2= 0{,}9924\ \ R^2(adj)=0{,}9914\ )$$

Figure 3. Effect of cutting conditions on machinability parameters

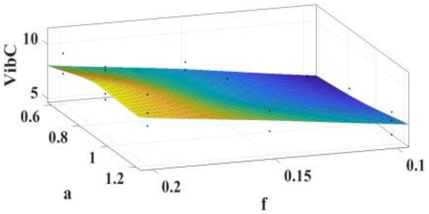

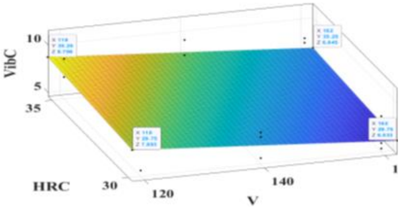

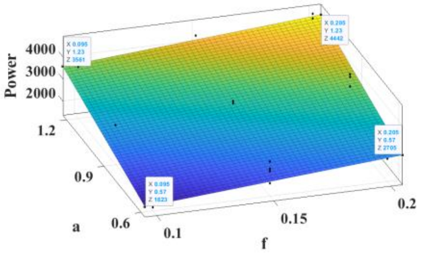

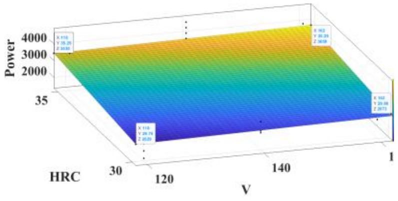

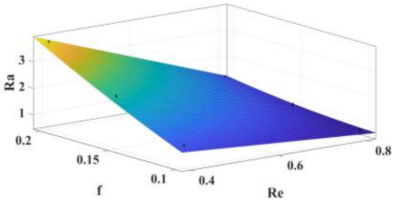

Regression models are given. It shows vibration on the chuck in equation 1 and vibration on the tool in equation 2.

$$VibM=-0{,}728+0{,}03863\,H-1{,}069\,Re+0{,}256\,a-0{,}00320\,v+2{,}574\,f+0{,}00924\,Re*v+2{,}478\,a*f \quad (1)$$

$$R^2=98{,}50\ \%\ ,R^2(pred)=97{,}41\ \%$$

$$VibC=17{,}46+0{,}1624\,H+2{,}361\,a-0{,}3187\,v+69{,}93\,f+0{,}001123\,v*v-0{,}2724\,v*f \quad (2)$$

$$R^2=99{,}07\ \%\ ,R^2(pred)=98{,}55\ \%$$

Equations related to ***f***, ***ap***, ***v***, material hardness and cutter radius and the Power and ***EC*** model are given in equations 3 and 4.

$$Power=-3637+69{,}4\,H-3860\,Re+2632{,}3\,a+4{,}452\,v+8233\,f+133{,}5\,H*Re \quad (3)$$

$R^2=99{,}00\ \%,\ R^2(pred)=98{,}43\ \%$

$$EC = -15{,}9 + 3{,}625\,H + 5{,}16\,Re - 8{,}068\,a - 0{,}1508\,v - 13{,}4\,f + 937\,f*f - 12{,}80\,H*f \qquad (4)$$

$R^2=98{,}25\ \%,\ R^2(pred)=97{,}11\ \%$

The ***Ra*** is shown in equation 5 depending on the material hardness, tool insert radius, ***ap*** and ***f***.

$$Ra = -0{,}926 - 0{,}02804\,H + 3{,}124\,Re + 0{,}1636\,a + 31{,}59\,f + 34{,}30\,f*f - 44{,}864\,Re*f \qquad (5)$$

$R^2=99{,}86\ \%,\ R^2(pred)=99{,}79\ \%$

Sound intensity is shown in equation 6 depending on material hardness, tool insert radius, ***ap***, ***v*** and ***f***.

$$Sound=49{,}92 + 0{,}3231\,H + 1{,}892\,Re + 6{,}785\,a + 0{,}04015\,v + 36{,}76\,f \qquad (6)$$

$R^2=97{,}48\ \%,\ R^2(pred)=96{,}44\ \%$

There is a strong correlation between ***PC*** and vibration[15]. An increase in ***PC*** indicates an increased cutting load of the machine tool. Therefore, the higher the ***PC***, the higher the vibration.

Power equation depending on ***f***, ***ap*** and material hardness value is given in equation 7; lathe chuck vibration value is given in equation 8. In this equation, the R^2 value is 96.28% and 92.79%.

$$Power=-5370 + 8339\,f + 2632\,a + 150{,}2\,H\ (R^2=96{,}28\ \%) \qquad (7)$$

$$VibM=-1{,}400 + 4{,}731\,f + 0{,}5972\,a + 0{,}04041\,H\ (R^2=92{,}79\%)$$

There is an excellent correlation between sound intensity and ***PC*** (r=0.94). In addition, sound intensity can be estimated from ***PC*** with an accuracy rate of R^2= 88.63%. There is a perfect correlation between sound intensity and lathe chuck vibration value (r=0.96). In addition, sound intensity can be estimated from ***PC*** with an accuracy rate of R^2= 92.91%.

$$Sound=69{,}82+0{,}002866\ x\ Power\ (R^2=88{,}63,\ r=0{,}94)$$

(9)

$$Sound=68{,}21+9{,}104\ x\ VibM\ (R^2=92{,}91,\ r=0{,}96)$$

(10)

$$Sound=68{,}332+0{,}001200\ power+5{,}768\ VibM\ (R^2=95.97)$$

(11)

$$VibM=0{,}2585+0{,}000289\ x\ Power\ (R^2=80.34,\ r=0{,}90)$$

(12)

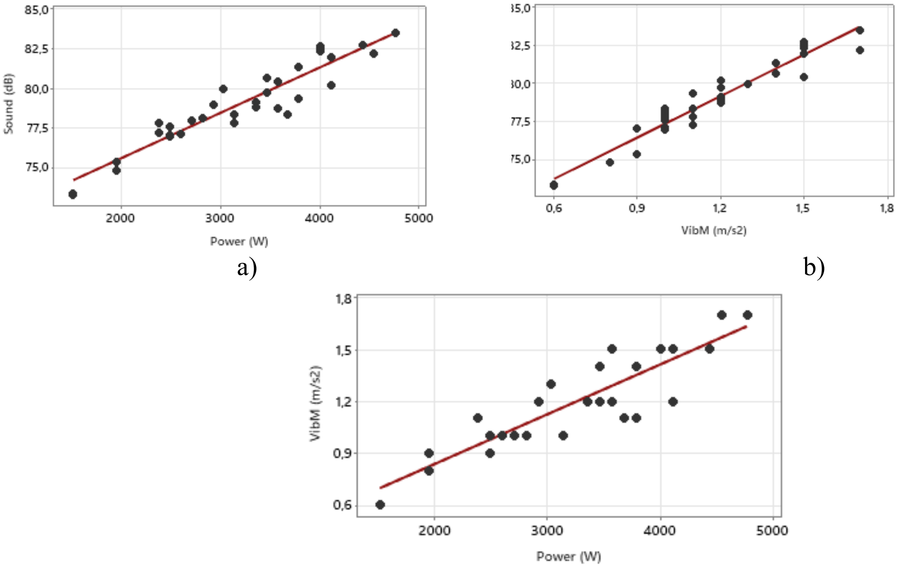

a)

b)

c)

Figure 4. Relationship of machining time, power consumption, vibration and surface roughness

Machining time is significant in terms of machinability[15]. Tool wear increases with increasing machining time. Tool wear affects vibration [30], cutting forces, ***EC*** and ***Ra*** [41].

In this experimental study, 30 HRC 17 4 PHSS was machined with a tool with a 0.8 mm toll ***Re***, 0.9 mm ***ap***, 0.1 mm/rev ***f*** and 160 m/min ***v***. 600 mm^3 of material was removed for each experiment. Vibration, ***PC***, sound intensity and ***Ra*** increased as the machining time increased. In other studies, as the amount of wear increases, ***EC*** increases [8][18], cutting force, friction energy, energy required for cutting [9][17], ***PC*** [13][34], ***Ra*** [25][41], friction surface area [37] and vibration [42] increase. *P= K0 x MRR x (1+Vb), Ko coefficient, MRR material removal amount, Vb tool wear represents.* Similar results were found in machining AISI H11 [15] steels.

mm^3	**HRC**	**Re**	**a**	**V**	**f**	**VibM (m/s2)**	**VibC (m/s2)**	**Power C. (W)**	**Sound L. (dB)**	**Ra (µm)**
200	30	0.8	0.9	160	0.1	1	4.9	2490.9	77,6	0.77
400	30	0.8	0.9	160	0.1	1,2	5,3	2523.5	78,1	0,85
600	30	0.8	0.9	160	0.1	1,5	5,9	2562.3	78,9	0,91

Table 3. Relationship machining time and vibration, power consumption, Sound level, Energy consumption and surface roughness

Weighted Multiple Optimization

The optimisation is of great importance in machining. Determining the ideal cutting conditions is very important in terms of machinability[15]. Choosing the perfect cutting conditions reduces ***EC*** [41], vibration, and ***Ra***[22].

There are five input parameters (material hardness, ***Re***, ***v***, ***f***, ***ap***) and six output parameters (chuck vibration, tool vibration, ***PC***, ***EC***, sound intensity and ***Ra***). The weighted optimisation method was used to determine the ideal cutting conditions for the perfect output parameters. Weighted optimization results are shown in Table 4.

Table 4. weighted multiple optimisation results

	VibM (m/s^2)	N*0,05	VibC (m/s^2)	N*0,15	Sound (dB)	N*0,05	Power (W)	N*0,05	EC (j/mm^3)	N*0,1	Ra (µm)	N*0,6	**TWOV**
1	0,6	0,018	5,2	0,070	73,2	0,044	1516,2	0,034	41,06	0,078	1,33	0,21	**0,436**

2	1	0,029	6,8	0,091	77,9	0,047	2707,5	0,022	27,93	0,053	2,48	0,39	**0,605**
3	1,5	0,044	8,3	0,111	82,5	0,049	4007,1	0,008	20,35	0,039	3,79	0,60	**0,807**
4	0,6	0,018	5,2	0,070	73,3	0,044	1516,2	0,034	41,06	0,078	1,33	0,21	**0,436**
5	1	0,029	6,8	0,091	77,9	0,047	2707,5	0,022	27,93	0,053	2,48	0,39	**0,605**
6	1,5	0,044	8,3	0,111	82,6	0,049	4007,1	0,008	20,35	0,039	3,79	0,60	**0,807**
7	0,8	0,024	7,5	0,100	74,8	0,045	1949,4	0,030	35,20	0,067	2,42	0,38	**0,625**
8	1,3	0,038	7,9	0,106	79,9	0,048	3032,4	0,018	23,47	0,045	3,76	0,60	**0,812**
9	1	0,029	5,5	0,074	78,3	0,047	3140,7	0,017	31,90	0,061	1,35	0,21	**0,412**
10	1,1	0,032	9,3	0,125	77,2	0,046	2382,6	0,025	32,26	0,061	1,35	0,21	**0,471**
11	0,9	0,026	5,2	0,070	77,0	0,046	2490,9	0,024	38,55	0,073	0,81	0,13	**0,341**
12	1,4	0,041	6,8	0,091	81,3	0,049	3790,5	0,010	25,66	0,049	0,96	0,15	**0,351**
13	1,1	0,032	7,4	0,099	77,8	0,047	2382,6	0,025	27,66	0,052	1,31	0,21	**0,431**
14	**1**	**0,029**	**4,9**	**0,066**	**77,6**	**0,046**	**2490,9**	**0,024**	**33,73**	**0,064**	**0,77**	**0,12**	**0,322**
15	1,2	0,035	8,7	0,117	78,8	0,047	3357,3	0,015	30,31	0,058	1,05	0,17	**0,402**
16	1,1	0,032	7,4	0,099	77,8	0,047	2382,6	0,025	27,66	0,052	1,31	0,21	**0,431**
17	1	0,029	6,1	0,082	78,1	0,047	2815,8	0,020	25,42	0,048	2,43	0,38	**0,582**
18	1,2	0,035	8,7	0,117	79,1	0,047	3357,3	0,015	30,31	0,058	1,05	0,17	**0,402**
19	0,9	0,026	5,1	0,068	75,3	0,045	1949,4	0,030	50,42	0,096	1,12	0,18	**0,416**
20	1,2	0,035	6,8	0,091	79,7	0,048	3465,6	0,014	31,29	0,059	2,23	0,35	**0,565**
21	1,7	0,050	11,2	0,150	82,2	0,049	4548,6	0,002	30,80	0,058	3,62	0,57	**0,833**
22	1	0,029	6,8	0,091	76,9	0,046	2490,9	0,024	38,55	0,073	2,25	0,36	**0,590**
23	1,5	0,044	8,4	0,113	82,3	0,049	4007,1	0,008	27,13	0,051	3,52	0,56	**0,779**
24	1,1	0,032	7,6	0,102	78,3	0,047	3682,2	0,011	49,86	0,095	1,24	0,20	**0,451**
25	1	0,029	6,2	0,083	77,1	0,046	2599,2	0,023	35,20	0,067	2,24	0,35	**0,573**
26	1,5	0,044	10,6	0,142	80,4	0,048	3573,9	0,013	32,26	0,061	3,65	0,58	**0,842**
27	1,1	0,032	6,8	0,091	79,3	0,047	3790,5	0,010	44,00	0,084	1,25	0,20	**0,430**
28	1,2	0,035	6,2	0,083	79,0	0,047	2924,1	0,019	39,60	0,075	0,81	0,13	**0,353**
29	1,5	0,044	10,9	0,146	81,9	0,049	4115,4	0,007	37,15	0,071	1,25	0,20	**0,470**
30	1,2	0,035	6,8	0,091	80,2	0,048	4115,4	0,007	47,77	0,091	0,71	0,11	**0,349**

31	1,4	0,041	7,9	0,106	80,6	0,048	3465,6	0,014	32,15	0,061	1,21	0,19	**0,420**
32	1	0,029	6,9	0,092	77,8	0,047	3140,7	0,017	52,69	0,100	0,62	0,10	**0,354**
33	1,5	0,044	7,9	0,106	82,7	0,050	4440,3	0,003	34,36	0,065	1,02	0,16	**0,385**
34	1	0,029	4,9	0,066	77,0	0,046	2490,9	0,024	50,60	0,096	0,61	0,10	**0,328**
35	1,2	0,035	8,8	0,118	78,7	0,047	3573,9	0,013	43,02	0,082	0,91	0,14	**0,403**
36	1,7	0,050	9,5	0,127	83,5	0,050	4765,2	0,000	27,66	0,052	1,33	0,21	**0,440**
	1,7		**11,2**		**83,5**		**4765,2**		**52,69**		**3,79**		
	1,2		**7,37**		**78,8**		**3143,7**		**34,59**		**1,76**		
	14,28		**33,50**		**1,61**		**20,76**		**2,48**		**56,25**		

According to the weighted optimisation method, the impact rate of mirror vibration is 5%, the impact rate of vibration in the tool is 15%, the impact rate of sound intensity is 5%, and the impact rate of the power generated in the machine tool is 5%, the impact rate of ***EC*** is 10%, and the impact rate of ***Ra*** is calculated as 60%. While determining the impact ratios, good surface quality is required as hard turning is a finish turning process. Therefore, the highest effect ratio was given to the ***Ra***.

14>34>11>30>12>28>32>33>15>18>35>9>19>31>27>13>16>1>4>36>24>29>10>20>25>17>22>2>5>7>23>3>6>8>21>26

The weighted optimisation method indicates the test sequence from the ideal cutting condition to the most non-ideal cutting condition.

Conclusion

The results obtained in machining 17-4 PH materials with two different hardness values can be briefly summarised as follows. The most influential parameter on the late chuck vibration value is the ***f***, which is 49.14%. The ***ap*** follows the ***f*** of 31.04%. With increasing ***Re*** and material hardness value, the vibration value on the chuck increases. As the ***v*** increases, the number of revolutions increases and the chuck vibration value increases. According to the cutting conditions, the chuck vibration value was estimated with an accuracy of 97.41%. In addition, the chuck vibration value could be evaluated with an accuracy of 92.79% based on only the ***f***, ***ap*** and hardness value.

The most significant parameter of the tool vibration is the ***f***. The effective rate of the ***f*** is 59.42%. The ***v*** with 19.99% follows the feed of as the number of revolutions increases with increasing ***v***, the chuck vibration increases while the tool vibration decreases. As with chuck vibration, tool vibration increases with increasing tool radius and workpiece hardness value. Tool vibration value estimated with 98.55% accuracy.

The most influential parameter on ***PC*** is the ***ap*** with 60.74%. The material hardness value follows the ***ap*** with 20.26%. ***PC*** increases with increasing ***ap***, material hardness value, ***f***, and ***Re***. Depending on the cutting conditions, the ***PC*** was created with an accuracy of 98.43%. In addition, the ***PC*** was determined with an accuracy of 96.28%, depending on the material hardness value, ***f*** and ***ap***.

EC depends on the processing time; with increasing cutting parameters, the processing time is shortened, and the ***EC*** is reduced. The ***f*** is the most influential ***EC*** parameter, with 47.88%. The material hardness value follows this with 24.76%. As material hardness value and tool tip radius increase, ***EC*** increases. Depending on the cutting conditions, ***EC*** can be estimated with an accuracy of 97.11%.

The most important parameters on the ***Ra*** are ***Re*** with 49.83% and ***f*** with 34.36% effect. While the ***Ra*** decreases with increasing ***Re***. The ***Ra*** increases with the increasing ***f***. A regression model was created with an accuracy of 99.14% according to the ***f*** and ***Re***.

The most influential parameters on sound intensity are ***ap*** (43.54%) and ***f*** (33.83%). The sound intensity increases as the ***ap*** and ***f*** increases. Sound intensity could be estimated with an accuracy of 96.44%.

A positive correlation of 0.94 was calculated between the sound intensity and the amount of power. The sound intensity increases with increasing ***PC***. A regression equation was created that predicts sound intensity with an accuracy of 88.63% according to ***PC***. There is a perfect correlation of 0.96 between sound intensity and lathe chuck vibration value. The sound intensity increases with increasing chuck vibration value. With the regression model created according to the chuck vibration value, the sound intensity could be estimated with 92.91% accuracy.

There is an excellent correlation of 0.90 between ***PC*** and chuck vibration. The chuck vibration value increased with increasing ***PC***. According to the mathematical equation results created according to the power value, the chuck vibration was predicted with an accuracy of 80.34%.

It has been determined as the ideal cutting condition, hardness of 30 HRC, ***v*** of 160 m/min, ***f*** of 0.1 mm/rev, ***ap*** of 0.9 mm and ***Re*** of 0.8 mm. According to these processing conditions, the machine performance increased by 20.76%; chuck vibration decreased by 14.28%, tool vibration by 33.50%, ***EC*** by 2.48%, ***Ra*** by 56.25%, and sound intensity by 1.61% decreased.

References

1. Journal AI, Lai Z, Wang C, et al (2020) Effect of cryogenic oils-on-water compared with cryogenic minimum quantity lubrication in finishing turning of 17-4PH stainless steel. Mach Sci Technol 24:1016–1036. https://doi.org/10.1080/10910344.2020.1815049
2. (1993) A. Leyland, D.B. Lewis, P.R. Stevenson, Low temperature plasma diffusion treatment of stainless steels for improved wear resistance, Surf Coat Technol 1993;62:608 – 617. 1993
3. Aydemir B (2006) Influence of heat treatment on hysteresis error of force transducers manufactured from 17-4PH stainless steel. 39:892–900. https://doi.org/10.1016/j.measurement.2006.03.014
4. Sivaiah P, Chakradhar D (2018) Moghadasi, A.; Hadad, M. (2019) Towards sustainable machining of 17-4 PH stainless steel using hybrid MQL-hot turning process. Energy Equipment and Systems, 7(4): 339–352. CIRP J Manuf Sci Technol 21:86–96
5. Ambhore N, Kamble D, Chinchanikar S (2020) Evaluation of Cutting Tool Vibration and Surface Roughness in Hard Turning of AISI 52100 Steel: An Experimental and ANN Approach. J Vib Eng Technol 8:455–462. https://doi.org/10.1007/s42417-019-00136-x
6. Shah D, Bhavsar S (2019) Effect of Tool Nose Radius and Machining Parameters on Cutting Force, Cutting Temperature and Surface Roughness-An Experimental Study of Ti-6Al-4V (ELI). Mater Today Proc 22:1977–1986. https://doi.org/10.1016/j.matpr.2020.03.163
7. Rafighi M, Özdemir M, Al Shehabi S, Kaya MT (2021) Sustainable Hard Turning of High Chromium AISI D2 Tool Steel Using CBN and Ceramic Inserts. Trans Indian Inst Met 74:1639–1653. https://doi.org/10.1007/s12666-021-02245-2

8. Chou YK, Song H (2004) Tool nose radius effects on finish hard turning. J Mater Process Technol 148:259–268. https://doi.org/10.1016/j.jmatprotec.2003.10.029

9. Grzesik W, Denkena B, Żak K, et al (2016) Energy consumption characterization in precision hard machining using CBN cutting tools. Int J Adv Manuf Technol 85:2839–2845. https://doi.org/10.1007/s00170-015-8091-1

10. Al-Shayea A, Abdullah FM, Noman MA, et al (2020) Studying and Optimizing the Effect of Process Parameters on Machining Vibration in Turning Process of AISI 1040 Steel. Adv Mater Sci Eng 2020:. https://doi.org/10.1155/2020/5480614

11. Shekarchian M, Moghavvemi M, Mahlia TMI, Mazandarani A (2011) A review on the pattern of electricity generation and emission in Malaysia from 1976 to 2008. Renew Sustain Energy Rev 15:2629–2642. https://doi.org/10.1016/j.rser.2011.03.024

12. For R (2009) a Nalysis of E Nergy U Se for O Ntario H Ospitals. 49–81

13. Zhao G, Zhao Y, Meng F, et al (2020) Prediction model of machine tool energy consumption in hard-to-process materials turning. Int J Adv Manuf Technol 106:4499–4508. https://doi.org/10.1007/s00170-020-04939-1

14. Duflou JR, Sutherland JW, Dornfeld D, et al (2012) Towards energy and resource efficient manufacturing: A processes and systems approach. CIRP Ann - Manuf Technol 61:587–609. https://doi.org/10.1016/j.cirp.2012.05.002

15. Şahinoğlu A (2022) Investigation of machinability properties of AISI H11 tool steel for sustainable manufacturing. Proc Inst Mech Eng Part E J Process Mech Eng 236:2717–2728. https://doi.org/10.1177/09544089221122004

16. Gupta MK, Sood PK, Singh G, Sharma VS (2017) Sustainable machining of aerospace material – Ti (grade-2) alloy:

Modeling and optimization. J Clean Prod 147:614–627. https://doi.org/10.1016/j.jclepro.2017.01.133

17. Khanna N, Shah P, Sarikaya M, Pusavec F (2022) Energy consumption and ecological analysis of sustainable and conventional cutting fluid strategies in machining 15–5 PHSS. Sustain Mater Technol 32:e00416. https://doi.org/10.1016/j.susmat.2022.e00416

18. Liu ZY, Guo YB, Sealy MP, Liu ZQ (2016) Energy consumption and process sustainability of hard milling with tool wear progression. J Mater Process Technol 229:305–312. https://doi.org/10.1016/j.jmatprotec.2015.09.032

19. Lu F, Zhou G, Liu Y, Zhang C (2022) Ensemble transfer learning for cutting energy consumption prediction of aviation parts towards green manufacturing. J Clean Prod 331:129920. https://doi.org/10.1016/j.jclepro.2021.129920

20. Kam M, Demirtaş M (2021) Analysis of tool vibration and surface roughness during turning process of tempered steel samples using Taguchi method. Proc Inst Mech Eng Part E J Process Mech Eng 235:1429–1438. https://doi.org/10.1177/09544089211001976

21. Maroju NK, Krishna PV, Jin X (2017) Assessment of high and low frequency vibration assisted turning with material hardness. Int J Mach Mach Mater 19:110–135. https://doi.org/10.1504/IJMMM.2017.082903

22. Salur E (2023) A Comprehensive Analysis of Surface Roughness , Vibration ,

23. Karaaslan F, Şahinoğlu A (2020) Determination of Ideal Cutting Conditions for Maximum Surface Quality and Minimum Power Consumption During Hard Turning of AISI 4140 Steel Using TOPSIS Method Based on Fuzzy Distance. Arab J Sci Eng 45:9145–9157. https://doi.org/10.1007/s13369-020-04635-y

24. Deshpande Y V., Andhare AB, Padole PM (2019) Application

of ANN to estimate surface roughness using cutting parameters, force, sound and vibration in turning of Inconel 718. SN Appl Sci 1:1–9. https://doi.org/10.1007/s42452-018-0098-4

25. Bhaskaran J, Murugan M, Balashanmugam N, Chellamalai M (2012) Monitoring of hard turning using acoustic emission signal. J Mech Sci Technol 26:609–615. https://doi.org/10.1007/s12206-011-1036-1

26. Panday G, Ashraf MZI, Ibn Muneer K, et al (2018) Assessing near-dry lubrication (35 ml/h) performance in hard turning process of hardened (48 HRC) AISI 1060 carbon steel. Int J Adv Manuf Technol 99:2045–2057. https://doi.org/10.1007/s00170-018-2629-y

27. Singh G, Kumar A, Aggarwal V, Singh S (2021) Experimental investigations and optimization of machining performance during turning of EN-31 steel using TOPSIS approach. Mater Today Proc 48:1089–1094. https://doi.org/10.1016/j.matpr.2021.07.381

28. Şahinoglu A, Rafighi M (2021) Machinability of hardened AISI S1 cold work tool steel using cubic boron nitride. Sci Iran 28:2655–2670. https://doi.org/10.24200/sci.2021.55772.4398

29. Ambhore N, Kamble D, Agrawal D (2022) Experimental Investigation of Induced Tool Vibration in Turning of Hardened AISI52100 Steel. J Vib Eng Technol. https://doi.org/10.1007/s42417-022-00473-4

30. Rao KV, Murthy BSN, Mohan Rao N (2015) Experimental study on surface roughness and vibration of workpiece in boring of AISI 1040 steels. Proc Inst Mech Eng Part B J Eng Manuf 229:703–712. https://doi.org/10.1177/0954405414531247

31. Kam M, Şeremet M (2021) Experimental investigation of the effect of machinability on surface quality and vibration in

hard turning of hardened AISI 4140 steels using ceramic cutting tools. Proc Inst Mech Eng Part E J Process Mech Eng 09544089211007366. https://doi.org/10.1177/09544089211007366

32. Mallick R, Kumar R, Panda A, Sahoo AK (2023) Hard Turning Performance Investigation of AISI D2 Steel under a Dual Nozzle MQL Environment. Lubricants 11:. https://doi.org/10.3390/lubricants11010016

33. Şahinoğlu A, Rafighi M, Kumar R (2022) An investigation on cutting sound effect on power consumption and surface roughness in CBN tool-assisted hard turning. Proc Inst Mech Eng Part E J Process Mech Eng 236:1096–1108. https://doi.org/10.1177/09544089211058021

34. Khanna N, Agrawal C, Dogra M, Pruncu CI (2020) Evaluation of tool wear, energy consumption, and surface roughness during turning of inconel 718 using sustainable machining technique. J Mater Res Technol 9:5794–5804. https://doi.org/10.1016/j.jmrt.2020.03.104

35. Sahinoğlu A, Ulas E (2020) An investigation of cutting parameters effect on sound level, surface roughness, and power consumption during machining of hardened AISI 4140. Mech Ind 21:. https://doi.org/10.1051/meca/2020068

36. Ahmad A, Akram S, Jaffery SHI, Khan MA (2023) Evaluation of specific cutting energy, tool wear, and surface roughness in dry turning of titanium grade 3 alloy. Int J Adv Manuf Technol 127:1263–1274. https://doi.org/10.1007/s00170-023-11580-1

37. Ning H, Zheng H, Wang G (2022) Establishment of Analytical Model for CFRP Cutting Force Considering the Radius of the Edge Circle

38. Kumar S, Tamilselvan P, Feroskhan M, et al (2023) Hard turning of AISI D2 steel with cubic boron nitride cutting inserts. Mater Today Proc 72:2002–2006. https://doi.org/10.1016/j.matpr.2022.07.338

39. Şahinoğlu A, Güllü A (2019) Investigation of the Relationship Between Current, Sound Intensity, Vibration and Surface Roughness in Machining of CuZn39Pb3 Material on Lathe Machine. J Polytech 0900:615–624. https://doi.org/10.2339/politeknik.426106

40. Olaru SC, Slătineanu L, Silitră M, et al (2017) Investigation of the sound intensity level in the case of a universal lathe. MATEC Web Conf 112:. https://doi.org/10.1051/matecconf/201711201025

41. Airao J, Nirala CK, Bertolini R, et al (2022) Sustainable cooling strategies to reduce tool wear, power consumption and surface roughness during ultrasonic assisted turning of Ti-6Al-4V. Tribol Int 169:107494. https://doi.org/10.1016/j.triboint.2022.107494

42. Li S, Li S, Hu Y, Popov E (2022) Experimental study on coupling characteristics of cutting temperature rise and cutting vibration under different tool wear states. Int J Adv Manuf Technol 118:907–919. https://doi.org/10.1007/s00170-021-07948-w

CHAPTER 4

EFFECTS OF MECHANICAL ASSEMBLY AND STRUCTURAL PARAMETERS ON THE PERFORMANCE OF PEM ELECTROLYZERS

1. **MUHAMMED ASIM KESERCİOĞLU** [1]
2. **KUBİLAY HAN** [2]

Introduction

In the 21st century, energy systems are being reshaped in line with the objectives of reducing dependence on fossil fuels and achieving carbon-free energy production. In this context, hydrogen has emerged as a key energy carrier for attaining “net-zero emissions targets”. Water electrolysis technologies play a vital role in balancing the inherently intermittent generation profiles of renewable energy sources (such as solar and wind) and in storing energy within chemical bonds (Sayed-Ahmed et al., 2024; Srour et al., 2023). Among these technologies, proton exchange membrane water electrolyzers (PEMWEs) stand out due to their ability to operate at

---

[1] Dr., Sakarya University of Applied Sciences, Department of Mechanical Engineering, Orcid: 0009-0003-3751-4224

[2] Dr., Sakarya University of Applied Sciences, Department of Mechanical Engineering, Orcid: 0000-0003-1472-2832

high current densities (2–6 A cm^{-2}) and their fast dynamic response characteristics. In addition, advantages such as a compact system design and the production of high-purity hydrogen (99.99%) make PEMWEs a particularly promising option for integration with variable renewable energy sources (Medina & Santarelli, 2010; Shiva Kumar & Himabindu, 2019).

Figure 1. Schematic representation of a PEM electrolyzer cell

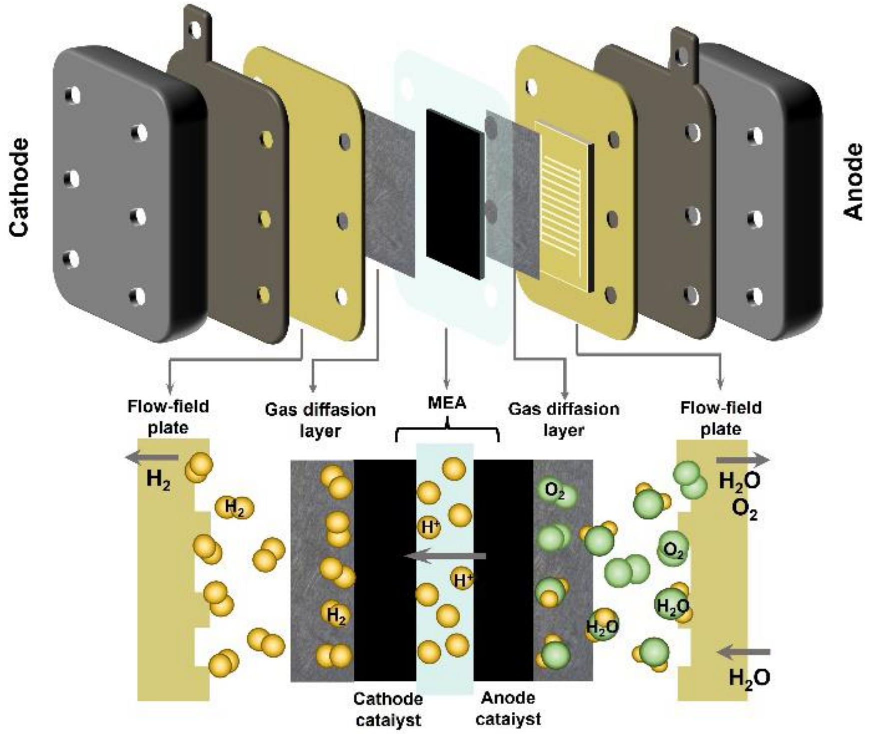

Source: (K. Zhang et al., 2022)

The large-scale commercialization of PEMWE technology and its transition toward terawatt-scale hydrogen production have not yet reached their full potential due to high capital costs and durability challenges during long-term operation. Although the majority of studies in the literature focus on reducing costs and improving efficiency by lowering the loading of electrochemical catalysts (iridium, platinum) or by advancing membrane chemistry, the mechanical design and assembly parameters of the electrolyzer stack have a decisive impact on overall system performance (X. Wang et al., 2023). In particular, the compressive pressure applied during stack assembly and the resulting contact conditions directly govern ohmic losses and mass transport resistances.

The compressive pressure applied during the assembly of a PEMWE stack is a critical parameter for minimizing the electrical contact resistance between components, ensuring gas and water sealing, and guaranteeing the formation of an optimal interface between the porous transport layers (PTLs) and the membrane electrode assembly (MEA) (Staudacher et al., 2025). Mechanical assembly is not merely a matter of static structural integrity; it is also a dynamic process that influences electrochemical reaction kinetics, mass transport, and thermal management within the cell. Insufficient compressive pressure leads to high interfacial contact resistances and, consequently, increased ohmic losses, whereas excessive compressive pressure results in the crushing of porous structures, hindering mass transport, mechanically damaging the membrane, and deforming the flow fields (Borgardt et al., 2019; Kesercioğlu et al., 2025).

This book chapter aims to examine the role of mechanical assembly and structural parameters in PEMWEs on cell performance in light of recent academic studies and experimental evidence reported in the literature. The chapter addresses the effects of compressive pressure on contact resistance and mass transport, the influence of bolt tightening torque and tightening sequences on pressure uniformity, end plate design and topology optimization, the impact of bipolar plate (BPP) flow-field designs on mechanical stress, the structural characteristics of porous transport layers, and membrane mechanical degradation mechanisms.

Effects of Compressive Pressure on Electrochemical Performance

One of the key factors determining the performance of PEMWE stacks is the degree of contact tightness between the cell components. The compressive pressure applied during assembly requires a delicate balance: while it reduces ohmic resistances that contribute to the overall cell impedance, it must simultaneously allow mass transport to proceed without restriction by avoiding limitations on the transport of reactants and products.

a. Contact Resistance and Ohmic Losses

In a PEMWE cell, a significant portion of the voltage losses originates from contact resistances formed at the interfaces between components. In particular, the interfaces between the bipolar plate and the PTL, as well as between the PTL and the catalyst-coated membrane (CCM), constitute critical regions where electron transfer occurs. At the microscopic scale, machined metal surfaces are inherently rough, and when two surfaces are brought into contact, the real contact area represents only a very small fraction of the nominal surface area. Electron flow is therefore constrained to pass through these limited asperity contact points; as a result, the effective conduction cross-section is reduced, and the local increase in current density leads to an increase in contact resistance (Srour et al., 2024).

Increasing the compressive pressure causes these surface asperities to undergo elastic or plastic deformation, thereby enlarging the real contact area. Studies reported in the literature demonstrate that contact resistance decreases sharply with increasing compressive pressure, often following a nonlinear trend that approaches saturation at higher pressures. For instance, in a comprehensive study conducted by Borgardt et al., it was reported that increasing the compressive pressure from 0.5 MPa to 2.0 MPa resulted in a pronounced reduction in ohmic resistance; however, when the pressure reached levels of 2.5–3.0 MPa, the decrease in resistance approached saturation (Borgardt et al., 2019). This saturation point represents the condition in which surface roughness features have effectively reached the maximum attainable contact area, and further increases in pressure no longer yield a meaningful improvement in electrical conductivity.

In experiments conducted by Selamet and co-workers on bolt tightening torque, it was observed that, for the specific cell design under investigation, increasing the torque from 3 N·m to 15 N·m led to an improvement in cell efficiency, whereas at excessive torque levels such as 20 N·m, the performance either remained unchanged or deteriorated (O. F. Selamet & Ergoktas, 2015). This behavior indicates that, beyond contact resistance, additional loss mechanisms become involved in the process. It should also be noted that the compressive pressure generated by these torque values depends on the specific characteristics of the cell, including its active area and the number of bolts.

In an experimental study conducted by Selamet and co-workers on high-pressure PEMWEs (Ö. F. Selamet et al., 2013), it was demonstrated that both cell and stack performance are highly sensitive to contact conditions. The study reported that, in particular, the thickness uniformity of titanium current collectors and the applied compressive force play a decisive role in intercell voltage distribution and ohmic losses. Under non-uniform contact conditions, a reduced effective utilization of the active area and a divergence of cell voltages at high current densities were observed; in contrast, when appropriate compression and homogeneous contact were ensured, the cell voltages converged and a more stable overall stack performance was achieved. These findings indicate that compressive pressure is a critical parameter not only for maintaining mechanical integrity, but also for reducing contact resistance and homogenizing current distribution across the stack.

Figure 2. Effect of tightening torque on cell performance

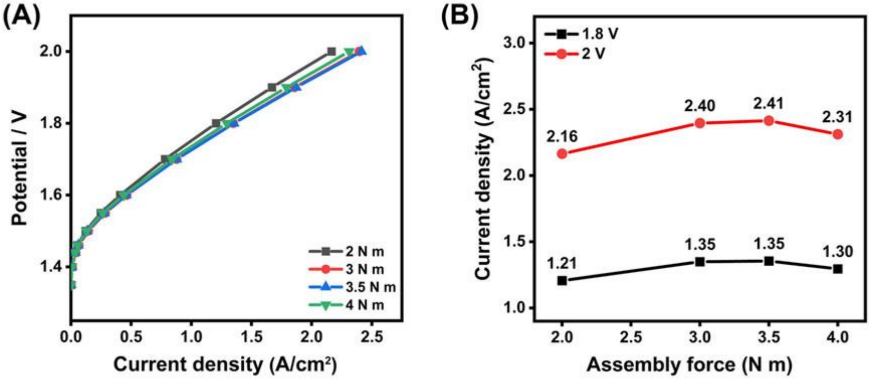

Source: (Hou et al., 2025)

In the study by Hou et al. illustrated in Figure 2 (Hou et al., 2025), the effect of the tightening torque applied during cell assembly on the performance of a PEMWE is demonstrated. As the tightening torque is increased from 2 N·m to the range of 3–3.5 N·m, a pronounced increase in the current density obtained at both 1.8 V and 2.0 V is observed. This improvement is attributed to a reduction in contact resistance between cell components and enhanced electrical contact. However, for the tested cell, a subsequent decline in performance at a torque level of 4 N·m indicates that excessive tightening may lead to PTL deformation, local contact degradation, and blockage of gas pathways.

b. Mass Transport and Structural Deformation

The advantage of compressive pressure in reducing contact resistance is counterbalanced, beyond a certain point, by an increase in mass transport resistance due to enhanced mechanical constraints imposed on porous structures. In PEMWEs, porous transport layers play a critical role in ensuring the homogeneous supply of water to the anode and the effective removal of oxygen gas generated by electrochemical reactions (Y. Liu et al., 2025). Under excessive compressive pressure, the porosity of PTL materials decreases, and the pore structure is partially constricted or altered due to deformation. This condition hinders the simultaneous transport of liquid water and gas phases, leading to the emergence of mass transport limitations at high current densities (Martin et al., 2022; Tolouei et al., 2026).

Titanium-based PTLs used on the anode side largely maintain their structural integrity due to their high mechanical rigidity; however, at elevated pressure levels, they may exhibit a tendency toward “intrusion” into the membrane. Such intrusion can lead to localized thinning of the membrane and a reduction in the effective active area. In addition, under high compressive pressure, the narrowing of PTL pores can impede the transport of water to the catalyst surface, promoting the formation of localized drying regions and associated temperature increases (H. Zhang et al., 2025). These structural and transport-related constraints are regarded as one of the fundamental mechanisms explaining why electrolyzer cell performance exhibits saturation behavior beyond a certain compressive pressure.

Mechanical Assembly Components and Design Parameters

The mechanical design of a PEMWE stack is a critical engineering process that determines not only electrochemical performance but also the safety, sealing integrity, and service life of the system. In this process, end plates, fastening elements, gaskets, and tightening procedures play a decisive role.

a. End Plate Design and Topology Optimization

End plates are thick, rigid components located at both ends of the stack that receive the compressive force from the bolts and transmit it to the active cell area. Traditionally manufactured from stainless steel, aluminum, or titanium, these plates tend to undergo elastic deformation under high compressive loads. Since the bolts are typically positioned around the periphery of the plate, the application of tightening force causes the edges to be compressed while the central region deflects outward. This behavior leads to the so-called “doming” effect, resulting in lower pressure in the center of the stack and higher pressure near the edges. Consequently, contact conditions across the active area lose their uniformity (Dey et al., 2019).

This non-uniformity in pressure distribution can significantly affect cell performance. In low-pressure regions (typically the center of the cell), contact resistance increases and current density decreases. As a result, current tends to concentrate in high-pressure regions where resistance is lower. This leads to localized heating and accelerated membrane aging in those regions (Al Shakhshir, 2018). Moreover, plate bending can reduce the compressive load applied to the gasket, thereby increasing the risk of leakage.

To overcome these issues and reduce the weight of end plates, topology optimization and Finite Element Analysis (FEA) methods are widely employed. In their studies on circular and square end plates, Jo et al. (Jo et al., 2020) developed designs in which material was retained only along load-bearing paths, while non-essential volumes were removed. Compared to conventional plates, the optimized designs achieved weight reductions of approximately 20–30%, while minimizing deformation and improving pressure distribution. In particular, removing material between bolt holes and adding stiffening ribs were shown to enhance the bending resistance of the plates.

In addition, some innovative designs employ hydraulic or pneumatic bladders placed between the end plate and the stack to achieve a highly uniform uniform pressure distribution over the active area (X. Wang et al., 2008). These systems are also capable of compensating for thickness variations arising from manufacturing tolerances.

b. Tightening Torque and Tightening Sequences

During cell assembly, both the magnitude of the tightening torque applied to the bolts and the sequence of its application are of critical importance for achieving the desired clamping force and compressive pressure. An improper tightening procedure may lead to stack warping, gasket displacement, and permanent deformations. To ensure a homogeneous distribution of compressive pressure, the star pattern or cross-tightening method is widely accepted as a standard procedure (*Guidelines for Pressure Boundary Bolted Flange Joint Assembly*, 2019).

In the cross-tightening method, bolts are tightened in opposing pairs with respect to the geometric center of the stack (for example, bolts located at the 12–6 positions followed by those at the 3–9 positions). The tightening process is not performed in a single step to reach the final torque value; instead, it is carried out in a stepwise manner. Initially, all bolts are tightened by hand to establish initial contact, followed by the application of approximately 30% of the target torque to generate the initial preload. Subsequently, the torque level is gradually increased to about 60%, and finally to 100% of the target torque value. This incremental and symmetric tightening approach minimizes elastic interaction effects, in which tightening one bolt induces relaxation in others, while ensuring balanced seating of the gaskets and cell components and achieving a more uniform compressive pressure throughout the stack. Finally, all bolts are verified in a circular sequence (Hu et al., 2023). Figure 3 schematically illustrates the arrangement of the tightening bolts in a PEMWE test cell and the recommended cross-tightening (star-pattern) sequence.

The relationship between the applied torque and the resulting axial force is governed by friction coefficients. Due to uncertainties in these friction coefficients, relying solely on a torque wrench may introduce significant error margins. Therefore, in critical applications, more precise control can be achieved by measuring bolt elongation or by employing hydraulic tensioners instead of torque-applied nuts.

Figure 3. Arrangement of tightening bolts in the PEMWE test cell and the tightening sequence for cross-tightening

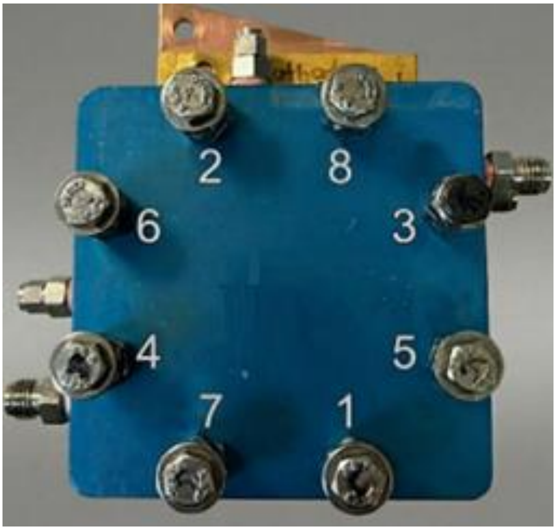

c. Gasket Selection and Sealing Strategy

Gaskets are used in PEMWEs to ensure the sealing of reactants, maintain isolation from the external environment, and prevent electrical short circuits. The selected gasket material and its design directly influence the distribution of assembly pressure across the stack.

The most commonly used gasket materials in PEMWEs are silicone, EPDM, and PTFE (Teflon), each offering distinct mechanical and chemical properties. PTFE provides advantages in aggressive electrochemical environments due to its high chemical resistance; however, its tendency toward cold flow may lead to thickness loss and a reduction in compressive force during long-term operation (O. F. Selamet & Ergoktas, 2015). EPDM and silicone gaskets exhibit better elastic recovery characteristics, but their resistance to acidic environments must be carefully evaluated.

Figure 4. Effect of gasket thickness on cell performance

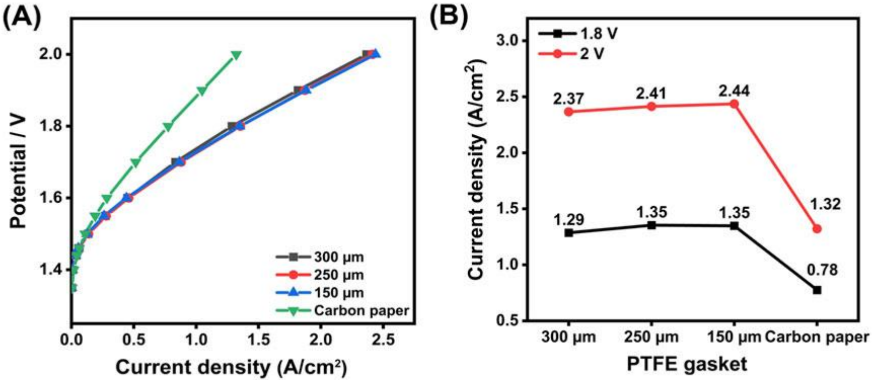

Source: (Hou et al., 2025)

In addition to gasket type, gasket thickness emerges as a critical design parameter in PEMWEs, not only in terms of sealing performance but also with respect to defining the contact conditions among the PTL–CCM–flow field interfaces. In the study shown in Figure 4 by Hou et al., different PTFE gasket thicknesses (150, 250, and 300 µm) were systematically compared; it was reported that excessively thin gaskets led to PTL deformation and sealing issues due to over-compression, whereas excessively thick gaskets limited cell performance as a result of insufficient interfacial contact (Hou et al., 2025). The most balanced electrochemical performance was achieved using a medium-thickness gasket (250 µm), which provided an appropriate compression ratio compatible with the employed PTL thickness. These findings clearly demonstrate that gasket thickness is a critical mechanical design parameter that must be considered in conjunction with the applied tightening torque.

In modern stack designs, hard stop mechanisms are employed to prevent excessive compression of the gasket and crushing of the PTL. In this approach, the gasket is seated within a dedicated groove or a fixed height offset is created on the bipolar plate. The compression process proceeds until metal-to-metal contact is established. As a result, the pressure applied to the PTL is precisely defined by the difference between the gasket groove depth and the PTL thickness, largely independent of the applied tightening torque (Y. Wei et al., 2024).

Structural Role of Bipolar Plate and Flow-Field Design

Bipolar plates (BPPs) are fundamental structural components in PEMWE stacks, fulfilling multiple functions such as electrical current conduction, distribution of reactant water, removal of generated gases, and provision of thermal management. The structural design and material properties of BPPs are key factors governing how mechanical stress is transmitted to the membrane. Figure 5 presents a top view, prior to assembly, of a serpentine flow-field bipolar plate together with a PTL positioned within the gasket frame.

Figure 5. Serpentine flow-field bipolar plate and the PTL positioned within the gasket frame

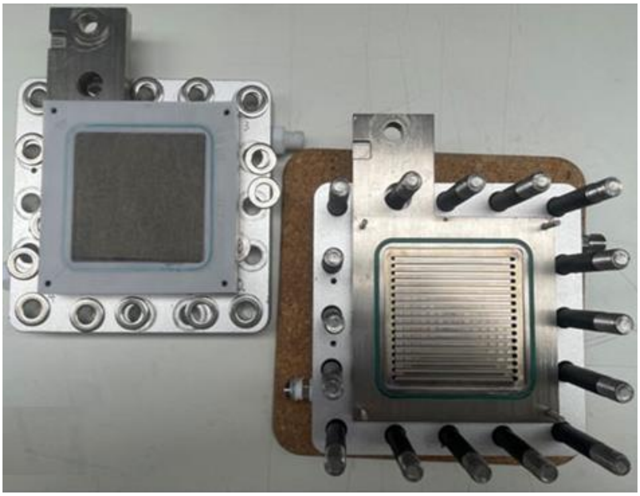

Source: (Hou et al., 2025)

a. Flow-Field Geometry and Mechanical Stress Distribution

Serpentine, parallel, and interdigitated flow-field designs commonly used in conventional PEM fuel cells are also employed in electrolyzers (C.-K. Wang, Huang, et al., 2025). However, the inherent *channel–land* structure of these designs gives rise to a heterogeneous stress distribution on the membrane.

Land regions apply compressive loading to the membrane through the PTL, thereby providing both electrical contact and mechanical support. In contrast, channel regions lack direct mechanical support. Under high compressive pressure and the anode–cathode pressure differential generated during operation, the membrane does not exhibit macroscopic flow into the channels; instead, it undergoes localized deformation toward the PTL pores beneath the land regions. When this heterogeneous deformation behavior is considered together with the mechanical rigidity of the PTL and the viscoelastic nature of the membrane, stress concentrations—particularly in the channel regions—and the development of shear stresses within the membrane may occur. Under long-term and cyclic operating conditions, such mechanical stresses increase the likelihood of structural degradation mechanisms, including fatigue-induced crack formation or localized thinning of the membrane (J. Liu, Liu, et al., 2024). Despite these challenges, high-pressure operation is preferred in many applications because it facilitates system integration and reduces the need for external gas compression.

As shown in Figure 6, with increasing cell compression, membrane deformation is predominantly concentrated beneath the land regions, whereas no pronounced macroscopic membrane flow or thickness increase is observed in the channel regions. This observation supports the conclusion that membrane deformation occurs not through macroscopic flow between land and channel regions, but rather through a localized intrusion mechanism into the PTL pores beneath the lands.

Figure 6. Comparison of membrane profiles beneath land and channel regions at different cell compression levels

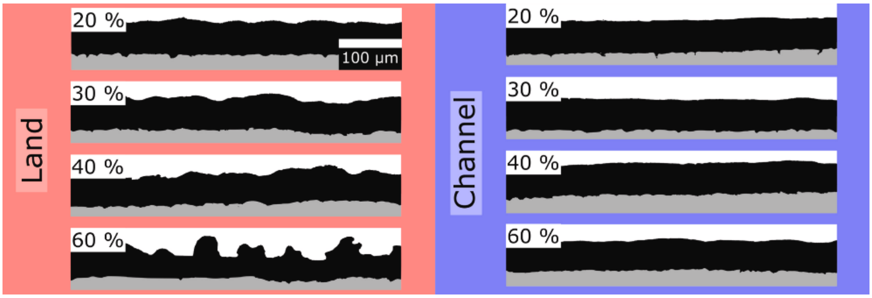

Source: (Cruz Ortiz et al., 2024)

Recent studies have shown that the use of titanium mesh (Ti-mesh) or porous flow-field structures instead of conventional channeled designs enables a much more homogeneous distribution of mechanical stress (Q. Wei et al., 2023). The study by Liu et al. (J. Liu, Liu, et al., 2024) demonstrated that a gradient porous titanium mesh structure distributes stress more uniformly over the MEA surface compared to serpentine channels. This design improves electron transport by maximizing contact points, while simultaneously preserving the mechanical integrity of the membrane and reducing crack formation in the catalyst layer. Nevertheless, porous flow-field structures must be carefully designed with respect to flow distribution and pressure drop; otherwise, hydrodynamic losses may increase.

b. Optimization of Land and Channel Widths

In conventional channeled flow-field designs, the selection of channel and land widths constitutes a critical engineering problem that directly affects cell performance. Wider land regions increase the electrical contact area and reduce contact resistance, while also providing improved mechanical support to the membrane. However, they hinder the transport of reactants to catalyst regions located beneath the lands and limit the effective utilization of the active area. Conversely, wider channels facilitate mass transport (water ingress and gas removal) and reduce pressure drop, but they increase contact resistance and elevate the risk of membrane sagging into the channels.

Studies and simulations reported in the literature generally indicate that channel widths in the range of 1.0–2.0 mm, with comparable land widths, provide a favorable performance balance; however, these values may vary depending on PTL rigidity, cell size, and end plate design (X. Zhang et al., 2019). Accordingly, these geometric ratios should be adjusted based on the stiffness of the employed PTL and the operating pressure.

c. Material Selection and Corrosion Resistance

The high anodic potentials and acidic environment present on the anode side of PEMWEs render the use of carbon-based materials impractical. Consequently, titanium is a more suitable choice for anode bipolar plates (Bazarah et al., 2022; K. Zhang et al., 2022). Although titanium exhibits excellent corrosion resistance, the formation of an insulating oxide layer (TiO_2) on its surface leads to an increase in contact resistance over time (T. Wang et al., 2022). This passivation phenomenon constitutes one of the primary causes of performance degradation during prolonged operation. In addition, the potential for hydrogen-induced degradation mechanisms (e.g., hydride formation under specific conditions) in titanium represents a mechanical concern under long-term operating conditions.

To mitigate these issues, titanium plates are commonly coated with noble metals such as gold, platinum, or iridium. In recent years, efforts to reduce costs have intensified research into alternative coatings, including niobium, tantalum, and conductive ceramic coatings (e.g., TiN, CrN) (Gago et al., 2016; Srour et al., 2024). More economical materials such as stainless steel can also be employed when protected by thick and pore-free coatings (for example, Au/Ti multilayer coatings); however, coating defects may still pose a risk of corrosion (Kellenberger et al., 2022; Rojas et al., 2021).

Porous Transport Layers (PTLs): Structural Characteristics and Performance

The PTL used on the anode side is one of the most critical components of a PEMWE. Its primary functions include conducting electrons from the current collector or flow-field structure to the catalyst layer, ensuring the homogeneous distribution of reactant water to the catalyst, and efficiently removing the generated oxygen gas. To effectively fulfill these functions, PTLs are typically fabricated from metal-based materials with high corrosion resistance and tailored porous structures. The mechanical and structural properties of the PTL play a decisive role in overall cell performance (Ghadbane et al., 2025; Y. Liu et al., 2025). Figure 7 presents representative images of a titanium felt–type PTL, obtained from the literature using X-ray tomography and optical microscopy.

Figure 7. Representative images of a titanium felt–type PTL obtained using X-ray tomography and optical microscopy

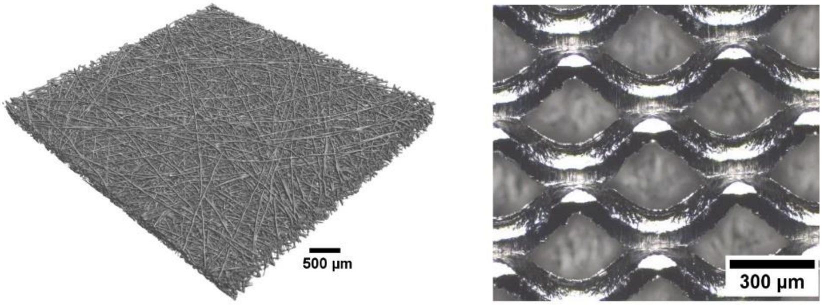

Source: (Sievert et al., 2026)

a. Comparison of Titanium Felt and Sintered Powder PTLs

The two most commonly used PTL types in PEMWEs are titanium felt fabricated from titanium fibers and plates produced by sintering titanium powders. These two materials exhibit significant differences in terms of mechanical behavior and performance characteristics (Ismael, 2026; Li et al., 2025).

Porous transport layers manufactured from sintered titanium powder are produced by sintering spherical or irregularly shaped titanium particles under high temperature and pressure conditions (G. Liu et al., 2025). This structure imparts high stiffness and mechanical strength to the material, resulting in very limited deformation under applied compressive pressure. The relatively smooth and geometrically uniform surface contributes to stable contact area formation and enables the preservation of structural integrity under high-pressure conditions (Borgardt et al., 2018). Owing to its smooth surface, a good interface with the catalyst layer can be achieved, leading to low contact resistance. However, its porosity is generally lower than that of felt-based structures, and the pore network may be more tortuous, which can limit mass transport at high current densities (J. Liu, Yang, et al., 2024). Due to its rigid nature, its ability to accommodate thickness variations within the stack is limited.

Titanium felt is typically manufactured by arranging micron-sized titanium fibers (for example, 20–50 μm in diameter) into a randomly oriented network, followed by sintering. This structure exhibits high porosity (approximately 60–80%) and displays a more flexible and compressible mechanical behavior compared to sintered titanium powder, with a lower elastic modulus (C.-K. Wang, Chan, et al., 2025; B. Zhang et al., 2025). The high porosity significantly enhances water and gas transport, providing advantages in terms of permeability; however, the fibrous morphology can lead to surface irregularities and increased roughness. Under applied compressive pressure, it has been reported that the rigid titanium fibers may locally intrude into the soft catalyst layer and polymer electrolyte membrane, potentially increasing contact resistance and causing mechanical damage (Mo et al., 2015).

b. PTL Intrusion and Interfacial Mechanics

The mechanical interaction between the PTL and the membrane is commonly described by the concept of *intrusion*. Intrusion refers to the penetration of PTL material (fiber tips or powder particles) into the soft polymer membrane structure under applied pressure (Lee et al., 2023).

A mild and well-controlled degree of intrusion can increase the interfacial contact area, thereby reducing electrical resistance. In addition, it promotes mechanical interlocking between the catalyst layer and the PTL, helping to prevent delamination. Excessive intrusion, however, reduces the effective thickness of the membrane and creates localized stress concentrations. In titanium felt structures, the penetration of individual fibers into the membrane may lead to pinhole formation and even membrane perforation. Such damage can increase the crossover of hydrogen and oxygen gases to the opposite electrodes, posing serious risks to system safety. To mitigate these risks, strategies such as surface treatment of PTLs (e.g., mechanical abrasion or polishing) or coating with a thin microporous layer (MPL) are being investigated. The MPL acts as a buffer layer between the coarse PTL and the delicate membrane, homogenizing the applied pressure and suppressing PTL intrusion (Borgardt et al., 2019; Stähler et al., 2020).

Membrane Mechanical Degradation: Creep and Thinning

The polymer electrolyte membrane (typically Nafion® and its derivatives), which constitutes the core of PEMWEs, is mechanically the weakest and most dynamic component of the system. Under operating conditions involving elevated temperature and pressure, the membrane exhibits viscoelastic behavior and gradually loses its mechanical integrity over time.

a. Compressive Creep

Membranes exhibit creep behavior under the compressive pressure applied during assembly and the hydrogen pressure experienced during operation (Salehmin et al., 2022). Creep is defined as the time-dependent permanent deformation of a material under a constant load (Afzal & Wang, 2025). In PEMWEs, the membrane is fully hydrated. Water molecules act as plasticizers between polymer chains, lowering the glass transition temperature and causing the material to soften.

Under high compressive pressure, the softened polymer chains undergo reorganization, and the membrane flows into the pores of the PTL or expands laterally. As a result of this process, the membrane thickness decreases permanently. Studies have shown that even under a 24-hour compression period, the membrane experiences significant thinning, with a large portion of this deformation being irreversible (Arthurs & Kusoglu, 2021).

b. Effects of Creep on Performance and Safety

Membrane thinning and creep are regarded as a dual mechanism that exerts both short-term and long-term effects on electrolyzer performance. In the short term, a reduction in membrane thickness shortens the ionic transport path for protons, which may temporarily reduce ionic resistance—particularly the high-frequency resistance (HFR)—and can lead to an apparent short-term performance improvement (C. R. Wang et al., 2025).

In contrast, membrane thinning gives rise to several adverse effects in the long term. As the membrane becomes thinner, the crossover of hydrogen and oxygen gases to the opposite electrode increases, which not only reduces the purity of the produced hydrogen but also raises the risk that the hydrogen concentration in oxygen exceeds the commonly accepted safety limit (typically ~2 vol% H_2 in O_2). At the same time, thinning and viscoelastic creep of the membrane material cause a gradual reduction in the preload applied through the bolts during assembly (García-Salaberri et al., 2025). This leads to a decrease in the effective compressive pressure within the cell and a weakening of interfacial contact areas; as a result, contact resistances increase and ohmic losses rise, causing a gradual decline in electrolyzer performance over time. In cases of excessive membrane thinning, the likelihood of direct contact between the anode and cathode electrodes increases, thereby introducing the risk of internal short circuits.

c. High-Pressure Operation and Mechanical Support

To increase hydrogen storage density and eliminate the need for mechanical compressors, PEMWEs are increasingly designed to operate at high cathode pressures (30–100 bar and above) (Ahmed et al., 2022; Hancke et al., 2022). In this operating mode, high-pressure hydrogen is present on the cathode side, while water and oxygen remain at near-atmospheric pressure on the anode side. This substantial pressure differential exerts a force on the membrane, pushing it toward the anode.

For the membrane to withstand this pressure, it must be effectively supported by the anode-side PTL. If the PTL pores are excessively large, localized bulging of the membrane into the PTL pores and an increased risk of rupture may occur. Therefore, in high-pressure systems, PTLs with small pore sizes, high rigidity, and smooth surface characteristics are preferred (Stähler et al., 2020). In addition, the use of PTFE-reinforced composite membranes is widely adopted in industrial applications to enhance mechanical strength and mitigate creep behavior (C. R. Wang et al., 2025).

Conclusion

The success of PEMWE technology depends not only on the activity of electrochemical catalysts, but also strongly on the mechanical assembly parameters that hold these components together and govern their interactions. The analysis presented in this chapter clearly demonstrates that mechanical design is an integral part of cell performance. Electrochemical efficiency is shown to be directly linked to parameters such as tightening torque, contact pressure, end plate stiffness, PTL–membrane deformation, and load distribution; failure to optimize these parameters can result in significant losses in both initial performance and long-term stability. In light of the findings discussed, the following key conclusions can be drawn:

a. **Optimum Pressure Balance:** It is not possible to define a universal and single optimum compressive pressure for PEMWE stacks, as the appropriate operating pressure depends directly on the mechanical properties, compressibility, and surface morphology of the employed PTL materials. Nevertheless, for each system, there exists an optimum pressure range in which ohmic contact resistances are sufficiently reduced while mass transport limitations and structural degradation associated with over-compression have not yet emerged. Therefore, compressive pressure should not be treated as a fixed value, but rather as a critical operating parameter that must be determined experimentally by considering material selection and stack-specific design features.

b. **Pressure Homogeneity:** End plate stiffness and bolt tightening procedures are critical for achieving a homogeneous pressure distribution across the active area. Non-uniform pressure leads to localized current density concentrations, hot spots, and premature membrane failure. Lightweight yet rigid end plates designed through topology optimization play a significant role in mitigating these issues.

c. **Material–Design Compatibility:** For high performance and durability, components must be selected using a holistic design approach. When thin membranes are employed, smooth-surfaced and fine-pore PTLs or coated BPPs should be preferred to prevent intrusion. While titanium felt PTLs offer superior mass transport characteristics, sintered powder PTLs provide higher pressure tolerance and surface uniformity.

d. **Time-Dependent Dynamics:** Due to the viscoelastic nature of the membrane, the pressure set during assembly decreases over time. This behavior may necessitate the use of spring washers or active pressure compensation systems in stack designs to accommodate bolt relaxation and differences in thermal expansion.

e. **Integrated Design Approach:** Next-generation design objectives—such as high-pressure operation, thin membranes, and low catalyst loadings—require sensitive integration not only at the electrochemical level but also at the micromechanical scale. In the future, FEA-based optimizations, advanced material combinations, and controlled assembly strategies will be key to achieving these goals.

Although research on the effects of mechanical assembly and structural parameters on PEMWE performance has increased in recent years, many technical and scientific challenges remain unresolved. In particular, the integration of sensors for real-time monitoring of interfacial contact pressure during operation represents a significant unmet need. Such monitoring systems would not only enable assessment of assembly quality but also provide a foundation for long-term performance tracking and predictive fault detection.

Furthermore, whether compressive pressure is distributed homogeneously over the cell surface is directly linked to electrochemical reaction rates and current density distributions. Consequently, integrated studies combining experimental approaches with multiphysics numerical analyses represent an important future research direction. It should also be recognized that the pressure applied during assembly tends to relax over time, potentially degrading contact quality and increasing electrical resistance. Therefore, the effects of long-term thermomechanical cycling, novel material combinations, and active pressure compensation mechanisms constitute key topics to be addressed in future work.

References

Afzal, J., & Wang, H. (2025). A review on sulfonated organic polymer based composite membranes for PEM water electrolyzers. *International Journal of Hydrogen Energy*, *123*, 100–117. https://doi.org/10.1016/j.ijhydene.2025.03.374

Ahmed, K. W., Jang, M. J., Park, M. G., Chen, Z., & Fowler, M. (2022). Effect of Components and Operating Conditions on the Performance of PEM Electrolyzers: A Review. *Electrochem*, *3*(4), 581–612. https://doi.org/10.3390/electrochem3040040

Al Shakhshir, S. (2018, May 16). *On the Effect of Clamping Pressure and Method on the Current Mapping of Proton Exchange Membrane Water Electrolysis*. 233rd ECS Meeting (May 13-17, 2018). https://ecs.confex.com/ecs/233/webprogram/Paper111024.html

Arthurs, C., & Kusoglu, A. (2021). Compressive Creep of Polymer Electrolyte Membranes: A Case Study for Electrolyzers. *ACS Applied Energy Materials*, *4*(4), 3249–3254. https://doi.org/10.1021/acsaem.0c03024

Bazarah, A., Majlan, E. H., Husaini, T., Zainoodin, A. M., Alshami, I., Goh, J., & Masdar, M. S. (2022). Factors influencing the performance and durability of polymer electrolyte membrane water electrolyzer: A review. *International Journal of Hydrogen Energy*, *47*(85), 35976–35989. https://doi.org/10.1016/j.ijhydene.2022.08.180

Borgardt, E., Giesenberg, L., Reska, M., Müller, M., Wippermann, K., Langemann, M., Lehnert, W., & Stolten, D. (2019). Impact of clamping pressure and stress relaxation on the performance of different polymer electrolyte membrane water electrolysis cell designs. *International Journal of Hydrogen Energy*, *44*(42), 23556–23567. https://doi.org/10.1016/j.ijhydene.2019.07.075

Borgardt, E., Panchenko, O., Hackemüller, F. J., Giffin, J., Bram, M., Müller, M., Lehnert, W., & Stolten, D. (2018). Mechanical characterization and durability of sintered porous transport layers for polymer electrolyte membrane electrolysis. *Journal of Power Sources*, *374*, 84–91. https://doi.org/10.1016/j.jpowsour.2017.11.027

Cruz Ortiz, E., van Treel, N., Koch, S., Vierrath, S., & Bühler, M. (2024). The effect of compression on PEM Electrolyzer membrane electrode Assemblies. *Journal of Power Sources*, *614*, 235018. https://doi.org/10.1016/j.jpowsour.2024.235018

Dey, T., Deshpande, J., Singdeo, D., & Ghosh, P. C. (2019). Study of PEM Fuel Cell End Plate Design by Structural Analysis Based on Contact Pressure. *Journal of Energy*, *2019*, 1–11. https://doi.org/10.1155/2019/3821082

Gago, A. S., Ansar, S. A., Saruhan, B., Schulz, U., Lettenmeier, P., Cañas, N. A., Gazdzicki, P., Morawietz, T., Hiesgen, R., Arnold, J., & Friedrich, K. A. (2016). Protective coatings on stainless steel bipolar plates for proton exchange membrane (PEM) electrolysers. *Journal of Power Sources*, *307*, 815–825. https://doi.org/10.1016/j.jpowsour.2015.12.071

García-Salaberri, P. A., van Eijk, L., Bangay, W., Ferner, K. J., Ha, M. H., Moore, M., Perea, I., Kusoglu, A., Secanell, M., Das, P. K., Firas, N., Pylypenko, S., Novy, M., Yandrasits, M., Saha, S. C., Bayat, A., Litster, S., & Zenyuk, I. V. (2025). Materials Engineering for High Performance and Durability Proton Exchange Membrane Water Electrolyzers. *ACS Applied Energy Materials*, *8*(18), 13050–13121. https://doi.org/10.1021/acsaem.5c01989

Ghadbane, A., Yuan, X.-Z., Platt, A., Malek, A., Shaigan, N., Dinu, M., Shahgaldi, S., & Fatih, K. (2025). A Review of Diagnostic Tools for Evaluating Porous Transport Layers for Proton Exchange Membrane (PEM) Water Electrolysis. *Electrochemical Energy Reviews*, *8*(1), 23. https://doi.org/10.1007/s41918-025-00256-x

Guidelines for Pressure Boundary Bolted Flange Joint Assembly (No. ASME PCC-1–2019). (2019). https://ssmalloys.com/wp-content/uploads/2024/10/ASME-PCC-1–2019.pdf

Hancke, R., Holm, T., & Ulleberg, Ø. (2022). The case for high-pressure PEM water electrolysis. *Energy Conversion and Management*, *261*, 115642. https://doi.org/10.1016/j.enconman.2022.115642

Hou, D., Qiao, G., Liu, L., Zhang, X., Yan, Y., & Du, S. (2025). Challenges in scaling up testing of catalyst coated membranes for proton exchange membrane water electrolyzers. *Frontiers in Energy Research*, *13*. https://doi.org/10.3389/fenrg.2025.1557069

Hu, B., He, S., Su, X., Xu, L., & Zhu, D. (2023). Experimental study of the effect of fastening bolts on PEMEC performance.

International Journal of Hydrogen Energy, *48*(90), 35050–35063. https://doi.org/10.1016/j.ijhydene.2023.05.116

Ismael, M. (2026). Performance enhancement of proton electrolyte membrane (PEM) water electrolyzers through modification of titanium-based porous transport layers (Ti-PTLs): A review. *Journal of Power Sources*, *665*, 238965. https://doi.org/10.1016/j.jpowsour.2025.238965

Jo, M., Cho, H.-S., & Na, Y. (2020). Comparative Analysis of Circular and Square End Plates for a Highly Pressurized Proton Exchange Membrane Water Electrolysis Stack. *Applied Sciences*, *10*(18), 6315. https://doi.org/10.3390/app10186315

Kellenberger, A., Vaszilcsin, N., Duca, D., Dan, M. L., Duteanu, N., Stiber, S., Morawietz, T., Biswas, I., Ansar, S. A., Gazdzicki, P., Wirkert, F. J., Roth, J., Rost, U., Brodmann, M., Gago, A. S., & Friedrich, K. A. (2022). Towards Replacing Titanium with Copper in the Bipolar Plates for Proton Exchange Membrane Water Electrolysis. *Materials*, *15*(5), 1628. https://doi.org/10.3390/ma15051628

Kesercioğlu, M. A., Boyacı San, F. G., Sözbir, N., & Çay, Y. (2025). Performance optimization of PEM electrolyzers: An experimental and Taguchi-based approach. *International Journal of Hydrogen Energy*, *152*, 150214. https://doi.org/10.1016/j.ijhydene.2025.150214

Lee, J. K., Schuler, T., Bender, G., Sabharwal, M., Peng, X., Weber, A. Z., & Danilovic, N. (2023). Interfacial engineering via laser ablation for high-performing PEM water electrolysis. *Applied Energy*, *336*, 120853. https://doi.org/10.1016/j.apenergy.2023.120853

Li, J., Xu, Y., Kuang, Y., Sun, L., Wang, F., Huang, X., Luo, M., Zhou, Y., Zou, J., Shu, J., Gan, S., Yan, J. L., & Liu, B. (2025). Porous transport layers for proton exchange membrane water electrolyzers. *Journal of Alloys and*

Compounds, *1041*, 183754. https://doi.org/10.1016/j.jallcom.2025.183754

Liu, G., Zhang, B., Shen, L., Yang, Y., Yang, K., Wang, J., & Wang, H. (2025). Effect of thickness for powder-sintered Ti porous transport layer on performance of PEM water electrolyzer. *International Journal of Hydrogen Energy*, *196*, 152574. https://doi.org/10.1016/j.ijhydene.2025.152574

Liu, J., Liu, H., Yang, Y., Tao, Y., Zhao, L., Li, S., Fang, X., Lin, Z., Wang, H., Tao, H. B., & Zheng, N. (2024). Efficient and Stable Proton Exchange Membrane Water Electrolysis Enabled by Stress Optimization. *ACS Central Science*, *10*(4), 852–859. https://doi.org/10.1021/acscentsci.4c00037

Liu, J., Yang, Y., Kerner, F., & Schröder, D. (2024). Comparative Analysis of Fiber-Based and Powder-Based Porous Transport Layers in Water Electrolysis for Green Hydrogen. *ACS Sustainable Chemistry & Engineering*, *12*(50), 18077–18089. https://doi.org/10.1021/acssuschemeng.4c06540

Liu, Y., Liu, S.-N., Yu, Q.-H., Dong, Z.-Q., Hao, L., & Mi, J. (2025). Progress in porous transport layer for hydrogen production via proton exchange membrane water electrolysis. *Rare Metals*, *44*(9), 5933–5956. https://doi.org/10.1007/s12598-025-03379-8

Martin, A., Trinke, P., Stähler, M., Stähler, A., Scheepers, F., Bensmann, B., Carmo, M., Lehnert, W., & Hanke-Rauschenbach, R. (2022). The Effect of Cell Compression and Cathode Pressure on Hydrogen Crossover in PEM Water Electrolysis. *Journal of The Electrochemical Society*, *169*(1), 014502. https://doi.org/10.1149/1945-7111/ac4459

Medina, P., & Santarelli, M. (2010). Analysis of water transport in a high pressure PEM electrolyzer. *International Journal of Hydrogen Energy*, *35*(11), 5173–5186. https://doi.org/10.1016/j.ijhydene.2010.02.130

Mo, J., Steen, S., Han, B., Kang, Z., Terekhov, A., Zhang, F.-Y., Retterer, S. T., & Cullen, D. A. (2015, July 27). Investigation of titanium felt transport parameters for energy storage and hydrogen/oxygen production. *13th International Energy Conversion Engineering Conference*. 13th International Energy Conversion Engineering Conference, Orlando, FL. https://doi.org/10.2514/6.2015-3914

Rojas, N., Sánchez-Molina, M., Sevilla, G., Amores, E., Almandoz, E., Esparza, J., Cruz Vivas, M. R., & Colominas, C. (2021). Coated stainless steels evaluation for bipolar plates in PEM water electrolysis conditions. *International Journal of Hydrogen Energy*, *46*(51), 25929–25943. https://doi.org/10.1016/j.ijhydene.2021.03.100

Salehmin, M. N. I., Husaini, T., Goh, J., & Sulong, A. B. (2022). High-pressure PEM water electrolyser: A review on challenges and mitigation strategies towards green and low-cost hydrogen production. *Energy Conversion and Management*, *268*, 115985. https://doi.org/10.1016/j.enconman.2022.115985

Sayed-Ahmed, H., Toldy, Á. I., & Santasalo-Aarnio, A. (2024). Dynamic operation of proton exchange membrane electrolyzers—Critical review. *Renewable and Sustainable Energy Reviews*, *189*, 113883. https://doi.org/10.1016/j.rser.2023.113883

Selamet, Ö. F., Acar, M. C., Mat, M. D., & Kaplan, Y. (2013). Effects of operating parameters on the performance of a high-pressure proton exchange membrane electrolyzer: Effects of operating parameters on the performance of a high-pressure PEM electrolyzer. *International Journal of Energy Research*, *37*(5), 457–467. https://doi.org/10.1002/er.2942

Selamet, O. F., & Ergoktas, M. S. (2015). Effects of bolt torque and contact resistance on the performance of the polymer electrolyte membrane electrolyzers. *Journal of Power Sources*, *281*, 103–113. https://doi.org/10.1016/j.jpowsour.2015.01.162

Shiva Kumar, S., & Himabindu, V. (2019). Hydrogen production by PEM water electrolysis – A review. *Materials Science for Energy Technologies*, *2*(3), 442–454. https://doi.org/10.1016/j.mset.2019.03.002

Sievert, T., Zerressen, S., Glüsen, A., Bram, M., Uhlenbruck, S., Bender, K., Vondahlen, F., Xiao, P., Cao, X., Guillon, O., Peters, R., Müller, M., Apfel, U.-P., & Vaßen, R. (2026). TiNb alloy coatings for anode PTLs in PEM water electrolyzers. *Journal of Power Sources*, *664*, 238944. https://doi.org/10.1016/j.jpowsour.2025.238944

Srour, T., Kumar, K., Martin, V., Dubau, L., Maillard, F., Gilles, B., Dillet, J., Didierjean, S., Amoury, B., Le, T. D., & Maranzana, G. (2024). On the contact resistance between the anode and the porous transport layer in a proton exchange membrane water electrolyzer. *International Journal of Hydrogen Energy*, *58*, 351–361. https://doi.org/10.1016/j.ijhydene.2024.01.134

Srour, T., Maranzana, G., Didierjean, S., Dillet, J., Kumar, K., & Maillard, F. (2023). Effect of a PTL Coating and the Clamping Pressure on the Performance of a PEM Electrolyzer Cell. *ECS Meeting Abstracts*, *MA2023-01*(36), 2114. https://doi.org/10.1149/MA2023-01362114mtgabs

Stähler, M., Stähler, A., Scheepers, F., Carmo, M., Lehnert, W., & Stolten, D. (2020). Impact of porous transport layer compression on hydrogen permeation in PEM water electrolysis. *International Journal of Hydrogen Energy*, *45*(7), 4008–4014. https://doi.org/10.1016/j.ijhydene.2019.12.016

Staudacher, M., Goes, D., Ahn, S., Vrucak, D., Gießmann, T., Bauer-Siebenlist, B., Leißner, T., Rudolph, M., Fleischer, J., Friedrich, B., & Peuker, U. A. (2025). Conceptual Recycling Chain for Proton Exchange Membrane Water Electrolyzers—Case Study Involving Review-Derived Model Stack. *Recycling*, *10*(3), 121. https://doi.org/10.3390/recycling10030121

Tolouei, N. E., Chabot, F. M., Yang, P., Lang, J. T., Hasa, B., Aryal, U. R., Zhu, G., Parkinson, D. Y., & Zenyuk, I. V. (2026). Effect of cell compression on the performance and the structure of proton exchange membrane water electrolyzer (PEMWE) assembly. *Electrochimica Acta*, *547*, 147871. https://doi.org/10.1016/j.electacta.2025.147871

Wang, C. R., Stansberry, J. M., Mukundan, R., Chang, H.-M. J., Kulkarni, D., Park, A. M., Plymill, A. B., Firas, N. M., Liu, C. P., Lang, J. T., Lee, J. K., Tolouei, N. E., Morimoto, Y., Wang, C., Zhu, G., Brouwer, J., Atanassov, P., Capuano, C. B., Mittelsteadt, C., … Zenyuk, I. V. (2025). Proton Exchange Membrane (PEM) Water Electrolysis: Cell-Level Considerations for Gigawatt-Scale Deployment. *Chemical Reviews*, *125*(3), 1257–1302. https://doi.org/10.1021/acs.chemrev.3c00904

Wang, C.-K., Chan, K.-W., Shen, M.-Y., & Kuan, Y.-D. (2025). Titanium felt coated with PTFE as a gas diffuser for proton exchange membrane fuel cell. *International Journal of Hydrogen Energy*, *148*, 149677. https://doi.org/10.1016/j.ijhydene.2025.05.307

Wang, C.-K., Huang, C.-H., Shen, M.-Y., & Kuan, Y.-D. (2025). Investigation of five flow channel designs in PEM electrolysis with titanium felt. *International Journal of Hydrogen Energy*, *139*, 956–962. https://doi.org/10.1016/j.ijhydene.2024.07.135

Wang, T., Cao, X., & Jiao, L. (2022). PEM water electrolysis for hydrogen production: Fundamentals, advances, and prospects. *Carbon Neutrality*, *1*(1), 21. https://doi.org/10.1007/s43979-022-00022-8

Wang, X., Song, Y., & Zhang, B. (2008). Experimental study on clamping pressure distribution in PEM fuel cells. *Journal of Power Sources*, *179*(1), 305–309. https://doi.org/10.1016/j.jpowsour.2007.12.055

Wang, X., Star, A. G., & Ahluwalia, R. K. (2023). Performance of Polymer Electrolyte Membrane Water Electrolysis Systems: Configuration, Stack Materials, Turndown and Efficiency. *Energies*, *16*(13), 4964. https://doi.org/10.3390/en16134964

Wei, Q., Fan, L., & Tu, Z. (2023). Hydrogen production in a proton exchange membrane electrolysis cell (PEMEC) with titanium meshes as flow distributors. *International Journal of Hydrogen Energy*, *48*(93), 36271–36285. https://doi.org/10.1016/j.ijhydene.2023.06.052

Wei, Y., Xing, Y., Zhang, X., Wang, Y., Cao, J., & Yang, F. (2024). A Review of Sealing Systems for Proton Exchange Membrane Fuel Cells. *World Electric Vehicle Journal*, *15*(8), 358. https://doi.org/10.3390/wevj15080358

Zhang, B., Yang, K., Shen, L., Duan, X., Zhao, S., Gao, W., Xu, C., & Wang, J. (2025). Development, exploration and optimization of porous titanium and titanium alloys: A review. *Journal of Science: Advanced Materials and Devices*, *10*(2), 100863. https://doi.org/10.1016/j.jsamd.2025.100863

Zhang, H., Zhu, J., Xu, J., Wang, C., Yuan, H., Dai, H., & Wei, X. (2025). Investigation on the influence of structural parameters in the porous transport layer on the mass transfer process within PEM water electrolyzer. *International Journal of Heat and Mass Transfer*, *253*, 127519. https://doi.org/10.1016/j.ijheatmasstransfer.2025.127519

Zhang, K., Liang, X., Wang, L., Sun, K., Wang, Y., Xie, Z., Wu, Q., Bai, X., Hamdy, M. S., Chen, H., & Zou, X. (2022). Status and perspectives of key materials for PEM electrolyzer. *Nano Research Energy*, *1*(3), 9120032. https://doi.org/10.26599/NRE.2022.9120032

Zhang, X., Higier, A., Zhang, X., & Liu, H. (2019). Experimental Studies of Effect of Land Width in PEM Fuel Cells with Serpentine Flow Field and Carbon Cloth. *Energies*, *12*(3), 471. https://doi.org/10.3390/en12030471

CHAPTER 5

FINITE ELEMENT-BASED STUDIES OF NATURAL CONVECTION IN ENCLOSURES FOR ENGINEERING SYSTEMS

1. GÜLNUR HAÇAT[1]

1. Introduction

Natural convection in enclosed domains is a fundamental transport phenomenon encountered in a wide range of engineering systems, including thermal management of electronic equipment, building energy systems, solar collectors, nuclear reactor components, heat exchangers, and geophysical and environmental applications. In such systems, fluid motion is induced by buoyancy forces arising from temperature-dependent density variations, without the presence of externally imposed flow. Despite the apparent simplicity of the physical mechanism, natural convection in enclosures exhibits complex flow structures, strong coupling between momentum and energy transport, and rich nonlinear behavior, particularly at moderate to high Rayleigh numbers (Bejan, 2013; Kakac et.al. 2013).

---

[1] Lecturer Dr., Yalova University, Rectorate, Scientific Research Projects Unit, Orcid: 0000-0001-7343-8466

Accurate prediction of natural convection phenomena is essential for the reliable design, optimization, and safety assessment of engineering systems. Experimental investigations, while invaluable, are often constrained by measurement difficulties, cost, and limited parametric flexibility. Analytical solutions are restricted to highly idealized configurations and simplified governing equations. Consequently, numerical simulation has become a primary tool for studying natural convection in enclosed geometries, enabling systematic investigation of the effects of geometry, boundary conditions, material properties, and external fields.

Among various numerical approaches, the finite element method (FEM) has emerged as a particularly powerful and flexible framework for modeling natural convection in enclosures. FEM offers significant advantages in handling complex geometries, non-uniform and anisotropic material properties, and mixed boundary conditions that frequently arise in practical engineering applications. Its variational foundation allows for systematic treatment of coupled partial differential equations governing fluid flow and heat transfer, and facilitates the incorporation of advanced stabilization techniques required for convection-dominated regimes (Nithiarasu et al., 2016).

Finite element-based studies of natural convection typically involve the solution of the incompressible Navier–Stokes equations coupled with the energy equation, often under the Boussinesq approximation (Szewc et al., 2011; Lee & Kim, 2012; Mayeli & Sheard, 2021). Depending on the application, additional physical effects such as magnetic fields, thermal radiation, porous media, phase change, or variable thermophysical properties may be incorporated into the governing equations. Over the past decades, extensive FEM research has been conducted on canonical enclosure configurations—such as square, rectangular, triangular, and cavity geometries—providing benchmark solutions and physical insight into flow patterns, heat transfer characteristics, and stability behavior.

From an engineering perspective, enclosure-type natural convection problems serve both as idealized models for real systems and as testbeds for the development and validation of numerical methodologies. Finite element formulations have been successfully applied to investigate the influence of key dimensionless parameters, including the Rayleigh, Prandtl, and Hartmann numbers, as well as geometric aspect ratios and boundary condition variations. These studies have contributed significantly to the understanding of heat transfer enhancement or suppression mechanisms, flow bifurcations, and transition to unsteady or chaotic regimes (Samaila, & Jha, 2024).

The objective of this book chapter is to provide a comprehensive overview of finite element-based studies of natural convection in enclosures, with particular emphasis on engineering applications. The chapter reviews the governing equations and modeling assumptions, discusses common finite element formulations and stabilization strategies, and summarizes representative numerical studies from the literature. Special attention is given to the interpretation of numerical results in terms of physical mechanisms and their implications for engineering design. By consolidating methodological and application-oriented perspectives, this chapter aims to serve as a useful reference for researchers and engineers engaged in the numerical modeling of natural convection systems.

1.1. Novelty and Contribution

The present study provides a focused and systematic finite element investigation of natural convection in enclosed domains, with particular emphasis on accurately capturing coupled flow and heat transfer phenomena under varying physical and geometrical conditions. The main novelty lies in the implementation and assessment of a robust FEM formulation that ensures numerical stability and accuracy over a wide range of Rayleigh numbers, including convection-dominated regimes.

In contrast to many existing studies that rely on simplified or problem-specific formulations, this work adopts a unified finite element framework capable of incorporating additional physical effects without compromising solution robustness. The study offers a comprehensive parametric analysis that elucidates the interplay between buoyancy-driven flow structures, thermal fields, and key dimensionless parameters. The results provide both physically consistent benchmark data and methodological insight, contributing to the reliable application of FEM in the simulation, analysis, and design of enclosure-type natural convection systems in engineering practice.

2. Literature Review

Natural convection is one of the fundamental flow regimes that arises due to buoyancy forces induced by density differences and plays a decisive role in governing heat transfer mechanisms, particularly in enclosed domains. In chemical engineering, the accurate modeling of natural convection is critical for assessing system performance and safety in a wide range of applications, including reactors, heat exchangers, energy systems, and process equipment. In this context, the finite element method (FEM) is a powerful numerical tool widely employed for modeling complex geometries and multiphysics interactions.

Türk and Tezer-Sezgin (2013) investigated natural convection flow in a square enclosure under the influence of a magnetic field using FEM. In their study, the Navier–Stokes and energy equations were nondimensionalized using the Boussinesq approximation, and magnetohydrodynamic (MHD) effects were incorporated into the model. The effects of the Rayleigh and

Hartmann numbers on the flow structure and heat transfer were analyzed in detail. The results demonstrated that the magnetic field suppresses natural convection by reducing flow velocities and decreasing the Nusselt number. This study constitutes an important reference for chemical and metallurgical processes where electromagnetic effects are significant (Türk & Tezer-Sezgin, 2013).

Alam and co-workers (2017) addressed a natural convection problem in a rectangular enclosure with a partially heated wall using FEM. Flow streamlines, isotherms, and average Nusselt numbers were computed for different Rayleigh numbers, and the influence of the heating configuration on the flow structure was examined. The results revealed that partial heating significantly alters the location and intensity of convection cells and directly affects heat transfer performance. Such configurations are particularly relevant for chemical engineering applications involving heat transfer from reactor walls or localized heat sources (Alam et al., 2017).

Taking a broader perspective on the natural convection literature, Abdulkadhim and colleagues (2021) presented a comprehensive review of natural convection in enclosed domains with complex geometries. The study systematically evaluated the effects of parameters such as geometry, boundary conditions, Rayleigh and Prandtl numbers, nanofluid usage, porous media, and magnetic fields on natural convection. FEM, finite volume, and finite difference methods were comparatively discussed, with particular emphasis on the flexibility provided by FEM in handling complex-shaped enclosures. This review serves as a comprehensive reference source for modeling strategies in engineering applications (Abdulkadhim et al., 2021).

Fichera and co-authors (2020) examined the natural convection problem by developing an analytical model beyond purely numerical approaches. For a rectangular enclosure with differentially heated vertical walls, the proposed model describes flow and heat transfer characteristics using simplified yet physically meaningful expressions. The analytical results were compared with numerical studies reported in the literature, demonstrating that the model yields reliable predictions within specific Rayleigh number ranges. This work provides an important benchmark reference for the validation of FEM-based models (Fichera et al., 2020).

Finally, Hasan and co-workers (2025) presented a comprehensive review of FEM-based studies on natural convection in enclosed domains with a focus on engineering applications. Square, rectangular, triangular, and irregular enclosures were systematically examined, with special attention given to contemporary topics such as nanofluids, porous media, phase change, and multiphysics interactions. The study clearly highlights the role of natural convection in the context of chemical engineering and emphasizes the importance of FEM in process design and optimization. This review offers a strong framework for book chapters and advanced-level literature discussions (Hasan et al., 2025).

When considered collectively, these studies clearly demonstrate that FEM provides high accuracy, geometric flexibility, and strong adaptability to multiphysics problems in the modeling of natural convection in enclosed domains. The need to accurately predict the effects of natural convection on heat and mass transfer in chemical engineering applications further underscores the importance of these numerical approaches.

The main characteristics of selected studies on natural convection in enclosures, including enclosure geometry, modeling methodology, and engineering relevance, are summarized in Table 1.

Table 1 Comparison of Key Studies on Natural Convection in Enclosures Using Finite Element and Analytical Approaches

Ref.	**Study**	**Geometry / System**	**Methodology**	**Physical Effects Considered**	**Key Findings**	**Relevance to Chemical Engineering Applications**
[1]	Türk & Tezer-Sezgin (2013)	Square enclosure	Finite Element Method (FEM)	Natural convection, magnetohydrodynamic (MHD) effects, Rayleigh and Hartmann numbers	Magnetic field suppresses buoyancy-driven flow, leading to reduced velocity magnitude and lower Nusselt numbers	Thermal control in chemical and metallurgical processes involving electromagnetic fields
[2]	Alam et al. (2017)	Rectangular enclosure with partially heated wall	Finite Element Method (FEM)	Natural convection, localized heating, Rayleigh number effects	Partial heating significantly alters flow structure and heat transfer characteristics	Modeling heat transfer from localized heat sources in reactors and process equipment
[3]	Abdulkadhim et al. (2021)	Complex-shaped enclosures	Review (FEM, FVM, FDM)	Geometry effects, nanofluids, porous media, MHD, dimensionless parameters	FEM provides superior flexibility and accuracy for	Design and analysis of chemically relevant systems

					natural convection in complex geometries	with non-standard geometries
[4]	Fichera et al. (2020)	Rectangular enclosure with differentially heated vertical walls	Analytical modeling	Natural convection, Rayleigh number dependence	Analytical model shows good agreement with numerical results within specific parameter ranges	Benchmarking and validation of FEM-based thermal models
[5]	Hasan et al. (2025)	Various enclosure geometries (square, rectangular, triangular, etc.)	Review (FEM-focused)	Nanofluids, porous media, multiphysics interactions	FEM-based approaches dominate engineering applications of enclosure natural convection	Heat and mass transfer modeling in chemical engineering and process systems

3. Interpretation of Numerical Results in Terms of Physical Mechanisms and Their Implications for Engineering Design

Numerical results obtained from finite element analyses of natural convection in enclosures provide not only quantitative distributions of velocity and temperature fields, but also valuable insight into the dominant physical mechanisms governing the system behavior. In this context, flow patterns, isotherms, and local and average Nusselt numbers derived from numerical simulations serve as primary indicators for assessing the relative importance of buoyancy forces, viscous effects, and thermal diffusion (Acharya, 2022).

With increasing Rayleigh number, the transition from conduction-dominated to convection-dominated regimes can be clearly observed in the numerical results. At low Rayleigh numbers, isotherms largely retain a parallel structure and the flow remains confined to weak circulation cells. As the Rayleigh number increases, thin thermal and hydrodynamic boundary layers, strong rotational flow structures, and the emergence of secondary vortices become evident. The accurate capture of such flow features is critical for evaluating the physical consistency of the finite element formulation and the effectiveness of the applied stabilization techniques (Bagchi & Kulacki, 2014).

Boundary conditions and geometric parameters also play a decisive role in the physical interpretation of numerical results (Rempfer, 2006). Variations in wall temperatures, imposed heat fluxes, or the presence of adiabatic surfaces directly influence the location, symmetry, and stability of convection cells. Similarly, the aspect ratio and geometric complexity of the enclosure affect the number and size of circulation cells, thereby determining the overall heat transfer performance. Finite element-based studies enable a systematic investigation of these effects, revealing causal relationships between design parameters and physical responses.

From an engineering design perspective, interpreting numerical results in light of the underlying physical mechanisms is essential not only for performance prediction, but also for design optimization. For example, in electronic cooling applications, identifying regions where natural convection is most effective allows for geometric modifications aimed at preventing hotspot formation. Likewise, in building and energy systems, understanding flow structures within enclosures provides guidance for reducing heat losses, enhancing thermal comfort, and improving energy efficiency (Pacheco et al., 2012).

The importance of physical interpretation becomes even more pronounced when additional effects such as magnetic fields, porous media, or variable fluid properties are incorporated into the model. In such cases, numerical results can be used to assess whether specific parameters act to suppress or enhance heat transfer, thereby offering controllable mechanisms for engineering design. Reliable and physically consistent results obtained using the finite element method contribute to identifying optimal parameter ranges for practical applications.

In summary, finite element-based numerical analysis of natural convection in enclosures should be regarded not merely as a computational tool, but as a means of gaining physical insight and supporting informed engineering design decisions. Careful and critical interpretation of numerical results in terms of physical mechanisms is indispensable for understanding the limitations of modeling assumptions and for ensuring the reliable transfer of numerical findings to real engineering systems.

Figure 1 presents a graphical summary of the finite element framework, governing equations, and characteristic temperature and flow fields used to analyze natural convection in engineering enclosures.

Figure 1 Graphical Abstract Illustrating Finite Element Modeling of Natural Convection in Engineering Enclosures

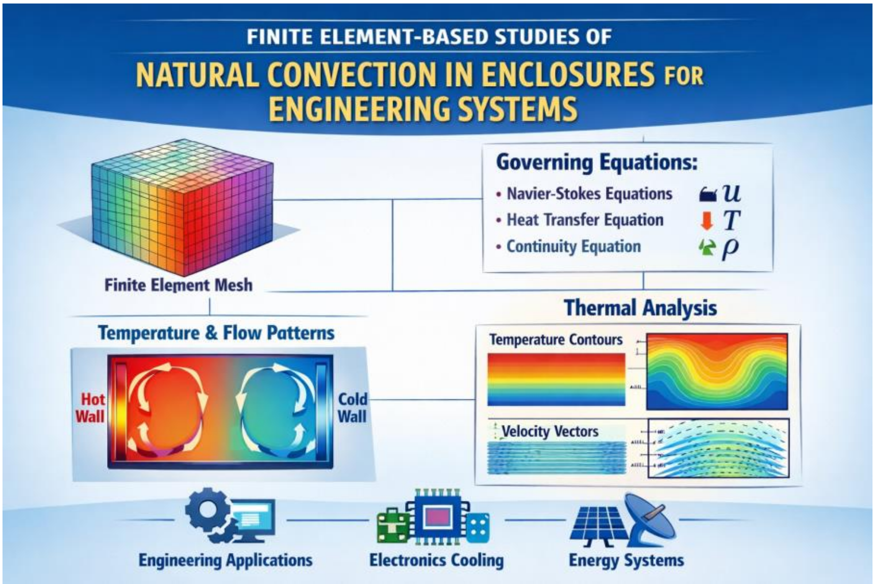

References

Acharya, N. (2022). Finite element analysis on the hydrothermal pattern of radiative natural convective nanofluid flow inside a square enclosure having nonuniform heated walls. *Heat Transfer, 51(1)*, 323-354.

Bagchi, A., & Kulacki, F. A. (2014). *Natural convection in superposed fluid-porous layers*. New York: Springer.

Bejan, A. (2013). *Convection heat transfer*. John wiley & sons.

Kakac, S., Yener, Y., & Pramuanjaroenkij, A. (2013). *Convective heat transfer*. CRC press.

Lee, H. G., & Kim, J. (2012). A comparison study of the Boussinesq and the variable density models on buoyancy-driven flows. *Journal of Engineering Mathematics, 75(1)*, 15-27.

Mayeli, P., & Sheard, G. J. (2021). A centrifugal buoyancy formulation for Boussinesq-type natural convection flows applied to the annulus cavity problem. *International Journal for Numerical Methods in Fluids, 93(3),* 683-702.

Nithiarasu, P., Lewis, R. W., & Seetharamu, K. N. (2016). *Fundamentals of the finite element method for heat and mass transfer*. John Wiley & Sons.

Pacheco, R., Ordóñez, J., & Martínez, G. (2012). Energy efficient design of building: A review. *Renewable and sustainable energy reviews*, *16*(6), 3559-3573.

Rempfer, D. (2006). On boundary conditions for incompressible Navier-Stokes problems. *Applied Mechanics Reviews*, *59*(3), 107-125.

Samaila, G., & Jha, B. K. (2024). On the combined effects of chemical reaction and nonlinear thermal radiation on natural convection heat and mass transfer over a vertical plate. *Boundary Value Problems*, *2024*(1), 115.

Szewc, K., Pozorski, J., & Taniere, A. (2011). Modeling of natural convection with smoothed particle hydrodynamics: non-Boussinesq formulation. *International Journal of Heat and Mass Transfer, 54(23-24)*, 4807-4816.

CHAPTER 6

PREDICTION of ADIABATIC FLAME TEMPERATURE in HYDROCARBON-HYDROGEN BLENDS: A GAUSSIAN PROCESS REGRESSION APPROACH CONSIDERING C/H ATOMIC RATIO, HYDROGEN FRACTION, and EQUIVALENCE RATIO

Melih YILDIZ [1]
Ahmet AKTÜRK [2]

INTRODUCTION

Conventional fuels, gasoline, diesel, kerosene are carbon-intensive fuels and non-renewable fuels. Therefore, the use of their blending with renewable fuels, like bioethanol, biodiesel, synthetic, and hydrogen, can allow decarbonization. Moreover, the blends also contribute to sustaining the energy sources by lowering the use of conventional fossil fuels. Fuel blending alters the chemical composition, combustion kinetics, and pollutant formation, such as carbon monoxide (CO), nitrogen oxides (NOx), soot, and unburned

---

[1] Assoc.Prof.Dr., Iğdır University, Department of Mechanical Engineering Orcid: 0000-0002-6904-9131

[2] Res. Assist. Dr., Iğdır University, Deparment of Mechanical Engineering, Orcid: 0000-0002-2985-2560

hydrocarbons (UHC). Among these, the blends of hydrocarbon and hydrogen fuels have received considerable attention, as hydrogen makes a significantly greater contribution to decarbonization (Gomes&et al., 2024). This is because hydrogen fuel does not contain carbon elements and has rapid flame propagation speed and wide range of flammability limits in air (4-75% by volume) (Habib$et al., 2024; Tang&et al., 2014), which allows for combustion with a lean mixture. Thus, the research on fuel blending with hydrogen has gained great attention in terms of efficiency, fuel consumption, and emissions.

Ji et al. (2018) investigated gasoline-hydrogen blending on a modified gasoline direct injection (GDI) engine for performance and emission evaluation by changing injection timing of gasoline. They reported that hydrogen addition could decrease hydrocarbon (HC) and carbon monoxide (CO) emissions by an average value of 33.10% and 18.28, respectively. Moreover, it was also stated that particulate number decreased by adding hydrogen. However, the addition of hydrogen brought about the increase in nitrogen oxides (NOx) emissions. Abdelwahed et al. (2025) performed the experimental studies on a diesel engine by adding hydrogen supplied at a 0.5 L/min of flow rate. They found that a hydrogen-diesel mixture provided a decrease in fuel consumption by 10%. Moreover, it resulted in a 13% reduction in CO and 17% in CO_2 emissions. Another significant result is that the diesel-hydrogen blend enabled a 17% reduction in NOx emissions. Gültekin et al. (2024) conducted a series of experimental studies to investigate the effects of diesel-hydrogen blending on the engine at a constant engine speed, various energy-based hydrogen fractions, and engine loads, as well as varying intake valve lift to increase volumetric efficiency. They concluded that energy-based hydrogen fraction up to 14% enhances the engine's performance and reduces emissions, whereas hydrogen over that fraction in the blend has a negative effect. Besides, the energy-based hydrogen fraction with 7% allowed a 40% reduction in soot emissions, 33% reduction in CO at a 9 Nm engine load. Das et al. (2022) investigate the hydrogen enrichment in a diesel engine by introducing flow rates of 7 L/min and 10 L/min of hydrogen to diesel, palm diesel, and blending fuel of diesel and palm biodiesel. They reported that the hydrogen addition with a 10 L/min flow rate to the palm biodiesel shows the most improvement in the combustion, emissions, and the engine's performance, which are a 20% decrease in brake specific fuel consumption, the reductions in hydrocarbon (HC), CO, and CO_2 emissions by 16%, 35%, and 12%, respectively. On the other hand, it was found that NOx increased by 13% compared to that of pure palm biodiesel.

Based on research in the literature, it is clear that the addition of hydrogen reduces carbon-based emissions, CO_2, CO, and HC, as hydrogen fuel doesn't contain carbon elements. However, as understood from the studies mentioned above, the NOx emission may have both increasing and decreasing trends when hydrogen is added; however, most of the research resulted in increasing NOx emissions. The NOx formation occurs by the reaction of nitrogen (N_2) in the mixture, at high temperature region in a combustion chamber. In particular, over 1800 K, the NOx formation exponentially increases (Çeper&et al., 2017; Maurya&et al., 2011). The prompt reactions also contribute to NOx formation at high temperature (Ali&et al., 2020) Thus, in general, it can be stated that the NOx formation stems from combustion temperature, and complex turbulent flow regime inside a combustion chamber (Wang&Yang, 2024). The addition of H_2 results in an increase in combustion temperature and flame propagation rate due to its high heating value and high flame velocity. Cellek and Pınarbaşı (2018) conducted a numerical study of combustion of natural gas-hydrogen blend in low-swirl industrial combustion boiler. They showed that high temperature zones expanded with the increase in H_2 fraction in the mixture. Cozzi and Coghe (2026) evaluated the effect of the addition of H_2 on a natural-gas swirl-stabilized flame. They observed a significant change in the flow field and flame structure, and a temperature increase near the flame front and the burner head caused the thermal NOx formation.

A lean hydrocarbon-air mixture has low flame stability since flame speed becomes so low that it may not be ignited (Ghazal&et al., 2024). The significant advantage of using hydrogen with hydrocarbon fuels is that it allows combustion in a lean mixture (Tunestal&et al., 2002). The addition of hydrogen increases the laminar burning velocity and the flame temperature, which in turn stabilizes flame propagation (Zhang&et al.,2009) Wang et al. (2014) stated that the engine fuelled with a gasoline-hydrogen blend can operate smoothly at a high excess air ratio, in contrast the gasoline-fueled engine suffers from cyclic variation due to low burning velocity and even incomplete combustion engine cycles. Penaranda et al. (2018) investigated the effect of hydrogen additions ranging from 5-10 % on port-injected methane-fueled SI engine in both stoichiometric and lean mixture conditions. They reported that hydrogen accelerates the first combustion phase and increases in-cylinder pressure by promoting early flame kernel expansion, in particular at over 10% concentration of hydrogen. It is also found that a higher concentration in the blend results in increasing NOx emissions at stoichiometric conditions. However, at lean conditions, NOx emissions considerably decreased, and the NOx concentration was found to be nearly negligible at an excess air ratio of 1.4.Thus, using hydrogen in a lean mixture reduces the amount of hydrocarbons used in the blend and may result in lower NOx formation due to low-temperature combustion in lean mixtures.

Hydrogen addition in a diesel engine is a prominent research subject as it has the potential to reduce the particulate matter (PM) and soot emissions, which are significant issues in diesel engines.

PM and soot emissions form primarily due to heterogeneous mixture distribution which is fuel-rich regions in the combustion chamber. Introducing hydrogen to diesel engine can reduce PM emission by means of decreasing the amount of diesel fuel injected into cyclinder. Thus, reducing diesel fuel rate brings about fewer fuel-rich regions, which result in lower PM and smoke emissions (Hosseini&et al., 2023; Liew&et al., 2010). Karagöz et al. (2016) investigated the emission formation on a diesel engine at a constant engine speed of 1100 rpm and full load by varying the energy amounts supplied by hydrogen fuel. They reported that the most improvements were attined in CO by 69.2% and smoke emissions by 58.6%. Bose and Maji (2009) conducted the experimental study to evaluate the diesel-hydrogen blend in a diesel engine at an constant speed of 1500 rpm and a engine power of 5.2 kW. The also used two different exhaust gas recirculation (EGR) rates in their study. They demonstrated that the best result was obtained at a diesel-hydrogen blend without EGR. On the other side, the diesel-hydrogen blend drastically increased NOx concentrations without EGR. Similarly, Zhao et al. (2020) found a decrease in NOx emission by using EGR in their experimental study on the isobutanol-gasoline spark ignition (SI) engine. They also stated that introducing hydrogen during EGR operation, combustion stability was improved.

The addition of hydrogen can also be considered to be a solution for improvement in combustion stability of biogas fuels, which have low calorific values. Although biogas is an alternative and sustainable fuel it mainly includes CH_4 (70% to 50% by volume) and CO_2 (%30 to 50% by volume) (Moghaddam&et al., 2015; Korbag&et al., 2021). Therefore, the concentration rate of CO_2 in biogas influences the calorific values of the biogas, and combustion characteristics like flame stability. Benaissa et al. (2021) numerically investigated the combustion characteristics of biogas-hydrogen blend by considering biogas content consisting of 60% CH_4 and 40%

CO_2 (v/v). They found that hydrogen addition, even a small amount, enhances the low-temperature combustion characteristics. Moreover, the laminar flame speed was determined to be two to three times higher in high-temperature conditions, which in turn increases the overall reactivity. Similarly, Zhen et al. (2014) stated that adding hydrogen allows flame stability in biogas combustion, in their study.

A literature survey reveals that hydrogen addition to hydrocarbon fuels is a prominent strategy for decarbonization and sustainability, as it reduces carbon-based emissions and the amount of hydrocarbon fuels used. Additionally, thanks to its superior properties, an improvement in the combustion process can be achieved in lean or highly diluted mixtures, as well as for fuels with lower heating values. In this regard, it should be noted that the laminar flame speed, adiabatic flame temperature, and flammability limit are the significant properties of a fuel. However, these distinctive properties change with mixture properties, which are stoichiometric, lean, rich mixtures, and/or diluted by EGR, in a combustion chamber. The current research presents a numerical study predicting the adiabatic flame temperature of hydrocarbon-hydrogen blends, depending on equivalence ratio (ϕ), C/H atomic ratio of hydrocarbon fuels, and hydrogen ratio by volume in the fuel blends. To predict the adiabatic flame temperature, the Gaussian Process Regression method was used using the data obtained with chemical-equilibrium-based combustion reactions.

MATERIAL AND METHODS

This research models the prediction of adiabatic flame temperature for hydrocarbon and hydrogen fuel mixtures by using Gaussian Process Regression (GPR). Therefore, the dataset was first created by obtaining values from the chemical-equilibrium combustion approach. The obtained values were then applied to the

GPR model, which involves training and testing processes. These processes were presented in the following subsections.

Creating the Dataset

To establish the data of adiabatic flame temperature, the combustion reaction given in Equation 1 was considered. In the equation, v_1 to v_{10} are the mole numbers, S is the stoichiometric mole number of air. ϕ is the equivalence ratio, and f denotes the hydrogen fraction in blends. The mole numbers, which are temperature and pressure-dependent (v_i (T, P)), were calculated based on the chemical equilibrium approach by adding six gas-phase equilibrium reactions as in Reference (Yıldız, 2024). Thus, the adiabatic flame temperature was determined by considering that the enthalpies of reactants and products are equal to each other, which is based on the first law of thermodynamics. The solution process was carried out by using the Matlab program, coded by Yıldız (2024).

$$\begin{aligned}(1-f)C_mH_n + fH_2 + \frac{S}{\phi}(O_2 + 3.773N_2) \\ \rightarrow v_1CO_2 + v_2CO + v_3H_2O + v_4H_2 + v_5O_2 \\ +v_6N_2 + v_7H + v_8O + v_9NO + v_{10}OH \qquad (1)\end{aligned}$$

Based on Equation 1, at a constant pressure and a certain temperature of reactants in the reaction, the adiabatic flame temperature depends on the C/H atomic ratio (*m/n*), hydrogen fraction (*f*), and the equivalence ratio (ϕ). Thus, by considering different levels of these variables, the adiabatic flame temperature values were calculated to create a dataset. The hydrocarbon fuels selected were methane (CH_4), ethane (C_2H_6), propane (C_3H_8), and octane used as a surrogate for gasoline, as these are conventional fuels and mostly evaluated by mixing hydrogen in the literature (Erdemir&et al., 2025; Aravindan&et al., 2024; Li&Yang, 2025). The equivalence ratio was considered in the range of 0.5 to 1.4, since local regions in a combustion chamber, which have different equivalence ratios, can occur, such as rich, stoichiometric and lean mixture zones.With their levels, a dataset of 360 samples was generated, as summarized in Table 1, which presents the variables for input parameters with their ranges and levels.

Table 1. The input parameters used for creating the data

Independent variable	Range/value	Level
C/H ratio	0.25, 0.33, 0.38, 0.41	4
Equivalence ratio-ϕ	0.5 to 1.4	10
Hydrogen fraction-*f*	0 to 0.4	9

Gaussian Process Regression: Mathematical Formulation

In this research, Gaussian Process Regression (GPR) was used to predict the adiabatic flame temperature. GPR is a probabilistic regression method capable of capturing nonlinear relationship (Chen&et al., 2013). The GPR use a kernel function to define the covariance structure between independent and dependent variables. Unlike other regression, the GPR predict probability distribution over a function (Huaiping&et al., 2017). In the present study, the atomic C/H ratio (x_1), equiavelance ratio (x_2), and hydrogen fraction (x_3) are input variables and the adiabatic flame temperature (y) is a dependent variable.

Thus, the general form of the GPR model is given in the following equation.

$$y_i = f(x_i) + \epsilon_i \tag{2}$$

In this equation, y_i is observed output-dependent variable, $f(x_i)$ is the value of latent function corresponding to x_i, and this function is obtained from Gaussian Process. ϵ_i is observation noise, and it is assumed to be independent and identically distributed with a Gaussian distribution as $\epsilon \sim \mathcal{N}(0, \sigma_n^2)$. σ_n^2 is noise variation.

The latent function *f(x)* is modeled as a Gaussian Process ($\mathcal{GP}$), defined by a mean function m(x) and kernel function $k(x, x')$ as follows (Schulz&et al., 2018).

$$f(x) \sim \mathcal{GP}\left(m(x), k(x, x')\right) \tag{3}$$

The kernel function determines the smoothness and correlation structure of the predicted function. In the current study, the Squared Exponential kernel function was employed, as it assumes that the underlying function is infinitely differentiable, which makes it suitable for smooth and continuous physical problems (Reyes&et al., 2018).

The kernel function is defined as follows.

$$k(x, x') = \sigma_f{}^2 \exp\left(-\frac{1}{2}(x - x')^T \ell^{-1}(x - x')\right) \tag{4}$$

In Equation 4, σ_f denotes the signal variance or standard deviation. The x and x' represent two input points, and compared by the kernel function, the ℓ is the individual length scales for each independent variable (x_1, x_2, x_3), which are optimized during training. They can be defined for three input vector ($x_1 \in \mathbb{R}^n, x_2 \in \mathbb{R}^n, x_3 \in \mathbb{R}^n$) as follows.

For complete input vector form;

$$x = \begin{bmatrix} x_1 \\ x_2 \\ x_3 \end{bmatrix} \in \mathbb{R}^3 \tag{5}$$

and,

$$x = \begin{bmatrix} x_1 \\ x_2 \\ x_3 \end{bmatrix}, \qquad x' = \begin{bmatrix} x_1' \\ x_2' \\ x_3' \end{bmatrix} \tag{6}$$

The length scales become in matrix form:

$$\ell = \begin{bmatrix} I_{n1}\ell_1^2 & 0 & 0 \\ 0 & I_{n1}\ell_1^2 & 0 \\ 0 & 0 & I_{n1}\ell_1^2 \end{bmatrix} \tag{7}$$

Thus, the terms in the exponent function given in Equation 4 is written by the following expression,

$$(x - x')^T \ell^{-1} (x - x') = \frac{\|x_1 - x_1'\|^2}{\ell_1^2} + \frac{\|x_2 - x_2'\|^2}{\ell_2^2} + \frac{\|x_3 - x_3'\|^2}{\ell_3^2} \tag{8}$$

By substituting Equation 8 into Equation 4, the kernel function becomes as in Equation 9.

$$k(x, x') = \sigma_f{}^2 \exp\left(-\frac{1}{2} \left(\frac{\|x_1 - x_1'\|^2}{\ell_1^2} + \frac{\|x_2 - x_2'\|^2}{\ell_2^2} + \frac{\|x_3 - x_3'\|^2}{\ell_3^2} \right) \right) \tag{9}$$

Prediction process

The GPR model was first trained by the data for posterior distribution of the latent function *f*. In this process, the hyperparameters ($\theta = \{\sigma_f^2, l_1, l_2, l_3, \sigma_n^2\}$) of the model requires to be optimized. The hyperparameters were optimized automatically into Matlab algorithm with the related option for the GPR model.

For new test data point x_* , the predicted dependent variable y_* is determined by Gaussian distribution and the predictive variance σ_* as follows.

$$p(y_* | x_* , x, y) = \mathcal{N}(y_*, \sigma_*^2) \tag{10}$$

The mean predicted value of y_*,

$$y_* = k_*^T (K + \sigma_n^2 I)^{-1} y \tag{11}$$

and, the variance σ_*,

$$\sigma_*^2 = k(x_*, x_*') - k_*^T (K + \sigma_n^2 \, I)^{-1} \, k_* + \sigma_n^2 \tag{12}$$

where k_*, kernel function vector between test point and all trained points as follows.

$$k_* = [k(x_1, x_*), \dots, k(x_n, x_*)]^T \tag{13}$$

The kernel function matrix (covariance matrix) *K* is expressed for *n* number of points as the following form.

$$K = \begin{bmatrix} k(x_1, x_1) & \dots & k(x_1, x_n) \\ . & \dots & . \\ . & \dots & . \\ . & \dots & . \\ k(x_n, x_1) & \dots & k(x_n, x_n) \end{bmatrix} \tag{14}$$

The pseudo-code of the algorithm executed for the GPR model is presented in Table 2.

To evaluate the predictive performance of the GPR, the square root (R^2) and the root mean squared error (RMSE), which are the indicators of the fitting capability of the model, was calculated with the following equations.

$$R^2 = 1 - \frac{\sum(y - y_*)^2}{\sum(y - \bar{y})^2} \tag{15}$$

and

$$RMSE = \left(\frac{1}{n} \sum (y - y_*)^2 \right)^{1/2} \tag{16}$$

RESULTS

In this section, it is dedicated to presenting the GPR model's performance and to reveal the effects of the input variables on the adiabatic flame temperature.

Table 2. The pseudo-code of the algorithm

```
begin
% Load dataset
load('data.txt');
➢   X=data(:,1:3), Y=data(:,4)
% Split data into training and testing
m=length(Y) % determine all observed data number
k=number % input the training data number
i=randperm(m,k); % randomly select the row number for training data
    ➢  %Training dataset
X_tr (j,:)=X(i,:); % inputs
Y_tr(j)=Y(i); % respond
    ➢  %Testing dataset
X_test=X; X_test(i,:)=[ ] % inputs
Y_test=Y; Y_test(i,:)=[ ] %respond
% Gaussian Process Regression
     ➢   Training stage
gprMdl=fitrgp( X_tr,Y_tr,…   % Training dataset
'KernelFunction','ardsquaredexponential',… % Kernel function
'BasisFunction','constant',...  % uses a constant mean
 'Standardize',true,'… % standardizes input variables
OptimizeHyperparameters','auto',…% optimize the hyper parameters-θ
'HyperparameterOptimizationOptions', struct('ShowPlots',false,'Verbose',0)…
  ); % configures the optimization
     ➢   Testing stage
Y_pred = predict(gprMdl, X_test);
% Evaluate performance
R2=1-sum((Y_test-Y_pred).^2)/sum((Y_test-sum(Y_test)).^2);
RMSE=sqrt(mean((Y_test-Y_pred).^2));

% Visualization
end
```

The model performance:

The GPR was trained with the randomly selected 250 samples of the calculated adiabatic flame temperature values dependent on the three variables, the C/H atomic ratio (x_1), *f*-hydrogen fraction (x_2), and ϕ-equivalence ratio (x_3). The remaining 110 samples of data were used for the testing process. The R^2 and RMSE parameters, which are assessed for model performance indicators (D.Caro&et al., 2023) were obtained with highly satisfactory results in both the training and testing processes.

Figure1 illustrates the calculated adiabatic flame temperature by the chemical equilibrium-based combustion model versus predicted temperature values by the GPR model. As shown in the figure, the predicted temperature values are in good agreement with the calculated temperature values, and the R^2 values resulted in 1.0 for both the training and testing processes. The RMSE value in the testing process was found to be higher than that of the training process; however, this RMSE value is still a reasonably adequate value for predicting the temperature values, as it maintains an R^2 value of 1.0.

Figure 1 Calculated versus predicted adiabatic flame temperature

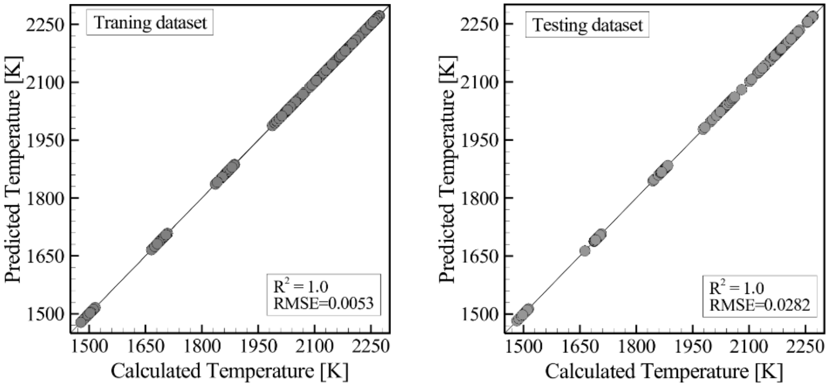

The distribution of the residuals for each sample data point is shown in Figure 2. As expected, the residuals resulted in higher values in the testing data than in the training dataset. Actually, such a result is expected in any algorithm, involving the training and testing process, since the prediction with testing data is executed over the training dataset.

Figure 2 Residuals for the predicted temperature values obtained at the training and testing processes

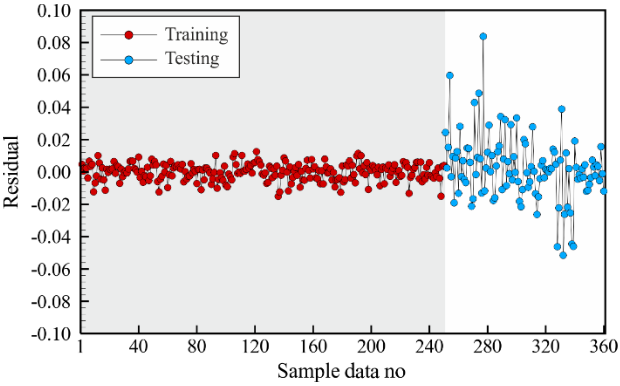

The combination effects of input variables on the adiabatic flame temperature:

Figure 3 shows the adiabatic flame temperature distribution by varying the input variables. Figure 3.a. demostrates the effect of the *C/H* atomic ratio of the hydrocarbon fuel and the fraction of hydrogen in the blends on the adiabatic flame temperature by maintaining a constant ϕ value of 1.0. As shown in the figure, the adiabatic flame temperature is sensitive to both input variables. However, the increases in the temperature values with the increasing *C/H* ratio are higher than with the increasing hydrogen fraction- *f*. Furthermore, the adiabatic flame temperatures reach peak values within the C/H ratio range of 3.5 to 4.0. The maximum temperature was obtained as 2274.47 K at about a C/H value of 0.364 and an *f* value of 0.4. At this C/H ratio of 0.364, the adding hydrogen up to *f*=0.4 led to an 8.47 K increase in temperature values.

Figure 3. The predicted adiabatic flame temperature distribution depending on (a) C/H atomic ratio and f (b) C/H atomic ratio and f, (c) f and ϕ (holding constant values; ϕ = 1.0, f=0.20, and C/H=0.33)

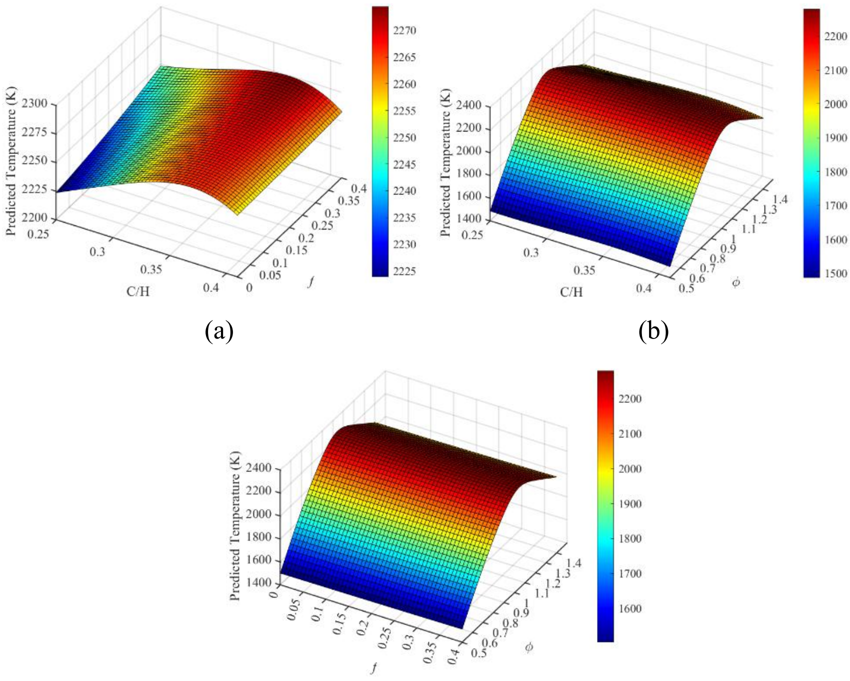

(a) (b)

(c)

Figure 3.b also illustrates the effect of the C/H ratio and ϕ on the temperature values at a constant hydrogen fraction, f = 0.2. The equivalence ratio has a great impact on the adiabatic flame temperature, and the maximum temperature values occurred in the vicinity of ϕ=*1*, corresponding to the stoichiometric air-fuel ratio. Moreover, the temperature values considerably decrease when the air-fuel mixture gets leaner (ϕ<1.0). Similarly, in the rich air-fuel conditions (ϕ >1.0), the temperature values have a decreasing trend due to inadequate oxygen in the combustion reaction. The variation

in temperature values with the equivalence ratio ϕ, are in a similar trend to the literature (Kuntikana&Prabhu, 2019; Gonca&et al., 2024). Considering the effect of the C/H ratio, the peak temperatures values were obtained at about a 0.364 value of the C/H atomic ratio, as in Figure 3.a. At ϕ=1.0, a 35.94 K increase in temperature was obtained from 0.25 to 0.364 values of the C/H atomic ratio.

The effects of f and ϕ on the adiabatic flame temperature are illustrated in Figure 3.c at a constant C/H ratio of 0.33. As the same manner in Figure 3.b, the impact of ϕ is more remarkable. Hydrogen addition (increasing f) gives rise to an increase in temperature values. However, the effect of the hydrogen fraction, f, on the temperature varied with the equivalence ratio- ϕ. The great impact of hydrogen addition on the adiabatic flame temperature was observed in the rich air-fuel mixtures (ϕ<1.0).

CONCLUSIONS

The current chapter presents the adiabatic flame temperature prediction of a hydrocarbon-hydrogen fuel blend by using the Gaussian Process Regression methodology. Initially, the solution of the chemical-based combustion model was used to create the dataset for the adiabatic flame temperature by considering three input variables. Data was, then, divided into two sets for training and testing process by randomly selection. Finally, the GPR was implemented for training and testing processes, respectively. The parameters, R^2 and RMSE, were evaluated to reveal the performance of the GPR. Considering the model performance and the influence of the input variables on the adiabatic flame temperature, the conclusions can be summarized as follows:

- The GPR model estimated the temperature with a remarkable degree of accuracy, as evidenced by R^2 values of 1.0 in both the training and testing stages. Thus, the GPR method enabled the establishment of a strong relationship between the input variables and the adiabatic flame temperature.

- Although the RMSE value during the testing phase showed a relative increase, it remained at a low magnitude.
- The adiabatic flame temperature of hydrocarbon-hydrogen blends is found to be sensitive to the C/H atomic ratio of the hydrocarbon fuel, hydrogen fraction, and equivalence ratio. However, the most effective factor was observed as the equivalence ratio. Besides, the maximum temperatures were attained in the vicinity of ϕ=1.0
- Hydrogen addition shows its great effect on the temperature at the rich air-fuel mixture (ϕ <1.0). At stoichiometric and lean air-fuel mixture, its impact on the temperature increase is lowered.
- The adiabatic flame temperature reached its peak values at the C/H atomic ratio of 0.364 for each equivalence ratio and hydrogen fraction.

REFERENCES

Abdelwahed, S.B., Hamdi, F., Gassoumi, M., Yahya, I., Moussa, N., Alrasheedi, N.H., Ennetta, R., Louhichi, B. (2025) Enhancing diesel engine performance through hydrogen addition. *Fire*, 8(5), 206. Doi: 10.3390/fire8050206

Ali, G., Zhang, T., Wu, W., Zhou,Y. (2020)Effect of hydrogen addition on NOx formation mechanism and pathways in MILD combustion of H_2 – rich low calorific value fuels. *International Journal of Hydrogen Energy*, 15(45), 9200-9210. Doi: 10.1016/j.ijhydene.2020.01.027

Aravindan, M., Kumar, G.P., Arulanandam, M.K., Murali, S., Sheoran, N., Waykole, N., Muthaiah, R., Sharma, P. (2024) Multi-objective optimization and analysis of chemical kinetics properties: Exploring the impact of different hydrogen blending ratios on LPG and methane-air mixtures. *Energy Conversion and Management:X*, 22, 100532. Doi: 10.1016/j.ecmx.2024.100532

Benaissa, S., Adouane, B., Ali, S.M., Mohammad, A. (2021) Effect of hydrogen addition on combustion characteristics of premixed biogas/hydrogen-air mixtures. *International Journal of Hydrogen Energy*, 35(46),18661-18677. Doi: 10.1016/j.ijhydene.2021.02.225

Bose, P.K., Maji, D. (2009) An experimental investigation on engine performance and emissions of a single cylinder diesel engine using hydrogen as inducted fuel and diesel as injected fuel with exhaust gas recirculation. *International Journal of Hydrogen Energy*, 11(34), 4847-4854. Doi: 10.1016/j.ijhydene.2008.10.077

Cellek, M.S., Pınarbaşı, A.(2018) Investigations on performance and emission characteristics of an industrial low swirl burner while burning natural gas, methane, hydrogen-enriched natural gas and hydrogen as fuels. *International Journal of Hydrogen Energy*, 2(43), 1194-1207. Doi: 10.1016/j.ijhydene.2017.05.107

Chen, J., Chan, L.L.T., Cheng, Y-C. (2013) Gaussian process regression based optimal design of combustion systems using flame images. *Applied Energy*, 111, 153-160. Doi: 10.1016/j.apenergy.2013.04.036

Cozzi, F., Coghe, A.(2006) Behavior of hydrogen-enriched non-premixed swirled natural gas flames. *International Journal of Hydrogen Energy*, 6(31), 669-677. Doi: 10.1016/j.ijhydene.2005.05.013

Çeper, B.A., Yıldız, M., Akansu, S.O., Kahraman, N. (2017) Performance and emission characteristics of an IC engine under SI, SI-CAI and CAI combustion modes. *Energy*, 136, 72-79.Doi: 10.1016/j.energy.2016.08.038

D.Caro, D., Ippolito, M., Cannarozza, M., Provenzano, G. Ciraolo, G. (2023) Assessing the performance of the Gaussian Process Regression algorithm to fill gaps in the time-series of daily actual evapotranspiration of different crops in temperate and continental zones zones using ground and remotely sensed data. *Agricultural Water Management*, 290, 108596. Doi: 10.1016/j.agwat.2023.108596

Das, S., Kanth, S., Das, B., Debbarma, S. (2022) Experimental evaluation of hydrogen enrichment in a dual-fueled CRDI diesel engine. *International Journal of Hydrogen Energy,* 20(47), 11039-51.Doi: 10.1016/j.ijhydene.2022.01.125

Erdemir, D., Dincer, I., Patel, D. (2025) Critical experimental evaluation of hydrogen blends with conventional fuels for enhanced power generator performance. *Fuel*, 380, 133226. Doi: 10.1016/j.fuel.2024.133226

Ghazal, R.M., Akroot, A., Wahhab, H.A.A., Alhamd, A.E.J., Hamzah, A.H., Bdaiwi, M.(2024) The influence of gas fuel enrichment with hydrogen on the combustion characteristics of combustors: A Review. *Sustainability,* 16(21), 9423. Doi: 10.3390/su16219423

Gomes, F.A.F., Yang, Y., Talei, M. (2024) Decarbonizing combustion with hydrogen blended fuels: An exploratory study of impact of hydrogen on hydrocarbon autoignition. *Fuel,* 364: 131028.Doi: 10.1016/j.fuel.2024.131028

Gonca, G., Sahin, B., Hocaoglu, M.F. (2024) The effects of equivalence ratio and temperature of different fuel mixtures on the performance and NO emission characteristics of a spark ignition engine. *Arabian Journal for Science and Engineering*, 49, 10431-10452. Doi: 10.1007/s13369-023-08352-0

Gültekin, N., Gülcan, H.E., Ciniviz, M. (2024) Investigation of the effects of hydrogen energy ratio and valve lift amount on performance and emissions in a hydrogen-diesel dual-fuel compression ignition engine. *International Journal of Hydrogen Energy,* 49,Part B, 352-366. Doi: 10.1016/j.ijhydene.2023.07.294

Habib, M.A., Abdulrahman, G.A.Q., Alquaity, A.B.S., Qasem, N.A.A.(2024) Hydrogen combustion, production, and applications: A review. *Alexandria Engineering Journal,* 100, 182-207.Doi: 10.1016/j.aej.2024.05.030

Hosseini, S.H., Tsolakis, A., Alagumalai, A., Mahian, O., Lam, S.S., Pan, J., Peng, W., Tabatabaei, M., Aghbashlo, M. (2023) Use of hydrogen in dual-fuel diesel engines. *Progress in Energy and Combustion Science*, 98(2023), 101100. Doi: 10.1016/j.pecs.2023.101100

Huaiping, M., Zhilhong, L. Xueyao, W. Shi, L. (2017) Temperature distribution measurement using the Gaussian Process Regression Method, *Mathematical Problems in Engineering*, 1(2017), 2147935. Doi: 10.1155/2017/2147935

Ji, C., Cong, X., Wang, S., Shi, L., Su, T., Wang, D. (2018) Performance of a hydrogen-blended gasoline direct injection engine under various second gasoline direct injection. *Energy Conversion and Management,* 171, 1704-1711. Doi: 10.1016/j.enconman.2018.06.112

Karagöz, Y., Güler, İ., Sandalcı, T., Yüksek, L., Dalkılıç, A.S. (2016) Effect of hydrogen enrichment on combustion characteristics, emissions and performance of a diesel engine. *International Journal of Hydrogen Energy*, 1(41), 656-665. Doi: 10.1016/j.ijhydene.2015.09.064

Korbag, I., Mohamed Saleh Omer, S., Boghazala, H., & Ahmeedah Aboubakr Abusasiyah, M. (2021). Recent Advances of Biogas

Production and Future Perspective. Abd El-Fatah Abomohra (Edt.) Biogas-Recent Advances and Integrated Approaches (1-40), IntechOpen. Doi: 10.5772/intechopen.93231

Kuntikana, P., Prabhu, S.V. (2019) Impinging premixed methane-air flame jet of tube burner: thermal performance analysis for varied equivalence ratios. *Heat and Mass Transfer*, 55, 1301–1315. Doi: 10.1007/s00231-018-2507-z

Li, J., Yang, J. (2025) Turbulent flame characteristics of ethane and blends with hydrogen. *Fuel*, 401, 135851. Doi: 10.1016/j.fuel.2025.135851

Liew, C., Li, H., Nuszkowski, J., Liu, S., Gattts, T., Atkinson, R., Clark, N. (2010) An experimental investigation of the combustion process of a heavy-duty diesel engine enriched with H_2. *International Journal of Hydrogen Energy*, 20(35), 11357-11365. Doi: 10.1016/j.ijhydene.2010.06.023

Maurya, R.K., Agarwal, A.K. (2011) Experimental study of combustion and emission characteristics of ethanol fuelled port injected homogeneous charge compression ignition (HCCI) combustion engine. *Applied Energy*, 4(88), 1169-1180. Doi: 10.1016/j.apenergy.2010.09.015

Moghaddam, E.A., Ahlgren, S., Hulteberg, C., Nordberg, A. (2015) Energy balance and global warming potential of biogas-based fuels from a life cycle perspective. *Fuel Processing Technology*, 132, 74-82. Doi: 10.1016/j.fuproc.2014.12.014

Penaranda, A., M.Boggio, S.D., Lacava, P.T., Merola, S., Irimescu, A. (2018) Characterization of flame propagation during early and late combustion for methane-hydrogen fueling of an optically accessible SI engine. *International Journal of Hydrogen Energy*, 52(43), 23538-557. Doi: 10.1016/j.ijhydene.2018.10.167

Reyes, A., Lee, D., Graziani, C., Tzeferacos, P. (2018) A new class of high-order methods for fluids simulation using Gaussian Process Modelling: One-Dimensional Case. *Journal of Scientific Computing*, 76, 443-480. Doi: 10.1007/s10915-017-0625-2

Schulz, E., Speekenbrink, M., Krause A. (2018) A tutorial on Gaussian process regression: Modeling, exploring and exploiting functions, *Journal of Mathematical Psychology*, 85, 1-16. Doi: 10.1016/j.jmp.2018.03.001

Tang, C., Zhang, Y., Huang, Z. (2014) Progress in combustion investigations of hydrogen enriched hydrocarbons. *Renewable and Sustainable Energy Reviews*, 30, 195-216. Doi: 10.1016/j.rser.2013.10.005

Tunestal, P., Christensen, M., Einewall, P., Andersson, T., Johansson, B., Jönsson, O. (2002) Hydrogen addition for improved lean burn capability of slow and fast burning natural gas combustion chambers. *SAE Technical Paper* 2002-01-2686. Doi: 10.4271/2002-01-2686

Wang, S., Ji, C., Zhang, B., Zhou, X. (2014) Analysis on combustion of a hydrogen-blended gasoline engine at high loads and lean condition. *Energy Procedia*, 61, 323-326. Doi: 10.1016/j.egypro.2014.11.1116

Wang, Z., Yang, X.(2024) NOx formation mechanism and emission prediction in turbulent combustion: A.Review. *Applied Science*, 14(14), 6104. Doi: 10.3390/app14146104

Yıldız, M. (2024) Chemical Equilibrium based combustion model to evaluate the effect of H_2 addition to biogases with different CO_2 contents. *International Journal of Hydrogen Energy*, 52, Part B, 1334-1344. Doi: 10.1016/j.ijhydene.2023.06.077

Zhang, Y., Wu, J., Ishizuka, S. (2009) Hydrogen addition effect on laminar burning velocity, flame temperature and flame stability of planar and a curved CH_4 – H_2 – air premixed flame. *International Journal of Hydrogen Energy*, 1(34), 519-527. Doi: 10.1016/j.ijhydene.2008.10.065

Zhao, L., Su, X., Wang, X. (2020) Comparative study of exhaust gas recirculation (EGR) and hydrogen-enriched EGR employed in a SI engine fueled by biobutanol-gasoline. *Fuel*, 268, 117194. Doi: 10.1016/j.fuel.2020.117194

Zhen, H.S., Leung, C.W., Cheung, C.S. (2014) A comparison of the heat transfer behaviors of biogas-H_2 diffusion and premixed flames. *International Journal of Hydrogen Energy*, 2(39), 1137-1144.

CHAPTER 7

A Performance, Cost, and Sustainability of Electric and Internal Combustion Engine UAVs

Öztürk Özdemir KANAT [1]
Yasin ÖZCAN [2]

1. Introduction

In the past years, UAVs have quickly become a revolutionary technology in the civilian and military sector and have revolutionized many industries. UAVs have a high degree of maneuverability, low operational costs, and they can be used to reduce the number of employees that work in dangerous settings; thus, they find numerous applications, which include agriculture, disaster management, logistics, environmental monitoring, and security operations (Kanat, 2023). Especially with the integration of advanced sensor systems and autonomous flight software, UAVs offer more accessible and effective solutions for tasks where traditional aircraft are insufficient or too expensive.

---

[1] Asst. Prof. Aircraft Maintenance And Repair/School of Civil Aviation, Kastamonu University, Türkiye, Orcid: 0000-0001-7914-0871

[2] Asst. Prof. Mechanical Engineering/Faculty of Engineering and Architecture, Kastamonu University, Kastamonu, Türkiye, Orcid: 0000-0003-3462-3735

In this regard, the bibliometric review carried out to investigate the trends in the literature yielded a keyword map example in Fig 1. The concepts that the map represents are that of energy efficiency, energy consumption, and trajectory optimization. This shows that sustainability, performance, and cost-related researches on UAVs have gained a top priority in UAV studies.

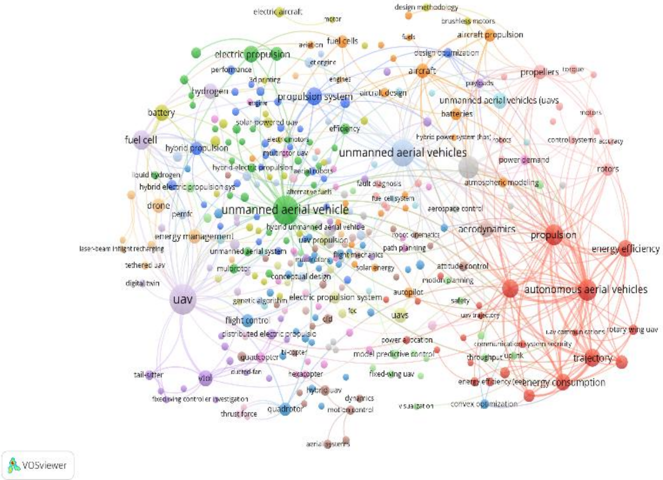

Fig.1. *Keyword relationships and research trends in the UAV literature*

The propulsion systems fitted in UAVs are important determinants of performance in the aircraft. The more popular today are the electric motors and the internal combustion engines. The efficiency of the electric motors is high with low maintenance, silent characteristics, and zero emissions (Yacef et al., 2017). Within its limited energy density, however, there is a problem that limits battery use a mission that needs to contain large payloads and extensive distances (Dehghani-Sanij et al., 2019). The internal combustion engines also have high energy density and long-range working capabilities, which makes them applicable in long distance tasks; yet, the internal combustion engines also have their share of demerits, in that they are more costly to maintain, consume a lot of fuel, and release a lot of carbon emissions. Comparisons of these two systems are strategic in two fronts; firstly, compared to other systems on an engineering front and secondly on the economic front of efficiency and sustainability. Specifically, the effects of costs of energy use, maintenance and purchase costs aspects have a significant overall influence on overall operating costs of the terminal in the long run. Additionally, the environmental impacts of UAVs are not limited to the usage phase. According to researchers (Yowtak et al., 2020), environmental impact varies considerably over the life cycle assessment of UAVs when battery manufacture, carbon intensity of the energy source, and weight capacity of a payload increase. This points to the importance of the inclusion of production and post-use processes in sustainability assessments.

In recent years, studies on hybrid-electric UAV systems have increased significantly in the literature. Duy & Kim, (2020) explored the hybrid-electric propulsion system and renewable energy integration where renewable energy-based hybrid solutions provided highly beneficial effects in the case of long-duration flights. Their work has, however, indicated that the existing battery energy density and hydrogen storage facilities inhibit the widespread adoption of the system. These findings indicate that in UAV research, it is no longer sufficient to compare only electric and internal combustion systems; hybrid, hydrogen fuel cell, and solar-powered alternatives must also be considered from a sustainability perspective. Research on UAV propulsion systems is not limited to electric and internal combustion engines. Recently, gas-powered fan propulsion systems have also gained attention in fixed-wing VTOL platforms. Zhu et al., (2025) found that gas-powered fans offer higher power density and longer range advantages compared to electric motors. However, while such systems have high energy density, they are noted to have disadvantages compared to electric solutions in terms of fuel consumption and environmental impacts. This finding highlights the need to consider not only current solutions but also alternative concepts expected to develop in the future when selecting power systems. This study aims to provide a comparative analysis of electric motor-powered and internal combustion engine-powered UAVs within the performance, cost, and sustainability triangle. Thus, it seeks to offer an evaluation of propulsion system selection for different mission scenarios, considering technical, economic, and environmental dimensions.

2. Performance Analysis

2.1. Power, range, endurance, load capacity

Basic performance requirements that are used to gauge operational effectiveness of an UAV are power generation, range, endurance and payload mass (Austin, 2010). These standards are correlated to the kind of propulsion machine as well as energy source employed. The use of electric motor systems is characterized by a high level of torque, quick response time, as well as 90% energy savings (Yacef et al., 2017). Nonetheless, batteries have a low energy density (150-300 Wh/kg) that restricts their use in missions with long range and heavy payload capacity (Dehghani-Sanij et al., 2019). Hence, electric UAVs are more commonly used on short- and medium-range missions involving reconnaissance, mapping and surveillance that are not power-intensive. Systems of internal combustion engines, in their turn, usually have an energy efficiency of about 30% (Heywood, 2018). Thanks to the high energy density of fuel (~12,000 Wh/kg), much longer flight times and ranges can be achieved. The uses of these traits include the ease of using them as part of the logistics transportation, wide-area scanning, and heavy-load transport missions, but more vibration, more noise, and more maintenance needs restrict the sensitive-work operations.

2.2. Advantages and Disadvantages According to Task Scenarios

Electric motor systems are preferred for short-range and light-load applications due to their low cost and quiet operation. But when the need is long-range transportation and heavy load transportation, then the internal combustion systems have better performance because of their high energy density. Electric systems demand fewer maintenance requirements and can interrogate longer at a time, which enable them to be applied in continuous monitoring applications (e.g., border surveillance), but may need additional stations because of their range limitations. Internal combustion systems find favor in tasks that require quick response like emergency service and disaster logistics, since the time needed to refuel is minimal, and that powered by these tools can have longer flight times. With this respect, it can be said that there is no single optimum system in the context of performances and the specific task demands are the determinant of the selection of the technology.

According to the task scenarios, each propulsion technology presents distinct advantages and limitations. Table 1 shows that electric UAVs favor short-range, low-payload, and low-noise missions, while internal combustion UAVs excel in long-range and heavy-load tasks.

Table 1. Advantages and Disadvantages According to Task Scenarios

Task Scenario Aspect	**Electric UAVs**	**Internal Combustion UAVs**
Short-Range Missions	Advantage	Disadvantage
Long-Range Missions	Disadvantage	Advantage
Light Payload Tasks	Advantage	Disadvantage
Heavy Payload Tasks	Disadvantage	Advantage
Stealth / Low-Noise Ops	Advantage	Disadvantage
Continuous Monitoring	Advantage	Limited by fuel logistics
Emergency / Rapid Response	Disadvantage	Advantage (fast refueling)

3. Cost Analysis

The cost-effectiveness of an UAV is evaluated based on initial investment costs, operating costs, and total cost of ownership (TCO) (Phillips et al., 2016). In fact, despite the initial investment cost disadvantage, the combined energy and maintenance costs make internal combustion engines more expensive to operate than electric motors. Dianovský et al., (2024) reported that electric motors consume 0.11 euro per hour with an efficiency of 90 percent whereas internal combustion engines use 0.54 euro per hour with an efficiency of 30 percent. The cost of energy is an important consideration, particularly for long-haul flights, since it has a direct influence on total operating costs. Electric propulsion can be very affordable, especially in situations where energy costs are a major issue. When evaluated in terms of maintenance costs during price analysis, maintenance expenses were calculated based on the frequency and complexity of activities needed for each propulsion system, including inspections, component replacements, and repairs. The cost of maintenance is fairly low compared to mechanical systems due to the fewer mobile components (Zhang et al., 2022).

Although internal combustion systems are superior in terms of ranged application and weight capacity, their maintenance and energy costs are too high leading to high overall operating costs. Electric UAVs are, however, more economically beneficial in the long term, because they are low-cost in terms of energy and maintenance (Zhou, 2025). The internal combustion systems are however tempting in the short term because they have nominal initial investment cost. Electric systems are, according to TCO perspective, a more affordable long-term operating solution overall, but it can also vary due to the mission scenario and conditions. Saif & Eminoglu, (2023) examined both the scientific research and industrial production dimensions of hybrid power systems in multi-rotor UAVs and emphasized that hybrid solutions have significant potential, particularly in increasing range and operational time. However, they also noted that hybrid systems bring integration complexity and additional costs. In this context, although electric UAVs continue to have constraints in cargo capacity and flight time, major prospects for improving endurance and lifting capabilities remain. Hybrid power systems are critical to these improvements because they increase available power while maintaining high overall efficiency primarily by raising the power-to-weight ratio and decreasing SFC. However, combining several power sources adds complexity, necessitating extra optimization in power control, management, and storage to assure consistent propulsion and effective use of surplus energy. Table 2 provides a concise comparison of electric and internal combustion UAV propulsion systems, summarizing the key differences in cost, efficiency, maintenance requirements, and operational performance based on the findings discussed above.

Table 2. Short Comparison of Electric vs. Internal Combustion UAV Propulsion Systems

Criteria	**Electric UAVs**	**Internal Combustion UAVs**
Operating Cost	Very low	High
Energy Cost (€/h)	~0.11	~0.54
Efficiency	High	Low
Maintenance	Low	High
Range / Endurance	Limited	Very high
Payload Capacity	Low	High
Initial Cost	Moderate–High	Low
TCO (Long Term)	More economical	More expensive
Main Limitation	Range & payload	Operating cost

4. Sustainability and Environmental Impact

Sustainability is not restricted to the emissions produced during the operations of the UAV technologies, it constitutes multiple aspects including the sources of energy operated in, production process, maintenance and recycling of end-life systems. Thus, it is important to determine carbon footprint, noise level productions, material lifecycle, and percentage of renewable energy source of the propulsion systems to have a better view of their long term environmental impacts. According to Yowtak et al., (2020), the high has a lower energy consumption and emissions impact than ICEVs over the vehicle use stage, but higher than in BEVs. The value of renewable energy source ratio is important due to this finding.

4.1. Carbon Footprint Comparison

During operation, Electric UAVs generate no direct CO_2 emissions. However, electricity used is also a determining factor of the advantage extent. Electricity that uses renewable sources (solar, wind) contributes most to the reduction of a carbon footprint, whereas electricity made by fossil sources may constrain such effect. Internal combustion engines in contrast, spew CO_2 and other greenhouse gases to the air because of the combustion of fuel during use(Heywood, 2018).

4.2. Noise Emission

Electric motors are considerably quiet than internal combustion engines because of their small and limited number of moving components and the high torque value at higher engine speeds (Zhang et al., 2022). This offers a great deal in the area of acoustic signatures, especially in cities, animal spotting, or military surveillance activities. Internal combustion engines, in contrast to these, however, are associated with a lot of noise pollution since they have faster combustion and exhaust noises.

4.3. Battery Production, Service Life, and Recycling

The extraction and processing of minerals like lithium, cobalt and nickel are needed in the processes involved in making the battery systems that are used in the electric UAVs (Nguyen-Phuoc et al., 2025). These procedures are considered to be risky to the environment in terms of their energy intensive process of mining and waste disposal (Harper et al., 2019). The battery life cycle is normally 500 to 1000 charge cycles depending on the circumstances under which it will operate. It is significant to recycle end-of-life batteries to avoid environmental pollution as well as to allow the reuse of valuable metals.

4.4. Fossil Fuel Production, Storage, and Logistics Impacts

The manufacture of gasoline or diesel fuels that are used as internal combustion and engines as an activity entails various processes. This involves a lot of emitted carbon emissions before any operation has started. Also, the transportation and origin of the fuel, especially in remote places, are logistical difficulties and an additional threat to the environmental situation (leaks, evaporation).

4.5. Renewable Energy Source Ratio

The sustainability potential of electric UAVs is directly related to the renewability rate of their energy source. According to IEA, (2022) data, more than 30% of global electricity production comes from renewable sources, and this percentage is expected to increase over the next 10 years. Internal combustion engines, on the other hand, are directly dependent on fossil fuels, which creates a more fragile structure in terms of energy supply security and climate goals.

4.6. Long-Term Environmental Risks

The greatest environmental risk of electric systems is battery waste management and ethical and ecological issues in raw material supply chains. In internal combustion systems, on the other hand, there is continuous emission production depending on fuel consumption. In the long term, electric systems have the potential to significantly reduce their environmental impact through advancements in energy storage and recycling technologies (Dehghani-Sanij et al., 2019). In general, electric UAVs have a much lower carbon footprint, operate silently, and have the potential for renewable energy integration. Internal combustion systems, despite their energy density and long-range advantages, create high environmental impacts both during operation and in the fuel production chain. Therefore, electric systems clearly stand out in tasks where sustainability is a priority. Table 3 summarizes the key sustainability-related factors for electric and internal combustion UAV systems, highlighting their differences in carbon emissions, noise levels, production impacts, energy sourcing, and long-term environmental risks.

Table 3. Summary of Key Sustainability Factors for UAV Propulsion Systems

Sustainability Factor	**Electric UAVs**	**Internal Combustion UAVs**
Carbon Footprint Comparison	No direct CO_2 emissions; depends on renewable electricity	High CO_2 and GHG emissions from fuel combustion
Noise Emission	Very low; minimal acoustic pollution	High noise from engine and exhaust
Battery Production, Service Life, and Recycling	Requires lithium-ion minerals; 500–1000 cycles; recycling essential	No battery lifecycle issues, but continuous fuel use has cumulative impacts
Fossil Fuel Production, Storage, and Logistics Impacts	None for operation; electricity source matters	High upstream impact (extraction, refining, transport)
Renewable Energy Source Ratio	Can use renewable electricity; improves sustainability	Fully dependent on fossil fuels
Long-Term Environmental Risks	Battery waste and mining ethics; potential improvement with technology	Continuous emissions; long-lasting environmental burden

5. Conclusion and Discussion

This paper evaluates the performance comparisons, costs and sustainability of the electric motor powered and internal combustion engines powered UAVs. Electric systems have the benefits of a low total cost of ownership, as the energy cost and maintenance cost is lower, and it provides a relatively cheap, quiet, and environmentally friendly alternative to fossil-powered propulsion at short- and medium-range missions. Internal combustion engines on the other hand exhibit an advantage in long-range and heavy-load performance because of their high energy density; but are not favorable in the long-term because of the maintenance costs and emissions. Other viable options encompass the hybrid systems, solar power platforms, hydrogen fuel cells/gas-powered concepts. These technologies can provide an advantage in particular mission situations, but they continue to be limited in cost, infrastructure demands and environmental costs. Also, new strategies, including AI-based fuel and route optimization, could increase the efficiency of energy and minimize emissions, especially in the cases of internal combustion and hybrid vehicles.

Electric and internal combustion propulsion technologies exhibit significant differences in terms of energy density, operational efficiency, cost structure, environmental performance, and mission suitability. In order to summarize these distinctions holistically, a comparative table has been constructed based on the performance, cost, and sustainability metrics adopted within the scope of this study. The table compiles the most essential characteristics of both propulsion systems, including specific energy (Wh/kg), propulsion efficiency, endurance capability, payload capacity, hourly operational cost, maintenance requirements, emission profile, and renewable energy integration potential.

As shown in Table 4 electric propulsion systems provide high efficiency, low noise, lower maintenance cost, and zero direct emissions, making them suitable for short- and medium-range missions and environmentally constrained operations. However, limited battery energy density restricts endurance and payload capacity. Conversely, internal combustion engines offer superior range and payload capabilities due to their substantially higher energy density, yet they suffer from higher fuel consumption, increased maintenance requirements, and significant greenhouse gas emissions.

Table 4. Comparative Evaluation of Electric vs. Combustion-Powered UAVs

Feature / Criterion	**Electric-Motor UAV**	**Internal Combustion Engine UAV**
Propulsion efficiency	High, around ~90%	Lower, around ~30%
Flight endurance / range	Suitable for short–medium-range missions; struggles at long range	Clear advantage in long-range and long-endurance flights
Payload capacity	Better for light–medium payloads (battery mass is restrictive)	More suitable for heavy payloads and large-volume cargo
Initial investment cost	Motor is generally cheap; battery cost adds up	Engine alone is not always expensive, but fuel system + maintenance make it more complex
Hourly energy cost	Low (~0.11 €/hour)	High (~0.54 €/hour)
Maintenance cost	Very low—few moving parts, simple upkeep	Many mechanical components → frequent and costly maintenance
Noise	Very low noise and vibration	High noise and vibration from engine and exhaust
Direct emissions	Zero CO_2 emissions during flight	High CO_2 and other emissions due to fuel combustion
Life-cycle impacts	Battery production (Li, Co, Ni) and recycling needed; can be sustainable if managed properly	Fuel production, refining, logistics, and leakage create significant burden throughout the entire chain
Renewable energy integration	Easy to charge with grid or PV; carbon footprint drops sharply as renewable share increases	Directly dependent on fossil fuels; poor compatibility with renewables (biofuel scenario would be separate)
Operational profile	Low operating and maintenance costs; long-term TCO advantage	High fuel + maintenance costs; long-term TCO may be disadvantageous
Typical missions	Mapping, surveillance, environmental monitoring, short/medium-range logistics, low-noise tasks	Long-range logistics, wide-area scanning, heavy-load transport
Main disadvantage	Low energy density → range and payload limitations	High emissions and noise; high fuel and maintenance costs

In conclusion, there is no single best propulsion system. Capabilities that determine selection of the system include mission requirements, payload capacity, operating duration and environmental requirements. Electric systems can be observed in most sustainability- and low-cost-oriented missions, and the internal combustion systems can be found in many long-range missions. Future studies on UAV-related recycling technology of batteries, hybrid power systems, and artificial intelligence optimization will make the UAVs even more sustainable and better performing in the future.

References

Austin, R. (2010). *Unmanned aircraft systems: UAVs design, development and deployment*. Hoboken, NJ: Wiley.

Dehghani-Sanij, A. R., Tharumalingam, E., Dusseault, M. B., & Fraser, R. (2019). Study of energy storage systems and environmental challenges of batteries. *Renewable and Sustainable Energy Reviews, 104*, 192–208.

Dianovský, R., Pecho, P., Bugaj, M., & Jackuliak, J. (2024). Economic efficiency comparison of unmanned aerial vehicles with conventional and alternative propulsion systems. *Transportation Research Procedia, 81*, 307–317.

Duy, V. N., & Kim, H. M. (2020). Review on the hybrid-electric propulsion system and renewables and energy storage for unmanned aerial vehicles. *International Journal of Electrochemical Science, 15*(6), 5296–5319.

Harper, G., Sommerville, R., Kendrick, E., Driscoll, L., Slater, P., Stolkin, R., Walton, A., Christensen, P., Heidrich, O., Lambert, S., Abbott, A., Ryder, K., Gaines, L., & Anderson, P. (2019). Recycling lithium-ion batteries from electric vehicles. *Nature, 575*(7781), 75–86.

Heywood, J. B. (2018). *Internal combustion engine fundamentals* (2nd ed.). New York, NY: McGraw-Hill Education.

International Energy Agency. (2022). *World Energy Outlook 2022*. Retrieved from https://iea.blob.core.windows.net/assets/c282400e-00b0-4edf-9a8e-6f2ca6536ec8/WorldEnergyOutlook2022.pdf

Kanat, Ö. Ö. (2023). The significance of unmanned aerial vehicles (UAVs) in strategic contexts. *Anadolu Strateji Dergisi, 5*(2), 75–87.

Nguyen-Phuoc, D. Q., Su, D. N., Truong, A., Li, Z.-C., & Oviedo-Trespalacios, O. (2025). How do perceptions of risk influence the adoption of electric motorcycles? A theory-based investigation considering the multidimensional nature of risk. *Transportation Research Part F: Traffic Psychology and Behaviour, 109*, 689–710.

Saif, E., & Eminoglu, I. (2023). Hybrid power systems in multi-rotor UAVs: A scientific research and industrial production perspective. *IEEE Access, 11*, 438–458.

Yacef, F., Rizoug, N., Bouhali, O., & Hamerlain, M. (2017). Optimization of energy consumption for quadrotor UAV. In *Proceedings of the International Micro Air Vehicle Conference and Flight Competition (IMAV)* (pp. 215–222). September.

Yowtak, K., Imiola, J., Andrews, M., Cardillo, K., & Skerlos, S. (2020). Comparative life cycle assessment of unmanned aerial vehicles, internal combustion engine vehicles and battery electric vehicles for grocery delivery. *Procedia CIRP, 90*, 244–250.

Zhang, B., Song, Z., Zhao, F., & Liu, C. (2022). Overview of propulsion systems for unmanned aerial vehicles. *Energies, 15*(2), 455.

Zhou, Y. (2025). Unmanned aerial vehicles based low-altitude economy with lifecycle techno-economic-environmental analysis for sustainable and smart cities. *Journal of Cleaner Production, 499*, 145050.

Zhu, Y., Huang, G., Xia, C., & Wu, Y. (2025). Aerodynamic design of fixed-wing VTOL aircraft powered by gas-driven fan propulsion system. *Aerospace Science and Technology, 162*, 110165.

CHAPTER 8

THERMAL AGING IN BUILDING ENVELOPES: A GLOBAL BIBLIOMETRIC MAPPING OF RESEARCH TRENDS

1. KAAN YAMAN[1]
2. FATİH ÜNAL[2]

Introduction

The contemporary understanding of urbanization, shaped by global sustainability goals, mandates that the building stock be not only environmentally friendly and energy-efficient but also capable of maintaining long-term performance durability. Within this context, the concept of thermal aging, situated at the intersection of building physics and materials science, necessitates a re-evaluation of how performance degradation in building envelopes over time impacts both energy efficiency and indoor comfort. Although research on this topic has been increasing in recent years, existing studies predominantly focus on specific material types or controlled test conditions, often lacking the holistic perspective required for macro-level policy development and strategic planning. Therefore,

---

[1] Research Assistant, Mersin University, Mechanical Engineering Department, Orcid: 0000-0002-8627-4082

[2] Assoc. Prof. Dr., Mersin University, Mechanical Engineering Department, Orcid: 0000-0001-6660-9984

interdisciplinary investigations into the causes, mechanisms, and consequences of thermal degradation in building envelopes must be supported by data-driven analytical approaches. This book chapter aims to address this gap by providing a quantitative mapping of the international literature, thereby repositioning the thermal aging phenomenon within the scientific discourse on the built environment.

The Global Energy Crisis and the Responsibility of the Built Environment

The first quarter of the twenty-first century confronts humanity with two simultaneous and interlinked crises: the rapid depletion of fossil fuel reserves and irreversible climate change. According to the latest report by the Intergovernmental Panel on Climate Change (IPCC, 2023), limiting the rise in global temperature to 1.5°C above pre-industrial levels requires a substantial reduction in carbon emissions by the year 2030. Achieving this target necessitates not only a transformation in energy production systems but also radical structural changes at the level of final energy consumption. At the heart of this transformation lies the building sector, which alone accounts for approximately 30% of global energy consumption and 26% of energy-related carbon emissions (International Energy Agency [IEA], 2024). Within the framework of global policy agendas such as the European Green Deal and the United Nations Sustainable Development Goals (SDGs), concepts like "Net Zero Energy Buildings" (NZEB) and "Positive Energy Buildings" (PEB) have evolved from being mere aspirational visions to becoming normative objectives that must be implemented. In this context, high-performance insulation systems that minimize the thermal transmittance of the building envelope have emerged as one of the most effective and cost-efficient passive strategies to enhance both energy efficiency and environmental sustainability. Aditya et al. (2017) emphasize that appropriate insulation applications can reduce heating and cooling loads by 50% to 70%. In a similar vein, Bereketoğlu (2023) conducted a study using the degree-day method to evaluate the regional energy performance of various insulation materials. The study highlighted that selecting materials in accordance with local climatic conditions constitutes a strategic leverage point for minimizing energy losses. Such strategic approaches at the building scale are not limited to passive solutions alone. For example, thermoelectric systems developed by Yaman, Dölek, and Arslan (2022) have demonstrated the potential to recover waste heat, thereby enhancing overall thermal efficiency and mitigating heat loss associated with material aging. This integrative approach not only contributes to reducing energy expenditures but also strengthens the adaptive capacity of buildings in the face of climate change.

In conclusion, high-performance insulation practices have a direct impact not only on theoretical energy efficiency metrics but also on the tangible reduction of the carbon footprint observed in real-world applications (Cabeza et al., 2010).

The Energy Performance Gap and the Thermal Aging Paradox

Current legal regulations and Energy Performance Certificate (EPC) frameworks largely classify buildings based on theoretical data determined during the design phase. However, a recurring issue highlighted in academic literature and real-world building operations is the significant discrepancy between these theoretical values and actual energy consumption-commonly referred to as the “Energy Performance Gap” (De Wilde, 2014). This gap reflects the deviation between projected consumption calculated via energy simulation tools (e.g., EnergyPlus, TRNSYS) and the measured values recorded during the building’s operational phase.

Beyond user behavior and other external variables, one of the most critical technical causes of this discrepancy is the physical and thermal property degradation of building envelope materials over time-commonly known as thermal aging (Jelle, 2011). From a building physics perspective, the thermal conductivity coefficient (λ) of an insulation material should be considered a time-dependent function, denoted as λ(t), rather than a fixed value that evolves in response to environmental conditions. Nonetheless, prevailing design practices still assume that the initial value measured under laboratory conditions remains valid for the building's entire service life. In reality, insulation materials are exposed to a range of environmental stressors in the field -including seasonal temperature fluctuations, high relative humidity, freeze-thaw cycles, and ultraviolet (UV) radiation- which cumulatively induce irreversible microstructural damage (Kumar et al., 2020; Ünal, 2024).

In this context, closed-cell foam insulation materials -such as Polyurethane (PUR), Polyisocyanurate (PIR), and Extruded Polystyrene (XPS)- which are widely used in the modern construction industry, initially exhibit low thermal conductivity due to the presence of low-conductivity blowing agents trapped within their cell structures during manufacturing. However, in accordance with the second law of thermodynamics, these gases gradually diffuse outward through the polymer matrix, while ambient air diffuses inward, irreversibly altering the material's internal gas-phase composition (Mukhopadhyaya et al., 2002). This phenomenon, known as gas diffusion, can lead to a decline in insulation performance by up to 20% within the first 5 to 10 years of service. Consequently, the resulting reduction in thermal resistance not only increases energy consumption and utility costs but also heightens the risk of surface condensation on building envelopes, fosters mold growth indoors, and deteriorates indoor air quality (IAQ). Over the long term, these issues can contribute to significant health risks, including the onset of Sick Building Syndrome (Simmler et al., 2005).

Historical Transformation: From the Montreal Protocol to Nanotechnology

The evolution of thermal aging research is closely intertwined with key historical turning points in materials science. Before the 1990s, chlorofluorocarbon (CFC) gases -despite their detrimental impact on the ozone layer- were widely used as blowing agents in foam insulation materials due to their low diffusion rates. However, the 1987 Montreal Protocol and subsequent environmental regulations led to the banning of CFCs, pushing the insulation industry toward more environmentally friendly, yet inherently more diffusion-prone alternatives such as HCFCs, HFCs, and pentane-based blowing agents (Papadopoulos, 2005). This transition has also had notable implications for refrigeration and cooling systems, where long-term performance losses and energy inefficiencies have been observed throughout the system's lifespan (Çelik, 2024).

This regulatory shift increased the relevance of accelerated aging tests and the need for long-term performance forecasting, leading to a marked increase in related publications in the academic literature beginning in the early 1990s. As the insulation landscape evolved, the early 2000s marked the rise of “third-generation” materials with enhanced thermal capabilities.

Technologies such as Vacuum Insulation Panels (VIPs) and aerogels -commonly referred to as Super Insulation Materials (SIMs)- offer thermal performance 5 to 10 times superior to that of conventional materials. However, these advanced systems are characterized by highly sensitive and complex aging mechanisms. For instance, the micro-perforation of a VIP panel can cause an immediate and irreversible loss of vacuum, thereby rendering its insulation performance ineffective (Baetens et al., 2010).

Consequently, a literature review covering the period from 1990 to 2025 must not be limited to a single class of materials.

Rather, it should comprehensively trace the technological evolution from mineral wool to nanostructured porous insulation, highlighting the shifting paradigms that have shaped the field of thermal aging in building envelopes.

Aim and Original Contribution of the Study

The inherently multidisciplinary nature of thermal aging in building envelopes -encompassing fields such as chemistry, physics, civil engineering, and mechanical engineering- has led to a fragmented and uneven development of the academic literature. Although numerous valuable review papers exist focusing on specific material groups, these studies are largely qualitative in nature and constrained by the subjective selections of individual researchers. In today’s era of accelerated scientific production, identifying overarching research trends, collaboration networks, and knowledge gaps among thousands of publications has become virtually impossible using manual approaches alone. This fragmentation has increased the relevance of big data methodologies and scientific mapping tools in literature analysis. In this context, Sümer (2025) emphasizes that bibliometric methodologies have become essential for accurately analyzing research trends in energy technologies.

This book chapter presents the first comprehensive bibliometric and scientometric study to systematically map the literature on "Thermal Aging in Building Envelopes" covering the period from 1990 to 2025. Drawing on a large-scale dataset retrieved from the Web of Science database, the study applies statistical and visual mapping techniques to address the following key research questions:

1. What is the temporal growth trajectory, and what are the critical turning points in thermal aging research?

2. Which countries, institutions, and authors have emerged as the most influential at the global level?
3. How have the dominant research themes evolved - from laboratory- based experiments to computational simulations and AI-driven applications?

By answering these questions, the chapter aims to assist researchers in identifying unexplored research gaps and formulating new hypotheses, while also providing evidence-based insights for policymakers. In doing so, it advocates for a paradigm shift in building energy regulations-from design-stage "initial performance" metrics to life-cycle-oriented "in-service performance" benchmarks (Zupic & Čater, 2015).

Theoretical Background

The phenomenon of thermal aging in building envelopes constitutes a multilayered problem situated at the intersection of thermodynamic principles in materials science, polymer chemistry, and the environmental boundary conditions of building physics. This section provides a comprehensive overview of the underlying physical mechanisms governing the long-term performance degradation of insulation materials, degradation pathways specific to various material classes, and the mathematical as well as experimental approaches developed in the literature to model these changes over time.

Heat Transfer Mechanisms and Physics of Aging

The performance of an insulation material is characterized by its thermal conductivity coefficient (λ). For a non-homogeneous porous material, the effective thermal conductivity (λ_{eff}) is defined as the superposition of four fundamental heat transfer mechanisms (Jelle, 2011).

$$\lambda_{eff} = \lambda_{solid} + \lambda_{gas} + \lambda_{rad} + \lambda_{conv}$$

These include solid conduction (λ_{solid}), which refers to phonon transfer through the solid matrix of the material -such as polymers or mineral fibers- and is directly proportional to the material's density; gas conduction (λ_{gas}), which arises from the collision of gas molecules within the pores and represents the most dynamic component affected by aging; thermal radiation (λ_{rad}), which accounts for the electromagnetic wave transfer between pore surfaces; and convection (λ_{conv}), which is generally negligible as long as the pore diameter remains below a certain threshold (typically around 4 mm). Thermal aging primarily results from significant changes over time in the λ_{gas} component, and secondarily from physical degradation in the λ_{solid} structure, such as oxidation or moisture absorption.

Gas Diffusion Models and Fick's Law

In closed-cell foams such as polyurethane (PUR), polyisocyanurate (PIR), and extruded polystyrene (XPS), thermal aging is primarily explained by the gradual alteration of the gas phase within the cells. This process consists of two simultaneous fluxes that can be modeled using Fick's Law of Diffusion:

The first is the fast phase, during which atmospheric gases - mainly nitrogen (N_2) and oxygen (O_2)- rapidly diffuse into the foam cells through the polymeric cell walls. The diffusion coefficients of these smaller air molecules are significantly higher compared to those of the larger blowing agents used during manufacturing.

The second is the slow phase, where low-conductivity blowing agents such as HFCs, HFOs, or pentane, initially trapped within the cell structure, gradually diffuse outward over time.

As a result of this bidirectional gas exchange, the thermal conductivity of the gas mixture inside the cells ($\lambda_{gas\text{-}mix}$) exhibits an asymptotic increase-from the initial value corresponding to the pure blowing agent (e.g., ~0.012 W/m·K) toward the thermal conductivity of stagnant air (~0.025 W/m·K) (Mukhopadhyaya et al., 2002).

Knudsen Effect and Nano-Porous Structures

In nanotechnological insulation materials such as Vacuum Insulation Panels (VIPs) and aerogels, heat transfer mechanisms are significantly influenced by the Knudsen Number (Kn). This dimensionless number is defined as the ratio of the mean free path of gas molecules (l_{mean}) to the characteristic pore diameter (d), i.e., $Kn = l_{mean} / d$.

During the aging process, ambient air gradually infiltrates the interior of VIPs, leading to an increase in internal pressure. As the internal pressure rises, the mean free path of gas molecules decreases, and the gas-phase thermal conductivity (λ_{gas}) exhibits a characteristic S-shaped increase (Simmler et al., 2005).

This nonlinear behavior implies that thermal aging in VIPs does not merely result in a gradual decline in performance but may ultimately cause a catastrophic loss of insulation function. Therefore, in such nano-porous materials, aging is directly linked not only to efficiency reduction but also to material failure risk over time.

Aging Characteristics by Material Type

Studies in the literature demonstrate that each category of insulation material exhibits a distinct “aging signature”, reflecting unique degradation patterns and mechanisms over time.

Cellular Plastics (PUR, PIR, XPS, EPS)

These petrochemical-derived materials represent the most commonly used group of thermal insulation products in the construction industry.

Polyurethane (PUR) and Polyisocyanurate (PIR): These materials undergo the most rapid aging phase within the first five years after production. This phenomenon, commonly referred to as thermal drift, results in an increase in the thermal conductivity (λ) from an initial value of approximately 0.022 W/m·K to levels as high as 0.028 W/m·K. According to Belanger and Berardi (2018), PIR boards without diffusion barriers (such as aluminum foil) may lose up to 20–25% of their initial insulation capacity over 25 years.

Extruded Polystyrene (XPS): XPS exhibits a closed-cell structure and undergoes a similar gas diffusion-based aging process as PUR and PIR. However, its higher resistance to water absorption makes it more suitable and durable in moisture-exposed applications (e.g., below-grade foundations, inverted roofs) compared to PUR.

Expanded Polystyrene (EPS): Unlike other cellular foams, EPS contains air-filled cells from the outset, and thus does not experience thermal aging related to gas diffusion. Instead, its aging behavior is predominantly associated with physical dimensional changes and moisture uptake over time.

Fibrous Materials (Mineral Wool, Glass Wool)

Mineral wools do not suffer from gas diffusion-related thermal aging due to their open-pore structures; the voids are inherently filled with air (λ ≈ 0.035–0.040 W/m·K). However, the "Achilles' heel" of these materials is their vulnerability to moisture.

Aging in fibrous insulation materials primarily occurs through two mechanisms:

1. **Gravity-Induced Settling:** In vertical applications (e.g., cavity walls), the insulation can gradually settle downward over time due to its own weight or building vibrations. This displacement leads to the formation of thermal bridges in the upper sections of the wall cavity.

2. **Moisture Accumulation:** The open-pore structure facilitates water vapor condensation within the material. When saturated, the thermal insulation capacity of mineral wool deteriorates drastically-effectively approaching zero (Sanders, 1996).

Advanced Insulation Materials (VIPs, Aerogels)

Vacuum Insulation Panels (VIPs): The service life of VIPs is predominantly determined by the permeability of the envelope material. Even a gradual internal pressure increase of just 1 mbar per year can, over a 25-year projection, lead to the complete loss of the panel's insulating properties. Furthermore, the saturation of internal "getters"—materials used to absorb residual gases—is another factor that accelerates the aging process (Baetens et al., 2010).

Aerogels: Silica aerogels are typically produced with hydrophobic surface treatments to repel moisture. However, prolonged exposure to ultraviolet (UV) radiation or high humidity can degrade these hydrophobic agents over time. Once compromised, the aerogel may begin to absorb moisture, which—due to capillary forces—can cause the collapse of its nanoporous structure, significantly impairing its thermal performance.

Environmental Degradation Parameters

The aging rate of insulation materials is determined not by ideal laboratory conditions, but by the dynamic environmental loads they are exposed to-namely heat, air, and moisture (HAM).

Temperature and the Arrhenius Relationship

Temperature increases the thermal mobility of polymer chains, thereby accelerating the gas diffusion coefficient. The aging rate (k) of polymeric insulation materials has an exponential dependence on temperature (T), which can be described by the Arrhenius equation:

$$\mathrm{k} = \mathrm{A}.\, e^{-Ea/(R.T)}$$

Here, E_a represents the activation energy, and R is the universal gas constant. This equation explains why aging processes occur significantly faster in high-temperature applications -such as roof insulation, where surface temperatures can reach 60–70°C during summer- compared to vertical façade systems (Celina, 2013).

Moisture and Hygrothermal Cycles

Water is one of the most critical degrading agents for insulation materials. The thermal conductivity of water (0.60 W/mK) is approximately 24 times higher than that of air. More importantly, when water within pores freezes, the thermal conductivity of ice can reach as high as 2.2 W/mK. Freeze–thaw cycles generate mechanical stress on pore walls, progressively damaging the microstructure of the material and causing irreversible deterioration. The frequent appearance of the keyword “moisture” in bibliometric analyses highlights the global relevance and severity of this issue (Kumaran, 2006).

Standards, Test Methods, and the Performance Gap

The historical development of thermal aging research has closely paralleled changes in measurement standards and the ongoing debate between "design" and "declared" thermal performance values.

From Static Methods to Dynamic Projections

Standards such as ISO 8301 and ASTM C518, commonly used during the 1990s, were designed to measure the instantaneous thermal performance of materials under dry and conditioned laboratory conditions. However, this static approach has proven inadequate in reflecting real-world building performance over time.

With the introduction of EN 13166 and ISO 11561 in the early 2000s, the concept of Accelerated Aging became a mandatory part of thermal performance evaluation. Among these methods, the most widely used is the Slicing Method, in which insulation boards are cut into thin layers to shorten the diffusion path of blowing agents. This technique simulates approximately 25 years of natural aging within a controlled laboratory environment (CEN, 2016).

Declared (λ_D) vs. Design (λ_{design}) Thermal Conductivity Values

According to European standards (EN ISO 10456), the Declared Thermal Conductivity (λ_D) provided by manufacturers is intended to represent the material's average performance over a 25-year period. However, for use in building energy simulations, the appropriate value is the Design Thermal Conductivity (λ_{design}), which accounts for real-life conditions. This value is calculated using the following equation:

$$\lambda_{design} = \lambda_D + F_T + F_M + F_A$$

The correction factors applied to declared thermal conductivity values play a critical role in accurately predicting a material's real-world performance. Specifically, FT accounts for temperature variations, FM addresses the influence of moisture content, and FA adjusts for the effects of aging over time. Together, these factors are used to convert the declared thermal conductivity (λ_D) into a more realistic design value (λ_{design}) suitable for energy simulations and performance assessments. However, one of the most widely discussed issues in the literature is the frequent omission or inconsistent application of these correction factors. This practice often leads to significant underestimations or overestimations of long-term thermal performance, thereby widening the gap between predicted and actual building energy use.

Numerical Modeling

In recent years, due to the high cost and time-intensive nature of physical testing, researchers have increasingly turned to numerical modeling techniques. Studies by Belanger and Berardi (2018) recommend integrating laboratory aging data into building energy simulation tools such as EnergyPlus or WUFI. Rather than relying on a fixed thermal conductivity value (λ), this approach incorporates a time-dependent function, λ(t), into the simulation process. Doing so enables a more accurate prediction of a building's energy consumption over a 50-year lifecycle, reflecting the material's thermal degradation under realistic service conditions.

Methodology

In this study, a bibliometric analysis approach was adopted to quantitatively examine the research landscape surrounding thermal aging in building envelopes. The research process was carried out in three stages: data collection, data filtering, and data analysis.

Data Source

The research data were obtained from the Web of Science (WoS) Core Collection database, selected for its comprehensive coverage of high-impact journals in the fields of engineering and materials science, as well as for the consistency of its bibliometric records. The dataset was compiled using publications indexed in the Science Citation Index Expanded (SCI-Expanded), which best represent the international literature.

Search Strategy

The search query was constructed using four core keywords combined with the logical operator "AND" to capture the fundamental dimensions of the topic while minimizing irrelevant results.

The search string used was: “thermal conductivity” AND “aging” AND “insulation” AND “buildings”.

This query was applied to the "Title", "Abstract", and "Keywords" fields of the publications. The selected time span for the study was from 1990 to 2025.

Data Filtering and Inclusion Criteria

The initial search yielded a total of 37 publications. To ensure reliability and consistency in the dataset, the following filtering criteria were applied:

Document Type Control: Since the study focuses on empirical research findings, only documents categorized as “Research Articles” were included in the analysis.

Exclusion of Non-Relevant Works: Five publications were excluded from the dataset because they were classified as either “Review Articles” or “Proceedings Papers.”

Final Dataset: After the filtering process, 32 full-text research articles were identified as suitable for analysis. These articles were exported in “Plain Text” format with “Full Record and Cited References” fields for input into bibliometric analysis software.

Analysis Tools

For the analysis and scientific mapping of the final dataset, the Bibliometrix package and its web-based interface Biblioshiny, both built on the R programming environment, were used (Aria & Cuccurullo, 2017). These tools enabled the visualization and interpretation of:

- Annual scientific output,
- Citation performance of publications,

- Keyword co-occurrence networks and conceptual structures.

Findings and Analytical Evaluation

The bibliometric analysis of the refined dataset -comprising 32 qualified research articles retrieved from the Web of Science- reveals significant statistical and conceptual patterns in the literature. In this section, the bibliometric maps and graphs are not only presented as numerical data but are also interpreted as indicators of the field's historical and sociological evolution.

Annual Scientific Production and Citation Impact

The trend in annual scientific output on thermal aging in building envelopes is presented in Figure 1. Upon examining the graph, it is evident that between 2010 and 2016, the annual number of publications remained extremely low and stagnant (0-1 articles per year). This suggests that the topic was still considered a niche research area during that period. However, post-2016, a noticeable upward trend emerged, culminating in 2021, which marked the peak of scientific production with 5 articles published in that year.

Temporal Evolution and Breakpoints of Scientific Production

The temporal evolution of scientific output on thermal aging in building envelopes is illustrated in Figure 1. Analyzing the morphological structure of the graph reveals that the interest in this research topic has followed a non-linear, event-driven trajectory rather than a steady linear progression.

Figure 1. Annual scientific production on thermal aging in building envelopes (1990–2025).

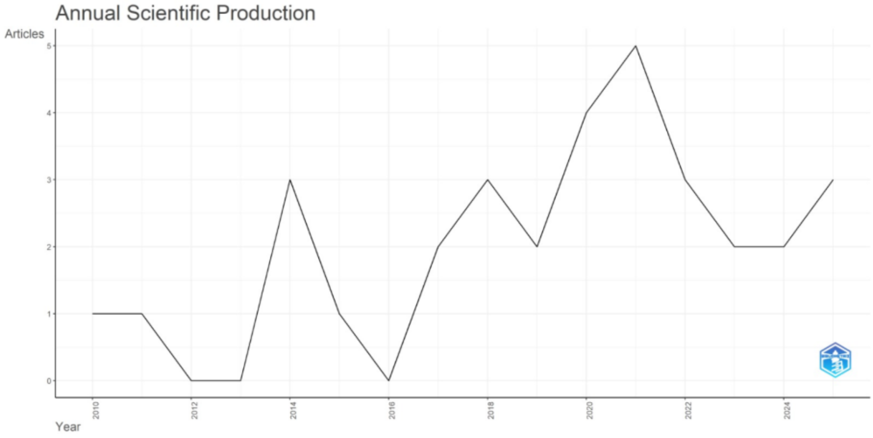

Incubation Phase (1990–2015): The left side of the graph, marked by a low and stagnant publication frequency, reflects the initial incubation stage of the field. During this period, annual production rarely exceeded one publication per year. Rather than being pursued as an independent research domain, thermal aging was largely treated as a secondary characteristic within broader studies focused on insulation materials.

Acceleration and Breakpoint (2016–2020): A significant upward trend emerges starting in 2016, representing a clear inflection point. This shift coincides with the enforcement of the Paris Climate Agreement (2015) and the increasing regulatory pressure for "real performance" assessments of building envelopes, especially in the context of national building codes and energy labeling systems.

Peak Phase (2021): The year 2021 marks the highest level of annual output with five publications, representing the "peak" point on the curve. This surge can be attributed to the post-COVID-19 emphasis on "healthy buildings" and "energy-saving" strategies, alongside the influence of the European Green Deal's "Renovation

Wave” initiative. Researchers began to reflect more critically on the long-term performance degradation of insulation materials in renovated or existing building stock, especially under aging and environmental stressors.

Citation Analysis and Impact Depth

To assess the qualitative impact of scientific production over time, the metric “Average Citations per Year” was analyzed, as visualized in Figure 2. This figure provides critical insight into the intellectual influence and scholarly reception of publications within the field.

Figure 2. Average citations per year for research on thermal aging in building envelopes (1990–2025).

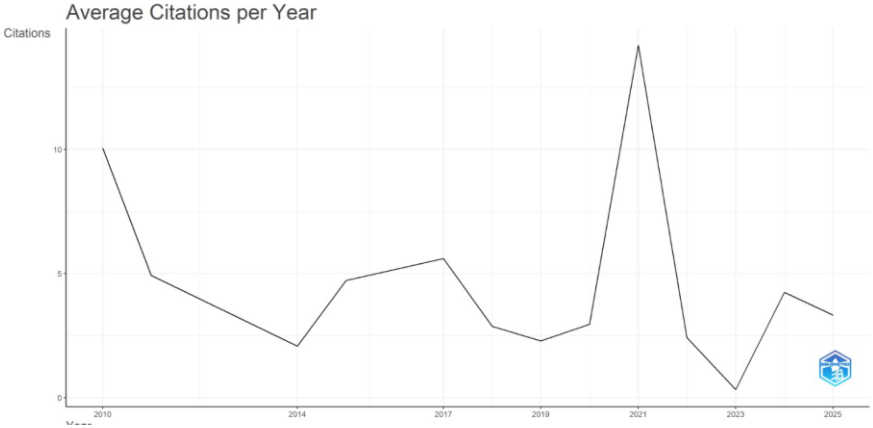

A close examination of the graph reveals pronounced citation spikes in the years 2010 and 2021, suggesting the publication of particularly influential works during these periods.

Impact of 2010: The elevated citation count observed in 2010 indicates the publication of foundational studies that introduced key methodologies—such as accelerated aging protocols or simulation-based modeling approaches. These publications appear to have served as seminal works, frequently cited by subsequent research and widely adopted in standard experimental procedures.

Breakpoint in 2021: In contrast, the 2021 spike is attributed not to methodological breakthroughs but rather to a sharp increase in interest and urgency surrounding the topic. This surge may reflect a growing recognition of thermal aging as a “hot topic” in response to evolving energy regulations and sustainability targets. Typically, scientific publications require a maturation period of 3–5 years to achieve high citation visibility; thus, such an early spike implies exceptional topical relevance and immediate applicability.

Distribution of Sources and Publication Concentration

Figure 3 presents the clustering of thermal aging research within specific academic journals, offering a bibliometric snapshot of the disciplinary boundaries and publication preferences that shape the field.

Figure 3. Most relevant journals contributing to the thermal aging literature (1990–2025).

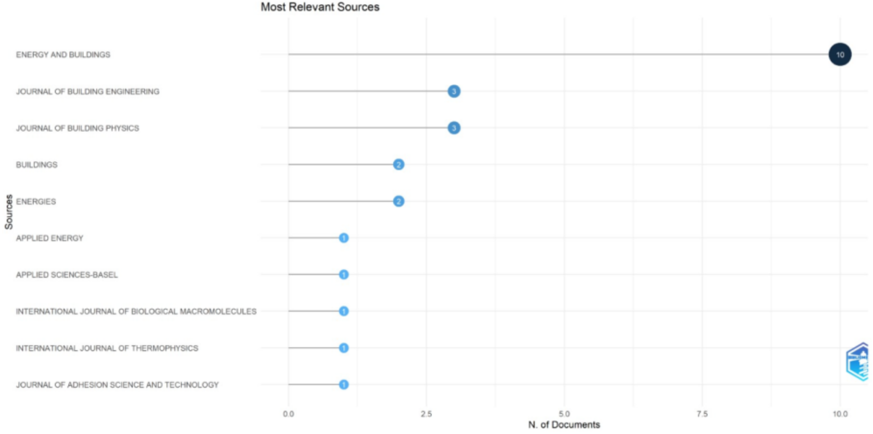

The dataset exhibits a distribution pattern consistent with Bradford’s Law of Scattering, whereby a small number of "core journals" account for the majority of publications, while the remainder are dispersed across a wider range of sources.

Energy and Buildings Dominance: Of the 32 analyzed articles, 10 (approximately 31%) were published in Energy and Buildings, confirming its status as a primary publication venue. This journal serves as a multidisciplinary bridge between materials science and building engineering, offering a neutral platform for cross-cutting research. Its focus on thermal aging extends beyond chemical degradation to explore its impact on building energy performance, distinguishing it from journals narrowly focused on polymer chemistry or materials degradation.

Secondary Foci: Journals such as the Journal of Building Engineering and the Journal of Building Physics represent secondary yet significant publication hubs. Their increasing prominence suggests a shift in the field toward practical engineering applications and numerical modeling frameworks, underscoring the growing relevance of thermal aging within real-world building performance analysis.

Collaboration Network Analysis and Patterns of Scientific Interaction

The generation of scientific knowledge is often shaped by patterns of collaboration among researchers. Figure 4 illustrates the structure of the collaboration network within the field, mapping the presence of “invisible colleges” that form through co-authorship relations over time.

Figure 4. Collaboration network map revealing regional research clusters in thermal aging literature (1990–2025).

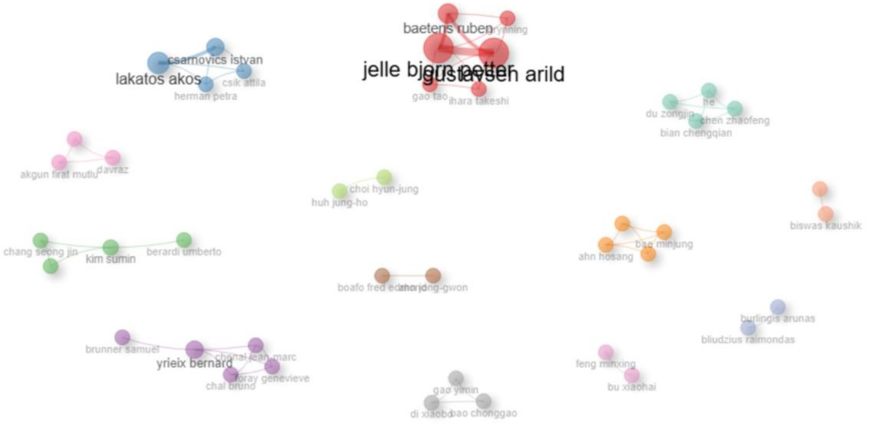

The map reveals a fragmented structure, indicating a field characterized more by regional clusters than by a centralized, cohesive research community.

Northern Europe Cluster (Red): This cluster is led by Jelle, B.P., and Gustavsen, A., based primarily in Norway. Their research agenda is strongly climate-driven, focusing on insulation performance under cold weather conditions. Their significant contributions to the study of Vacuum Insulation Panels (VIPs) and laboratory aging protocols position this cluster as methodologically influential, though somewhat geographically bounded.

North America/Italy Cluster (Green-Pink): This group, represented by Berardi, U. (Canada) and Italian collaborators, shows a strong focus on foam insulation materials (e.g., PUR and PIR). Their work emphasizes accelerated aging and long-term performance prediction in polymeric materials.

Central/Eastern Europe Cluster (Blue): Led by Lakatos, A. (Hungary), this group centers around experimental approaches and real-scale validation of material performance degradation over time.

Notably, the field has yet to coalesce into a fully “universalized” network, suggesting that thermal aging research remains governed by localized concerns, region-specific climatic conditions, and material availability, which continue to define the dominant research priorities.

Conceptual Structure and Thematic Map Analysis

To uncover the cognitive evolution of the field, a dual analysis was conducted using the Keyword Co-occurrence Network (Figure 5) and the Thematic Map (Figure 6). These bibliometric visualizations help delineate the dominant topics and intellectual shifts within thermal aging research in building envelopes.

Figure 5. Keyword Co-occurrence Network in Thermal Aging Literature (1990–2025)

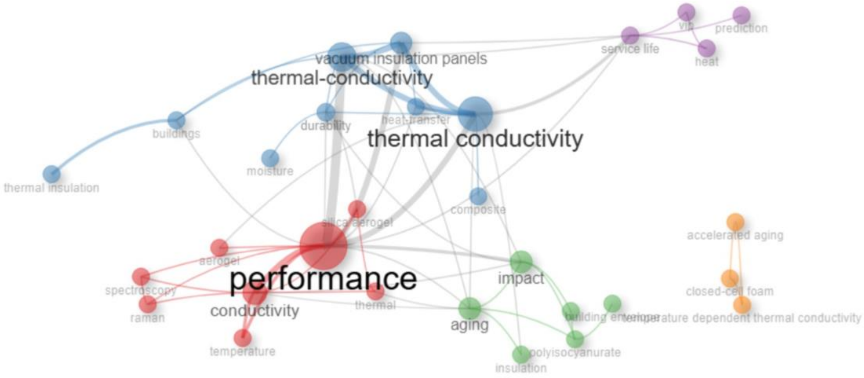

Interpretation of the Keyword Network (Figure 5): The largest and most central node in the network is "Performance", which is conceptually significant. This indicates a paradigmatic transition in the literature—from material identification and basic characterization ("What is this material?") to performance-based evaluation ("What does this material do in a building context?"). Furthermore, the prominence of "Silica Aerogel" and "Vacuum Insulation Panels" over traditional materials such as "Polystyrene" reflects a clear academic shift toward advanced nanotechnological insulation solutions.

Figure 6: Strategic Thematic Map Based on Relevance and Development (1990–2025)

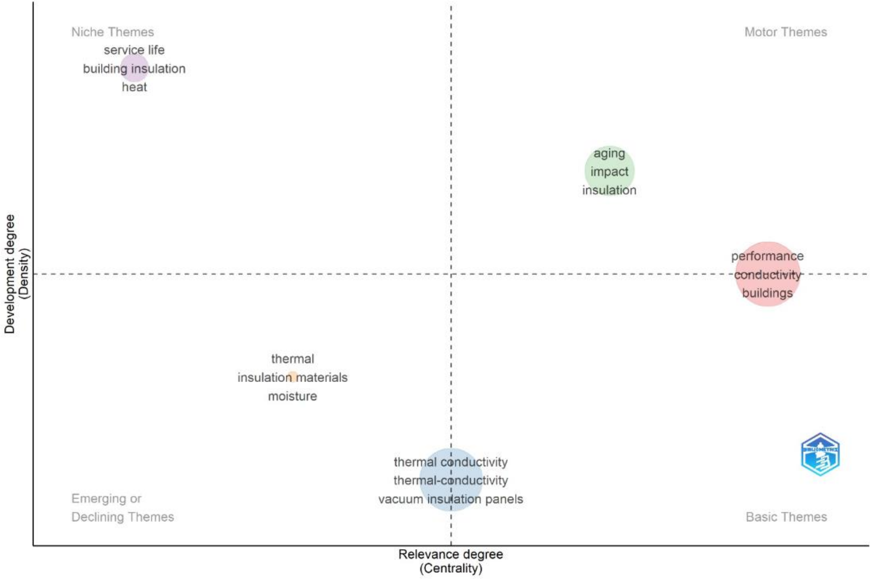

Interpretation of the Thematic Map (Figure 6): The thematic map classifies research topics into four quadrants, based on density (Y-axis: level of development) and centrality (X-axis: thematic relevance):

Motor Themes (Upper Right - Q1): Topics such as "Aging," "Impact," and "Insulation" are both conceptually mature and centrally positioned within the field. These constitute the intellectual driving forces of thermal aging research.

Basic Themes (Lower Right - Q4): The prominence of "Thermal conductivity" in this quadrant suggests that it has become a well-established area of consensus—widely studied and theoretically saturated, with limited room for novel contributions.

Emerging or Declining Themes (Lower Left - Q3): The positioning of "Moisture" in this quadrant is perhaps the most critical insight from this analysis. As discussed in the theoretical framework, moisture poses a severe threat to insulation performance. However, the bibliometric evidence indicates that moisture-related degradation remains a marginal topic, with most studies disproportionately focused on thermal aging due to temperature effects. This exposes a major research gap in the literature. The data clearly signal the need for future investigations to prioritize hygrothermal aging, integrating moisture dynamics into performance modeling, and long-term durability assessments.

These conceptual patterns highlight the evolving focus of the field and suggest strategic directions for further interdisciplinary inquiry.

Discussion

This study has provided a bibliometric map of the literature on thermal aging in building envelopes between 1990 and 2025. The findings demonstrate not only a quantitative expansion in the field but also a significant methodological and conceptual transformation. In this section, the results are interpreted along three main dimensions in light of ongoing academic debates.

Policy Drivers and the Impact of the Renovation Wave

The upward trend in scientific production after 2016 and the peak publication year in 2021 (as illustrated in Figure 1) are strongly correlated with a paradigm shift in global energy policy. The European Union’s Green Deal and the subsequent Renovation Wave initiative have redirected the focus from new construction to retrofitting existing building stock.

In the context of updating the energy performance certificates (EPCs) of existing buildings, the question of how insulation materials applied 10 to 20 years ago are performing today has brought the topic of thermal aging from a niche concern to the mainstream of building science research. The spike in publications and citation activity in 2021 (Figure 2) reflects the scientific community's response to this emerging policy-driven demand. Increasingly, the literature now interrogates not only the "initial" thermal conductivity values (λ_{initial}) of insulation materials, but also their long-term or "end-of-life" performance (λ_{aged}).

The Moisture Paradox and an Unaddressed Research Gap

One of the most striking and concerning findings of this study is the marginal position of the keyword "Moisture" in the Strategic Thematic Map (Figure 6), where it appears under the quadrant of Emerging or Declining Themes. As elaborated in the Theoretical Framework, the thermal conductivity of water is approximately 24 times higher than that of air, and empirical studies have shown that moisture ingress can reduce insulation performance by up to 70% (Sanders, 1996).

Despite this, bibliometric evidence indicates that the majority of the literature focuses narrowly on thermal aging mechanisms driven by heat and gas diffusion, while largely overlooking the coupled effect of heat and moisture-known as hygrothermal aging. This points to a critical research gap. Given that insulation materials are rarely completely dry under real-world conditions, performance models that assume a moisture-free state are likely to produce overly optimistic lifespan estimates.

Methodological Shift: From Laboratory Testing to Digital Twins

The centrality of terms such as "Simulation" and "Performance" in the keyword co-occurrence network (Figure 5) reflects a methodological pivot in the field. During the late 1990s and early 2000s, accelerated aging tests—such as the slicing method—were considered the gold standard for assessing long-term insulation performance. However, the high cost and time-consuming nature of these tests have prompted researchers to explore alternative strategies.

The findings indicate a growing trend, led by studies such as Belanger and Berardi (2018), toward integrating empirical data from laboratory tests into Building Energy Simulation (BES) tools. Rather than using static values of λ, researchers now aim to model its evolution as a time-dependent function, λ(t), and simulate its impact on a building's energy consumption over a 50-year lifespan within a digital twin environment. This hybrid approach represents a more proactive method for addressing the performance gap between designed and actual building energy use.

CONCLUSION AND RECOMMENDATIONS

This book chapter has presented a comprehensive bibliometric and scientometric analysis of the global literature on thermal aging in building envelopes, focusing on peer-reviewed research published between 1990 and 2025 in the Web of Science Core Collection. The analysis of 32 high-quality research articles has helped clarify the intellectual structure, social networks, and forward trajectories of the field.

Key Takeaways

The main findings of the study can be summarized as follows:

Maturation of the Field: Thermal aging has evolved from a niche sub-topic within material science into a central concern within building physics and sustainability research, as reflected by its dominance in top-tier journals such as Energy and Buildings.

Material-Specific Research Fragmentation: The collaboration networks (Figure 4) reveal a geographic and material-based divergence—Northern Europe focusing on VIPs and Southern/North America on foam-based materials. This divergence challenges the development of a universal aging standard.

Underrepresentation of Moisture: Despite being a critical factor that significantly degrades insulation performance, moisture remains underexplored in bibliometric maps. Most existing models are based on the assumption of dry conditions.

Implications for Industry and Policymakers

Standard Revisions: Regulatory bodies such as ISO and CEN should move beyond declared values (λ_D) and mandate the use of aged design values (λ_design) in energy performance certificates to better reflect long-term material performance.

On-Site Verification: To address the performance gap, insulation efficiency should be verified not only during the design phase but also via thermographic inspections at the 5th and 10th years of the building's life.

Future Research Directions

To advance the field and fill existing research gaps, future studies should focus on the following areas:

1. **Hygrothermal Aging Models:** Develop multivariate models that incorporate not only temperature but also relative humidity, precipitation, and other climatic stressors.
2. **Artificial Intelligence and Machine Learning:** Use big data and machine learning algorithms to predict thermal aging trends, thereby reducing reliance on lengthy and expensive laboratory tests.
3. **Longitudinal In-Situ Monitoring:** Implement real-world sensor-based systems in buildings to gather

long-term performance data (5–10 years), thereby validating simulation models and improving predictive accuracy.

In conclusion, thermal aging remains an invisible yet critical barrier to achieving Net Zero Energy Building goals. While the field is clearly moving from laboratory experiments toward digital modeling and simulation, critical factors such as moisture remain underrepresented. Bridging this gap will be essential for developing more resilient, accurate, and policy-relevant models of building energy performance.

References

Aditya, L., Mahlia, T. I., Rismanchi, B., Ng, H. M., Hasan, M. H., Metselaar, H. S. C., ... & Aditiya, H. B. (2017). A review on insulation materials for energy conservation in buildings. *Renewable and sustainable energy reviews*, *73*, 1352-1365.

Aria, M., & Cuccurullo, C. (2017). bibliometrix: An R-tool for comprehensive science mapping analysis. *Journal of informetrics*, *11*(4), 959-975.

Baetens, R., Jelle, B. P., Thue, J. V., Tenpierik, M. J., Grynning, S., Uvsløkk, S., & Gustavsen, A. (2010). Vacuum insulation panels for building applications: A review and beyond. *Energy and Buildings*, *42*(2), 147-172.

Baetens, R., Jelle, B. P., Thue, J. V., Tenpierik, M. J., Grynning, S., Uvsløkk, S., & Gustavsen, A. (2010). Vacuum insulation panels for building applications: A review and beyond. *Energy and Buildings*, *42*(2), 147-172.

Belanger, D., & Berardi, U. (2018, May). The impact of aging on the effective thermal conductivity of foam insulation: A simulation investigation using laboratory characterization data. In *Proceedings* *of the 10th conference of IBPSA-Canada, Montreal, QC, Canada* (pp. 9-10).

Bereketoğlu, S. (2024). Energy analysis of the provinces in the Southeastern Anatolia Region: An evaluation using artificial and natural insulation materials with the degree-day method. *WAPRIME,* 1(1), 26–44. https://doi.org/10.5281/zenodo.14931663

Cabeza, L. F., Castell, A., Medrano, M., Martorell, I., Pérez, G., & Fernández, I. (2010). Experimental study on the performance of insulation materials in Mediterranean construction. *Energy and Buildings*, *42*(5), 630-636.

Celina, M. C. (2013). Review of polymer oxidation and its relationship with materials performance and lifetime prediction. *Polymer Degradation and Stability*, *98*(12), 2419-2429.

Celina, M. C. (2013). Review of polymer oxidation and its relationship with materials performance and lifetime prediction. *Polymer Degradation and Stability*, *98*(12), 2419-2429.

CEN (European Committee for Standardization) (2016). *Thermal insulation products for buildings - Factory made products of phenolic foam (PF) - Specification* (EN 13166:2012+A2:2016). Brussels: CEN. https://standards.iteh.ai/catalog/standards/cen/26294808-e988-441d-afb7-31c27c9ed397/en-13166-2012a2-2016?srsltid=AfmBOoqc0lk5xhP4WBVBqLcSLdJjv_3NUAkxpml-5mpmfQ_ZRJ7IxSlN

Çelik, C. (2024). Performance analysis of DX and flooded evaporators with eco-friendly refrigerants in medium-scale food storage systems. *WAPRIME,* 1(1), 16–25. https://doi.org/10.5281/zenodo.14931590

De Wilde, P. (2014). The gap between predicted and measured energy performance of buildings: A framework for investigation. *Automation in construction*, *41*, 40-49.

Intergovernmental Panel on Climate Change (IPCC). (2023). *Climate Change 2023: Synthesis Report*. Geneva: IPCC. https://www.ipcc.ch/report/ar6/syr/downloads/report/IPCC_AR6_SYR_FullVolume.pdf

International Energy Agency (IEA). (2024). *World Energy Outlook 2024*. IEA Publications. https://iea.blob.core.windows.net/assets/140a0470-5b90-4922-a0e9-838b3ac6918c/WorldEnergyOutlook2024.pdf

Jelle, B. P. (2011). Traditional, state-of-the-art and future thermal building insulation materials and solutions–Properties, requirements and possibilities. *Energy and buildings*, *43*(10), 2549-2563.

Kumar, D., Alam, M., Zou, P. X., Sanjayan, J. G., & Memon, R. A. (2020). Comparative analysis of building insulation material properties and performance. *Renewable and Sustainable Energy Reviews*, *131*, 110038.

Mukhopadhyaya, P., Bomberg, M. T., Kumaran, M. K., Drouin, M., Lackey, J., Van Reenen, D., & Normandin, N. (2002). Long-term thermal resistance of polyisocyanurate foam insulation with impermeable facers. *ASTM Special Technical Publication*, *1426*, 351-365.

Papadopoulos, A. M. (2005). State of the art in thermal insulation materials and aims for future developments. *Energy and Buildings*, 37(1), 77-86.

Sanders, C., Heat, A., New, M. T. T., & Parts, R. I. E. (1996). IEA-Annex 24 HAMTIE. *Final report*, *2*.

Simmler, H., Brunner, S., Heinemann, U., Schwab, H., Kumaran, K., Mukhopadhyaya, P., ... & Erb, M. (2005). Vacuum Insulation Panels-Study on VIP-components and panels for service life prediction of VIP in building applications (Subtask A).

Sümer, D. (2025). Sustainable energy applications in stenter machines in Germany a bibliometric analysis of research trends. *WAPRIME*, 2(1), 1–12. https://doi.org/10.5281/zenodo.16980641

Ünal, E. K. (2024). Analytical and numerical investigation of viscous heating in parallel-plate Couette flow. *WAPRIME,* 1(1), 57–69. https://doi.org/10.5281/zenodo.14931785

Yaman, K., Dölek , S., & Arslan , G. (2025). Performance analysis of a thermoelectric generator (TEG) for waste heat recovery. *WAPRIME,* 2(1), 13–20. https://doi.org/10.5281/zenodo.16980562

Zupic, I., & Čater, T. (2015). Bibliometric methods in management and organization. *Organizational research methods*, *18*(3), 429-472.

CHAPTER 9

THE IMPACT OF DYNAMIC AGING ON THERMAL PERFORMANCE DEGRADATION AND ENERGY CONSUMPTION OF BUILDING INSULATION MATERIALS

1. KAAN YAMAN[1]
2. FATİH ÜNAL[2]

Introduction

Energy consumption in the building sector constitutes approximately one-third of the total final energy consumption in both developed and developing nations, with a significant portion of this expenditure attributed to heating and cooling demands (Jelle, 2011; Papadopoulos, 2005). Similarly, thermodynamic and energy analyses conducted on furnaces, cold storage facilities, and waste heat recovery systems consistently demonstrate the decisive impact of envelope and body insulation on fuel consumption and heat recovery potential (Erdoğan & Şentürk Acar, 2024; Çelik, 2024; Yaman, Dölek, & Arslan, 2025). Within this framework, enhancing

---

[1] Research Assistant, Mersin University, Mechanical Engineering Department, Orcid: 0000-0002-8627-4082

[2] Assoc. Prof. Dr., Mersin University, Mechanical Engineering Department, Orcid: 0000-0001-6660-9984

the thermal performance of the building envelope and minimizing heat losses has become a fundamental component of strategies targeting energy efficiency improvement and greenhouse gas emission reduction.

Particularly in recent years, driven by escalating energy prices and the necessity to combat climate change, the precise selection and thickness optimization of thermal insulation materials have acquired strategic importance for both residential and commercial buildings (Aditya et al., 2017; Jelle, 2011). A detailed study comparing artificial and natural insulation materials based on the degree-day method for various provinces clearly illustrates the explicit influence of climate zone and material choice on optimum insulation thickness and annual energy consumption (Bereketoğlu, 2024).

In prevailing design practices and numerous national/international standards, the thermal conductivity coefficient (λ) of insulation materials is generally treated as a constant parameter, often under the assumption that it remains invariant over time in energy performance calculations. However, specifically in closed-cell polymer foams (such as EPS, XPS, PUR, PIR, etc.), the thermal conductivity (λ) increases throughout the service life due to phenomena such as blowing agent diffusion, thermo-oxidative degradation, UV exposure, morphological deformation, and moisture ingress. Consequently, the thermal resistance ($R=d/\lambda$) decreases, leading to a measurable increase in operational energy consumption (Bae, Ahn, Kang, Choi, & Choi, 2022; Berardi, 2018; Stovall, 2012).

Analogously, analytical and numerical studies have revealed that viscous heat generation can significantly alter the temperature field in channels involving high shear rates and thin flow layers, indicating that internal heat generation terms must not be neglected in heat transfer problems (Ünal, 2024). This primary phenomenon affecting insulation is termed "dynamic aging" and is frequently overlooked in conventional energy simulations.

This book chapter comprehensively addresses the phenomenon of dynamic aging in thermal insulation materials within the following interconnected contexts: (i) fundamental physical and chemical mechanisms, (ii) material-specific aging behaviors, (iii) mathematical modeling approaches, (iv) proposed tables of dynamic aging coefficients, and (v) energy loss formulations utilizing the degree-day method. The objective is to produce a readily applicable reference text for both materials science researchers and engineers conducting building energy simulations and optimum insulation thickness studies, while also providing relevance to applications such as industrial furnaces, cold storage units, and waste heat recovery systems.

The Concept of Aging in Thermal Insulation Materials

The aging of thermal insulation materials is defined as the process where time-dependent changes in the material's physical, chemical, or morphological structure cause an increase in the thermal conductivity coefficient (λ) and a subsequent reduction in the thermal resistance (R) (Domínguez-Muñoz, Cejudo-López, Carrillo-Andrés, & Ruiz, 2010; Jelle, 2011; Papadopoulos, 2005). This process is generally irreversible and persists throughout the service life of the material.

For a single-layer insulation board, the thermal resistance R(t) is fundamentally defined using the material's thickness d and the time-dependent thermal conductivity coefficient λ(t) by the following essential relationship:

$$R(t) = \frac{d}{\lambda(t)}$$

The process of dynamic aging leads to changes occurring within the material's internal structure, resulting in a time-dependent increase in the thermal conductivity coefficient λ(t). According to the relationship stated above, this increase causes a reduction in the material's thermal resistance R(t).

This decrease in thermal resistance, under a constant temperature difference (ΔT), leads to a rise in the heat flux (Q(t)) over time. This situation signifies an increase in heat losses/gains occurring through the building envelope, and consequently, results in an increase in the annual energy consumption (E(t)).

This simple thermodynamic relationship clearly demonstrates that the aging of insulation materials has a direct and negative effect on both indoor thermal comfort and the operational costs of the structure (Domínguez-Muñoz et al., 2010; Jelle, 2011). These findings emphasize the critical importance of the long-term performance degradation (devaluation) of insulation materials in energy efficiency analyses.

Aging in insulation materials is multidimensional, too complex to be reduced to a single mechanism. Different material classes, various environmental conditions, and distinct application details create an interaction field that determines the aging behavior (Aditya et al., 2017; Le & Pásztory, 2021). The most frequently encountered aging types from an engineering perspective are summarized in Table 1.

Table 1 Major aging types and mechanisms of action in insulation materials.

Aging Type	Mechanism of Action	Prominent Materials
Thermal Aging	Temperature-dependent intra-cellular gas diffusion, viscoelastic relaxation	EPS, XPS, PUR, PIR
Chemical Aging	Thermo-oxidative degradation, chain scission (breakage), cross-link dissolution	PUR, PIR, PE, PVC
Moisture Aging	Water absorption, capillary uptake, freeze-thaw cycles	Glass Wool, Stone Wool, Cellulose
UV Aging	Photo-oxidation, surface cracking, discoloration	EPS, PUR, Uncoated foams
Mechanical Aging	Compression, crushing, fatigue, dimensional change/deformation	Fibrous materials, ground-based XPS/PUR
Electrical Aging	Dielectric breakdown, "treeing," localized heating	Cable insulation, specialized systems

In closed-cell polymer foams, thermal and chemical aging (specifically, blowing agent diffusion and oxidation) are the dominant mechanisms. Conversely, in fibrous and mineral-based materials, moisture content and hygrothermal effects are the predominant factors influencing performance degradation (Aditya et al., 2017; Bae et al., 2022; Le & Pásztory, 2021).

Dynamic Aging Mechanisms

Intra-Cellular Gas Diffusion in Closed-Cell Foams

Closed-cell polymer foams, such as EPS, XPS, PUR, and PIR, contain blowing agents with low thermal conductivity during manufacturing. Over time, the following sequence of events occurs:

- The blowing agent gas (e.g., pentane, HFO) initially trapped within the cells diffuses out into the ambient environment.

- Ambient air components (N_2, O_2) concurrently diffuse into the internal cells.
- The thermal conductivity of the resulting gas mixture within the cells increases.
- Consequently, the effective thermal conductivity of the material, λ(t), increases.

This process is characterized by Fick's laws of diffusion, and its characteristic time scale is approximately expressed by the relationship $t \sim L^2/D$. Here, L represents the typical cell size or board thickness, and D ise difüzyon katsayısını temsil eder (Bae et al., 2022; ISO, 1999; Stovall, 2012). The diffusion coefficient is dependent on the polymer matrix structure, temperature, and cell wall thickness. Thicker boards generally exhibit slower aging rates, whereas thinner boards show faster aging. For this reason, accelerated aging tests employing thin slicing methods are defined in standards such as ISO 11561 and ASTM C1303 (ASTM International, 2023; ISO, 1999).

Morphological Deformation and Cell Collapse

Thermal cycling, prolonged mechanical loads, and compression applied during installation can lead to permanent deformation and partial cell collapse within the foam's cell walls. This morphological change results in an increase in the effective density, a decrease in porosity, and consequently, an increased contribution of the solid phase to the material's thermal conductivity (Jelle, 2011; Stovall, 2012).Experimentally, a power-law relationship has been widely observed between the thermal conductivity (λ) and the density (ρ) in many foam materials, approximated as (Le & Pásztory, 2021):

$$\lambda \; \alpha \; \rho^{n} \quad (n \approx 1.3 - 2.0)$$

This relationship is particularly important for evaluating the long-term performance of XPS and PUR boards utilized under load, such as in sub-slab or inverted roof applications.

Moisture Effect on Fibrous and Mineral-Based Materials.

For fibrous thermal insulation materials, such as glass wool, stone wool, and cellulose, the dominant component of dynamic aging is typically the moisture content. The porous structure of these materials absorbs water vapor and liquid water in varying proportions. The filling of pores with water introduces the water phase, which possesses a significantly higher thermal conductivity compared to air, consequently causing an increase in λ (Aditya et al., 2017; ISO, 2007; Le & Pásztory, 2021). In engineering applications, the following empirical expression is commonly utilized to approximate the effect of moisture on thermal conductivity:

$$\lambda_{eff}(t) = \lambda_{dry}[1 + aw(t)]$$

Here, λ_{dry} represents the thermal conductivity of the dry material, w(t) is the moisture content by mass fraction (mass percentage/100), is the moisture-sensitivity coefficient dependent on the specific material type. The coefficient a has been reported to range between 0.15 and 0.25 for glass wool and cellulose (Le & Pásztory, 2021). Furthermore, freeze-thaw cycles can cause crack formation in the microstructure and permanent alterations in the pore structure, further impairing both the mechanical strength and thermal properties (ISO, 2007).

Thermo-oxidative Chemical Aging

Chemical degradation occurring in the presence of oxygen and elevated temperature in polymer-based insulation materials is defined as "thermo-oxidative aging" (Celina et al., 2019; Liu et al., 2024). During this process, reactions such as polymer chain scission (breakage), cross-link dissolution or rearrangement, and free radical formation advance. Consequently, the material's molecular weight distribution, glass transition temperature (T_g), mechanical modulus, and fracture behavior are altered. These changes can lead to an increase in thermal conductivity through secondary effects, including the formation of microcracks, increased porosity, or cell wall thinning (Celina et al., 2019; Liu et al., 2024). The temperature dependence of the aging rate is typically modeled using an Arrhenius-type equation:

$$k(T) = k_0 \exp\left(-\frac{E_a}{RT}\right)$$

In this equation, k(T) is the aging rate constant, E_a is the activation energy, R is the universal gas constant, and T is the absolute temperature. The parameters k_0 ve E_a can be estimated using data derived from accelerated aging experiments conducted at various temperatures (Celina et al., 2019).

UV-Induced Aging

The UV component of solar radiation initiates photo-oxidative degradation in polymer materials, leading to phenomena such as discoloration, chalking, surface cracking, loss of mechanical strength, and changes in surface wettability (Maraveas, 2024). While these effects may not cause a significant direct change in λ, they can indirectly accelerate the dynamic aging process by increasing the material's moisture and gas permeability. Therefore, the provision of UV protection by finishing layers in external wall insulation systems is of critical importance.

Dynamic Aging Modeling

To effectively incorporate dynamic aging into energy calculations, the time-dependent thermal conductivity function, λ(t), must be represented by an appropriate mathematical model. Commonly used models in the literature include linear increase, logarithmic increase, asymptotic approximation, and Arrhenius-based temperature-dependent approaches (Berardi, 2018; Domínguez-Muñoz et al., 2010; Jelle, 2011).

Linear Increase Model

The simplest approach is the model that assumes the thermal conductivity increases linearly over time:

$$\lambda(t) = \lambda_0 + k_{lin}t$$

Here, λ_0 represents the initial thermal conductivity, and k_{lin} denotes the amount of increase occurring per unit of time (e.g., in W/mK·year). Although most materials typically exhibit a faster rate of increase in the initial years followed by a slower rate later on, the linear model can be utilized as a first approximation in engineering calculations, particularly when field data is insufficient (Domínguez-Muñoz et al., 2010).

Logarithmic Aging Model

In systems primarily controlled by gas diffusion, the increase in λ can be observed to decelerate logarithmically over time. In such cases, an expression of the form:

$$\lambda(t) = \lambda_0[1 + a\ln(1 + bt)]$$

can simultaneously represent the rapid increase observed in the early stages and the approach to saturation over the long term. The parameters a and b are typically fitted to the experimental data using regression analysis. The logarithmic formula has been demonstrated in several studies to be successful in the long-term λ prediction for EPS and XPS materials (Bae et al., 2022; Kim et al., 2024).

Asymptotic Approximation Model

One of the models possessing the most physical interpretation for closed-cell foams is the asymptotic approximation model, which stipulates that λ(t) will approach a specific upper limit value (λ_∞) asymptotically over time:

$$\lambda(t) = \lambda_\infty - (\lambda_\infty - \lambda_0)e^{-ct}$$

In this expression, λ∞ represents the stable thermal conductivity that will be reached in the long term, and c is the aging rate coefficient (with units of year^{-1}) temsil eder. The ratio λ_∞/λ_0 quantifies the aging potential of the material, while the parameter c expresses the rate at which this potential is approached (Berardi, 2018; Bae et al., 2022).

Arrhenius-Based Temperature-Dependent Models

The λ(t) models presented above are generally valid for a specific reference temperature. When the service temperature changes significantly, the temperature dependence of the aging rate must also be modeled. For instance, the aging rate coefficient c in the asymptotic model can be expressed using the following relationship:

$$c(T) = c_0 \exp\left(-\frac{E_a}{RT}\right)$$

By utilizing an expression of this form, accelerated aging data obtained at various elevated temperatures can be evaluated within a single comprehensive framework, allowing for the prediction of the long-term performance at normal service temperatures (Celina et al., 2019; Liu et al., 2024).

Proposed Dynamic Aging Coefficients and Methodology

This section introduces dynamic aging coefficients derived from experimental data and established standards, intended for use as initial assumptions in engineering calculations. These dimensionless coefficients are designed to be directly applied in degree-day methods and basic R/U-value estimations. The derivation methodology consists of four main steps:

1. **Literature review and data compilation:** A systematic review was conducted of studies reporting long-term thermal conductivity changes for key insulation classes: closed-cell foams (EPS, XPS, PUR, phenolic foam), fibrous mineral wools, and cellulose/natural fiber insulation (Aditya et al., 2017; Bae et al., 2022; Berardi, 2018; Domínguez-Muñoz et al., 2010; Le & Pásztory, 2021; Stovall, 2012). The data sources included accelerated aging tests performed according to ISO 11561 (ISO, 1999), product-specific testing based on EN 13164 and EN 13165 (European Committee for Standardization [CEN], 2015, 2016), Long-Term Thermal Resistance (LTTR) determination via ASTM C1303 (ASTM International, 2023), and field observations.

2. **Normalization and reference aging coefficient:** For each material class, the initial thermal conductivity λ0 and the long-term stable value λ∞ were determined, and the normalized increase ratio was calculated as:

$$\Delta\boldsymbol{\lambda}/\boldsymbol{\lambda}_{\mathbf{0}} = \frac{\boldsymbol{\lambda}_{\infty} - \boldsymbol{\lambda}_{\mathbf{0}}}{\boldsymbol{\lambda}_{\mathbf{0}}}$$

   Excluding outlier values, and considering the reported minimum–maximum ranges in the literature, a representative central value was selected for a 25-year service life and a "moderate" severity climate (approximately 2000–3000 K·day HDD). This resulting coefficient is defined as φage in Table 2 (Domínguez-Muñoz et al., 2010; Jelle, 2011; Papadopoulos, 2005).

3. Climate correction factors: It was hypothesized that the aging of closed-cell materials is primarily correlated with the cumulative temperature difference and duration between the material and the external environment, whereas moisture and hygrothermal effects dominate in fibrous materials (Aditya et al., 2017; Le & Pásztory, 2021). Within this framework, reported $\Delta\lambda/\lambda_0$ results for regions with varying annual HDD values were compared, and climate correction factors were derived for "mild," "moderate," and "cold" climate bands (Bae et al., 2022; Kim et al., 2024; Stovall, 2012). These coefficients were correlated with the parameters proposed in Table 3 and Table 4 to facilitate the integration of the $\lambda(t)$ function into the degree-day method.

4. Scaling of climate and time effects: It was assumed that the long-term aging of polymer materials can, in most cases, be effectively represented by a first-order asymptotic function (Berardi, 2018; Celina et al., 2019; Liu et al., 2024). Representative values for the characteristic time constant τ and the asymptotic ratio λ_∞/λ_0 were selected based on studies indicating that aging in closed-cell foams approaches saturation within the first 5–10 years (Bae et al., 2022; Stovall, 2012). Conversely, smaller φ_{age} and α_{lin} values were proposed for fibrous and cellulose-based materials to represent the slower and lower-amplitude changes they exhibit (Le & Pásztory, 2021).

As a result of this methodology, the coefficients presented in Tables 2–4 have been structured into a semi-empirical parameter set, grounded in long-term thermal performance assessments consistent with ISO 11561, EN 13164, EN 13165, ISO 10456, and ASTM C1303, making them directly usable by practitioners (ASTM International, 2023; CEN, 2015, 2016; ISO, 1999, 2007).

Lifetime Dynamic Aging Coefficient (φ_{age})

A dimensionless coefficient has been defined for each material group to express the average increase in thermal conductivity over the lifetime of the material:

$$\lambda_{life-avr} = \lambda_0(1 + \varphi_{age})$$

Here, φ_{age}, quantifies the average increase in the λ value relative to the initial thermal conductivity λ_0 throughout the entire service life of the material.

Table 2 The proposed lifetime dynamic aging coefficient is φ_{age} (–)

Material Group	**Description**	**φ_{age} (Proposed)**
EPS (Uncoated)	Standard external facade application, moderate climate	0.08
EPS (Within Coated System)	ETICS or similar systems, well-protected	0.05
XPS (Sub-slab/Floor Application)	Exposed to mechanical load and wet environments	0.12
XPS (Inverted Roof, good drainage)	Partially wet conditions, protected from UV	0.10
PUR/PIR (Coated Sandwich Panel)	Closed-cell foam contained within metal cladding	0.15
PUR/PIR (Site-applied Spray Foam)	In-situ application, more susceptible to diffusion	0.20
Phenolic Foam	Closed-cell structure, relatively stable	0.12
Glass Wool (with good vapor control)	Well-controlled moisture, interior wall/roof application	0.02
Glass Wool (High moisture risk detail)	Attic space, poor vapor control	0.05
Stone Wool	Mineral-based, thermal aging negligible	0.01
Cellulose Insulation	Hygroscopic, with adequate vapor control	0.05

Cellulose (High moisture risk)	Roof/attic blow-in application, poor moisture control	0.10

Relative Aging Coefficients (α_lin) for the Linear Model

In cases where the linear model is desired for use, λ(t) can be approximated by:

$$\lambda(t) = \lambda_0(1 + \alpha_{lin}t)$$

Here, t is the time in years, and α_{lin} represents the relative (percentage) annual increase rate.

Table 3 Proposed Relative Coefficients for the Linear Aging Model, α_{lin} (year^{-1})

Material Group	**Target 25-Year Total Increase**	**Proposed α_{lin} (year^{-1})**
EPS (Uncoated)	**≈ 8%**	**0.0035**
XPS (Sub-slab/Floor)	**≈ 12%**	**0.0050**
PUR/PIR (Sandwich Panel)	**≈ 15%**	**0.0060**
PUR/PIR (Spray Foam)	**≈ 20%**	**0.0080**
Phenolic Foam	**≈ 12%**	**0.0050**
Glass Wool (Controlled Moisture)	**≈ 2%**	**0.0008**
Glass Wool (High Moisture Risk)	**≈ 5%**	**0.0020**
Stone Wool	**≈ 1%**	**0.0004**
Cellulose (Controlled Moisture)	**≈ 5%**	**0.0020**
Cellulose (High Moisture Risk)	**≈ 10%**	**0.0040**

These coefficients are selected based on the targeted total increase over a defined service period. For instance, if $\alpha_{lin} = 0.006$ is adopted for a PUR/PIR sandwich panel, the thermal conductivity after 25 years approaches the order of $\lambda \approx \lambda_0(1 + 0.006 \times 25) \approx 1.15\ \lambda_0$.

Asymptotic Model Parameters (λ_∞/λ_0 ve c)

The asymptotic model is defined as:

$$\lambda(t) = \lambda_\infty - (\lambda_\infty - \lambda_0)e^{-ct}$$

Two fundamental parameters have been selected to model the dynamic change in the thermal conductivity coefficient. The first parameter, λ_∞/λ_0, represents the ratio of the long-term upper limit conductivity coefficient (λ_∞), which is theoretically attainable at the end of the aging process, to the initial conductivity coefficient (λ_0). This ratio indicates the ultimate level of the material's potential performance degradation. The second fundamental parameter, c (year^{-1}) , represents the rate of approach for the thermal conductivity value to this λ_∞ limit over time. These parameters are of critical importance for quantitatively defining the aging characteristic of the insulation material and the performance it will exhibit throughout its service life.

Table 4 Proposed Parameters for the Asymptotic Aging Model

Material Group	**λ_∞/λ_0 (Proposed)**	**c (year^{-1}, Proposed)**	**λ_∞/λ_0 at 10 Years (Approx.)**
EPS (Uncoated)	**1.12**	**0.1**	**≈ 1.08**
XPS (Sub-slab/Floor)	**1.20**	**0.12**	**≈ 1.13**
PUR/PIR (Sandwich Panel)	**1.25**	**0.15**	**≈ 1.16**
PUR/PIR (Spray Foam)	**1.30**	**0.18**	**≈ 1.19**
Phenolic Foam	**1.22**	**0.12**	**≈ 1.14**

These parameters represent a curve where, for example, if $\lambda_\infty/\lambda_0 = 1.25$ and $c = 0.15$ are adopted for a PUR/PIR sandwich panel, the λ/λ_0 ratio rises to the range of 1.15-1.20 within the first 10-15 years and subsequently approaches saturation (Bae et al., 2022; Berardi, 2018; Stovall, 2012).

Effects on Thermal Resistance and Energy Performance

As a result of the aging of the insulation material, $\lambda(t)$ increases, while the thermal resistance for a constant thickness d decreases as follows:

$$R(t) = \frac{d}{\lambda(t)}$$

In multi-layer building components (external walls, roofs, floors, etc.), the total thermal resistance is calculated by summing the resistances of all layers:

$$R_{total}(t) = R_{si} + \sum_i \frac{d_i}{\lambda_i(t)} + R_{se}$$

Here, R_{si} ve R_{se} are the interior and exterior surface film resistances, respectively. The increase in the thermal conductivity $\lambda(t)$ of the insulation layer leads to a noticeable increase in the overall U-value (thermal transmittance) of the component, especially in cases where the insulation layer contributes the largest share to $R_{total}(t)$ (e.g., thick PUR/PIR layers in heavy wall systems):

$$U(t) = \frac{1}{R_{total}(t)}$$

Consequently, it is essential to consider not only the initial U-value U(0) but also the U(t) curve throughout the entire service life of the building component (Jelle, 2011; Le & Pásztory, 2021).

Formulations Applicable for Calculating Energy Losses

Instantaneous Heat Loss

The instantaneous heat loss Q(t) through a single-layer insulation board, assuming a constant interior and exterior temperature difference ΔT, is expressed as:

$$Q(t) = A.\Delta T \frac{\lambda(t)}{d}$$

where, A is the area of the wall/component. For a multi-layer building component, the relationship $Q(t)=AU(t)\Delta T$ is used, where U(t) is derived from the total thermal resistance expression $R_{total}(t)$ provided previously.

Annual Energy Loss via the Degree-Day Method

Using the degree-day method, the annual heating load can be approximately calculated as:

$$E_{year}(t) = \frac{A.DD.24.\lambda(t)}{d}$$

Here, DD, is the annual Heating Degree-Day (HDD) value for the relevant climate zone, and 24 is the conversion factor from days to hours (Domínguez-Muñoz et al., 2010; Jelle, 2011). To represent aging using a lifetime average correction factor, the instantaneous thermal conductivity λ(t) can be substituted by $\lambda_{life\text{-}avg} = \lambda_0(1 + \varphi_{age})$:

$$E_{year,life-avg} \approx \frac{A.DD.24.\lambda_0(1+\varphi_{age})}{d}$$

This formulation enables the impact of dynamic aging on energy consumption to be represented simply by a multiplicative factor during the design phase.

Additional Energy Consumption Due to Aging

To numerically express the effect of aging, the difference between the annual energy consumption before and after aging can be defined as the additional annual energy consumption:

$$\Delta E(t) = E_{year}(t) - E_{year}(0)$$

The cumulative additional energy consumption over the entire service life is calculated by integrating the annual difference:

$$\Delta E_{cumulative} = \sum_{y=1}^{N} [E_{year}(y) - E_{year}(0)]$$

If detailed year-by-year λ(y) data is unavailable, the approximate total additional energy consumption can be estimated using the φ_{age} coefficient:

$$\Delta E_{cumulative} \approx N.[E_{year}(y) - E_{year}(0)]$$

Life Cycle Cost Analysis

If the unit energy cost (C_{energy}, e.g., \$/kWh) is known, the additional life cycle cost arising from dynamic aging is calculated by:

$$C_{LCC,aging} = \sum_{y=1}^{N} \Delta E(y).\, C_{energy}$$

This magnitude allows for the assessment of different insulation materials, not only based on their initial investment cost, but also in terms of their life cycle costs (Papadopoulos, 2005; Stovall, 2012).

Aging Tests and Standards (Brief Summary)

The primary standards utilized for the experimental characterization of dynamic aging are summarized below:

- **ISO 11561 (1999):** Defines the slicing-based method for determining the long-term change in thermal resistance in closed-cell plastic insulation materials using accelerated laboratory techniques (ISO, 1999).
- **EN 13164 (XPS) and EN 13165 (PUR/PIR):** Regulates product specifications and the principles for determining the declared thermal conductivity ($\lambda_{declared}$) for factory-made XPS and PUR/PIR products used in buildings; aged λ values are based on ISO 11561 and related tests (CEN, 2015, 2016).
- **ISO 10456 (2007):** Defines temperature and moisture correction factors and statistical approaches to be used in calculating design and declared thermal values for various building materials (ISO, 2007).

- **ASTM C1303 (2023):** Describes the accelerated slice-and-scale methodology for estimating the Long-Term Thermal Resistance (LTTR) of closed-cell foam insulation (ASTM International, 2023).

These standards provide the fundamental framework for reliably determining the $\lambda_{default}$, λ_{design} and $\lambda_{declared}$ values used in projects, by correlating them with the experimental data underpinning the dynamic aging coefficients proposed in Tables 2–4.

Discussion: The Dynamic Aging – Energy – Economics Relationship

This book chapter successfully unifies three areas often treated separately within a common framework: (i) materials science, (ii) thermal modeling, and (iii) energy-economics analysis. Gas diffusion, thermo-oxidative aging, UV effects, and morphological changes in closed-cell polymer foams are the primary factors dictating the $\lambda(t)$ curve (Bae et al., 2022; Berardi, 2018; Celina et al., 2019). Conversely, moisture content, hygrothermal cycles, and freeze-thaw effects dominate in fibrous/mineral materials, although their thermal aging is typically more limited compared to polymer foams (Aditya et al., 2017; Le & Pásztory, 2021).

In the modeling dimension, linear, logarithmic, and asymptotic $\lambda(t)$ models, alongside Arrhenius-based temperature-dependent approaches, have been presented. Simple yet physically correlated versions of these models are suitable for integration into energy simulation software and degree-day-based calculations (Berardi, 2018; Domínguez-Muñoz et al., 2010). In the energy-economics dimension, the impact of the $\lambda(t)$ function on annual energy consumption (E_{year}), cumulative extra energy consumption

($\Delta E_{cumulative}$) , and life cycle cost (C_{LCC}) has been demonstrated through explicit formulas.

Notably, the parameter sets proposed in this chapter φ_{age}, α_{lin} and (λ_∞/λ_0, c) —provide a practical toolkit for future parametric studies and optimum insulation thickness analyses. These parameters can be calibrated using manufacturer declarations or experimental studies to obtain more accurate, location/country-specific coefficients. Consequently, the λ values used in insulation design can evolve from being mere initial catalog values to dynamic quantities dependent on time and service conditions.

Conclusion and Proposed Research Agenda

The dynamic aging of insulation materials is a phenomenon that directly impacts the actual operating energy performance of buildings and can lead to significant deviations if neglected. In closed-cell polymer foams, blowing agent diffusion, thermo-oxidative chemical processes, and morphological deformation; and in fibrous and mineral materials, moisture and hygrothermal effects, cause the $\lambda(t)$ curve to change significantly over time (Aditya et al., 2017; Bae et al., 2022; Berardi, 2018; Le & Pásztory, 2021).

In summary, this chapter has:

- Explained the fundamental mechanisms of dynamic aging and their material-specific differences.
- Presented the primary aging models used in the literature (linear, logarithmic, asymptotic, Arrhenius-based).
- Summarized the accelerated aging methods specified by EN/ISO/ASTM standards.
- Demonstrated the effects of $\lambda(t)$ on energy performance and life cycle cost using degree-day-based energy loss formulas.

- Developed "proposed dynamic aging coefficients" (Tables 2–4) that are directly usable in engineering practice.

Key topics highlighted for the forward-looking research agenda include:

- Calibration of the coefficients presented in Tables 2–4 with experimental data for different climate zones, building types, and occupancy scenarios, and the establishment of country/region-specific coefficient sets.
- Widespread adoption of two- and three-dimensional thermal-moisture analyses and corresponding experimental validations for hygrothermal aging scenarios where moisture and temperature interact.
- Hybridization of physics-based models (diffusion + chemical kinetics) with machine learning approaches to improve λ(t) prediction under multi-variable service conditions.
- Utilization of optimum insulation thickness, carbon cost, and life cycle cost studies incorporating the dynamic aging effect as a decision support tool for policymakers and standard developers.

Within this framework, the establishment of dynamic aging as a standard assessment component in insulation design will contribute to a more realistic approach toward both energy efficiency and long-term sustainability goals.

References

Aditya, L., Mahlia, T. I., Rismanchi, B., Ng, H. M., Hasan, M. H., Metselaar, H. S. C., ... & Aditiya, H. B. (2017). A review on insulation materials for energy conservation in buildings. *Renewable and Sustainable Energy Reviews*, *73*, 1352–1365.

ASTM International. (2023). *Standard test method for predicting long-term thermal resistance of closed-cell foam insulation (ASTM C1303/C1303M-23)*.

Bae, M., Ahn, H., Kang, J., Choi, G., & Choi, H. (2022). Determination of the long-term thermal performance of foam insulation materials through heat and slicing acceleration. *Polymers*, *14*(22), 4926.

Berardi, U., & Nosrati, R. H. (2018). Long-term thermal conductivity of aerogel-enhanced insulating materials under different laboratory aging conditions. *Energy*, *147*, 1188–1202.

Bereketoğlu, S. (2024). Energy analysis of the provinces in the Southeastern Anatolia Region: An evaluation using artificial and natural insulation materials with the degree-day method. *WAPRIME, 1*(1), 26-44.

Celina, M., Linde, E., Brunson, D., Quintana, A., & Giron, N. (2019). Overview of accelerated aging and polymer degradation kinetics for combined radiation-thermal environments. *Polymer Degradation and Stability*, *166*, 353–378.

Çelik, C. (2024). Performance analysis of DX and flooded evaporators with eco-friendly refrigerants in medium-scale food storage systems. *WAPRIME, 1*(1), 16-25.

Domínguez-Muñoz, F., Anderson, B., Cejudo-López, J. M., & Carrillo-Andrés, A. (2010). Uncertainty in the thermal conductivity of insulation materials. *Energy and Buildings*, *42*(11), 2159–2168.

Erdoğan, M., & Acar, M. Ş. (2024). Thermodynamic analysis of a tunnel biscuit oven and heat recovery system. *WAPRIME*, *1*(1), 1-15.

European Committee for Standardization (CEN). (2012). *Thermal insulation products for buildings—Factory made extruded polystyrene foam* (EN 13164:2012). Brussels, Belgium: CEN.

European Committee for Standardization (CEN). (2012). *Thermal insulation products for buildings. Factory made rigid polyurethane foam (PU) products. Specification* (EN 13165: 2013+A2:2017). Brussels, Belgium: CEN.

International Organization for Standardization (ISO). (1999). *Ageing of thermal insulation materials–Determination of the long-term change in thermal resistance of closed-cell plastics (accelerated laboratory test methods)* (ISO 11561:1999).

International Organization for Standardization (ISO). (2007). *Building materials and products – Hygrothermal properties – Tabulated design values and procedures for determining declared and design thermal values* (ISO 10456:2007).

Jelle, B. P. (2011). Traditional, state-of-the-art and future thermal building insulation materials and solutions–Properties, requirements and possibilities. *Energy and Buildings*, *43*(10), 2549–2563.

Kim, J. H., Kim, S. M., & Kim, J. T. (2024). Comparison of thermal conductivity and long-term change of building insulation materials according to accelerated laboratory test methods of ISO 11561 and EN 13166 standard. *Energies*, *17*(23), 6105.

Liu, X., Yang, R., Xu, Z. P., Ye, Y., Tang, G. S., Zhao, M., ... & Meng, X. Z. (2024). Characterization of polymer aging: A review. *Chinese Journal of Polymer Science*, *42*(11), 1642–1660.

Maraveas, C., Kyrtopoulos, I. V., Arvanitis, K. G., & Bartzanas, T. (2024). The aging of polymers under electromagnetic radiation. *Polymers*, *16*(5), 689.

Papadopoulos, A. M. (2005). State of the art in thermal insulation materials and aims for future developments. *Energy and Buildings*, *37*(1), 77–86.

Stovall, T. K. (2012). *Closed cell foam insulation: A review of long term thermal performance research*.

Ünal, E. K. (2024). Analytical and numerical investigation of viscous heating in parallel-plate Couette flow. *WAPRIME, 1*(1), 57-69.

Yaman, K., Dölek, S., & Arslan, G. (2025). Performance analysis of a thermoelectric generator (TEG) for waste heat recovery. *WAPRIME, 2*(1), 13-20.

CHAPTER 10

ADVANCES IN THERMAL COMFORT WITH MACHINE LEARNING APPLICATIONS

M. ÖZGÜN KORUKÇU[1]

Introduction

This chapter aims to fill the gap between thermal comfort and machine learning fields. Advances in thermal comfort regarding machine learning applications are reviewed, and how machine learning can be used in thermal comfort are explained.

Since thermal comfort is a concept that includes personal preferences, several definitions appear in the literature. According to Aybers (1978), it is the state in which no discomfort arises from temperature or other air conditions; Anonymous (1993a) describes it as the state of being pleased with the thermal environment; (Anonymous, 1993b) defines it as the condition in which minimal physiological effort is required to regulate internal body temperature; and (Anonymous, 1995) characterizes thermal comfort as the conditions under which the thermal environment is satisfactory. Thermal comfort depends on both environmental and

---

[1] Prof. Dr., University of Bursa Uludağ, Department of Mechanical Engineering, Orcid: 0000-0002-4761-4304

personal factors. Figure 1 shows the environmental and personal factors that influence thermal comfort.

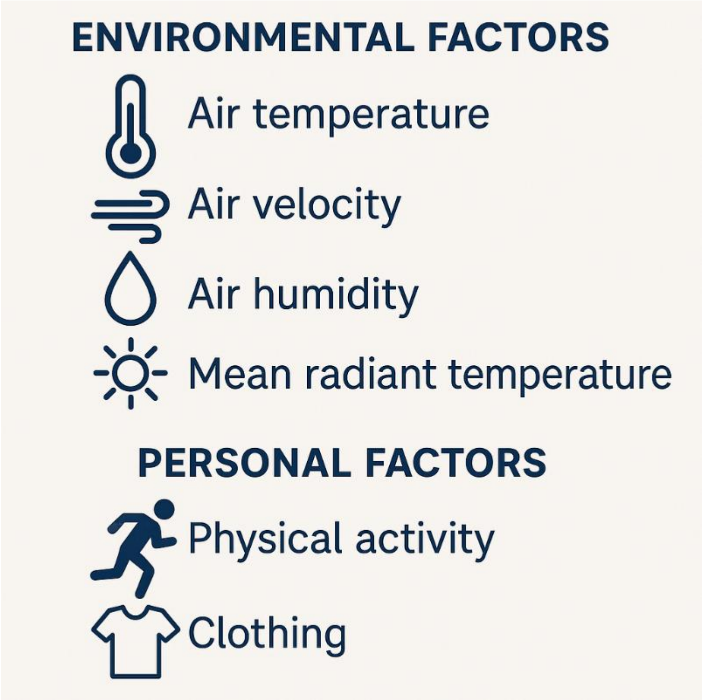

Figure 1 Thermal comfort parameters.

Artificial intelligence (AI) is a scientific field concerned with the development of systems that enable computers to exhibit human-like intelligence. AI typically seeks to imitate human cognitive capabilities such as learning, problem-solving, reasoning, perception, and language processing. There are various definitions of AI. According to Britannica, artificial intelligence is defined as "the ability of a digital computer or computer-controlled robot to perform tasks commonly associated with intelligent beings" (Britannica, n.d.). Another source describes AI as the design and development of intelligent agents—systems that perceive their environment and act to achieve their goals (Russel & Norvig, 2010).

The idea that machines could think like humans was first proposed by Turing. He reformulated the question "Can machines think?" through a more concrete, test-based approach known as the "Imitation Game." This test aims to evaluate whether a machine can demonstrate human-like intelligence. Turing emphasized the "universal" qualities of digital machines, arguing that digital computers could perform tasks similar to human intelligence. The paper addresses objections related to mathematical limitations, consciousness arguments, and human-machine differences, and Turing suggests that machines could develop the ability to "learn" through training processes (Turing, 1950). This forms one of the foundational pillars of the modern understanding of artificial intelligence. AI includes subfields such as Machine Learning, Deep Learning, Natural Language Processing, Neural Networks, and Image Processing.

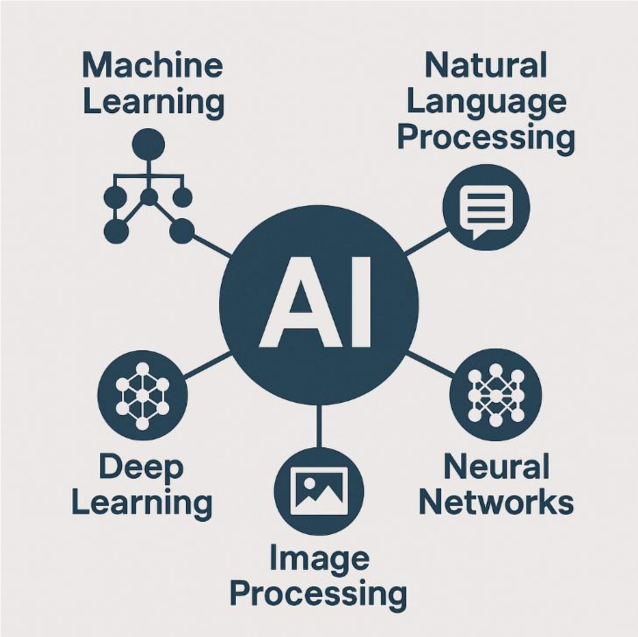

Figure 2 Artificial Intelligence subfields.

There are several studies regarding thermal comfort with machine learning. Recent research in this field is investigated and reviewed.

Yu et al. (Yu et al., 2025) investigated the integration of reinforcement learning (RL) within an urban climate modeling framework to assess how RL-based HVAC control influenced indoor comfort, energy efficiency, and local urban climate. Their results showed that RL improved performance relative to default control strategies, although the magnitude of improvement varied by climatic region, with warmer cities benefiting more. RL-driven control strategies altered indoor temperatures and introduced subtle changes in outdoor urban climate, demonstrating the two-way interactions between buildings and their surroundings. The authors also found that RL models trained in cities with greater seasonal variability transferred more effectively to other climates, indicating the value of cross-city learning. Overall, the study highlighted the need for climate-sensitive RL design and suggested future developments toward multi-objective learning and fully coupled global simulations.

Al Sayed et al. (Al Sayed et al., 2024) conducted a comprehensive technical and conceptual review of reinforcement learning (RL) applications for HVAC control in intelligent buildings. They analyzed studies published since 2019 and showed that RL offered promising adaptability compared to traditional controllers but remained sparsely deployed in real buildings (only 23% of cases). Their review revealed that most training environments lacked realistic variability in external factors such as occupancy, pricing, and weather, leading to poor generalization and high computational retraining costs. The authors argued that metareinforcement learning could improve adaptability by training agents across diverse tasks, reducing retraining needs. Overall, the review highlighted the methodological gaps hindering real-world adoption and emphasized future research directions focusing on scalable, generalizable RL deployment.

Sun et al. (Sun et al., 2024) conducted a comprehensive review of 90 peer-reviewed studies to evaluate how artificial intelligence has been applied to personalised indoor comfort across thermal, air quality, acoustic, and visual domains. They found that research overwhelmingly prioritised thermal comfort, representing 97.75% of existing studies, while indoor air quality, acoustics, and visual comfort remained substantially under-explored. Their analysis showed that AI models such as neural networks, support vector machines, and random forests achieved high prediction accuracy but rarely integrated multidimensional or human-centric indicators such as physiology, psychology, or behaviour. The authors proposed a multidimensional framework that fused environmental and personal factors to guide future model development and highlighted critical gaps in cross-domain modelling, real-world adaptability, and privacy-aware data handling. Overall, the review emphasised the need for holistic, inclusive, and ethically grounded AI-driven comfort systems in the built environment.

Togashi (Togashi, 2025) conducted a systematic review of 79 studies to analyse how reinforcement learning reward functions were designed for HVAC control, highlighting their impact on energy–comfort optimisation. The study revealed 68 unique reward formulations, demonstrating substantial heterogeneity that hindered comparability and lacked theoretical justification for weighting choices. The author also identified four common design techniques—occupancy consideration, comfort deadbands, error exponentiation, and acceptable limits—but found no consistent methodological pattern for combining them. Based on these findings, the paper proposed a structured, piecewise reward function framework to provide a common baseline while preserving RL flexibility. Overall, the review underscored the need for more principled reward formulation and greater standardisation to advance RL-based HVAC optimisation research.

Adibhesami and Hassanzadeh (Adibhesami & Hassanzadeh, 2025) investigated the integration of advanced HVAC technologies with reinforcement learning (RL) controllers to improve energy performance and thermal comfort in low-energy buildings under Tehran’s extreme climate conditions. Their simulations showed that deep RL outperformed conventional Q-learning, reducing energy use intensity by 25% (from 250 to 200 kWh/m² annually) and bringing predicted mean vote values into the ASHRAE comfort range, while reducing dissatisfaction levels from 40% to 10%. The deep RL model also achieved ~50% higher prediction accuracy, enabling more adaptive temperature regulation in response to changing occupancy and weather patterns. When compared with rule-based and model predictive control schemes, RL delivered additional savings of 10–15% while using fewer input features, demonstrating strong operational robustness. Overall, the study highlighted RL-based HVAC control as a viable pathway for sustainable urban building management in hot-arid climates, while recommending real-world pilots and multi-objective optimization for future research.

Gharbi et al. (Gharbi et al., 2025) performed a comparative simulation study to evaluate the performance of reinforcement learning (RL) versus traditional proportional–integral–derivative (PID) control for HVAC operation in dynamic building environments. They showed that while PID maintained stability under predictable conditions, RL significantly improved energy efficiency and thermal comfort by adapting to disturbances such as occupancy spikes and weather fluctuations. Their model-free Q-learning framework autonomously optimized setpoints using real-time sensor data, achieving smoother temperature regulation and up to 55% energy savings relative to PID. The authors also demonstrated that RL produced tighter comfort bounds and reduced oscillatory behaviour, although at the cost of higher training complexity. Overall, the study highlighted RL's potential to transform building energy management by enabling scalable, adaptive HVAC control beyond the limitations of conventional rule-based strategies.

Su et al. (Su et al., 2025) developed an explainable reinforcement learning (XRL) framework to regulate multi-zone household HVAC systems while simultaneously reducing demand response (DR) costs and maintaining personal thermal comfort. They introduced an explainable proximal policy optimization (XPPO) algorithm that replaced opaque neural networks with interpretable decision trees, enabling legal compliance with explainability requirements in regions such as China, the EU, and the U.S. Simulation results showed that XPPO reduced electricity cost by 22.4% compared with non-DR operation and achieved convergence within 15 minutes on standard hardware, outperforming conventional genetic and deep RL methods in efficiency and transparency. The approach successfully preserved indoor temperatures within user comfort limits even under environmental uncertainty, demonstrating superior adaptability relative to PPO, DDPG, and fuzzy logic controllers. Overall, the study highlighted XRL as a promising pathway toward legally transparent, efficient, and user-centric HVAC optimization in smart homes.

Roussel et al. (Roussel et al., 2025) carried out a comparative case study to evaluate the performance of seven artificial intelligence models for temperature prediction in a large industrial building. Their results showed that Gradient Boosting algorithms—particularly XGBoost and LightGBM-achieved the highest accuracy, with XGBoost reaching a mean absolute error of 0.32 °C for a 5-minute prediction horizon, outperforming deep learning methods such as LSTM, GRU, and CNN architectures. The authors demonstrated that model choice needed to reflect building physics, as the low thermal inertia and rapid heating response favored decision-tree-based approaches over complex neural networks. Feature importance analysis further revealed that external temperature and heating relay states were the dominant predictors of indoor thermal behavior. Overall, the study highlighted that well-tuned Gradient Boosting models offered an efficient pathway for industrial thermal management, contributing to predictive control, energy savings, and improved comfort under Industry 4.0 applications.

Upasani et al. (Upasani et al., 2025) examined how self-reported comfort perceptions could be interpreted through machine learning to better understand thermal comfort dynamics in buildings. They collected environmental, physiological, and subjective labeling data, then applied explainable models—including SHAP and partial dependence analysis—to identify the drivers of thermal satisfaction. Their results showed that air temperature, radiant temperature, and metabolic rate were the dominant predictors of comfort perception, though individual-level interpretation varied substantially. The study demonstrated that interpretable machine learning could reveal nonlinear comfort relationships and enable personalised comfort insights beyond traditional heat-balance models. Overall, the authors highlighted that explainability tools were essential for translating black-box models into actionable indoor comfort strategies and for supporting human-centric smart building operation.

Amangeldy et al. (Amangeldy et al., 2025) conducted a pilot study to classify thermal comfort responses in young adults using multimodal sensing and machine learning. They collected environmental data, wearable physiological signals, and self-reported comfort scores in a controlled space, then evaluated multiple classifiers, including random forests, support vector machines, and deep learning models. Their results showed that contextual-feature–augmented models achieved the highest accuracy in predicting ASHRAE 7-point comfort votes, demonstrating that comfort recognition improved substantially when physiological and contextual variables were combined. SHAP-based explainability analysis revealed that relative humidity, heart rate variability, and temperature were the dominant predictors influencing thermal perception. Overall, the study highlighted the promise of context-aware ML for personalised comfort assessment and recommended larger-scale experiments for improving model generalizability.

Almadhor et al. (Almadhor et al., 2025) developed a digital twin–driven deep learning framework to predict personalised thermal comfort while enabling energy-efficient HVAC operation in smart buildings. Their system combined real-time sensor data, long short-term memory (LSTM) networks, and an attention mechanism to dynamically capture temporal and spatial variations in indoor environments. The results showed that the model outperformed conventional deep learning architectures, achieving higher comfort prediction accuracy and enabling proactive HVAC adjustments that reduced energy consumption. The authors also demonstrated that digital twin integration improved model interpretability and adaptability by linking virtual simulations with measured building behaviour. Overall, the study highlighted the potential of digital twin–based AI approaches for personalised comfort management and future applications in intelligent building automation.

Avci (Avci, 2025) applied machine learning techniques to predict thermal comfort by incorporating contextual factors such as building type, climate zone, ventilation strategy, and seasonal variation. Using over 61,000 samples from the ASHRAE Global Thermal Comfort Database II, eight models were trained, and XGBoost achieved the best performance after hyperparameter tuning. The results showed that macro-contextual variables—particularly climate class and season—were more influential in predicting thermal sensation than conventional indoor parameters such as air temperature and humidity. The study demonstrated that including broader contextual factors improved model generalizability but reduced precision relative to approaches using physiological data. Overall, the research highlighted the trade-off between accuracy and applicability in thermal comfort modelling and emphasized the value of scalable machine learning frameworks for building design and policy.

Jacob et al. (Jacob, 2024) evaluated machine learning models to benchmark personal thermal comfort by training classifiers on sensed environmental and physiological data. Their results showed that decision trees, k-nearest neighbors, neural networks, support vector machines, AdaBoost, and particularly random forests achieved classification accuracies above 70%, with random forests exceeding 75%. The study demonstrated that a small set of strongly correlated features—mean wrist temperature, air temperature, humidity, and preference labels—enabled robust comfort prediction. The authors highlighted limitations related to small open-source datasets but presented a systematic modeling framework suitable for occupant-centric HVAC control. Overall, the work established new benchmark performance levels for personal comfort modeling and illustrated the feasibility of lightweight ML approaches for adaptive cooling applications.

Briegel et al. (Briegel et al., 2024) developed a multi-scale machine learning framework to map outdoor human thermal comfort at high spatial resolution across urban environments. They combined remote sensing data, micro-meteorological simulations, and statistical downscaling to generate minute-scale Universal Thermal Climate Index (UTCI) predictions with ~200 m spatial precision. Their results showed that the model successfully captured local heat stress dynamics—including heat-retention patterns, shading effects, and surface type influences—which are typically invisible in coarse city-scale models. Validation demonstrated strong agreement with ground-based measurements, confirming that machine learning enhanced both temporal and spatial sensitivity. Overall, the study highlighted the potential of data-driven approaches for fine-grained heat-risk assessment, urban planning, and climate adaptation strategies.

Assymkhan and Kartbayev (Assymkhan & Kartbayev, 2024) designed an IoT-enabled indoor thermal comfort prediction system using machine learning algorithms, specifically support vector machines (SVM) and random forests. They deployed environmental sensors in real buildings to collect temperature, humidity, and airflow data, which served as inputs to train comfort classification models. Experimental results showed that both SVM and random forest models effectively recognised thermal comfort states, with random forests demonstrating higher robustness under varying indoor conditions. The authors highlighted the benefits of remote monitoring and automated comfort assessment for smart building management. Overall, the study demonstrated the feasibility of integrating ML with IoT infrastructure to improve indoor comfort awareness and control capability.

Karyono et al. (Karyono et al., 2024) developed and validated an artificial intelligence model to determine indoor thermal comfort with greater accuracy than conventional analytical methods. Using field measurement data from actual buildings, the researchers calibrated machine learning algorithms to classify comfort states and compared their outputs against standard indices. Their results showed that the AI model achieved high agreement with occupant responses and improved prediction capability in naturally ventilated environments where conventional methods typically underperformed. The study demonstrated that AI captured nonlinear interactions between environmental variables, offering more realistic comfort mapping across diverse indoor conditions. Overall, the authors concluded that artificial intelligence provided a more adaptive and context-aware approach to comfort assessment suitable for smart building applications.

Kocaman et al. (Kocaman et al., 2024) examined how demographic characteristics influence thermal sensation and satisfaction and evaluated machine learning models for predicting these responses. Using survey and environmental data collected from mixed-mode office buildings in İzmir, they showed that gender, age, and thermal history significantly affected perceived sensation, while education and income were more strongly associated with satisfaction levels. Their comparative analysis demonstrated that Random Forest and K-Nearest Neighbors provided the most accurate thermal sensation predictions, whereas Decision Trees and Random Forest best captured satisfaction outcomes, with model accuracies reaching up to 99% in some cases. The study highlighted that incorporating demographic features improved prediction capability relative to conventional comfort indices such as PMV. Overall, the authors concluded that demographic-aware machine learning offers a viable pathway for more personalised comfort assessment and adaptive indoor environment control.

Boutahri and Tilioua (Boutahri & Tilioua, 2024) developed a machine-learning-based predictive framework to estimate thermal comfort and enhance HVAC energy efficiency in smart buildings. Using environmental and occupant-feedback data collected through Raspberry Pi sensor networks and post-occupancy surveys, they trained four algorithms: Support Vector Machines, Artificial Neural Networks, Random Forests, and XGBoost. Their findings showed that Random Forest and XGBoost achieved the highest prediction accuracy, outperforming SVM and ANN in estimating Predicted Mean Vote (PMV) values, with R^2 values exceeding 0.96. The study demonstrated that HVAC control systems could improve both comfort conditions and energy use when equipped with data-driven predictive models. Overall, the authors concluded that ML-based control strategies offered a promising path for intelligent building operation and recommended future exploration of reinforcement learning and model predictive control for real-time optimization.

Xi et al. (Xi et al., 2024) investigated indoor thermal comfort in traditional “Hankou Lifen” dwellings and compared it with modern residences using field measurements, surveys, and machine-learning models. Their results showed that traditional houses exhibited poorer thermal performance, higher humidity, inadequate ventilation, and lower comfort scores due to ageing construction and altered passive design features. Linear regression models indicated that residents in old dwellings had higher neutral temperatures and narrower acceptable comfort ranges, particularly among elderly occupants with reduced heat tolerance. Machine learning approaches—especially XGBoost and LightGBM—outperformed conventional PMV-based predictions and revealed that operative temperature, mean radiant temperature, and humidity were dominant predictors of comfort, while personal factors such as age, floor level, and metabolic rate also played notable roles. Overall, the study demonstrated that data-driven models enhanced understanding of comfort dynamics in heritage buildings and supported strategies for their sustainable renovation and climate adaptation.

As observed, numerous studies have been conducted on machine learning (ML), which is a subfield of artificial intelligence (AI), in the context of thermal comfort. The suitability of ML models in thermal comfort research depends on the specific objectives and characteristics of the study. Table 1 presents a general evaluation of commonly used ML models and their appropriateness for thermal comfort applications.

The key considerations for model selection in these studies are provided in Tables 1 and 2. In Table 1, supervised learning models, and in Table 2, unsupervised learning models are given.

The key considerations for model selection in these studies are provided in Table 3.

Table 4 offers several recommendations based on the applications of ML models. Naturally, each model has its own strengths and limitations. Therefore, the selection should be made based on the dataset, computational constraints, and the desired outcomes.

Table 1 Supervised learning models.

SUPERVISED LEARNING MODELS	
These models are suitable for predicting thermal comfort indices (e.g., PMV, TSV) when labeled data (thermal comfort feedback) are available.	
Regression Models:	
Linear Regression	Simple and interpretable. Suitable for modeling linear relationships between input variables (e.g., temperature, humidity) and thermal comfort indices. *Use Case:* Predicting PMV based on variables such as air temperature, relative humidity, and clothing insulation (CLO).
Support Vector Regression (SVR):	Suitable for small datasets. Captures nonlinear relationships. *Use Case:* Predicting thermal comfort under complex indoor environmental conditions.
Tree-Based Models:	
Random Forest (RF):	Effectively handles nonlinear relationships and variable interactions. Appropriate for studies containing mixed numerical and categorical data. Robust against outliers and missing data. *Use Case:* Estimating thermal sensation in diverse environments.Farklı ortamlarda ısıl duyum tahmini.
Gradient Boosting Machines (GBM, XGBoost, LightGBM, CatBoost):	Provide higher accuracy than Random Forest for smaller datasets. Capable of capturing fine-grained patterns. *Use Case:* Optimizing thermal comfort parameters with a focus on energy efficiency.

Table 2 Unsupervised learning models.

UNSUPERVISED LEARNING MODELS	
These models are suitable for clustering and grouping thermal comfort preferences without the need for labeled data.	
K-means and K-means++	Simple and effective for grouping individuals with similar thermal preferences. Suitable for studies aiming to segment comfort zones. *Use Case:* Grouping individuals based on clothing insulation and air temperature preferences.
Hierarchical Clustering	Suitable for small datasets with complex relationships. Provides a visual dendrogram for analyzing clusters. *Use Case:* Analyzing seasonal variations in thermal comfort preferences.
Gaussian Mixture Models (GMMs)	More flexible than K-means and capable of capturing overlapping clusters. Appropriate for datasets with uncertain or fuzzy boundaries. *Use Case:* Clustering thermal sensation votes.
HYBRID AND ADVANCED MODELS	
Bayesian Neural Networks (BNN)	Capture uncertainty, making them suitable for personalized thermal comfort modeling. *Use Case:* Dynamically adjusting indoor settings based on real-time predictions.
Reinforcement Learning (RL)	Used for adaptive control of indoor environments. Optimizes thermal comfort and energy efficiency in real time. *Use Case:* Smart HVAC systems that learn user preferences and adapt accordingly.

Table 3 The key considerations for model selection.

Data Availability:

Labeled Data: Supervised learning (e.g., Random Forest, ANN).
Unlabeled Data: Unsupervised learning (e.g., K-means++).

Data Complexity:

Linear Relationships: Linear Regression.
Nonlinear Relationships: Random Forest, ANN, or SVR.

Dataset Size:

Small: SVR, K-means, or Random Forest.
Large: ANN, Gradient Boosting.

Computational Resources:

Low: Linear Regression, K-means.
High: ANN, Gradient Boosting.

Objective:

Prediction: Supervised models (e.g., SVR, ANN).
Clustering: Unsupervised models (e.g., K-means, GMM).

Table 4 ML Model Recommendations Based on Use Cases in Thermal Comfort Studies

Group Comfort Analysis: K-means++ or Hierarchical Clustering.

Personalized Comfort Prediction: ANN or Random Forest.

Energy Optimization: Reinforcement Learning or Gradient Boosting.

Real-Time Applications: Bayesian Neural Networks or RL.

Conclusion

Thermal comfort is a challenging domain due to the large number of interacting parameters that influence human perception and environmental conditions. Traditional approaches are often insufficient for accurately characterizing or predicting thermal comfort, especially in dynamic and personalized indoor environments. In parallel, artificial intelligence has become increasingly prevalent across scientific and engineering fields, offering new opportunities for modelling complex systems.

In this book chapter, recent thermal comfort studies employing machine learning—an important subfield of artificial intelligence—were examined in detail. Commonly used machine learning models were briefly explained, and guidance was provided on their applicability under different research conditions. Furthermore, the advantages and limitations of these models were critically assessed to support appropriate selection and implementation in future work.

It is anticipated that this chapter will be beneficial for researchers and practitioners working in heating, ventilation, air conditioning (HVAC), energy optimization, indoor environmental quality, and thermal comfort modelling. By presenting an integrated overview of machine learning approaches in thermal comfort research, this study aims to support more robust, adaptive, and data-driven decision-making in the field.

References

Adibhesami, M. A., & Hassanzadeh, A. (2025). *Optimizing HVAC energy efficiency in low-energy buildings : a comparative analysis of reinforcement learning control strategies under Tehran climate conditions*. https://doi.org/10.1017/dce.2025.10014

Al Sayed, K., Boodi, A., Sadeghian, R., & Beddiar, K. (2024). Reinforcement learning for HVAC control in intelligent buildings : A technical and conceptual review. *Journal of Building Engineering*, *95*(June), 110085. https://doi.org/10.1016/j.jobe.2024.110085

Almadhor, A., Ghazouani, N., Bouallegue, B., & Kryvinska, N.

(2025). *Digital twin based deep learning framework for personalized thermal comfort prediction and energy efficient operation in smart buildings*. 1–17.

Amangeldy, B., Imankulov, T., Tasmurzayev, N., & Aibagarov, S. (2025). *A Pilot Study on Thermal Comfort in Young Adults : Context-Aware Classification Using Machine Learning and Multimodal Sensors*. 1–30.

Anonymus. 1993a). ASHRAE handbook – Fundamentals, chapter 8. Atlanta: American Society of Heating, Refrigeration and Air-Conditioning Engineers. 29p.

Anonymous. (1993b). *"ASHRAE handbook – Fundamentals, chapter 37", Atlanta: American Society of Heating, Refrigeration and Air-Conditioning Engineers, 1993*. 1993.

Anonymous. (1995). *"ISO 7730, Moderate thermal environments – Determination of the PMV and PPD indices and specification of the conditions for thermal comfort", International Organization for Standardization, Geneva, 1995*. 7730.

Assymkhan, N., & Kartbayev, A. (2024). *Advanced IoT-Enabled Indoor Thermal Comfort Prediction Using SVM and Random Forest Models*. *15*(8), 1040–1050.

Avci, A. B. (2025). Machine learning-based prediction of thermal comfort : exploring building types , climate , ventilation strategies , and seasonal variations. *Building Research & Information*, *3218*, 1–18. https://doi.org/10.1080/09613218.2025.2462932

Aybers, N. 1978. Isıtma, havalandırma ve iklim tesisleri. Uçer Matbaacılık, 9-25s.

Boutahri, Y., & Tilioua, A. (2024). Results in Engineering Machine learning-based predictive model for thermal comfort and energy optimization in smart buildings. *Results in Engineering*, *22*(January), 102148. https://doi.org/10.1016/j.rineng.2024.102148

Briegel, F., Wehrle, J., Schindler, D., & Christen, A. (2024). *High-*

resolution multi-scaling of outdoor human thermal comfort and its intra-urban variability based on machine learning. 1667–1688.

Britannica. (n.d.). *https://www.britannica.com/technology/artificial-intelligence*.

Gharbi, A., Ayari, M., Albalawi, N., & Touati, Y. El. (2025). *Intelligent HVAC Control : Comparative Simulation of Reinforcement Learning and PID Strategies for Energy Efficiency and Comfort Optimization*. 1–16.

Jacob, J. C. (2024). *A Machine Learning Approach to Benchmark Thermal Comfort*. 363–368. https://doi.org/10.1145/3671127.3699676

Karyono, K., Abdullah, B. M., Cotgrave, A., Bras, A., & Cullen, J. (2024). Engineering Applications of Artificial Intelligence Field studies of the Artificial Intelligence model for defining indoor thermal comfort to acknowledge the adaptive aspect. *Engineering Applications of Artificial Intelligence*, *133*(PD), 108381. https://doi.org/10.1016/j.engappai.2024.108381

Kocaman, E., Kuru, M., & Calis, G. (2024). Machine learning thermal comfort prediction models based on occupant demographic characteristics. *Journal of Thermal Biology*, *123*(June), 103884. https://doi.org/10.1016/j.jtherbio.2024.103884

Roussel, J., Lafhaj, Z., Yim, P., Danel, T., & Ducoulombier, L. (2025). *Performance of Various Artificial Intelligence Models for Predicting Temperature in an Industrial Building — A Case Study*. 1–27.

Russel, S., & Norvig, P. (2010). Artificial intelligence. In *Artificial Intellegence: A Modern Approach (3rd Edition)* (Vol. 4). https://doi.org/10.1109/ICCAE.2010.5451578

Su, Y., Xu, M., Liu, X., Tan, M., Wang, R., & Yang, C. (2025). *Explainable reinforcement learning for enhancing personal thermal comfort and optimizing demand response in household multi-zone HVAC system*.

Sun, S., Li, H., & Khudhair, A. L. I. (2024). *A Comprehensive Literature Review of Personalised Indoor Comfort : Artificial Intelligence Approaches and Applications. 2021.*

Togashi, E. (2025). Energy & Buildings Reward function design in reinforcement learning for HVAC Control : A review of thermal comfort and energy efficiency Trade-offs. *Energy & Buildings*, *348*(August), 116439. https://doi.org/10.1016/j.enbuild.2025.116439

Turing, A. (1950). On Computing Machinery and Intelligence. *Mind*, *49*, 433–460. https://doi.org/10.1007/978-3-319-53280-6_11

Upasani, N., Guerra, O., & Joosstens, F. (2025). *Understanding thermal comfort using self - reporting and interpretable machine learning.*

Xi, H., Wang, B., & Hou, W. (2024). Machine learning-based prediction of indoor thermal comfort in traditional Chinese dwellings : A case study of Hankou Lifen. *Case Studies in Thermal Engineering*, *61*(August), 105048. https://doi.org/10.1016/j.csite.2024.105048

Yu, J., Schreck, J. S., Gagne, D. J., Oleson, K. W., Li, J., Liang, Y., Liao, Q., Sun, M., Topping, D. O., & Zheng, Z. (2025). *Reinforcement Learning (RL) Meets Urban Climate Reinforcement Learning (RL) Meets Urban Climate Modeling : Investigating the Efficacy and Impacts of RL-Based HVAC Control.*

CHAPTER 11

The Nuclear Energy Renaissance in Maritime: A Strategic Outlook for a Carbon-Neutral Future

Mehmet Ali KALLİOĞLU[1]

Introduction

Environmental pollution and associated climate change constitute a major source of global concern. In this context, reducing greenhouse gas (GHG) emissions stands out as a primary objective for various industries. The maritime transport sector possesses an undeniably negative environmental impact (Bayraktar and Yüksel 2023). According to the International Energy Agency's 2023 report, international shipping is responsible for approximately 5% of energy-related emissions and roughly 700 million tons (Mt) of annual carbon dioxide (CO_2) emissions. Furthermore, since 2008, both global trade volume and international transport activities have increased by nearly 50%. Parallel to this increase, energy use in the transport sector has risen by 5%, with the sector's oil consumption reaching 4.2 million barrels per day (mb/d) in 2023 (How the shipping sector could save on energy costs – Analysis 2025).

To address these challenges and implement global decarbonization strategies, the International Maritime Organization

---

[1] Assistant Professor, Batman University, Besiri OSB Vocational School, Orcid: 0000-0002-6874-1564

(IMO) has adopted comprehensive measures over the last decade to reduce greenhouse gases originating from maritime transport. The IMO has set targets for a minimum of 40% reduction in carbon emissions by 2030, at least 80% by 2040, and net-zero emissions by 2050, compared to 2008 levels (MEPC 2023). Consistent with the long-term temperature goal of the Paris Agreement, this target commits to the gradual reduction and eventual elimination of emissions (Fetting 2020). In this regard, Nuclear Energy (NE) is identified as a significant alternative energy source for marine vessels within the scope of the IMO's decarbonization and fuel efficiency activities (Bayraktar and Yüksel 2023). Due to its high and sustainable energy density compared to other potential alternative marine fuels, and its unique status as the only technology offering the potential to simultaneously eliminate various emission types (CO_2, CH_4, NO_x, SO_x, and Particulate Matter), nuclear propulsion is projected to play a critical role in the decarbonization of the maritime sector (Schøyen and Steger-Jensen 2017).

Nuclear marine propulsion took its initial steps with pioneering military and civil vessels. While demonstrating technology’s potential, these early trials also revealed significant economic and operational challenges. Historically, nuclear marine propulsion originated as military technology. The USS Nautilus submarine, commissioned in the 1950s, marked the first revolutionary step in this field. Unlike traditional diesel-electric submarines, Nautilus was capable of operating for weeks without surfacing or refueling. This capability created a strategic revolution in submarine operations and rendered nuclear power indispensable in the military domain (Carlton, Smart, and Jenkins 2011).

Following this military success, the US-built NS Savannah became the first civil nuclear ship in 1962. This development was followed by Germany's cargo/research vessel Otto Hahn in 1968 and Japan's Mutsu in 1970. Although these pioneering vessels were technically successful, they failed to achieve commercial sustainability due to high operating costs, complex fuel cycles, and political restrictions regarding port access (Freire and de Andrade 2015). The sole exception to this trend is Russia's nuclear icebreaker fleet, which represents the most successful and economically imperative application of nuclear propulsion in the commercial sector. Thanks to their ability to operate for extended periods without refueling under harsh Arctic conditions, these vessels enable year-round navigation of the Northern Sea Route.

Table 1. Summary of Key Literature on Nuclear Propulsion in Commercial Shipping

Name	Country	Ship Type	Period /Status	Key Features and Outcomes
Savannah	USA	Passenger / Cargo (Mixed)	1962–1970 (Withdrawn from service)	• Proved the technical feasibility of commercial nuclear propulsion but was not considered economically viable. • The first commercial nuclear-powered ship. • Rated power: 80 MW.
Otto Hahn	Germany	Ore Carrier / Research	1968–1979 (Converted)	• One of the earliest ships to use an integrated pressurized water reactor concept (iPWR). • Excellent technical reliability; however, due to lack of commercial feasibility, it was later converted to diesel propulsion.
Mutsu	Japan	Special Cargo /Research	1974 (Trials) – 1990s	• Failed to achieve commercial success due to shielding-related technical issues (radiation leakage) and public opposition. • Rated power: 36 MW.

Sevmorput	USSR / Russia	LASH (Barge Carrier) / Container	1988–Present (In service)	• The only nuclear-powered cargo ship still in service. • Has icebreaking capability and operates on the Northern Sea Route (NSR). • Uses a KLT-40 reactor with 135 MWt thermal power.

The historical development of commercially oriented nuclear-propelled ships is summarized in Table 1. The cases of NS Savannah, NS Otto Hahn, NS Mutsu, and Sevmorput demonstrate that nuclear propulsion is technically feasible in maritime applications; however, its implementation has been limited to a small number of vessels and, in most cases, to relatively short service periods. Figure 1 presents images of these ships.

Figure 1. Historical nuclear-powered merchant and cargo vessels: (a) NS Savannah (United States), (b) NS Otto Hahn (Germany), (c) NS Mutsu (Japan) and (d) Sevmorput (Soviet Union/Russia).

While the potential of nuclear propulsion in commercial shipping has long been a subject of debate, recent literature indicates a growing body of research examining both technological suitability and regulatory and socio-economic barriers within a holistic framework. Early applications (Savannah, Otto Hahn, Mutsu) demonstrated technical feasibility; however, widespread adoption was not achieved due to limited port access, high costs, and issues regarding public perception (Freire and Andrade 2015; Schøyen and Steger-Jensen 2017). Current research emphasizes that next-generation Small Modular Reactors (SMRs) and Molten Salt Reactors (MSRs) significantly enhance viability for commercial fleets, owing to their higher safety standards, passive cooling mechanisms, and compact reactor architectures (Ghimire and Waller 2023).

The consensus in the literature indicates that nuclear propulsion constitutes a robust alternative, particularly for deep-sea shipping, due to advantages such as zero operational emissions, high power density, long range, and fuel price stability. It is noted that these advantages align closely with the IMO's 2050 carbon-neutral targets. However, the majority of studies indicate that significant gaps exist in areas such as a harmonized international regulatory framework, political acceptance, and port access, rather than in technical feasibility (Duong et al. 2025).

Furthermore, ensuring nuclear *safety* and nuclear *security* requirements, along with establishing a high security culture against accidents, sabotage, and cyber threats, are recurrent critical themes in the literature (Constantin and Subki n.d.) Economic evaluations point towards a competitive Total Cost of Ownership (TCO) in the long term, driven by the low and stable cost of nuclear fuel, despite high initial investment costs. Nevertheless, it is emphasized that uncertain liability and insurance mechanisms pose a serious barrier to commercial widespread adoption. Recent studies suggest that these barriers can be overcome through a clarified liability regime in international law and financial risk-sharing models (Navigating nuclear energy in maritime. | LR n.d.).

While the existing literature on nuclear propulsion provides valuable historical, technical, regulatory, and economic insights, it remains fragmented across diverse research themes. Table 2 summarizes key academic contributions in chronological order, highlighting the evolution of nuclear marine technologies, recurring challenges identified by researchers, and specific gaps that this study addresses through a TOWS-based strategic assessment. This mapping demonstrates that, although technological feasibility has long been recognized, persistent regulatory, economic, and socio-political barriers continue to shape the prospects of nuclear propulsion in commercial shipping.

Table 2. Summary of Key Literature on Nuclear Propulsion in Commercial Shipping

Authors / Year	Research Focus	Reactor Type / Technology	Key Findings	Identified Gap
(Vergara and McKesson 2002)	Economic feasibility of nuclear propulsion for high-performance cargo vessels	PWR	Demonstrated that nuclear propulsion becomes economically competitive for long-range, high-power ships.	Lacks comparison with modern carbon pricing mechanisms (ETS) and alternative e-fuel pathways.
(Roscini 2002)	International legal status of nuclear-powered ships	–	Highlighted port-state denial rights and unresolved legal ambiguity under international law.	Provides no strategic or regulatory solutions.
(Carlton et al. 2011)	Engineering and safety requirements for nuclear ships	PWR	Addressed shielding, stability, collision protection, and design constraints for nuclear vessels.	Not connected to strategic assessments of opportunities or threats.
(Hirdaris et al. 2014)	Potential application of SMRs in commercial shipping	SMR & PWR	Demonstrated that SMRs can be integrated into ship design and offer safety advantages, but regulatory gaps persist.	Limited to technical aspects; does not address fuel cycle, port acceptance, or geopolitical risks.
(Freire and Andrade 2015)	Historical analysis of nuclear merchant ships	PWR	Confirmed technical operability of nuclear ships but emphasized economic, socio-political, and port-access failures.	Does not link historical lessons to opportunities arising from modern SMR/MSR technologies.

(Schøyen and Steger-Jensen 2017)	Historical insights and future implications for nuclear propulsion	PWR	Showed that nuclear propulsion is technically sound but economically constrained; port-state acceptance is a major obstacle.	Does not evaluate modern financing models (leasing, PaaS) or their applicability.
(Chen et al. 2020)	Incident classification for marine nuclear power plants	Marine Nuclear Power Plants	Proposed a new INES-like classification method based on defense-in-depth and radiological impact criteria.	Focuses on safety culture; does not address commercialization or economic feasibility.
(Kunze 2022)	Role of Gen-IV reactors in maritime decarbonization	MSR, HTGR, SMR	Identified Gen-IV reactors as highly promising due to passive safety and high energy density.	Does not provide a strategic roadmap or cross-sector adoption framework.
(Wang, Zhang, and Zhu 2023)	Environmental challenges and regulatory gaps in nuclear maritime applications	SMR & PWR	Identified major gaps in liability, governance, and port-state acceptance.	No TOWS-based strategy or regulatory mitigation model.
(Bayraktar and Yüksel 2023)	SWOT–AHP assessment of nuclear propulsion	SMR & PWR	Found strong strengths (zero emissions, high power) but major regulatory and perceptual weaknesses.	SWOT outcomes not translated into actionable TOWS strategies.
(Bayraktar and Pamik 2023)	Comparison of nuclear vs. fossil icebreakers using VIKOR	PWR	Confirmed operational superiority of nuclear icebreakers; fossil-fuel ships remain cost-competitive.	Focuses on icebreakers only; findings not generalized to commercial freight shipping.

(Wang 2025)	Legal and policy framework for integrating nuclear power into maritime applications	FNPP (Floating Nuclear Power Plants)	Demonstrated that current regulations (SOLAS, INF Code) are insufficient; national legal reforms are emerging.	Clarifies regulatory gaps but lacks integration with technical and economic dimensions.
(Duong et al. 2025)	Nuclear propulsion as a sustainable solution for maritime decarbonization	SMR	Showed strong alignment of SMRs with global decarbonization targets.	Does not examine external constraints such as insurance, geopolitics, and port acceptance.
(Navigating nuclear energy in maritime. | LR n.d. 2025)	Future outlook for the use of nuclear energy in maritime transport	SMR & PWR	Highlights the potential role of nuclear technologies in reaching 2050 climate targets.	Does not propose a structured transition pathway or TOWS-based strategic model.
(Constantin and Subki n.d.2025)	Marine-based nuclear power plant concepts	SMR & PWR	Demonstrates growing maturity of maritime-suitable SMR/MSR designs.	Lacks commercialization models, deployment strategies, and regulatory integration.

The literature generally indicates that while nuclear propulsion has reached technological maturity, the primary challenges are concentrated around regulatory frameworks, social acceptance, port access, and financial liability. Conversely, it is highlighted that the design and safety advantages offered by SMR and MSR technologies hold the potential to mitigate these barriers. In this context, it is frequently argued that future research must focus as much on public policy, risk management, insurance mechanisms, market acceptance, and port infrastructure requirements as on technology assessments.

Upon examining existing studies, it is observed that research has largely focused on specific areas such as technical feasibility, safety architecture, and cost components; whereas comprehensive strategic assessments that collectively address technological, legal, economic, and socio-political dimensions remain limited. Notably, there is a distinct absence of academic work that moves beyond static analyses describing the status quo, to adopt a TOWS approach that translates the interactions between internal and external factors into actionable strategies within the context of commercial shipping. Aiming to bridge this gap, this study adopts the TOWS matrix as its methodological foundation, systematically matching strengths and weaknesses with opportunities and threats to facilitate the critical shift from 'situation analysis' to 'strategy formulation.' Consequently, the study aims to provide concrete strategic recommendations that transform fragmented data into an integrated roadmap to enhance the viability of nuclear propulsion in the maritime sector.

Methodological Framework and Analysis Process

In this study, the objective is to determine the strategic positioning of nuclear energy usage in commercial vessels and to develop action strategies appropriate to this position. Within the scope of the analysis, a thematic content analysis approach was employed to identify the factors used in the TOWS matrix. In the initial phase, a comprehensive literature review was conducted, scanning technical reports from international organizations (IMO, IAEA, OECD/NEA), peer-reviewed articles, sector evaluations, and historical examples of nuclear ships. Statements derived from these sources were categorized into thematic groups based on similar subject areas and conceptual affinities. These themes were consolidated under the headings of technological competence, safety and security, economic viability, regulatory framework, logistical/operational constraints, and socio-political acceptance.

By comparing these themes, elements that were recurring, critical for transformation, or subject to critique were identified; only those factors that were emphasized as common denominators across different studies and created a significant impact on the strategic assessment of nuclear propulsion were included in the final factor list. In the final stage, these factors were classified to align with the four components of the TOWS matrix (Strengths, Weaknesses, Opportunities, Threats). This method enables the development of four fundamental strategic approaches by systematically matching the internal capabilities (Strengths and Weaknesses) of enterprises or projects with external environmental conditions (Opportunities and Threats). Table 3 presents the structure and characteristics of the TOWS matrix utilized in this study.

Table 3. Classification of TOWS Matrix Strategy Types

Strategy Type	Description	Strategic Purpose
SO (Maxi–Maxi)	Strategies that aim to maximize the use of internal strengths to fully exploit external opportunities.	To combine strengths with opportunities and maximize strategic advantages.
WO (Mini–Maxi)	Strategies that focus on reducing internal weaknesses by making use of existing external opportunities.	To overcome or minimize weaknesses through the leverage of opportunities.
ST (Maxi–Mini)	Strategies that use internal strengths to mitigate or neutralize the impact of external threats.	To utilize strengths to counteract threats and reduce external risks.
WT (Mini–Mini)	Defensive strategies are designed to minimize both internal weaknesses and external threats simultaneously.	To adopt a risk-reduction approach that reduces vulnerabilities and threats together.

Figure 2 illustrates the fundamental stages of the strategic analysis process followed in this study. The process commenced with a qualitative pre-assessment covering safety, technical suitability, economic feasibility, and environmental impact dimensions; this assessment facilitated the systematic identification of internal (strengths and weaknesses) and external (opportunities and threats) factors through SWOT analysis. Subsequently, the relevant factors were matched within the TOWS matrix to generate SO, WO, ST, and WT strategy sets; in the final stage, these strategies were evaluated holistically to derive the final strategic recommendation. This workflow reinforces the methodological consistency of the study and the traceability of the decision-making processes.

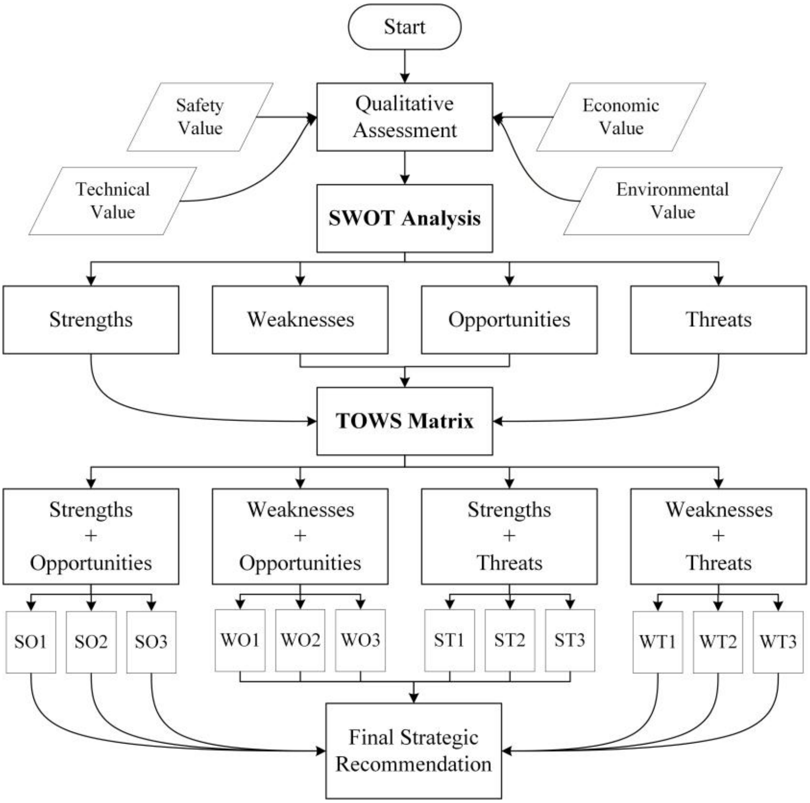

Figure 2. Flowchart of the SWOT–TOWS Integrated Strategy Development Model

Results and Discussion

Breakdown of Factors

In this study, the TOWS matrix constructed to evaluate the strategic feasibility of nuclear propulsion in commercial vessels is built upon four main axes: (i) technological competence, (ii) regulatory and institutional framework, (iii) economic and operational parameters, and (iv) socio-political and environmental impacts. To identify these factors, findings obtained from current literature, international reports (IMO, IAEA, OECD/NEA), and historical examples of nuclear ships were examined using a comprehensive and holistic approach.

- **Technological Factors:** Next-generation nuclear propulsion systems based on SMR and MSR were analyzed in terms of safety levels, power density, fuel consumption, maintenance requirements, passive safety mechanisms, and lifecycle performance. Additionally, the current maturity level of the technology was established by considering the differences between early-era reactors and modern designs.
- **Regulatory and Legal Factors:** The lack of a uniform global regulation for nuclear maritime transport, port access policies, licensing processes, liability and insurance regimes, and inter-state jurisdictional conflicts were addressed as key determinants.
- **Economic and Operational Factors:** Capital Expenditure (CAPEX), Operational Expenditure (OPEX), fuel price stability, Total Cost of Ownership (TCO), route lengths, operational efficiency, and fleet renewal policies were included within the scope of the evaluation.
- **Socio-Political and Environmental Factors:** Public perception, environmental risk assessments, political sensitivities of port states, levels of social acceptance, and the potential contribution to carbon-neutral goals were examined.

This classification of factors provided the necessary data set for the objective determination of strengths, weaknesses, opportunities, and threats to be used in the TOWS analysis; simultaneously, it systematically revealed the multi-dimensional structure of the feasibility of nuclear propulsion in commercial shipping.

a. Internal Factors: Strengths

- **S1. Superior Energy Density:** While the energy density of 3-5% enriched uranium is approximately 3,900,000 MJ/kg, marine diesel stands at only 42-46 MJ/kg. This substantial difference minimizes fuel tank volume on board, thereby significantly increasing cargo capacity (*deadweight gain*) (Kunze 2022).
- **S2. Refueling-Free Operation:** Depending on reactor designs, vessels can operate for 10 to 30 years without refueling. This capability eliminates dependency on bunkering infrastructure and prevents route deviations, ensuring logistical efficiency (Bayraktar and Pamik 2023).
- **S3. Passive Safety (Gen IV - MSR):** Molten Salt Reactors (MSRs), owing to their negative temperature coefficient and ability to operate near atmospheric pressure, possess the capability to self-terminate the reaction without operator intervention in the event of an accident (Furfari and Mund 2022).
- **S4. Zero Emissions (Operational):** Emissions of CO_2, SOx, NOx, and particulate matter are zero during the *Tank-to-Wake* (TTW) process. This aligns perfectly with the IMO's 2050 decarbonization targets (Eide, Chryssakis, and Endresen 2013).
- **S5. Price Stability:** Nuclear fuel costs constitute a minor fraction of the total operating expenses (OPEX). This structure insulates ship operators from price volatility

associated with fossil fuels or alternative fuels such as green ammonia (Vergara and McKesson 2002).

b. Internal Factors: Weaknesses

- **W1. High Capital Expenditure (CAPEX):** Construction costs for nuclear vessels are 2.5 to 3.5 times higher than those of conventional ships. To achieve economic viability, a serial production approach (economies of scale) is a prerequisite (Schøyen and Steger-Jensen 2017).
- **W2. Requirement for Nuclear Expertise:** There is a critical scarcity of qualified engineers with nuclear certification in the commercial maritime sector. In addition to the lengthy and costly training processes, the prevailing short-term employment models in shipping are structurally incompatible with the continuity required by nuclear safety culture (Carlton et al. 2011).
- **W3. Weight and Stability Issues:** The biological shielding and collision barriers required by reactors impose significant weight on the vessel. This impacts the ship's center of gravity and trim stability, necessitating radical structural changes in naval architecture, such as the reconfiguration of the engine room layout (Carlton et al. 2011).
- **W4. Waste Management:** The discharge and final disposal of spent nuclear fuel represent one of the most complex technical and political challenges, requiring a rigid "Cradle-to-Grave" chain of responsibility (Wang et al. 2023).

c. External Factors: Opportunities

- **O1. Indirect Electrification:** This involves utilizing nuclear reactors in floating power plants to produce Green Ammonia, rather than placing them directly on board for propulsion. This approach secures a "zero-carbon" fuel supply chain for ammonia-fueled vessels while circumventing the port access restrictions faced by nuclear ships (Kunze 2022).
- **O2. Leasing Business Model:** This refers to models (e.g., Core Power) where the reactor ownership remains with the technology provider (vendor), and the shipowner purchases only the "energy." This model facilitates access to technology by eliminating the shipowner's high CAPEX burden and waste management risks (Small Modular Reactors - World Nuclear Association n.d.).
- **O3. Carbon Taxation:** The EU Emissions Trading System (EU ETS) and potential IMO carbon levies will increase the cost of fossil fuels, thereby significantly highlighting the "Lifecycle Cost (LCC)" advantage of nuclear propulsion (Vergara, McKesson, and Walczak 2012).
- **O4. Niche Markets (Arctic Routes):** On the Northern Sea Route (NSR), which is opening up due to melting ice, nuclear icebreakers and container ships can establish strategic dominance in regions with scarce bunkering infrastructure, owing to their extended range capabilities (Schøyen and Steger-Jensen 2017).
- **O5. Technology Transfer:** This represents the potential to utilize over 700 reactor-years of operational data from the military sector (submarines and aircraft carriers) to

validate the safety and reliability of next-generation commercial SMRs (Freire and Andrade 2015).

d. External Factors: Threats

- **T1. Regulatory Deadlock:** The 1962 Brussels Convention on the Liability of Operators of Nuclear Ships has not entered into force. Furthermore, IMO SOLAS Chapter VIII covers only legacy Pressurized Water Reactors (PWR) and is outdated for modern technologies. This creates a significant legal vacuum in international maritime law (Wang et al. 2023).
- **T2. Port State Denial:** As evidenced by the *Mutsu* and *Savannah* cases, the authority of port states (under UNCLOS) to refuse entry of nuclear vessels into their territorial waters and ports due to public pressure or political reasons threatens the sustainability of commercial operations (Roscini 2002).
- **T3. Market Lock-in:** Investments in methanol by industry leaders such as CMA CGM and Maersk risk creating a path dependence for the global fuel supply chain towards chemical fuels (ammonia/methanol). This could channel infrastructure investments in this direction, thereby constraining the market share for nuclear propulsion and creating a technological lock-in (CMA CGM and Maersk join forces to accelerate the decarbonization of the shipping industry n.d.).
- **T4. Liability and Insurance Uncertainty:** Existing international nuclear liability regimes (Paris and Vienna Conventions) do not clearly cover "mobile" reactors. The risk of uncertain and potentially unlimited liability in the event of an accident acts as a deterrent for private sector investors (Kalmanson 1975).

- **T5. Nuclear Security Risks:** The risk of nuclear fuel (particularly 20% enriched uranium - HALEU) becoming a target for piracy or terrorist attacks during maritime transport heightens global security concerns (Kunze 2022).

Strategic Options and Action Plans

The four primary strategy groups derived from this matrix are classified as SO (Maxi-Maxi), WO (Mini-Maxi), ST (Maxi-Mini), and WT (Mini-Mini).

SO Strategies (Strengths – Opportunities / Maxi-Maxi)

The mechanism of SO strategies aims to create capacity expansion, competitive advantage, and sustainable growth by matching the organization's internal strengths with emerging opportunities in the external environment. This approach is based on the principle of transforming existing structural advantages into proactive and developmental strategies to maximize environmental opportunities.

1. **SO1. Integration of Energy Density into Green Fuel Production (S1 + S2 + O1):** The advantages of high energy density and long-term operation without refueling should be integrated with floating nuclear power platform concepts (*offshore SMR/MSR*) to be utilized in green ammonia production. In this way, a "zero-carbon fuel supply chain" can be established for the sector, without direct onboard nuclear propulsion.
2. **SO2. Mitigating Risk via Passive Safety and Leasing Models (S3 + O2):** The passive safety advantages of MSRs should be combined with "Energy-as-a-Service" or leasing business models to mitigate both the technical

risk perception and the CAPEX burden on shipowners. This structure, where ownership remains with the technology provider (*vendor-ownership*), will accelerate commercial acceptance.

3. **SO3. Leveraging Zero-Emission Operations in Carbon Pricing Regimes (S4 + O3):** The operational zero-emission advantage of nuclear propulsion must be converted into a direct cost benefit within the EU ETS and upcoming IMO carbon levy mechanisms. This strategy provides a distinct competitive advantage in Total Cost of Ownership (TCO) and lifecycle costs for nuclear-propelled fleets.
4. **SO4. Establishing Strategic Dominance in Arctic Niche Markets (S1 + S2 + O4):** In Arctic routes where bunkering infrastructure is scarce, the unlimited range advantage provided by nuclear power can be utilized to create a strategic monopolistic effect for icebreakers and container vessels.

WO Strategies (Weaknesses – Opportunities / Mini-Maxi)

The fundamental mechanism of WO strategies is based on utilizing external opportunities (O) to eliminate or reduce the impact of the organization's internal weaknesses (W). This approach is founded on improving and enhancing institutional capacity deficiencies by supporting them with environmental opportunities. Thus, existing opportunities serve as a transformative lever that prevents internal weaknesses from turning into permanent strategic disadvantages.

5. **WO1. Mitigating High CAPEX via Leasing Models Strategy (W1 + O2):** Through business models where reactor ownership remains with the vendor, the issue of high initial capital expenditure which is 2.5–3.5 times

higher for nuclear vessels compared to conventional ones can be mitigated. This approach lowers the commercialization threshold of nuclear propulsion, facilitating market entry.

6. **WO2. Bridging the Expertise Gap via Technology Transfer Strategy (W2 + O5):** The accumulated operational know-how and training curricula spanning over 700 reactor-years in naval nuclear propulsion can be adapted to commercial maritime training. Through this technology and knowledge transfer, the shortage of qualified nuclear engineers in the sector can be reduced while reinforcing safety culture.
7. **WO3. Offsetting Weight/Stability Constraints via Arctic Value Proposition Strategy (W3 + O4):** Although weight increases and architectural modifications due to reactor shielding and containment requirements are costly, the capability for continuous operation and reliability provided in Arctic routes economically **offsets** these engineering trade-offs.
8. **WO4. Circumventing Waste Management Challenges via Floating Facilities Strategy (W4 + O1):** Utilizing the nuclear reactor as a "floating power plant" rather than directly on a merchant vessel allows for the transfer of waste discharge and storage processes from the ship operator to the stationary facility operator. Thus, the operational and legal waste management burden on commercial vessels is minimized.

ST Strategies (Strengths – Threats / Maxi-Mini)

The mechanism of ST strategies aims to neutralize, limit, or mitigate the impact of external threats (T) by utilizing the organization's strengths (S). This approach is based on the principle of transforming existing structural and technological superiorities into protective, balancing, and resilience-enhancing strategies against potential risks.

9. **ST1. Strategy to Mitigate Port State Denial via Passive Safety Systems (S3 + T2):** The "passive safety" features of Gen IV MSRs, which require no human intervention, should be utilized as a persuasion tool to address the safety concerns of port authorities and local governments, thereby providing technical assurance and minimizing political obstruction or port entry bans.
10. **ST2. Strategy to Minimize Geopolitical Risks via Refueling-Free Operation (S2 + T5):** The capability for long-term operation without refueling eliminates the necessity for vessels to stop or bunker in critical straits or high-risk zones. This enhances the security of the nuclear fuel supply chain while limiting the operational **exposure** to piracy or terrorist threats.
11. **ST3. Strategy to Overcome Market Lock-in via Zero-Emission Operations (S4 + T3):** Despite the emerging "market lock-in" towards chemical fuels like methanol or ammonia, the "operational zero-emission" advantage of nuclear propulsion elevates this technology to a privileged position within increasingly stringent climate policies. This environmental superiority provides robust competitive resilience against the market dominance of alternative fuels.
12. **ST4. Utilizing High Energy Density as Economic Resilience Against Regulatory Gaps (S1 + T1):** Despite uncertainties in the legal framework and the "regulatory deadlock," the logistical advantages offered by nuclear power density (minimum storage space, maximum cargo

capacity) create a **compelling economic incentive** for shipowners, sufficient to offset the costs associated with the regulatory maturation process.

WT Strategies (Weaknesses – Threats / Mini-Mini)

The mechanism of WT strategies aims to minimize the impact of external threats (T) while simultaneously reducing the organization's internal weaknesses (W). This approach is based on the principle of formulating defensive, damage-mitigating, and risk-averse strategies that ensure the concurrent management of both internal vulnerabilities and external risks.

13. **WT1. Harmonization of International Legal Frameworks and Standardization of Insurance Regimes (W1 + W4 + T1 + T4):** High CAPEX burdens, waste management liabilities, legal uncertainties, and insurance issues constitute a consolidated risk cluster. To manage these risks, a "joint regulatory framework" must be established in cooperation with the IMO and IAEA, clarifying liability limits to instill investor confidence.
14. **WT2. Integrated Management of Nuclear Personnel Shortage and Security Threats (W2 + T2 + T5):** The shortage of nuclear operational personnel must be addressed in conjunction with port state security concerns and geopolitical risks. In this context, an internationally accredited "Nuclear Maritime Academy" should be established to cultivate human capital and improve global security perceptions through standardized training protocols.
15. **WT3. Optimization of Weight and Engineering Constraints via Modular Designs (W3 + T3):** In scenarios where market lock-in towards alternative fuels (methanol/ammonia) increases, heavy and fixed reactor

architectures may reduce economic flexibility. To counter this threat, R&D on exchangeable and modular "containerized reactor" systems should be incentivized to minimize weight disadvantages in naval architecture and conversion costs.

16. **WT4. Mitigation of Waste Management and Geopolitical Pressures via Integrated Security Policies (W4 + T5):** To reduce geopolitical pressures and security risks arising during the management and transfer of spent fuel, international control mechanisms under IAEA supervision and institutional assurance systems, such as multinational "Nuclear Fuel Banks," must be strengthened.

Conclusions and Assessment

This study has analyzed the feasibility of nuclear propulsion in commercial shipping through the TOWS matrix, situating the barriers to adoption and potential opportunities within a holistic strategic framework. The results of the analysis demonstrate that the primary barrier to nuclear propulsion is not "technical maturity"; rather, the core challenge lies within the axes of economic modeling, regulatory uncertainties, and socio-political acceptance. The key findings and strategic inferences obtained are as follows:

1. **Necessity of Business Model Transformation (Transition from Ownership to Service):** The study has shown that the high Capital Expenditure (CAPEX) associated with nuclear vessels is difficult to finance through traditional ship ownership models. In this context, the **WO1 and SO2 strategies** developed in the TOWS analysis prove that "Energy-as-a-Service" or leasing models—where reactor ownership remains with the technology provider and

the shipowner purchases only energy—represent the most realistic roadmap for commercialization.

2. **Harmonization of the Regulatory Framework:** It has been identified that existing IMO SOLAS regulations do not cover modern reactor technologies (SMR/MSR) and that the legal void (*Regulatory Deadlock*) created by the 1962 Brussels Convention puts commercial operations at risk. In line with the **WT1 strategy**, the study emphasizes that a hybrid regulatory framework established through IMO and IAEA cooperation, along with standardized insurance regimes, is a critical prerequisite for securing investor confidence.
3. **Port Access and Hybrid Solutions:** The right of port states to deny entry to nuclear vessels (Port State Denial) and public pressure threaten operational sustainability. Conversely, the study proposes an innovative solution through **strategies SO1 and WO4**: positioning nuclear reactors as "Floating Nuclear Power Plants" (FNPP) to produce Green Ammonia/Methanol, rather than mounting them directly onboard. This "indirect electrification" approaches both circumvents port access issues and creates a zero-carbon fuel supply chain for the maritime sector.
4. **Security Perception and Human Capital:** The shortage of nuclear-qualified personnel in the sector and security risks have been addressed under the **WT2 strategy**. The study concludes that the technical reliability of Gen-IV reactors (MSR) with passive safety features must be supported by an internationally accredited "Nuclear Maritime Academy" and transparent training protocols.

In summary, this study concludes that while nuclear energy is technically the most competent alternative for achieving IMO 2050 targets, realizing this potential depends less on technological advancement and more on the simultaneous execution of financial risk-sharing models (leasing), global legal reforms, and strategies to build societal trust.

References

Bayraktar, M., & Pamik, M. (2023). Nuclear power utilization as a future alternative energy on icebreakers. *Nuclear Engineering and Technology, 55*(2), 580–586.

Bayraktar, M., & Yüksel, O. (2023). Analysis of the nuclear energy systems as an alternative propulsion system option on commercial marine vessels by utilizing the SWOT-AHP method. *Nuclear Engineering and Design, 407*, 112265.

Carlton, J. S., Smart, R., & Jenkins, V. (2011). The nuclear propulsion of merchant ships: Aspects of engineering, science and technology. *Journal of Marine Engineering & Technology, 10*(2), 47–59.

Chen, Y., Liu, J., Cai, Q., & Li, A. (2020). Study on rating method of nuclear events in marine nuclear power plant. In *IOP Conference Series: Earth and Environmental Science* (Vol. 440, p. 042103). IOP Publishing.

CMA CGM & Maersk. (n.d.). *CMA CGM and Maersk join forces to accelerate the decarbonization of the shipping industry*. Retrieved December 2, 2025, from https://www.maersk.com/news/articles/2023/09/19/cma-cgm-and-maersk-join-forces-to-accelerate-the-decarbonization-of-the-shipping-industry

Constantin, A., & Subki, H. (n.d.). *Overview of SMR designs for maritime-based nuclear power plants*. International Atomic Energy Agency (IAEA).

Duong, P. A., Ha, J., Lee, C., & Kang, H. (2025). Nuclear propulsion for merchant ships: A path to sustainable maritime energy. *International Journal of Sustainable Energy, 44*(1), 2579469.

Eide, M. S., Chryssakis, C., & Endresen, Ø. (2013). CO2 abatement potential towards 2050 for shipping, including alternative fuels. *Carbon Management, 4*(3), 275–289.

Fetting, C. (2020). *The European Green Deal* (ESDN Report). European Sustainable Development Network.

Freire, L. O., & de Andrade, D. A. (2015). Historic survey on nuclear merchant ships. *Nuclear Engineering and Design, 293*, 176–186. doi:10.1016/j.nucengdes.2015.07.031

Furfari, S., & Mund, E. (2022). Advanced nuclear power for clean maritime propulsion. *The European Physical Journal Plus, 137*(6), 747.

Ghimire, L., & Waller, E. (2023). Small modular reactors: Opportunities and challenges as emerging nuclear technologies for power production. *Journal of Nuclear Engineering and Radiation Science, 9*(4), 044501.

Hirdaris, S. E., Cheng, Y. F., Shallcross, P., Bonafoux, J., Carlson, D., Prince, B., & Sarris, G. A. (2014). Considerations on the potential use of nuclear small modular reactor (SMR) technology for merchant marine propulsion. *Ocean Engineering, 79*, 101–130.

International Energy Agency. (2025). *How the shipping sector could save on energy costs – Analysis*. Retrieved from https://www.iea.org/commentaries/how-the-shipping-sector-could-save-on-energy-costs

International Maritime Organization. (2023). *2023 IMO strategy on reduction of GHG emissions from ships* (Resolution MEPC.377(80)). Marine Environment Protection Committee.

Kalmanson, A. G. (1975). *Nuclear-powered merchant ships: Some legal and regulatory considerations*. University of California.

Kunze, C. D. (2022). *The role of Generation IV nuclear reactors in decarbonising international shipping: A multi-criteria decision making (MCDM) framework for matching potential decarbonisation pathways to different ship types and size*. (Unpublished thesis or report).

Lloyd's Register. (n.d.). *Navigating nuclear energy in maritime*. Retrieved December 10, 2025, from https://www.lr.org/en/knowledge/research-reports/2025/navigating-nuclear-energy-in-maritime/

Roscini, M. (2002). The navigational rights of nuclear ships. *Leiden Journal of International Law, 15*(1), 251–265.

Schøyen, H., & Steger-Jensen, K. (2017). Nuclear propulsion in ocean merchant shipping: The role of historical experiments to gain insight into possible future applications. *Journal of Cleaner Production, 169*, 152–160.

Vergara, J. A., & McKesson, C. B. (2002). Marine technology nuclear propulsion in high-performance cargo vessels. *Marine Technology and SNAME News, 39*(01), 1–11.

Vergara, J., McKesson, C., & Walczak, M. (2012). Sustainable energy for the marine sector. *Energy Policy, 49*, 333–345.

Wang, Q. (2025). China's law and policy initiatives for integrating nuclear energy in maritime applications: A critical review. *Progress in Nuclear Energy, 179*, 105538.

Wang, Q., Zhang, H., & Zhu, P. (2023). Using nuclear energy for maritime decarbonization and related environmental challenges: Existing regulatory shortcomings and improvements. *International Journal of Environmental Research and Public Health, 20*(4), 2993.

World Nuclear Association. (n.d.). *Small modular reactors*. Retrieved December 2, 2025, from https://world-

nuclear.org/information-library/nuclear-power-reactors/small-modular-reactors/small-modular-reactors

CHAPTER 12

DESIGN PRINCIPLES AND MATERIAL STRATEGIES FOR ARCHIMEDES SPIRAL WIND TURBINE BLADES: A CRITICAL REVIEW

BUKET ÖZTÜRK[1]
UMUT SUCU[2]
MUSTAFA ÖNCÜL[3]

INTRODUCTION

Rapid population growth and accelerating industrialization continue to drive global energy demand upward, with annual increases of approximately 4–5% reported worldwide (Şenel & Koç, 2015). At the same time, the progressive reduction of fossil fuel reserves and their well-documented environmental impacts have increased the search for sustainable and low-carbon energy alternatives (Şenel & Koç, 2015). Within this context, wind energy has emerged as one of the most strategically important renewable resources, owing to its clean nature, operational reliability,

---

[1] İzmir Katip Çelebi University, Mechanical Engineering Department, Orcid: 0009-0007-8074-899X

[2] İzmir Katip Çelebi University, Mechanical Engineering Department, Orcid: 0009-0007-7220-3017

[3] Assist. Prof. Dr., İzmir Katip Çelebi University, Mechanical Engineering Department, Orcid: 0000-0002-4441-6353

inexhaustibility, and comparatively low operating costs (Şenel & Koç, 2015). By reducing dependence on fossil fuels, wind power plays a significant role in mitigating greenhouse gas emissions and limiting the effects of global warming (Bashir, 2021). Reflecting these advantages, the global installed capacity of wind energy has been increasing at an annual rate exceeding 10%, making it the fastest-growing renewable energy technology (Şenel & Koç, 2015). Long-term projections further underline this trend, with the International Renewable Energy Agency (IRENA) estimating that wind-generated electricity could account for up to 36% of total global electricity production by 2050 (Çiftci, Erdoğan, & Genç, 2023).

Wind turbines are engineered systems that convert the kinetic energy of moving air into electrical power through aerodynamic interaction between the rotor and the wind (Şenel & Koç, 2015). From a fundamental design perspective, modern wind turbines are broadly classified into two principal categories, as illustrated in Figure 1, Horizontal Axis Wind Turbines (HAWTs) and Vertical Axis Wind Turbines (VAWTs). HAWTs employ a conventional configuration in which the rotor axis is aligned with the prevailing wind direction and energy extraction is predominantly governed by lift-based aerodynamic mechanisms (Bashir, 2021). In contrast, VAWTs are characterized by a rotor axis oriented perpendicular to the incoming wind, enabling omnidirectional operation without the need for yaw control systems (Korawan & Febritasari, 2024). Owing to their directional independence, compact geometry, and comparatively low noise emissions, VAWTs are frequently preferred for urban environments and small-scale power generation, where wind conditions are often turbulent and space constraints are significant (Faisal et al., 2025; Korawan & Febritasari, 2024; Roga et al., 2022).

Figure 1: Types of wind turbines

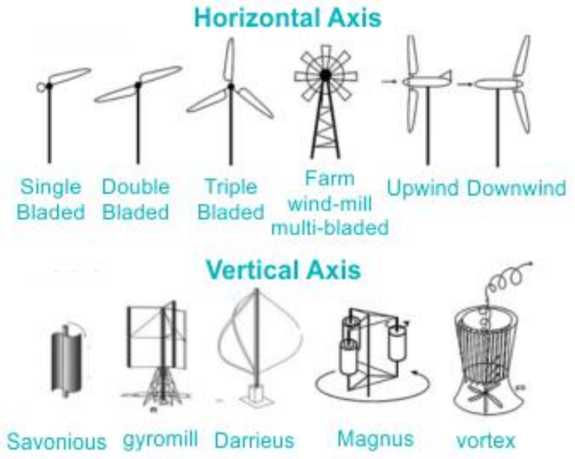

Reference: (*Testbook, n.d.*)

In recent years, increasing attention has been directed toward understanding the role of fluid–solid interaction in governing the dynamic performance of Archimedes Spiral Wind Turbine (ASWT) blades. In particular, recent studies examining the influence of composite coating applications on the modal characteristics of Glass Fiber Reinforced Polymer (GFRP) and Carbon Fiber Reinforced Polymer (CFRP) blades have demonstrated that surface coatings can act as a decisive parameter in controlling vibration behavior and flow-induced structural stability, especially under low-Reynolds-number operating conditions typical of spiral turbine configurations (Mehri Khansari & Moghtader-ahar, 2025). From an aerodynamic standpoint, blade efficiency is strongly linked to the lift-to-drag (L/D) ratio, where higher values directly translate into improved energy conversion performance. Achieving such performance requires blade materials that combine excellent fatigue resistance under cyclic loading, low density to limit gravitational and inertial effects, and sufficient strength and stiffness to withstand fluctuating wind loads (Pradeep et al., 2019; Cheng et al., 2025; Çiftci, Erdoğan, & Genç, 2023). Consequently, composite materials have become the dominant material choices for wind turbine blades due to their favorable strength-to-weight ratios and tailored anisotropic properties (Koul, 2025; Roga et al., 2022). More recently, growing sustainability demands have accelerated research into thermoplastic composites (TPCs), which offer recyclability alongside robust mechanical performance, positioning them as promising alternatives for next-generation wind turbine blades (Cheng et al., 2025). Within this material framework, the blade root region emerges as a critical structural zone, as it experiences the highest stress concentrations and governs load transfer to the hub. Studies have shown that multi-material and multi-layer optimization of thickness distribution and material-stacking sequences in this region can simultaneously enhance load-bearing capacity and reduce overall blade weight where complex load paths arise from their unconventional spiral geometry (Hermansen & Lund, 2024b).

The ASWT, illustrated in Figure 2 and forming the primary focus of this chapter, represents an unconventional wind turbine concept distinguished by its characteristic spiral blade geometry (Faisal et al., 2025; Kamal et al., 2022). In contrast to conventional propeller-type HAWTs, which rely predominantly on lift-based aerodynamic mechanisms, the ASWT operates through a hybrid energy extraction approach that combines both lift and drag forces (Faisal et al., 2025). This dual-mode interaction enables effective performance under low to moderate wind speeds, typically in the range of 2–8 m/s, and under highly turbulent flow conditions, making the ASWT particularly attractive for urban and built environments (Faisal et al., 2025; Korawan & Febritasari, 2024). One of the defining advantages of the ASWT is its inherent ability to achieve passive yaw alignment, as the drag contribution and spiral geometry naturally orient the rotor with respect to the incoming wind without the need for complex active control systems (Faisal et al., 2025; Korawan & Febritasari, 2024). Despite these advantages, the

ASWT is not without limitations; notably, its spiral configuration can induce relatively high thrust loads compared to conventional propeller-type HAWTs, which poses additional challenges for structural design, material selection, and long-term durability (Salah Samiani & Boroushaki, 2025).

Figure 2: Archimedes Spiral Wind Turbine (ASWT)

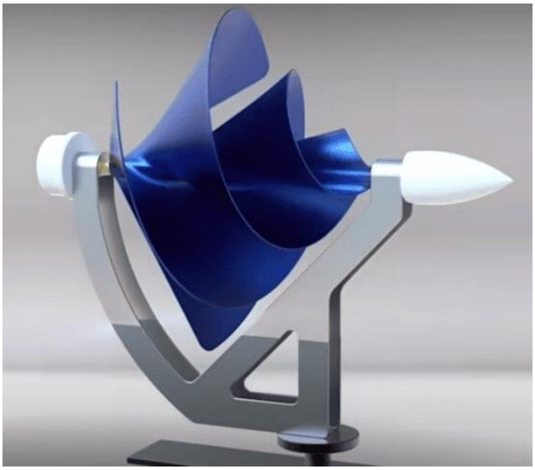

Reference: (Laawun Energy Solutions Australia Pty Ltd, n.d.)

Extensive research has been conducted to improving the aerodynamic performance of ASWT, with particular emphasis on geometric optimization strategies such as span angle variation (Figure 3) and aerofoil profile selection (Kamal et al., 2022; Korawan & Febritasari, 2025; Refaie et al., 2021; Refaie et al., 2022; Salah Samiani & Boroushaki, 2025). However, research on the structural performance and development of special materials for ASWT blades remains relatively limited in the existing literature (Mehri Khansari & Moghtader-ahar, 2025). In particular, there is a notable lack of comprehensive research evaluating the applicability of next-generation composite materials, especially sustainable and highly recyclable systems, under the distinctive loading conditions characteristic of ASWT operation, including low rotational speeds, elevated thrust forces, and complex load paths induced by the spiral geometry (Çiftci, Erdoğan, & Genç, 2023; Arivalagan et al., 2023).

In parallel, additive manufacturing technologies, most notably Fused Deposition Modeling (FDM), have gained increasing attention in wind turbine blade research due to their low cost, rapid prototyping capability, and design flexibility (Gebel & Ermurat, 2021). Experimental studies on Polylactic Acid (PLA)-based, 3D-printed wind turbine blades have demonstrated that printing parameters exert a direct influence on aerodynamic efficiency and overall performance, highlighting the strong coupling between manufacturing strategy and functional behavior (Arivalagan et al., 2023). These findings indicate that FDM-based approaches can serve not only as prototyping tools but also as valuable research platforms for systematically exploring the interplay between material selection, manufacturing parameters, and performance in ASWT blade development.

Figure 3: Different configurations of the seashell-shaped wind turbine according to the opening angle: (a) logarithmic spiral and (b) Archimedean spiral

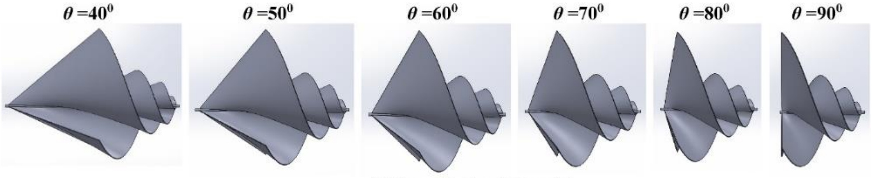

(a) Logarithmic spiral model

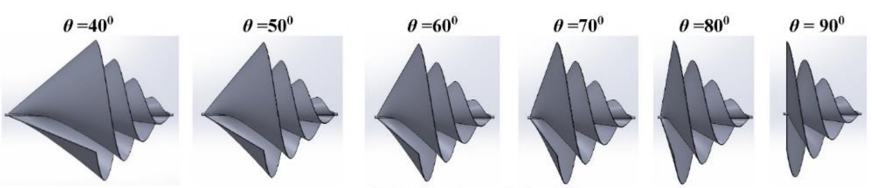

(b) Archimedean spiral model

Reference: (Hamid & Abd El Maksoud, 2023)

This chapter aims to systematically examine the evolution of wind turbine blade materials and to critically assess their suitability for application in the unconventional ASWT, a concept that offers low noise emissions and favorable efficiency under the low-speed, turbulent wind conditions typical of urban environments. Adopting a comprehensive literature-based review approach, the study synthesizes recent advances in blade design, composite material systems, and manufacturing strategies, with particular emphasis on their relevance to the distinctive structural and aerodynamic demands imposed by spiral blade geometries. By identifying material properties and design strategies that best align with the performance, durability, and sustainability requirements of ASWTs, this review seeks to clarify current research gaps and provide a coherent framework to guide future material development and blade design efforts for next-generation urban wind energy systems.

BACKGROUND: WIND TURBINE BLADE DESIGN PRINCIPLES

Wind turbine blades function simultaneously as highly optimized aerodynamic surfaces and as primary load-bearing structural components, requiring a carefully balanced integration of aerodynamic efficiency and mechanical integrity (Faisal et al., 2025). In modern wind energy systems, blades are manufactured almost exclusively from composite materials, owing to their high specific strength, stiffness tailoring capability, and fatigue resistance under cyclic loading conditions (Bucur, Malael, & Breban, 2020; Bucur, Malael, & Predescu, 2021; Jiang et al., 2022). The structural design of a blade is therefore inherently multidisciplinary, encompassing the definition of the aerodynamic profile, accurate assessment of aerodynamic and inertial loads, informed selection of blade materials, and the design of internal interfaces and load-transfer mechanisms (Hermansen & Lund, 2024b). From a structural standpoint, a typical blade architecture consists of an external shell (aeroshell), internal load-carrying elements such as spar caps and shear webs, and a reinforced blade root region. The aeroshells, forming the suction and pressure sides, primarily define the aerodynamic shape and are commonly realized as sandwich structures to enhance buckling resistance while maintaining low weight (Mishnaevsky et al., 2017). These shells are structurally supported by main spar caps or box-spar configurations, connected through shear webs that efficiently resist bending and torsional loads during operation (Jiang et al., 2022; Hermansen & Lund, 2024b). The spar caps, typically subjected to alternating tension–tension and compression–compression cyclic stresses during blade rotation, are among the most critical structural elements and are often designed with tapered thickness distributions to optimize material usage while maintaining load-carrying capacity (Fragkos & Theotokoglou, 2025; Jiang et al., 2022). At the blade root, where loads are transferred to the hub, the structure is commonly reinforced and may adopt a monolithic composite configuration to ensure structural continuity and durability under high stress concentrations (Arivalagan et al., 2023). Consequently, contemporary blade design methodologies decouple external aerodynamic geometry from internal structural layout, allowing aerodynamic optimization to proceed in parallel with structurally driven internal architectures such as spar caps and shear webs (Hermansen & Lund, 2024b).

As outlined in the Introduction, the power output and aerodynamic efficiency of a wind turbine rotor are strongly governed by the ratio of lift (L) to drag (D) generated by the blade aerofoil, commonly expressed as the L/D ratio (Koul, 2025). This parameter becomes particularly critical for small- and micro-scale wind turbines, where operation at low Reynolds numbers constrains aerofoil selection and often leads to reduced aerodynamic performance if conventional profiles are employed (Arivalagan et al., 2023; Koul, 2025). From an aerodynamic design standpoint, blade optimization seeks to maximize lift while minimizing drag along the span through careful control of parameters such as aerofoil geometry, twist (torsional) distribution, and taper ratio, all tailored to the local flow conditions. However, aerodynamic optimization must be reconciled with structural requirements, especially in the blade root region, where load transfer to the hub dominates design considerations. In this region, thicker and stiffer aerofoil profiles are typically adopted to ensure sufficient structural integrity, whereas toward the blade tip, a gradual reduction in profile thickness is favored to enhance aerodynamic efficiency, increase energy capture, and mitigate losses associated with tip vortex formation. In spiral blade geometries such as those employed in ASWTs, the continuously varying flow direction along the blade span introduces pronounced three-dimensional flow effects that differ fundamentally from those observed in conventional straight-bladed HAWT configurations (Arivalagan et al., 2023).

In addition to aerodynamic considerations, wind turbine blades are subjected to a complex combination of mechanical loads during operation. These include flap wise loads acting perpendicular to the blade plane as a result of wind pressure, edgewise loads acting parallel to the blade plane due to gravitational forces and torque transmission, and cyclic fatigue loads arising from continuous rotation and fluctuating aerodynamic forces (Arivalagan et al., 2023; Fragkos & Theotokoglou, 2025; Korawan & Febritasari, 2025; Pradeep et al., 2019). The simultaneous action of these load components plays a decisive role in governing blade durability, material selection, and long-term structural reliability.

The structural behavior of a wind turbine blade is governed by its dynamic response to aerodynamic loads acting simultaneously under inherently unsteady wind conditions. Fluctuations in wind speed and direction generate time-dependent bending and torsional moments along the blade span, producing deformation responses that are strongly influenced by the elastic and viscoelastic characteristics of the blade material. From a structural dynamics standpoint, a key design objective is to mitigate flow-induced vibrations by ensuring that the blade’s natural frequencies remain sufficiently separated from dominant excitation frequencies associated with rotor rotation and aerodynamic forcing. This requirement becomes particularly critical for ASWT blades, which tend to exhibit a broader and less uniformly distributed spectrum of natural frequencies due to their non-uniform geometry and complex load paths, thereby necessitating more detailed dynamic and modal evaluations (Mehri Khansari & Moghtader-ahar, 2025).

Dynamic behavior plays a decisive role in both aerodynamic stability and long-term structural integrity of wind turbine blades. When blade natural frequencies approach operational excitation frequencies, adverse aeroelastic phenomena such as resonance, flap–torsion coupling, and dynamic instability may arise, potentially accelerating fatigue damage and compromising performance. Consequently, blade mass distribution, stiffness characteristics, and geometric parameters are carefully optimized during the design process to maintain safe frequency separation across the operating envelope. In spiral turbine configurations, the continuously varying local flow direction along the blade introduces complex three-dimensional mode shapes that differ fundamentally from those of conventional straight-bladed HAWTs. These effects influence not only aerodynamic efficiency but also the mechanisms by which vibrations are initiated, amplified, and damped over time. Moreover, the periodic onset of flow separation along the spiral surface introduces low-frequency excitation components that must be explicitly accounted for in dynamic and aeroelastic analyses of ASWT blades (Kamal et al., 2022; Mehri Khansari & Moghtader-ahar, 2025).

Material selection plays a decisive role in determining the structural performance, service life, and life-cycle cost of wind turbine blades (Arivalagan et al., 2023). From a mechanical design perspective, blade materials must combine low density to limit gravitational and inertial effects, high specific strength and adequate stiffness to withstand combined flap wise and edgewise loads, and excellent resistance to fatigue under long-term cyclic loading (Pradeep et al., 2019; Cheng et al., 2025). In addition to mechanical requirements, environmental durability against ultraviolet radiation, moisture ingress, temperature fluctuations, and icing is essential to preserve structural integrity throughout the operational lifetime of the blade (Cheng et al., 2025). More recently, sustainability considerations have become an integral part of material selection, as conventional thermoset matrices present significant challenges in terms of recyclability and environmental impact (Çiftci, Erdoğan, & Genç, 2023). As a result, increasing research attention has been directed toward recyclable material systems, with TPCs emerging as promising candidates due to their robust mechanical properties, weldability, and potential for closed-loop recycling (Cheng et al., 2025; Savran, Yılmaz, Öncül, & Sever, 2022).

Finally, the operating environment and aerodynamic concept of the ASWT impose additional constraints on material behavior. Designed primarily for urban applications characterized by low to moderate wind speeds, approximately 2–8 m/s, the ASWT relies on a hybrid lift–drag energy extraction mechanism rather than purely lift-based operation (Faisal et al., 2025; Refaie et al., 2021). This configuration can generate relatively high thrust loads, placing stringent demands on structural stability and damage tolerance of the blade material system. These considerations collectively underscore the need for tailored material and manufacturing strategies that address the unique aerodynamic, structural, and sustainability requirements of ASWT blades, providing a clear rationale for the focused evaluation presented in the subsequent sections.

ARCHIMEDES SPIRAL WIND TURBINE (ASWT) AND MODERN BLADE MATERIALS

Wind turbine blade materials play a central role in determining aerodynamic performance, operational efficiency, and long-term structural durability of wind energy systems (Faisal et al., 2025; K. S., 2024). As blades typically represent the most costly single component of a wind turbine, their material selection has a direct influence on both initial investment and lifecycle costs (Faisal et al., 2025). The historical evolution of blade technology reflects a gradual transition from heavy, rigid metallic structures toward lightweight, flexible, and damage-tolerant composite materials capable of meeting increasingly demanding performance requirements (Faisal et al., 2025). To ensure reliability and safety across diverse operating conditions, international standards such as IEC 61400 have established comprehensive guidelines governing the structural design, manufacturing processes, testing procedures, and repair methodologies of wind turbine blades (Cheng et al., 2025; Firoozi, Firoozi, & Hejazi, 2024).

Early wind turbine blades were commonly fabricated from steel, as exemplified by large-scale installations such as the Grandpa’s Knob turbine (1941). However, the excessive weight of metallic blades severely limited their applicability in modern turbine designs by increasing gravitational loads, reducing energy transmission efficiency, and accelerating fatigue-related failures (Faisal et al., 2025; K. S., 2024). Wood was later adopted as an alternative material, particularly for small-scale turbines, due to its low cost and ease of processing (K. S., 2024; Mishnaevsky et al., 2017). Nevertheless, wooden blades were ultimately found to lack the strength, fatigue resistance, and environmental durability required for large and high-performance wind turbines (K. S., 2024). These inherent limitations of traditional materials have driven a decisive shift toward composite material systems, which offer superior strength-to-weight ratios, enhanced fatigue performance, and greater design flexibility.

GFRP remains the most widely used composite material in wind turbine blade manufacturing, primarily because it offers a pragmatic balance between mechanical performance and economic feasibility (K. S., 2024). Compared to CFRP, GFRP is significantly less costly and is therefore favored for large-scale production, where material cost strongly influences overall turbine economics (K. S., 2024). Industrially, GFRP blades are commonly produced using Vacuum-Assisted Resin Transfer Molding (VARTM), a process well suited for manufacturing large composite structures with relatively low tooling costs (Mishnaevsky et al., 2017; Cheng et al., 2025). Despite these advantages, GFRP exhibits a lower stiffness-to-weight ratio than CFRP, which can limit its applicability in increasingly long and slender blades (K. S., 2024). Moreover, the thermoset polymer matrices typically employed pose significant sustainability challenges, as they are difficult to recycle at the end of the blade's approximately 20-year service life, contributing to long-term environmental waste streams (Cheng et al., 2025; Çiftci, Erdoğan, & Genç, 2023). To address stiffness limitations associated with conventional E-glass fibers, the industry has increasingly turned toward high-modulus glass fiber variants, which provide improved mechanical performance while retaining cost advantages relative to carbon fibers (Cheng et al., 2025).

In contrast, CFRP offers markedly superior structural performance, characterized by exceptional tensile strength, reaching values of up to 7000 MPa, and significantly higher stiffness, making it particularly attractive for load-critical blade regions (Cheng et al., 2025; K. S., 2024). The strategic use of unidirectional (UD) CFRP layers in spar caps has been shown to reduce blade structural weight by approximately 31%, highlighting its effectiveness in mitigating gravitational and fatigue loads in large blades (Jiang et al., 2022). Nevertheless, the high cost of carbon fibers remains a major barrier to their widespread adoption, especially in cost-sensitive applications and small-scale turbine systems (K. S., 2024). As a compromise solution, hybrid composite systems that combine different fiber reinforcements have been increasingly adopted to balance mechanical efficiency and cost (K. S., 2024; Cheng et al., 2025). Such hybrid architectures enable targeted material placement and are often optimized using advanced approaches such as Discrete Material and Thickness Optimization (DMTO), allowing improvements in static strength, buckling resistance, and fatigue performance while minimizing material usage (Hermansen & Lund, 2024b).

Conventional GFRP, CFRP, and hybrid composite blade systems are predominantly based on thermoset matrices, and the growing difficulty associated with their end-of-life disposal has become a major driver for the adoption of recyclable TPCs in wind turbine applications (K. S., 2024). Unlike thermoset resins, which form permanent three-dimensional cross-linked networks that cannot be remelted or reshaped, thermoplastics undergo reversible physical transformations when subjected to heat, enabling repeated softening, reforming, and material recovery (Msigwa et al., 2022; Cheng et al., 2025). This fundamental distinction allows TPCs to directly address the escalating landfill burden associated with decommissioned blades while maintaining competitive mechanical performance (Cheng et al., 2025). Beyond recyclability, TPCs offer additional functional advantages, most notably weldability through fusion joining, which enables the fabrication of segmented or modular blades with high structural continuity and damage tolerance—features that are particularly attractive for complex geometries and distributed manufacturing strategies (Cheng et al., 2025; Pradeep et al., 2019).

Recent concepts of “next-generation” wind turbine blades further illustrate the transformative potential of TPCs. For instance, designs employing recycled low-density polyethylene (LDPE) matrices reinforced with continuous carbon or glass rods have been proposed as analogs to reinforced concrete systems, in which the matrix primarily transfers loads while the reinforcements carry the majority of structural stress (Çiftci, Erdoğan, & Genç, 2023). In such architectures, resin consumption is minimized, and full recyclability is achieved by thermally separating the LDPE matrix from the reinforcement phase at the end of service life. This approach not only enables near-zero resin waste but also aligns material efficiency with circular-economy principles, positioning thermoplastic composite systems (TPCS) as promising candidates for sustainable and high-performance blade designs. A comparative summary of conventional and emerging blade material systems, including mechanical performance, weight, cost, fatigue behavior, manufacturability, and recyclability, is provided in Table 1.

Table 1: Comparison of overall performance of materials

Criterion	Wood/Early Metals	GFRP	CFRP	Hybrid (GF/CF)	TPCs
Mechanical performance	Low strength (wood); excessive weight and early failure (steel)	Adequate strength, moderate stiffness	Very high strength and stiffness (up to ~7000 MPa)	High, tunable strength–stiffness balance	High toughness and sufficient stiffness
Weight efficiency	Poor (metal); limited to small scale (wood)	Low–moderate density	Excellent (~20–30% weight	Optimized for performance/weight	Lightweight

			reduction)		
Cost level	Low (wood)	Low–moderate	Very high (main limitation)	Moderate	Moderate; reduced life-cycle cost
Fatigue resistance	Poor	Good, but durability limited	Excellent	Good to excellent (design-dependent)	High damage tolerance
Manufacturing suitability	Conventional forming	VARTM / vacuum infusion	Specialized, high-precision processes	Compatible with DMTO and VARTM	Weldable; fast processing; adaptable
Recyclability	Biodegradable/reusable	Poor (thermoset matrix)	Poor (thermoset matrix)	Poor (thermoset-based)	Excellent (remeltable, reusable)

Reference: (K S, 2024; Faisal et al., 2025; Fragkos & Theotokoglou, 2025; Cheng et al., 2025; Jiang et al., 2022; Çiftci, Erdoğan, & Genç, 2023; Mishnaevsky et al., 2017; Hermansen & Lund, 2024b; Pradeep et al., 2019; Bucur, Malael, & Predescu, 2021; Msigwa et al., 2022)

To evaluate the relevance of contemporary blade material systems for ASWT applications, it is first necessary to examine the fundamental design characteristics that distinguish ASWTs from conventional wind turbine concepts. Increasing global energy demand, coupled with the need for sustainable and decentralized power generation in urban environments, has positioned the ASWT as a promising alternative within the small- to medium-scale wind energy sector (Faisal et al., 2025). The ASWT is a biologically inspired design, drawing conceptual inspiration from natural growth patterns such as the Fibonacci spiral and the golden ratio, which are reflected in its continuously varying blade geometry (Salah Samiani & Boroushaki, 2025; Faisal et al., 2025). Structurally classified as an unconventional type of horizontal-axis wind turbine, the ASWT is distinguished by its spiral blade configuration, which enables high efficiency at low to moderate wind speeds, inherent passive alignment with the incoming wind, and reduced acoustic emissions (Faisal et al., 2025; Salah Samiani & Boroushaki, 2025).

The aerodynamic efficiency of the ASWT arises from its unique ability to exploit a synergistic combination of lift and drag forces during operation. At very low wind speeds, typically as low as 2.5 m/s, drag forces dominate and initiate rotor motion, while at higher wind speeds the contribution of lift becomes increasingly significant, enhancing overall power extraction efficiency (Faisal et al., 2025; Kamal et al., 2022; Salah Samiani & Boroushaki, 2025). Unlike conventional lift-based turbines that generally require wind speeds exceeding 5 m/s for effective operation, the ASWT is specifically designed to perform under low and highly variable wind conditions commonly encountered in urban environments (Refaie et al., 2021; Faisal et al., 2025). Moreover, the drag-induced forces acting on the spiral blades enable passive yaw control, allowing the rotor to automatically align with the wind direction without the need for complex active control or electronic yaw systems (Faisal et al., 2025; Salah Samiani & Boroushaki, 2025). Combined with its low tip speed ratio, typically in the range of 1.0 to 2.0, and aerodynamically smooth spiral surfaces that suppress large-scale turbulence, the ASWT achieves notably low noise levels, reported to be on the order of 45 dB(A), further reinforcing its suitability for urban deployment (Faisal et al., 2025; Song et al., 2022). These aerodynamic advantages, however, are inseparably linked to distinct structural loading conditions that directly influence blade material selection and manufacturing strategies. The ASWT commonly consists of three spiral blades arranged with a 120° angular offset around the rotational axis, forming a conical rotor configuration, as illustrated in Figure 4 (Faisal et al., 2025; Kim et al., 2014).

Figure 4: Definition of the blade angle for an ASWT rotor

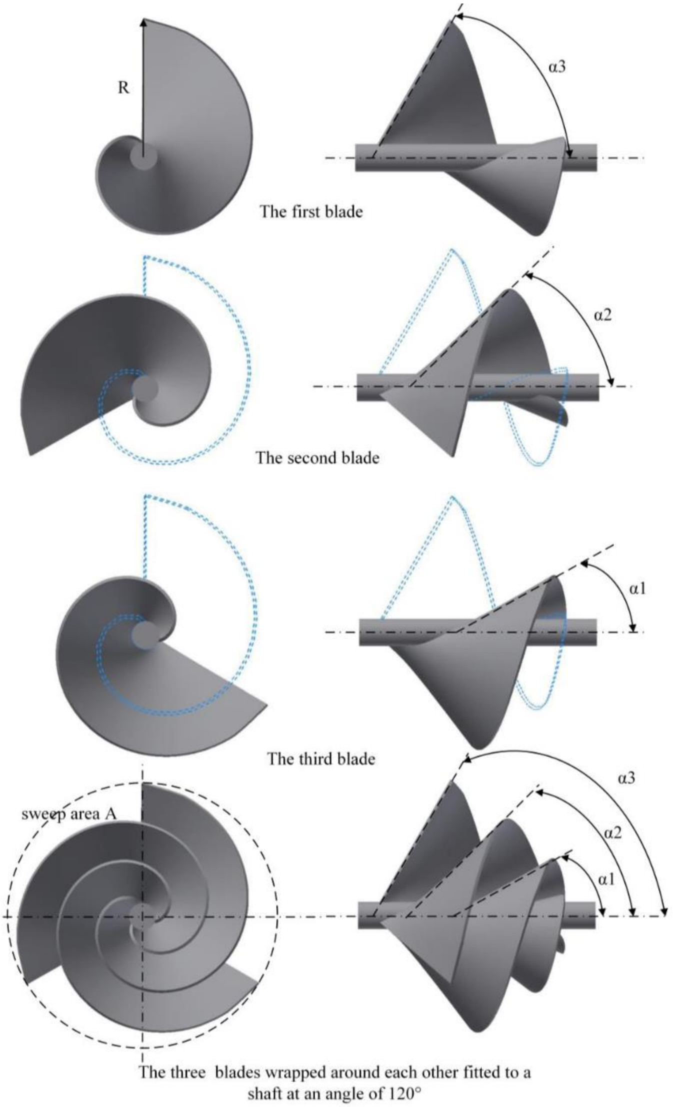

Reference: (Song et al., 2023)

While this geometry enhances aerodynamic performance, it also introduces two critical design constraints. First, ASWTs experience comparatively higher thrust loads than conventional propeller-type HAWTs, a consequence of their drag–lift hybrid operating principle (Salah Samiani & Boroushaki, 2025; Kamal et al., 2022). These thrust forces can be further amplified when the turbine is integrated with shroud or duct systems, thereby imposing stringent requirements on blade stiffness, strength, and long-term durability (Refaie et al., 2022; Faisal et al., 2025). Second, the complex curvilinear and continuously varying spiral geometry poses significant manufacturing challenges when conventional composite fabrication techniques are employed. As a result, specialized forming approaches have been explored to accommodate the geometric complexity of ASWT blades (Kamal et al., 2022; Kamal et al., 2023; Arivalagan et al., 2023).

Material utilization in ASWT research has evolved markedly over time, shifting from an initial emphasis on geometric feasibility and prototyping flexibility toward strategies aimed at improving structural reinforcement and dynamic stability in response to manufacturing and loading challenges. Early experimental studies explored the use of metallic blades for small-scale ASWT configurations, employing specialized forming techniques to achieve the required spiral geometry. However, these metal-based designs were found to be limited by excessive weight and inadequate fatigue performance under cyclic loading, leading to premature failure and restricting their applicability for long-term operation (Kamal et al., 2022; Mehri Khansari & Moghtader-ahar, 2025). As a result, research attention subsequently shifted toward additive manufacturing approaches, particularly the use of FDM with PLA, to enable rapid and cost-effective fabrication of micro-scale ASWT models with complex curvilinear geometries (Kamal et al., 2022; Kamal et al., 2023). While PLA-based blades exhibit improved structural behavior compared to materials such as ABS, their mechanical strength and durability remain insufficient for operational ASWT applications subjected to high thrust and fatigue loads (Arivalagan et al., 2023).

More recent studies reflect a further evolution in material strategy, focusing on enhancing the structural performance of ASWT blades through composite-based reinforcement approaches. In particular, the application of carbon/epoxy and glass/epoxy composite coatings onto conventionally formed metallic blades has been proposed as a means of combining the geometric formability of metals with the superior strength, stiffness, and fatigue resistance of fiber-reinforced composites (Mehri Khansari & Moghtader-ahar, 2025). This hybrid approach directly addresses the high thrust forces characteristic of ASWT operation and has demonstrated potential for improving dynamic behavior and vibration stability. A comparative overview of these material strategies, including their intended role in ASWT development, structural suitability, manufacturing requirements, cost implications, recyclability, and long-term operational viability, is summarized in Table 2. The table highlights a clear progression from prototyping-oriented materials toward structurally driven solutions, while also revealing persistent trade-offs between mechanical performance, manufacturing complexity, and sustainability that continue to shape material selection for ASWT blades.

Table 2: Comparative Analysis of ASWT Blade Materials

Criterion	PLA (FDM)	Metallic Blades	Composite Coatings (Carbon/Epoxy – Glass/Epoxy)
Primary Role in ASWT	Geometric prototyping and micro-scale testing	Early experimental blades for small turbines	Structural reinforcement of ASWT blades

Structural Capability	Very limited; suitable only for prototypes	Limited; high weight and poor fatigue resistance	High; improves stiffness, strength, and dynamic stability
Typical Scale of Use	Micro / laboratory scale	Small-scale experimental systems	Small to medium operational blades
Manufacturing Approach	FDM additive manufacturing	Specialized metal forming (e.g., conical roll-bending)	Composite coating on metallic substrates (VARTM / infusion)
Cost Level	Very low	High	High (carbon fiber dominant cost factor)
Fatigue Performance	Poor	Poor	Good to very good

Reference: (Arivalagan et al., 2023; Kamal et al., 2022; Kamal et al., 2023; Mehri Khansari & Moghtader-ahar, 2025; Cheng et al., 2025; Mishnaevsky et al., 2017; Refaie et al., 2022)

TPCS emerge as the next logical material platform for ASWT blades because they uniquely address the combined aerodynamic, structural, manufacturing, and sustainability challenges identified in existing material strategies. Unlike prototyping-oriented polymers such as PLA or metallic blades that are limited by weight and fatigue performance, TPCs provide a balanced combination of high specific strength, inherent toughness, and improved damage tolerance—attributes that are essential for resisting the high thrust loads and complex cyclic stresses characteristic of ASWT operation (Arivalagan et al., 2023; Kamal et al., 2022; Faisal et al., 2025). Compared with thermoset-based composite coatings, thermoplastic matrices enable fusion welding, repairability, and modular blade assembly, offering greater manufacturing flexibility for the highly curvilinear spiral geometries of ASWT blades while reducing sensitivity to defects associated with complex lay-up processes (Pradeep et al., 2019; Cheng et al., 2025; Hermansen & Lund, 2024b). Most importantly, the intrinsic recyclability of TPCs directly addresses the end-of-life limitations of conventional epoxy-based systems, which have become a critical concern as wind turbine blades reach decommissioning age (Msigwa et al., 2022; Çiftci, Erdoğan, & Genç, 2023). Collectively, these advantages position TPCS not as incremental alternatives, but as transformative material solutions capable of bridging the gap between geometric feasibility, structural reliability, scalable manufacturing, and environmental sustainability in next-generation ASWT blade design (Cheng et al., 2025; K. S., 2024).

DISCUSSION: CRITICAL EVALUATION OF MATERIAL RESEARCH FOR ARCHIMEDES SPIRAL TURBINE BLADES

The critical evaluation of material research for ASWT blades indicates that no single material system is universally optimal; rather, the appropriate material strategy is strongly dependent on the intended scale and maturity of the application. For prototyping and micro-scale ASWT development, PLA remains the most practical choice due to its excellent compatibility with FDM, which enables rapid, low-cost fabrication of highly complex spiral geometries and supports iterative aerodynamic and structural testing (Arivalagan et al., 2023). At the level of operational urban turbines, where performance requirements increase and economic constraints become decisive, strategically optimized hybrid composite systems combining glass and carbon fibers represent the most balanced solution. By selectively placing carbon fiber reinforcements only in high-stress regions, such hybrid architectures effectively manage the high thrust loads characteristic of ASWT operation while maintaining acceptable cost levels, offering a pragmatic compromise between the superior mechanical performance of CFRP and its high material cost (Hermansen & Lund, 2024b). Looking toward long-term sustainability and large-scale urban deployment, TPCS emerge as the most promising material platform. In addition to providing competitive mechanical performance and enhanced damage tolerance, their intrinsic recyclability directly addresses end-of-life challenges associated with conventional thermoset composites. Moreover, the weldability of thermoplastic matrices through fusion joining offers a decisive advantage in manufacturing complex spiral geometries, positioning TPCs as a viable and sustainable solution for mass-produced ASWT blades in future urban energy systems (Cheng et al., 2025).

The vast majority of existing wind turbine blade research has been developed around the structural integrity and aerodynamic optimization of conventional large-scale HAWTs employing standardized airfoil families such as NACA, LS, and LM profiles, where both geometry and manufacturing routes are well established (Hermansen & Lund, 2024b; Koul, 2025). In contrast, studies addressing the spiral blade concept remain confined to a relatively narrow and underexplored material and design space, with a pronounced disconnect between the turbine's complex curvilinear geometry and the capabilities of modern composite manufacturing technologies. A clear scale-related bias is evident in the literature, as most structural investigations of spiral blades are limited to micro-scale prototypes fabricated using FDM and PLA, prioritizing geometric feasibility over realistic mechanical performance; although PLA exhibits improved structural behavior compared to ABS, it remains inadequate for the high load-bearing capacity, fatigue resistance, and long-term environmental durability required for operational ASWTs (Arivalagan et al., 2023; Mehri Khansari & Moghtader-ahar, 2025). At the same time, the direct transfer of conventional thermoset composite systems such as GFRP and CFRP to spiral geometries is hindered by manufacturing incompatibilities, since techniques like VARTM are highly sensitive to the continuous twist, taper, and curvature of spiral blades, leading to an elevated risk of defects such as fiber waviness, void formation, and misalignment that compromise structural reliability (Bucur, Malael, & Predescu, 2021; Hermansen & Lund, 2024b). Compounding these challenges is the relative neglect of structural optimization strategies explicitly tailored to the high axial thrust loads inherent to ASWT operation, which arise from the combined lift–drag power extraction mechanism and impose severe demands on the blade root and spar cap regions (Refaie et al., 2021; Refaie et al., 2022; Song et al., 2022). Despite the demonstrated effectiveness of advanced approaches such as Discrete Material and Thickness Optimization (DMTO) in satisfying buckling, static strength, and fatigue constraints while minimizing mass in conventional blades, their systematic adaptation to spiral geometries has yet to be widely reported or validated, leaving a critical gap between conceptual ASWT designs and structurally optimized, manufacturable blade solutions (Hermansen & Lund, 2024b).

Addressing the material and structural challenges of spiral blade design is essential for advancing ASWT technology from a laboratory-scale concept to an industry-relevant solution capable of contributing meaningfully to global urban sustainability objectives. Urban areas are responsible for more than 65% of global energy consumption and approximately 70% of anthropogenic carbon emissions, underscoring the urgent need for decentralized, low-impact renewable energy technologies that can be effectively integrated into the built environment (Faisal et al., 2025). In this context, the ASWT’s ability to operate efficiently at very low wind speeds—down to approximately 2.5 m/s—combined with its inherently low noise emissions, represents a critical advantage for social acceptance and deployment on residential and commercial buildings (Faisal et al., 2025; Msigwa et al., 2022). At the same time, the distinctive geometric and structural demands of spiral blades create an opportunity to move beyond conventional thermoset composite technologies and adopt fully recyclable TPCS, thereby enabling a near–zero-waste design philosophy aligned with circular economy principles (Çiftci, Erdoğan, & Genç, 2023; Roga et al., 2022). Advanced thermoplastic matrices, such as the Elium® family, have demonstrated competitive mechanical durability while offering the ability to be repeatedly melted and reprocessed, making true closed-loop recycling feasible for wind turbine blades (Cheng et al., 2025). Moreover, the fusion-joining capability inherent to TPCs provides a practical manufacturing solution for complex spiral geometries, allowing prefabricated blade segments to be welded seamlessly into structurally continuous assemblies. This approach not only simplifies production and reduces defect sensitivity but also lowers manufacturing costs and environmental impact, reinforcing the case for TPCs as a key enabler of scalable, sustainable ASWT deployment in future urban energy systems (Koul, 2025; Cheng et al., 2025).

To advance ASWT blade technology toward robust commercial viability, future research must systematically address the remaining gaps in structural optimization, material–manufacturing compatibility, and end-of-life sustainability. From a design standpoint, there is a clear need for the development and validation of multidisciplinary optimization (MDO) frameworks specifically adapted to the complex, continuously curvilinear geometry of spiral blades. Approaches such as Discrete Material and Thickness Optimization (DMTO) should be extended beyond conventional HAWT applications to enable the simultaneous optimization of material systems (CFRP, GFRP, or hybrid architectures) and laminate configurations, with the explicit aim of managing high thrust loads while minimizing structural mass and satisfying critical constraints related to buckling resistance, static strength, and high-cycle fatigue performance (Hermansen & Lund, 2024b). In parallel, advanced manufacturing research should focus on demonstrating the industrial scalability of spiral blade production using TPCS. This includes pilot-scale validation of processes such as pultrusion and optimized VARTM/infusion routes adapted for thermoplastic matrices, as well as the refinement of fusion-joining techniques required to assemble large, segmented spiral blades with high structural integrity and repeatability (Cheng et al., 2025; Koul, 2025). Finally, the long-term sustainability of ASWT blades demands rigorous evaluation of fully recyclable matrix systems, particularly emerging concepts based on recycled LDPE matrices reinforced with carbon or glass fiber ribs. By eliminating thermoset resins and enabling efficient material separation and reuse, such architectures offer the potential to achieve near-complete recyclability and support a genuinely circular economic model for ASWT blade production (Çiftci, Erdoğan, & Genç, 2023). Collectively, these research directions define a clear roadmap for transforming spiral turbine blades from experimental prototypes into scalable, high-performance, and environmentally responsible components of future urban wind energy systems.

CONCLUSION

This study critically examines the evolution of wind turbine blade materials within the context of the ASWT, where geometric complexity, structural integrity, and urban sustainability requirements converge. Blade materials must simultaneously deliver high strength and stiffness, low density to mitigate gravitational effects, and excellent fatigue resistance under cyclic loading over a typical service life of approximately 20 years (Pradeep et al., 2019). Conventional thermoset-based composites, particularly GFRP and CFRP, satisfy many of these mechanical demands, with reported ultimate tensile strengths reaching up to 7 GPa (Cheng et al., 2025; Jiang et al., 2022). However, their application to ASWT blades introduces two fundamental limitations: significant challenges in end-of-life disposal due to poor recyclability (Çiftci, Erdoğan, & Genç, 2023), and substantial manufacturing difficulties when applied to the continuously curved, spiral blade geometry. While

PLA remains widely used for small-scale geometric modeling and prototyping (Arivalagan et al., 2023), it lacks the mechanical robustness required for operational deployment (Arivalagan et al., 2023). As a result, recent research trends increasingly emphasize green design principles that prioritize lightweight construction, ease of disassembly, and recyclability, including heterogeneous blade concepts based on recycled thermoplastic matrices such as LDPE, which offer high recyclability while minimizing or eliminating thermoset resin usage (Çiftci, Erdoğan, & Genç, 2023; Jureczko & Mrówka, 2022).

Based on the comparative analyses presented in this chapter, TPCS emerge as the most suitable long-term material solution for the industrial-scale realization of spiral turbine blades. A key advantage of TPCs lies in their manufacturability: the ability to employ fusion welding enables complex blades to be produced as modular segments and assembled with high structural continuity, thereby simplifying production, repair, and scalability (Salah Samiani & Boroushaki, 2025; Cheng et al., 2025). From a sustainability perspective, TPCs support closed-loop recycling schemes that are increasingly critical for urban energy infrastructure. In terms of structural performance, although ASWTs typically operate at low blade tip speed ratios in the range of 1.0–2.0, thermoplastic composite architectures provide sufficient toughness and damage tolerance to withstand the high axial thrust loads inherent to lift–drag hybrid operation, while remaining compatible with high-performance fiber reinforcements and optimized matrix systems (Jiang et al., 2022; Kamal et al., 2022).

Future research efforts should focus on bridging the gap between current prototyping-oriented studies and full-scale industrial deployment. In particular, advanced structural optimization frameworks should be systematically applied to spiral blade geometries, with the potential to achieve mass reductions of up to 31% while satisfying stringent requirements related to buckling, static strength, and fatigue life (Hermansen & Lund, 2024b). In parallel, the fabrication of large-scale thermoplastic composite profiles using processes such as pultrusion, together with the experimental validation of fusion-joining techniques, should be prioritized to demonstrate manufacturing feasibility at industrial scale (Cheng et al., 2025). Comprehensive fluid–solid interaction (FSI) analyses are also required to quantify the influence of blade deformation on aerodynamic performance and rotor dynamics (Mehri Khansari & Moghtader-ahar, 2025). Beyond wind energy, the underlying principles of spiral blade design and thermoplastic material integration may further extend to related applications, such as hydrokinetic turbines operating under low-flow conditions (Mehri Khansari & Moghtader-ahar, 2025; Jureczko & Mrówka, 2022).

In conclusion, the development of efficient, small-scale, and sustainable spiral turbine technologies holds particular strategic importance for the Republic of Türkiye's national energy objectives. Türkiye has significantly expanded its installed wind power capacity, increasing from 9,253 MW in May 2021 to 10,976 MW by December 2022 (Çiftci, Erdoğan, & Genç, 2023). While earlier studies estimated the national onshore wind potential at approximately 48,000 MW (Şenel & Koç, 2015), updated data released by the Ministry of Energy and Natural Resources in December 2024 indicate a substantially larger resource base, with 57,786 MW of onshore potential at sites exceeding an average wind speed of 6.5 m/s at 100 m height, and an additional 20,788 MW of offshore potential above 7.5 m/s (Republic of Turkey Ministry of Energy and Natural Resources, n.d.). Given the high cost associated with importing critical wind turbine components such as blades, gearboxes, and generators, the localization of blade manufacturing has become a strategic necessity (Şenel & Koç, 2015). In this context, sustained support from national institutions such as The

Scientific and Technological Research Council of Turkey (TÜBİTAK) and Small and Medium Enterprises Development and Support Administration (KOSGEB) for research and development of recyclable composite technologies is essential. Such a localization- and sustainability-driven approach not only reduces external dependency but also contributes directly to long-term economic growth and technological sovereignty (Şenel & Koç, 2015).

REFERENCES

Arivalagan, S., Sappani, R., Čep, R., & Kumar, M. S. (2023). Optimization and experimental investigation of 3D printed micro wind turbine blade made of PLA material. *Materials, 16*(6), 2508. https://doi.org/10.3390/ma16062508

Bashir, M. B. (2021). Principle parameters and environmental impacts that affect the performance of wind turbine: An overview. *Arabian Journal for Science and Engineering, 47*(7), 7891–7909. https://doi.org/10.1007/s13369-021-06357-1

Bucur, I. O., Malael, I., & Breban, S. (2020). Horizontal-axis wind turbine blades manufacture with composite materials. *IOP Conference Series: Materials Science and Engineering, 916*(1), 012012. https://doi.org/10.1088/1757-899X/916/1/012012

Bucur, I. O., Malael, I., & Predescu, M. (2021). Vertical axis wind turbine blade manufacturing using composite materials. *2021 10th International Conference on ENERGY and ENVIRONMENT (CIEM)*, 1–5. https://doi.org/10.1109/ciem52821.2021.9614931

Cheng, X., Fan, Z., Du, B., Chen, L., He, J., Long, W., Su, G., & Liu, J. (2025). A review of thermoplastic composites on wind turbine blades. *Composites Part B: Engineering, 299*, 112411. https://doi.org/10.1016/j.compositesb.2025.112411

Çiftci, C., Erdoğan, A., & Genç, M. S. (2023). Investigation of the Mechanical Behavior of a New Generation Wind Turbine Blade Technology. *Energies, 16*(4), 1961. https://doi.org/10.3390/en16041961

Faisal, A. E., Lim, C. W., Al-Quraishi, B. A., Alkawsi, G., Tan, C. H., Milano, J., Phing, C. C., Al-Farhany, K., & Tiong, S. K. (2025). Investigating the techniques used for improving the aerodynamic performance of Archimedes Spiral Wind Turbines: A comprehensive review and future work avenues. *Results in*

Engineering, 25, 103992. https://doi.org/10.1016/j.rineng.2025.103992

Firoozi, A. A., Firoozi, A. A., & Hejazi, F. (2024). Innovations in Wind Turbine Blade Engineering: Exploring Materials, Sustainability, and Market Dynamics. *Sustainability, 16*(19), 8564. https://doi.org/10.3390/su16198564

Fragkos, P. F., & Theotokoglou, E. E. (2025). Computational analysis of a wind turbine blade for different advanced materials. *Materials, 18*(11), 2447. https://doi.org/10.3390/ma18112447

Gebel, M. E., & Ermurat, M. (2021). Investigation of polymer matrix continuous fiber reinforced composite part manufacturability for composite additive manufacturing. *Journal of the Faculty of Engineering and Architecture of Gazi University, 36*(1), 57–67. https://doi.org/10.17341/gazimmfd.606618

Hamid, H., & Abd El Maksoud, R. M. (2023). *A comparative examination of the aerodynamic performance of various seashell-shaped wind turbines. Heliyon, 9*(6), e17036. https://doi.org/10.1016/j.heliyon.2023.e17036

Hermansen, S. M., & Lund, E. (2024b). Multi-material and thickness optimization of a wind turbine blade root section. *Structural and Multidisciplinary Optimization, 67*(7). https://doi.org/10.1007/s00158-024-03811-0

Jiang, Y., Finnegan, W., Flanagan, T., & Goggins, J. (2022). Optimisation of highly efficient composite blades for retrofitting existing wind turbines. *Energies, 16*(1), 102. https://doi.org/10.3390/en16010102

Jureczko, M., & Mrówka, M. (2022). Multiobjective optimization of Composite Wind Turbine Blade. *Materials, 15*(13), 4649. https://doi.org/10.3390/ma15134649

K S, V. (2024). Performance evaluation of composite materials for wind turbine blade design. *International Journal for Research in Applied Science and Engineering Technology, 12*(12), 889–900. https://doi.org/10.22214/ijraset.2024.65917

Kamal, A. M., Nawar, M. A. A., Attai, Y. A., & Mohamed, M. H. (2022). Blade design effect on Archimedes spiral wind turbine performance: Experimental and numerical evaluations. *Energy, 250*, 123892. https://doi.org/10.1016/j.energy.2022.123892

Kamal, A. M., Nawar, M. A. A., Attai, Y. A., & Mohamed, M. H. (2023). Archimedes spiral wind turbine performance study using different aerofoiled blade profiles: Experimental and numerical analyses. *Energy, 262*, 125567. https://doi.org/10.1016/j.energy.2022.125567

Kim, K., Ji, H., Kim, Y., Lu, Q., Baek, J., & Mieremet, R. (2014). Experimental and numerical study of the aerodynamic characteristics of an Archimedes spiral wind turbine blade. *Energies, 7*(12), 7893–7914. https://doi.org/10.3390/en7127893

Korawan, A. D., & Febritasari, R. (2024). Experimental investigations of number of blades effect on Archimedes spiral wind turbine performance. *Mechanical Engineering for Society and Industry, 4*(2), 198–209. https://doi.org/10.31603/mesi.12373

Korawan, A. D., & Febritasari, R. (2025). Corrigendum to "experimental investigations of number of blades effect on Archimedes spiral wind turbine performance" [mesi vol. 4, no. 2 (2024) pp 198-209]. *Mechanical Engineering for Society and Industry, 5*(1), 286–287. https://doi.org/10.31603/mesi.13996

Koul, P. (2025). Innovations in blade design for enhancing wind turbine efficiency: A review of aerodynamic, structural, and material advancements. *International Journal of Energetica, 9*(2), 12. https://doi.org/10.47238/ijeca.v9i2.258

Laawun Energy Solutions Australia Pty Ltd. (n.d.). *Our products*. Retrieved December 1, 2025, from https://www.laawunenergy.com.au/our-products

Mehri Khansari, N., & Moghtader-ahar, A. (2025). The effect of composite coating on dynamic behavior of glass/epoxy and carbon/epoxy Archimedes wind turbine blade: Considering fluid solid interaction. *Journal of Design Against Fatigue, 3*(1), 1–18. https://doi.org/10.62676/jdaf.2025.3.1.10

Mishnaevsky, L., Jr., Branner, K., Petersen, H. N., Beauson, J., McGugan, M., & Sørensen, B. F. (2017). Materials for wind turbine blades: An overview. *Materials, 10*(11), 1285. https://doi.org/10.3390/ma10111285

Msigwa, G., Ighalo, J. O., & Yap, P.-S. (2022). Considerations on environmental, economic, and energy impacts of wind energy generation: Projections towards Sustainability Initiatives. *Science of The Total Environment, 849*, 157755. https://doi.org/10.1016/j.scitotenv.2022.157755

Pradeep, A. V., Prasad, S. V. S., Suryam, L. V., & Kumari, P. P. (2019). A comprehensive review on contemporary materials used for blades of wind turbine. *Materials Today: Proceedings, 19*, 556–559. https://doi.org/10.1016/j.matpr.2019.07.732

Refaie, A. G., Abdel Hameed, H. S., Nawar, M. A. A., Attai, Y. A., & Mohamed, M. H. (2021). Qualitative and quantitative assessments of an Archimedes spiral wind turbine performance augmented by a concentrator. *Energy, 231*, 121128. https://doi.org/10.1016/j.energy.2021.121128

Refaie, A. G., Hameed, H. S. A., Nawar, M. A. A., Attai, Y. A., & Mohamed, M. H. (2022). Comparative investigation of the aerodynamic performance for several Shrouded Archimedes Spiral

Wind Turbines. *Energy, 239*, 122295. https://doi.org/10.1016/j.energy.2021.122295

Republic of Türkiye Ministry of Energy and Natural Resources, General Directorate of Energy Affairs. (n.d.). Rüzgar. Retrieved December 6, 2025, from https://enerji.gov.tr/eigm-yenilenebilir-enerji-kaynaklar-ruzgar

Roga, S., Bardhan, S., Kumar, Y., & Dubey, S. K. (2022). Recent technology and challenges of wind energy generation: A Review. *Sustainable Energy Technologies and Assessments, 52*, 102239. https://doi.org/10.1016/j.seta.2022.102239

Salah Samiani, O., & Boroushaki, M. (2025). Optimal design of Archimedes wind turbine using genetic algorithm. *Energy, 314*, 134157. https://doi.org/10.1016/j.energy.2024.134157

Savran, M., Yılmaz, M., Öncül, M., & Sever, K. (2022). Manufacturing and modeling of polypropylene-based hybrid composites by using multiple-nonlinear regression analysis. *Scientific Research Communications, 2*(1). https://doi.org/10.52460/src.2022.002

Song, K., Huan, H., & Kang, Y. (2023). Aerodynamic performance and wake characteristics analysis of Archimedes spiral wind turbine rotors with different blade angle. *Energies, 16*(1), 385. https://doi.org/10.3390/en16010385

Şenel, M. C., Koç, E. (2015). "Dünyada ve Türkiye'de Rüzgâr Enerjisi Durumu-Genel Değerlendirme," *Mühendis ve Makina*, cilt 56, sayı 663, s. 46-56.

Testbook. (n.d.). *Wind power plant: Working, diagram, types, advantages & plants in India.* Retrieved November 30, 2025, from https://testbook.com/electrical-engineering/wind-power-plant-and-its-working

Zarzoor, A., Jaber, A., & Shandookh, A. (2024). 3D printing for Wind Turbine Blade Manufacturing: A review of materials, design optimization, and challenges. *Engineering and Technology Journal, 0*(0), 1–17. https://doi.org/10.30684/etj.2024.144841.1646

CHAPTER 13

COLD CHAIN TRANSPORTATION: RECENT TRENDS, TECHNOLOGICAL INNOVATIONS, AND SUSTAINABILITY CHALLENGES

SERVET GİRAY HACIPAŞAOĞLU[1]

Introduction

Cold chain logistics is used to preserve the standard and quality of temperature-sensitive food items (fresh and frozen foods), pharmaceuticals and pharmaceutical products (pharmaceutical or biologic drugs) and vaccines by continually controlling their temperature from the point of production to the end consumer (Pajić, Andrejić, & Chatterjee, 2024). The availability of maritime transport of frozen food developed the international food market. The first recorded shipment was frozen meat from Buenos Aires to France in 1877 (James, James, & Evans, 2006, Behdani, Fan, & Bloemhof, 2019).

The inefficiency of this system has large economic, environmental and social costs, with some estimating that as much as one-third of all food produced for human consumption is lost or wasted in the food value chain (Heard & Miller, 2016). Increasing

---

[1] Research Assistant Ph.D., Kocaeli University, Department of Mechanical Engineering, Orcid: 0000-0001-6698-3562

the capacity of the cold chain is a major potential contributor towards food security and waste reduction, especially in developing countries (Pajić et al., 2024, Dong, Xu, & Miller, 2020). For example, cold storage capacity in China grew from 54 million m^3 in 2010 to 105 million m^3 in 2018 (Dong et al., 2020).

The primary function of refrigerated transport systems is to maintain equilibrium temperature. Since refrigerated transport systems are usually not designed to remove excess heat, applications of refrigerated transport usually require that the food be at the desired temperature prior to loading (James et al., 2006). The Vapor Compression Refrigeration Cycle (VCRS) is used by most refrigerated transport systems (Minetto, Fabris, Marinetti, & Rossetti, 2023, Maiorino, Petruzziello, & Aprea, 2021). Transport systems will typically operate if power is supplied to the compressor system, but mobile refrigeration systems experience more stress and strain than fixed systems due to the variable conditions to which they are exposed. Transport systems tend to be more constrained on size and weight, require higher reliability because resupply and maintenance over time are more difficult, and are exposed to more extreme environments such as acceleration, vibration, and direct exposure to solar radiation. This leads to a greater need for modeling and optimization (Maiorino et al., 2021, Gupta et al., 2023).

This study discusses the energy performance and environmental impact of refrigerant in VCRS systems, as well as strategies to substitute for VCRS with other technologies in energy saving applications. It focuses on engineering approaches used to improve the performance of heat pump systems, the thermal load modeling and the environmental burden (GHG emissions).

Evaluation of Thermodynamic Performance and Refrigerant Selection

The evaluation of thermodynamic performance and refrigerant selection plays a crucial role in optimizing the efficiency, sustainability, and environmental impact of cooling and power generation systems. A comprehensive assessment enables the identification of suitable working fluids that balance high energy efficiency with low global warming potential.

Limitations of Vapor Compression Refrigeration Systems

The most common cooling system for vehicles on the road is a VCRS that is often run from auxiliary diesel engines (Minetto et al., 2023, Maiorino et al., 2021). Transport refrigeration units are often over-sized to handle a range of normal design operating conditions. However, the output may be as much as 1.75 times the calculated thermal load (Tassou, De-Lille, & Ge, 2009, Maiorino et al., 2021). The design coefficient of performance (COP) is low, because mobile systems experience a wide variety of environmental and operating conditions (James et al., 2006). Design COP is typically between 0.5 and 1.5. VCRS units are also sensitive to load changes and tend to cycle on/off or modulate their capacity to maintain set point temperature leading to lower efficiencies (Tassou et al., 2009). If belt-driven or driven indirectly by the vehicle engine, low load, idling (low speed) or engine stop conditions lead to particularly low efficiencies and poor fuel economy (Maiorino et al., 2021). A schematic representation of the VCRS is shown in Figure 1, and the corresponding lnP-h diagram is shown in Figure 2.

Figure 1. Schematic representation of the VCRS

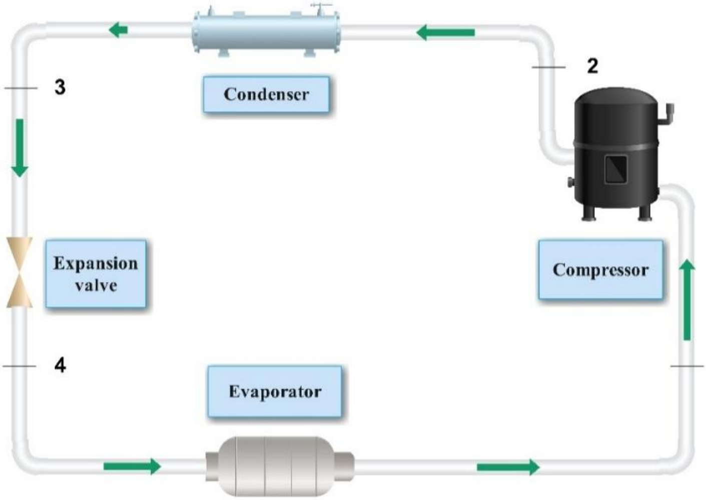

Figure 2. lnP-h diagram of the VCRS

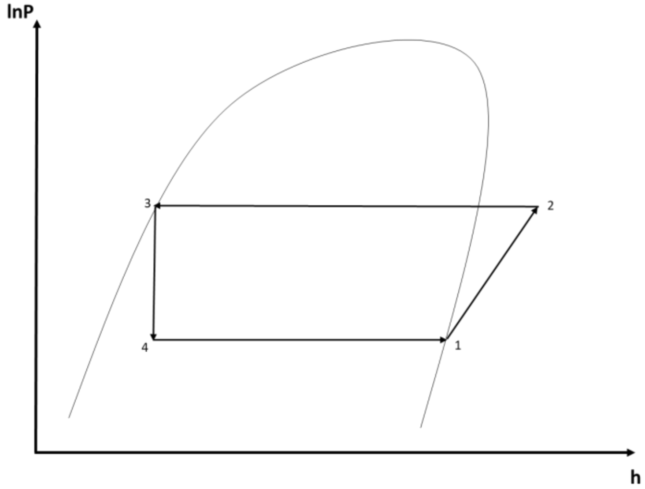

Environmental Impact of Refrigerants

The total greenhouse gas (GHG) emissions of refrigerated transport systems originate from two main sources:

Indirect Emissions (Energy Consumption)

These emissions come from the diesel fuel burnt for the refrigeration system which makes up between 70% and 91% of the emissions from the systems (Wu et al., 2022). The GHG emissions from VCRS units driven by diesel engines can account for up to 40% of total GHG emissions for a vehicle's main mode of propulsion (Tassou et al., 2009, Niu et al., 2025b).

Direct Emissions (Refrigerant Leakage)

Truck refrigeration systems using HFCs such as R404A and R507A again have a high GWP (Minetto et al., 2023, Gao et al., 2021). Open-type compressor construction and truck vibration usually result in annual refrigerant loss rates of 10-37% in mobile refrigeration systems, which are much higher than stationary refrigeration systems. International treaties such as the Kigali Amendment have started phasing down refrigerants with high global warming potential (high-GWP) and have incentivized the use of low-global warming potential natural working fluids (NWFs) (Gao et al., 2021).

Applications of Natural Working Fluids (NWFs)

Natural working fluids such as ammonia (NH_3), carbon dioxide (CO_2), or hydrocarbons (propane, isobutane, etc.) are amongst the most promising ways to develop a potentially less harmful refrigeration system. These fluids have low GWP and zero ODP and can replace many of the synthetic refrigerants with a high GWP.

R744 (CO_2) Systems

CO_2 is non-toxic and non-flammable, and as such is the only natural refrigerant suitable for many compact applications. It is used in applications from marine transport to frigate containers. However, the transcritical conditions generally used in these applications can be difficult to operate efficiently, and subcritical operation may be needed at high ambient temperatures (Minetto et al., 2023). Thus, advanced cycle modifications, such as adding ejectors, parallel compression and Internal Heat Exchangers (IHX), can have an important effect on the performance of the overall system. For example, when using an ejector-based system, the COP can increase up to 15.9% compared with a customary CO_2 refrigeration cycle (Maiorino et al., 2021).

Ammonia (R717)

Due to its very high efficiency and very low environmental impact, R717 (ammonia) is still the most widely used refrigerant in large-scale cold stores and shipping (Gao et al., 2021). As R717 is toxic, a mixture of R717 and R744 (CO_2) is often used in cascade systems (often R717-R744 systems) to minimize refrigerant charge while taking advantage of high thermal efficiency and low environmental impact (Yalama et al., 2022).

Hydrocarbons (HCs – R290)

R290 (propane) systems bring a 10% to 30% higher COP in medium- and low-temperature applications relative to a R404A-based system but require special precautions and a maximum refrigerant charge due to high flammability. These standards include the international safety standard EN 378, which includes maximum refrigerant charge, ventilation requirements and safety design criteria to enable the use of confined or other potentially safe refrigerants in stationary and mobile refrigeration systems (Minetto et al., 2023, Maiorino et al., 2021).

Advanced Cooling Technologies and System Design

In recent years, improved cooling systems and designs for stationery and mobile applications have resulted in more energy-efficient, more sustainable, and more reliable refrigeration systems, through the application of novel cycle designs, highly efficient controls, and environmentally superior working fluids/refrigerants.

Thermal Energy Storage (TES) Systems / Phase Change Materials (PCM)

Compared to regular thermal energy stores, PCMs offer the possibility of storing large amounts of cooling energy and subsequently releasing them at peak loads or in the case of multiple drop openings (multi-drop deliveries). This allows refrigeration using PCM-based systems to reduce electrical power consumption and CO_2 emissions by 22 to 56% compared to conventional VCRS systems (Wu et al., 2022). PCMs are also included in the insulation in walls. This allows for the thermal load on the building to be reduced, and delays the peak heat flow through a wall, leading to room temperatures that are more stable. Key PCM properties are high latent heat of fusion, the melting temperature comparable to the temperature of the wall, and high thermal conductivity. Therefore, PCMs are very suitable for cost-effective and energy-efficient sustainable cold chain applications (Maiorino et al., 2021).

Thermal Compressor Systems (Absorption / Adsorption)

The systems replace the mechanical compressor in a conventional VCRS with a "thermal compressor" powered by waste heat from an external source, such as a diesel engine's exhaust, reducing the fuel consumption and indirect emissions of the refrigeration system (Maiorino et al., 2021, Tassou et al., 2009). These systems have been tested up to 6 and 10 kW but are still only a concept because they depend heavily on the load on the engine. At light loads, for example when idling, as in a stop-and-go traffic scenario typical for city driving, where exhaust temperatures are at most 150 °C, providing sufficient heat requires back-up (Minetto et al., 2023). A backup burner or a secondary cooling system, such as eutectic plates, is required to maintain continuous operation. These additional systems help maintain engine temperature and cooling power when the engine is at low load or the vehicle stationary (Maiorino et al., 2021).

Air Cycle Refrigeration Systems

Air cycle refrigeration systems use air as a refrigerant. Air has a zero-emission advantage over synthetic refrigerants such as R404A (Minetto et al., 2023). Air cycle refrigeration systems are comparatively less affected by the part-load conditions than VCRS equipment, allowing them to be more efficient at providing any amount of cooling. In modeling studies, air cycle systems designed for use at low temperatures had a COP of 0.53 at −20 °C. The benefits of energy reduction can be as high as 35% over a customary VCRS at partial load conditions (Tassou et al., 2009). The drawbacks are a low COP compared to vapor compression systems and a limited availability of commercial components for the transport refrigeration market. Research continues miniaturization of components, turbomachinery optimization, and heat recovery implementation to improve performance and commercialization of the technology (Maiorino et al., 2021).

Innovative Power Sources

Numerous new technologies are being developed to reduce diesel engine and fossil fuel utilization in transport refrigeration systems with the goal of improving energy efficiency and reducing carbon emissions. These new technologies partially or fully replace the mechanical drive system and may be used in stationery and mobile systems.

Hydrogen-Powered Refrigeration Systems (HPRS)

These are hybrid electric systems that use Proton Exchange Membrane Fuel Cells (PEMFCs) as a supplementary clean energy source, with Li-ion batteries, to power the refrigeration system without having to run the vehicle's main engine, such as when the latter is idling at a distribution point, or in urban delivery loops. Experimental trials suggest that HPRS systems can operate for over 4 hours in the most demanding urban driving conditions without an interruption of supply to guarantee cooling availability. Fuel savings of over 10% have been claimed for HPRS over diesel-powered refrigeration units, and a reduction in carbon dioxide emissions of approximately 3650 kg per vehicle per year. The results indicate the potential of PEMFC-battery hybridization to improve energy efficiency, operational flexibility, and sustainability for future hydrogen-powered transport refrigeration applications (Segura et al., 2023).

Photovoltaic (PV) Systems

The VCRS units can be powered using photovoltaic (PV) panels mounted on the roof of the truck to capture solar energy. This makes it economic to deploy the technology on long-haul, or chilled urban delivery routes, reducing the requirement for the diesel engine truck alternator to power the refrigeration unit (James et al., 2006). With optimal PV oversizing strategies and battery integration techniques, where PV capacity, storage capacity and cooling energy requirements are well matched, the case studies showed CO_2 emissions savings reaching up to 89% compared to conventional diesel power plants. The payback was estimated to be 6 years based on fuel savings and reduction in maintenance costs across the system's lifetime. Results suggest the technology can provide economic and environmental savings through solar assisted refrigeration when coupled with hybrid battery-PCM systems and energy management strategies to counteract variations in solar and thermal inputs (Meneghetti, Dal Magro, & Romagnoli, 2021).

Recent Studies Employing Advanced Cooling Techniques

Goudarzi & Taghizadeh, (2023) analytically studied the two-cycle Rankine-ejector refrigeration system for an internal combustion engine waste heat recovery and compared it with the novel Rankine absorption system. They used environmentally-friendly R1233zd and R32. According to the outcomes of the research conducted, this paper proved that the novel cycle would have performance improvement with a higher output. The COP was around 69.99%. Liang et al., (2020) studied a heat-driven refrigeration system for refrigerated trucks with a S-CO_2 power cycle that is integrated with a T-CO_2 refrigeration cycle, with the expander of the S-CO_2 power cycle driving the compressors of the T-CO_2 refrigeration cycle. The S-CO_2/T-CO_2 combined cycle with a common-cooler configuration was shown to be thermodynamically feasible and have a performance comparable to that of the conventional refrigeration cycle. The engine exhaust heat was found to be adequate for the cooling duty required by a refrigerated truck. Shi, Tian, & Shu, (2020) proposed and optimized a multi-mode CO_2 based combined refrigeration and power cycle system, which can work in refrigeration, power generation, or combined power and refrigeration modes for the waste heat recovery of an engine of a refrigerated truck. Simulation results indicated a reduction in the fuel consumption of 2.9 to 3.4% and an increase in the power output of 1.6 to 4.8% in the combined mode. Zhang et al., (2021) proposed a transcritical CO_2 Rankine cycle and ejector refrigeration cycle for the waste heat recovery of a cruise ship. Multi-objective optimization, based on Artificial Bee Colony (ABC) algorithm, was applied to gain maximum useful energy production in Mode-S and Mode-SAW of a cruise ship. It was reported that ejector refrigeration outperformed reference cycles in Mode-S with 863.3 kW for maximum cooling production and 202.9 kW of net power. Maximum high-temperature heating production at Mode-SAW was reported as 960.5 kW. Zhu et al., (2025) modified CO_2 combined power and ejector-expansion refrigeration cycle with dual evaporators and cascaded ejectors for dual-temperature refrigerate trucks with lower exergy destruction, with 10.22% higher exergy efficiency in refrigeration/freezing mode, high refrigeration and freezing capacity of 18.79 kW and 33.80 kW respectively, and short payback period of 4.994 years. Butrymowicz et al., (2021) experimentally field tested a prototype low pressure steam indirect transfer subsystem in a proof-of-concept waste heat recovery system for small marine engines, tested with both an ejector refrigeration cycle and a shipboard heating system. The tests demonstrated that, from flue gas waste heat, a compact refrigerant ejector refrigeration system could deliver 30 kW of clutch cooling, and a further 60 kW of waste heat could be captured via the water jacket of the engine for heating. Chen, et al., (2013) went on to theoretically model and experimentally test a hybrid ejector and CO_2 vapor compression (VC) vehicle air conditioning system. The vehicle exhaust gas was used to drive the ejector, which provided sub-cooling for the CO_2 VC sub-system. From thermodynamic modeling, the hybrid system had a COP of 0.584, showing a 22% improvement over a single ejector cycle. Pan et al., (2020) proposed a hybrid use (topping RSCBC and bottoming EERC) of regenerative supercritical CO_2 Brayton cycle (RSCBC) and ejector expansion refrigeration cycle (EERC) respectively to produce power and refrigeration from engine waste heat for refrigerated trucks. The zeotropic mixture of refrigerants R32/CO_2 (0.9/0.1) exhibited the best performance, having the highest refrigerating capacity of 225.5 kW and COP_{comb} of 2.05. The RSCBC/EERC system could be a solution to the above, providing more refrigeration capacity and power to be used for the vehicle when refrigeration is not necessary. Yüksel & Hacıpaşaoğlu, (2025) investigated the integrated organic Rankine and ejector refrigeration cycle for mobile cooling applications, using four eco-friendly refrigerants: R134a, R290, R1233zd(E) and n-Pentane. The overall system COP, during the parametric study, the refrigerant R1233zd(E) provided the best overall performance. The best working fluid for an integrated power/cooling system was R1233zd(E), followed by R290 as the second-best fluid. The schematic diagram of the EERC can be seen in Figure 3, while the lnP-h diagram of the EERC can be seen in Figure 4.

Figure 3. Schematic representation of the EERC

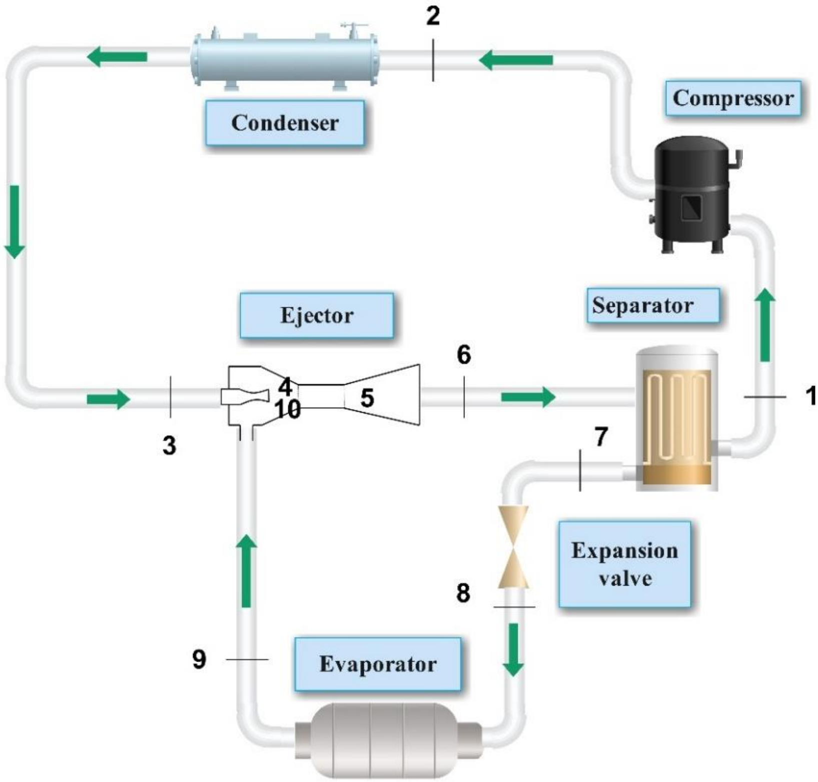

Figure 4. lnP-h diagram of the EERC

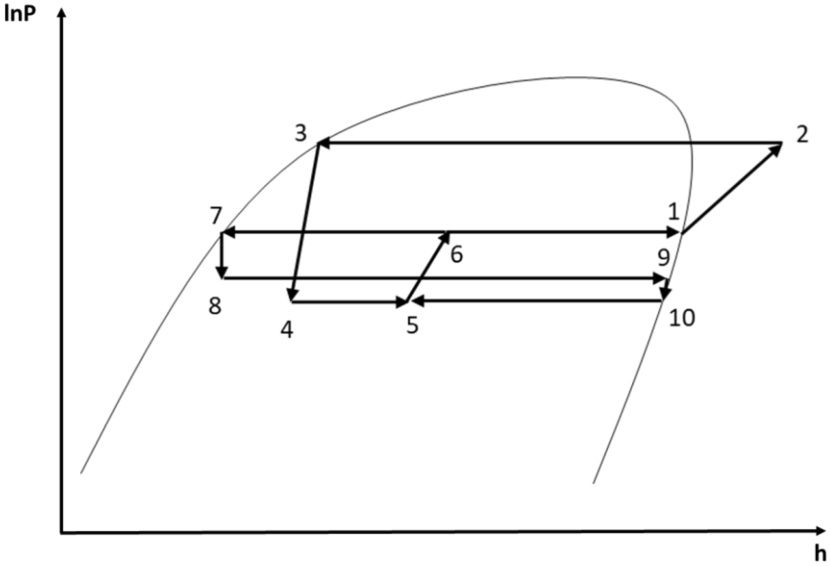

Heat and Mass Transfer Modeling and Optimization

In this section the thermal modeling approaches for the refrigerated transport systems are presented. Thermal modeling is the approach to predict heat and mass transfer that occur during their transport. This section provides the objectives of the thermal modeling approaches and the underlying concepts. The following chapter covers models used to describe the airflow and temperature distribution using Computational Fluid Dynamics (CFD). Advanced modeling methods such as Graph-based hybrid optimization methods (GraPHsep) are covered to model the system for multiple conditions as well as methods to lower the thermal load to improve the energy performance of the system.

Purpose and Scope of Thermal Modeling

The thermal model is used to predict the heat and mass transfers during the transport, either on the level of the air of the cargo compartment or on the level of the product. An acceptable dynamical model should consider all transfer modes, namely the exchange of heat between the surrounding air and the walls, solar radiation, conduction in the cargo compartment structure, and air leakages. Furthermore, the model should also account for time-dependent effects such as ambience, door openings, loading/unloading functions, to assess the transport and model the cooling load extracted by the refrigeration system (James et al., 2006).

Computational Fluid Dynamics (CFD)

CFD is also used to calculate the airflow and temperature distribution in refrigerated vehicles. CFD tools can show how those variables change in such environments due to, for example, the stacking of goods and the placement of air ducts (Zhao, Zhang, & Xu, 2020). Testing has shown that the use of air channels reduces the maximum temperature difference of the air temperature within the cargo hold from 12 to 8 °C. CFD modeling is used to assess the effectiveness of air curtains in preventing warm air entering the cargo hold when doors to the hold are opened, thereby maintaining a uniform temperature during loading and unloading (James et al., 2006). In general, efficient design of advanced refrigeration systems will benefit greatly from CFD-based analysis.

Advanced Modeling Approaches

The Graph-based Hybrid Separation (GraPHsep) method is a graph theory-based novel methodology for the design and optimization of refrigeration cycles. Contrary to previous work carried out in optimization, e.g., when a cycle is optimized under a single condition of operation, GraPHsep considers the optimization of the relevant cycles under the four representative conditions (summer/winter and frozen/chilled). The method uses a graph of linked components for the thermodynamic cycle to find the optimum layouts for the different situations. The layouts are then combined into one flexible configuration, so the motion modes can be switched over with minimal hardware changes. This enables operational flexibility and better environmental performance through better cycle implementation (Niu et al., 2025a). An example of the GraPHsep tool for multidisciplinary design is the design of a CO_2 refrigeration system. The results of a study provided possibilities for switching the system between chill and freeze modes and achieving a Total Equivalent Warming Impact (TEWI) value that is 18% lower than that of a standard R404A refrigeration system. This shows that GraPHsep is a multi-objective design tool for sustainable next-gen refrigeration systems (Niu et al., 2025a).

Thermal Load Reduction Strategies

The thermal load reduction strategies include cooling demand reduction and energy use reduction from refrigerated transport. The total thermal load is driven by the solar load, the heat gains due to air infiltration during the opening of the door, conduction through the insulating panels and the respiration heating from the product.

Air Infiltration Control

For example, during multi-drop operations over several stops, where 50 doors might be opened and closed to access, load and unload a number of pieces of freight, warm air entry to the cargo area is the source of up to 30% of the system's energy consumption, causing increased compressor workload and instability in the conditions maintained in the cargo area (James et al., 2006). Air curtains, or strip curtains can be used to limit air infiltration. CFD analysis of a carefully designed air curtain system can result in a 71% reduction in air infiltration, enabling a reduced cooling load. Appropriate control of air infiltration can thus improve the thermal inertia, energy efficiency, and longevity of refrigerated stores and transport (James et al., 2006, Maiorino et al., 2021).

Insulation and Performance Degradation

The efficiency of insulating materials used in refrigerated transport units generally declines with time (3 to 5% for every year of use). This increase in the thermal load generally causes more energy to be required to maintain the target temperature as it becomes less efficient (James et al., 2006). The main degrading factors reducing thermal insulation performance are moisture absorption, mechanical stress, UV radiation, and aging of the material. Because Vacuum Insulation Panel (VIP)s have extremely low thermal conductivities (in the range of 0.002 to 0.004 W/m·K), VIPs can be a very good alternative to conventional polyurethane foams in thermal insulation applications. The high price of manufacture, along with its susceptibility to thermal bridging (heat loss through contact between panels and imperfect aspects of the infrastructure), is limiting its use. Work continues to enable composites and hybrid insulation systems to be low cost, lightweight, long life and high performance, to provide thermal protection for future cold-chain transport systems (Maiorino et al., 2021).

Sustainability Metrics and Conclusion

Sustainability assessment of refrigerated transport systems addresses the transport systems' sustainability in terms of energy efficiency and carbon emissions along their entire life cycle. Total emissions are typically expressed as TEWI, Life Cycle Climate Performance (LCCP) or as a carbon footprint estimate. These indicators identify how the design of the refrigeration system, the refrigerant used, and strategies employed to control the heat gain can help to minimize the carbon footprint of cold-chain logistics. The cost-effectiveness of the process, the routing of vehicles and fuel consumption are also important aspects of sustainable cold-chain logistics. The replacement of high-GWP refrigerants with low GWP alternatives, along with the adoption of renewable energy and state-of-the-art controls, can create a more resilient, cost-effective, and lower carbon cold chain system.

Life Cycle Analysis and Emissions

Life cycle metrics, including TEWI and LCCP, can be useful in assessing the environmental impact of refrigeration systems. These metrics take both the direct emissions due to refrigerant leakage and indirect emissions due to energy use into account. Life Cycle Assessment (LCA) studies have demonstrated that in the use phase of VCRS the most important contributor (84-91% of the system's carbon footprint) is energy consumption (Wu et al., 2022). Replacing a conventional refrigerant (e.g. R404A) with low GWP refrigerant R744 (CO_2) can reduce the carbon footprint of the system by 3.2-3.9% over a typical 10-year lifetime. An alternative is PCM-based cold storage systems (PCCSS) charged through the electric grid. PCCSS can reduce the entire value chain's carbon footprint by up to 56% compared to VCRS when the lower emission factor of the electric grid is accounted for. This illustrates the potential for refrigerant replacement, renewably powered equipment and thermally optimized storage equipment in cold chain transport systems (Wu et al., 2022).

Cost–Efficiency Balance

Cold-chain logistics can also be modeled as Complex Vehicle Routing Problems (VRP) that have additional objectives such as minimizing distance, vehicle fuel cost, refrigeration cost, carbon emission cost (carbon tax). Such routing problems can be modeled with the objective of minimizing the total cost of the logistics operation, which can be defined as the sum of vehicle fixed cost, cost of fuel, carbon emission cost, cooling cost, cost of time penalty and cost of split compensation (Xu et al., 2023). Improving the load factor of a truck reduces costs and the carbon footprint of the transportation process and leads to fewer trips that consume energy in the infrastructure. Practical advanced optimization schemes also allow for the use of time windows, load divisibility, multi-depot deliveries and alternative delivery profiles (Zulkefly et al., 2021). Complete VRP optimization approaches in China indicated a potential for reducing total distribution cost by 35% and that this integrated logistics-energy-environmental optimization approach could support sustainable refrigerated transport (Xu et al., 2023).

Conclusion and Future Trends

Sustainable solutions would require more efficient cold chains, low-GWP refrigerants and, in the end, successful commercialization of next-generation HPRS and CO_2 systems, coupled with energy-efficient, reliable, and sustainable electric and hybrid transport systems. In support, a common set of testing methods and a common Life Cycle Inventory (LCI) database are needed to quantitatively compare the performance of those systems. Such a move would allow these systems to be further improved in terms of energy efficiency, reliability, durability, and environmental friendliness, resulting in improved refrigeration systems. To conclude, the future of cold-chain transportation will be one of advanced thermodynamic design combined with renewable energy, as well as data-driven lifecycle analysis technologies, to create a resilient, efficient, carbon-neutral cold-chain refrigeration infrastructure.

References

Yüksel, M. A. & Hacıpaşaoğlu, S. G. (2025). Energy Analysis of the Integrated Organic Rankine Ejector Cycle For Cooling Transport Vehicles. *Isarc 7. International Uludağ Scientific Research Congress*, 3 - 04 Ekim, Bursa, 106-120.

Behdani, B., Fan, Y., & Bloemhof, J. M. (2019). Cool chain and temperature-controlled transport: An overview of concepts, challenges, and technologies. In *Sustainable Food Supply Chains: Planning, Design, and Control through Interdisciplinary Methodologies* (pp. 167–183). Elsevier. https://doi.org/10.1016/B978-0-12-813411-5.00012-0

Butrymowicz, D., Gagan, J., Łukaszuk, M., Śmierciew, K., Pawluczuk, A., Zieliński, T., & Kędzierski, M. (2021). Experimental validation of new approach for waste heat recovery from combustion engine for cooling and heating demands from combustion engine for maritime applications. *Journal of Cleaner Production*, *290*. https://doi.org/10.1016/j.jclepro.2020.125206

Chen, X., Worall, M., Omer, S., Su, Y., & Riffat, S. (2013). Theoretical studies of a hybrid ejector CO2 compression cooling system for vehicles and preliminary experimental investigations of an ejector cycle. *Applied Energy*, *102*, 931–942. https://doi.org/10.1016/j.apenergy.2012.09.032

Dong, Y., Xu, M., & Miller, S. A. (2020). Overview of cold chain development in china and methods of studying its environmental impacts. *Environmental Research Communications*, *2*(12). https://doi.org/10.1088/2515-7620/abd622

Gao, E., Cui, Q., Jing, H., Zhang, Z., & Zhang, X. (2021, August 1). A review of application status and replacement progress of refrigerants in the Chinese cold chain industry. *International Journal of Refrigeration*, Vol. 128, pp. 104–117. Elsevier Ltd. https://doi.org/10.1016/j.ijrefrig.2021.03.025

Goudarzi, K., & Taghizadeh, A. (2023). A Combined Power and Ejector Refrigeration Cycle System for Thermal Energy Recovery from the Waste Heat of Internal Combustion Engine. *Journal of Energy and Power Technology*, *05*(01), 1–23. https://doi.org/10.21926/jept.2301006

Gupta, P., Kumar, P., Elarga, H., & Hafner, A. (n.d.). *Refrigerated Transportation and Cold-chain Logistics in India-Current Status and Future Prospects*. https://doi.org/10.18462/iir.icr.2023.0371

Heard, B. R., & Miller, S. A. (2016, November 15). Critical research needed to examine the environmental impacts of expanded refrigeration on the food system. *Environmental Science and Technology*, Vol. 50, pp. 12060–12071. American Chemical Society. https://doi.org/10.1021/acs.est.6b02740

James, S. J., James, C., & Evans, J. A. (2006, September). Modelling of food transportation systems - a review. *International Journal of Refrigeration*, Vol. 29, pp. 947–957. https://doi.org/10.1016/j.ijrefrig.2006.03.017

Liang, Y., Sun, Z., Dong, M., Lu, J., & Yu, Z. (2020). Investigation of a refrigeration system based on combined supercritical CO2 power and transcritical CO2 refrigeration cycles by waste heat recovery of engine. *International Journal of Refrigeration*, *118*, 470–482. https://doi.org/10.1016/j.ijrefrig.2020.04.031

Maiorino, A., Petruzziello, F., & Aprea, C. (2021). Refrigerated transport: State of the art, technical issues, innovations and challenges for sustainability. *Energies*, *14*(21). https://doi.org/10.3390/en14217237

Meneghetti, A., Dal Magro, F., & Romagnoli, A. (2021). Renewable energy penetration in food delivery: Coupling photovoltaics with transport refrigerated units. *Energy*, *232*. https://doi.org/10.1016/j.energy.2021.120994

Minetto, S., Fabris, F., Marinetti, S., & Rossetti, A. (2023, August 1). A review on present and forthcoming opportunities with natural working fluids in transport refrigeration. *International Journal of Refrigeration*, Vol. 152, pp. 343–355. Elsevier Ltd. https://doi.org/10.1016/j.ijrefrig.2023.04.015

Niu, H., Cui, M., Wang, B., & Shi, W. (2025). Numerical study on a multifunctional small-capacity refrigeration system for logistics cold storage based on the GraPHsep method. *Applied Thermal Engineering*, *280*. https://doi.org/10.1016/j.applthermaleng.2025.128109

Niu, H., Liu, X., Wang, B., Wang, Y., Liu, Y., & Shi, W. (2025). Assessment of GHG emissions from small-capacity logistics cold storage in China based on field measurements. *Energy and Buildings*, *345*. https://doi.org/10.1016/j.enbuild.2025.116117

Pajić, V., Andrejić, M., & Chatterjee, P. (2024). Enhancing Cold Chain Logistics: A Framework for Advanced Temperature Monitoring in Transportation and Storage. *Mechatronics and Intelligent Transportation Systems*, *3*(1). https://doi.org/10.56578/mits030102

Pan, M., Bian, X., Zhu, Y., Liang, Y., Lu, F., & Xiao, G. (2020). Thermodynamic analysis of a combined supercritical CO2 and ejector expansion refrigeration cycle for engine waste heat recovery. *Energy Conversion and Management*, *224*. https://doi.org/10.1016/j.enconman.2020.113373

Segura, F., Vivas, F. J., Andújar, J. M., & Martínez, M. (2023). Hydrogen-powered refrigeration system for environmentally friendly transport and delivery in the food supply chain. *Applied Energy*, *338*. https://doi.org/10.1016/j.apenergy.2023.120945

Shi, L., Tian, H., & Shu, G. (2020). Multi-mode analysis of a CO2-based combined refrigeration and power cycle for engine waste heat recovery. *Applied Energy*, *264*. https://doi.org/10.1016/j.apenergy.2020.114670

Tassou, S. A., De-Lille, G., & Ge, Y. T. (2009). Food transport refrigeration - Approaches to reduce energy consumption and environmental impacts of road transport. *Applied Thermal Engineering*, *29*(8–9), 1467–1477. https://doi.org/10.1016/j.applthermaleng.2008.06.027

Wu, J., Liu, G., Marson, A., Fedele, A., Scipioni, A., & Manzardo, A. (2022). Mitigating environmental burden of the refrigerated transportation sector: Carbon footprint comparisons of commonly used refrigeration systems and alternative cold storage systems. *Journal of Cleaner Production*, *372*. https://doi.org/10.1016/j.jclepro.2022.133514

Xu, B., Sun, J., Zhang, Z., & Gu, R. (2023). Research on Cold Chain Logistics Transportation Scheme under Complex Conditional Constraints. *Sustainability (Switzerland)*, *15*(10). https://doi.org/10.3390/su15108431

Zhang, Q., Luo, Z., Zhao, Y., & Pavel, S. (2021). Thermodynamic analysis and multi-objective optimization of a transcritical CO2 waste heat recovery system for cruise ship application. *Energy Conversion and Management*, *227*. https://doi.org/10.1016/j.enconman.2020.113612

Zhao, Y., Zhang, X., & Xu, X. (2020, January 1). Application and research progress of cold storage technology in cold chain transportation and distribution. *Journal of Thermal Analysis and Calorimetry*, Vol. 139, pp. 1419–1434. Springer Science and Business Media B.V. https://doi.org/10.1007/s10973-019-08400-8

Zhu, Y., Liang, Y., Liang, Y., Kong, B., Pan, M., Wang, Z., & Deng, H. (2025). Analysis of modified CO2 based combined power and ejector-expansion refrigeration cycle with dual evaporators activated by engine exhaust. *International Journal of Green Energy*, *22*(6), 974–989. https://doi.org/10.1080/15435075.2023.2195483

Zulkefly, N. S., Hishamuddin, H., Rashid, F. A. A., Razali, N., Saibani, N., & Rahman, M. N. A. (2021). The effect of transportation disruptions on cold chain sustainability. *Evergreen*, *8*(2), 262–270. https://doi.org/10.5109/4480702

Ялама, В. В., Хмельнюк, М. Г., Яковлева, О. Ю., & Трандафілов, В. В. (2022). Modern refrigeration solutions for maritime sector and marine refrigeration transport. *Refrigeration Engineering and Technology*, *58*(4), 184–194. https://doi.org/10.15673/ret.v58i4.2568

BİDGE